Universidade de São Paulo
Instituto de Física

Otimização de pontos quânticos de submonocamada de InAs/GaAs crescidos sobre GaAs(001) com uma reconstrução de superfície (2 × 4) para fotodetectores de radiação infravermelha

Ahmad Al Zeidan

Orientador: Prof. Dr. Alain André Quivy

Tese de doutorado apresentada ao Instituto de Física como requisito parcial para a obtenção do título de Doutor em Ciências.

Banca Examinadora:
Prof. Dr. Alain André Quivy – IFUSP
Prof. Dr. Danilo Mustafa – IFUSP
Prof. Dr. Fernando Josepetti Fonseca – EPUSP
Prof. Dr. Germano Maioli Penello – UFRJ
Prof. Dr. Fernando Massa Fernandes – (UCL – Univ. Cath. Louvain - Bélgica)

São Paulo
2023

FICHA CATALOGRÁFICA
Preparada pelo Serviço de Biblioteca e Informação do Instituto de Física da Universidade de São Paulo

Al-Zeidan, Ahmad

Otimização de pontos quânticos de submonocamada de InAs/GaAs crescidos sobre GaAs(001) com uma reconstrução de superfície (2 × 4) para fotodetectores de radiação infravermelha. São Paulo, 2023.

Tese (Doutorado) - Universidade de São Paulo. Instituto de Física. Depto. Física dos Materiais e Mecânica.

Orientador: Prof. Dr. Alain André Quivy

Área de Concentração: Física da Matéria Condensada.

Unitermos: 1. Epitaxia por feixe molecular; 2. Pontos quânticos; 3. Submonocamada de InAs; 4. Fotodetectores; 5. Infravermlho..

USP/IF/SBI-042/2023

University of São Paulo
Institute of Physics

Optimization of InAs/GaAs submonolayer quantum dots grown on GaAs(001) with a (2 × 4) surface reconstruction for infrared photodetectors

Ahmad Al Zeidan

Supervisor: Prof. Dr. Alain André Quivy

Thesis submitted to the Physics Institute of the University of São Paulo in partial fulfillment of the requirements for the degree of Doctor of Science.

Examining Committee:

Prof. Dr. Alain André Quivy – IFUSP
Prof. Dr. Danilo Mustafa – IFUSP
Prof. Dr. Fernando Josepetti Fonseca – EPUSP
Prof. Dr. Germano Maioli Penello – UFRJ
Prof. Dr. Fernando Massa Fernandes – (UCL – Univ. Cath. Louvain - Bélgica)

São Paulo
2023

Acknowledgements

My first thanks and praise go to God, the almighty, who has provided me with strength and encouragement in all the challenging moments of this work. Then I would like to take this opportunity to express my gratitude to the people who have always been there for me and who have influenced my life in so many ways.

First and foremost, I am deeply indebted to my doctoral advisor Prof. Dr. Alain André Quivy. To him, I extend my sincere gratitude for all his support, encouragement, guidance, help, and especially his patience and advices over the past seven years since I have been under his supervision as a master's student.

I am also deeply indebted to Prof. Paul Simmonds and his group at Boise State University, especially Kevin Vallejo and Katie Sautter, for their efforts in growing some samples included in this thesis. I thank you for the financial support you provided for growing and shipping the samples at your own expense.

My special thanks to Prof. Paul Koenraad and Dr. Raja Gajjela of the Eindhoven University for performing X-STM measurements on the samples of this thesis.

In addition, I would like to thank Prof. Christoph Deneke and Ailton Garcia for their assistance in training me for using the MBE system at the Brazilian Nanotechnology National Laboratory (LNNano). A special thanks should be given to Dr. Jefferson Bettini, from LNNano, who measured one sample shown in this thesis by transmission electron microscopy (TEM).

I am extremely grateful to all the members of the MBE group at LNMS, namely, Thales Borrely, Tiago de Cantalice, Marcelo de Lima, Victor Curbelo, Geraldo Chagas, and especially Sérgio Urahata for his support and help in revising my thesis.

To my friends Ahmad Aghe, Fuad Arisheh, Khalid Alhamady, Mahmoud Alhalak, and Tarek Fawaz for their moral support. And there are many more and I am equally grateful to all of them.

My sincere thanks go to all the staff of the Institute of Physics and the Post-Graduate Office (CPG) belonging to the University of São Paulo, and especially Prof. Lucy Assali, for their assistance with the official documents.

I would like to express my sincere thanks for the financial support provided by the Coordenação de Aperfeiçoamento de Pessoal de Nível Superior - Brasil (CAPES) - Finance Code 001 and CNPq (grant 311687/2017-2).

Ahmad Al Zeidan

São Paulo, June 2023

Dedication

I dedicate this work to my dear family, especially my parents Ibrahim and Mariam, as well as my loving wife Maram and my little daughter Layana for their unconditional love, support, and encouragement.

"Our responsibility is to do what we can, learn what we can, improve the solutions, and pass them on"

Richard P. Feynman
Nobel Prize in Physics in 1965

Abstract

In the present work, we have investigated the application of InAs/GaAs submonolayer quantum dots (SML-QDs) as a new type of nanostructures for mid-infrared detection, which are slowly replacing conventional Stranski-Krastanov quantum dots (SK-QDs) in some specific applications. Photoluminescence (PL) and cross-seccional scanning tunneling microscopy (X-STM) were used to investigate and optimize their growth conditions. Subsequently, several infrared photodetectors based on InAs/GaAs SML-QDs were grown by molecular beam epitaxy, processed in a clean room by photolithography, and finally tested extensively to determine how their performance improves when grown with a (2×4) surface reconstruction, achieved either at low temperatures (490 °C) with a low As flux (8.0×10^{-8} Torr) or at high temperatures (528 °C) with a high As flux (7.0×10^{-7} Torr). Since one drawback of SK-QDs is their low surface density—which is roughly 10-100 times lower than that of SML-QDs—we also propose a way to further increase their density using the seed concept. By pre-depositing InAlAs quantum dots, which naturally have a density 10 times higher than InAs SK-QDs, the strain field generated by the first layer of InAlAs QDs can serve as a seed to nucleate the second layer of InAs QDs, which helps to increase their density when the separation is kept small.

Keywords: Photodetectors; Quantum dots; InAs Submonolayer; Molecular beam epitaxy; InAlAs.

Resumo

No presente trabalho, investigamos a aplicação de pontos quânticos de submonocamada de InAs/GaAs (SML-QDs) como um novo tipo de nanoestruturas para a detecção de radiação no infravermelho médio, que vem aos poucos substituindo os pontos quânticos convencionais de Stranski-Krastanov (SK-QDs) em algumas aplicações específicas. As técnicas de fotoluminescência (PL) e microscopia de varredura por tunelamento em seção transversal (X-STM) foram utilizadas para investigar e otimizar suas condições de crescimento. Posteriormente, vários fotodetectores de radiação infravermelha baseados em SML-QDs de InAs/GaAs foram crescidos por epitaxia de feixe molecular, processados em uma sala limpa por fotolitografia e, finalmente, testados extensivamente para determinar o desempenho deles quando crescidos com uma reconstrução de superfície (2×4) que pode ser alcançada em baixas temperaturas (490 °C) com baixo fluxo de As (8.0×10^{-8} Torr) ou em altas temperaturas (528 °C) com alto fluxo de As (7.0×10^{-7} Torr). Como uma das desvantagens dos SK-QDs é a baixa densidade superficial deles—que é aproximadamente 10-100 vezes menor que a dos SML-QDs—também propomos uma maneira de aumentar a densidade dos próprios InAs SK-QDs usando o conceito de semente. Ao pré-depositar pontos quânticos de InAlAs, que naturalmente possuem uma densidade cerca de dez vezes maior que a dos SK-QDs de InAs, o campo de tensão gerado pela primeira camada de QDs de InAlAs pode influenciar a nucleação dos SK-QDs de InAs na segunda camada, o que contribui para aumentar a densidade de nanoestruturas na camada superior quando a camada de GaAs entre as duas é mantida muito fina.

Palavras-chave: Fotodetectores; pontos quânticos; submonocamada de InAs; epitaxia por feixe molecular; InAlAs.

List of Figures

Figure 1-1: Thermal imaging (infrared) illustrating (a) the thermal insulation faults of a house; (b) the frontal neck thermogram showing a hot pattern over the region of the right side of the thyroid; (c) the monitoring of an onion crop. The legend on the right side represents the temperature color ramp in℃. 33

Figure 1-2: The global market for infrared detectors by region and application. During the period 2021-2031, it is expected to grow 7.7% (CAGR, compound annual growth rate). 33

Figure 2-1: Schematics of the electromagnetic spectrum showing the range of the visible and IR spectra. 36

Figure 2-2: Atmospheric transmission spectrum showing two IR windows at 3-5 µm and 8-14 µm regions. 37

Figure 2-3: Schematic diagram of how thermal IR detectors operate. 38

Figure 2-4: Relative spectral response of a photon and thermal detector. 39

Figure 2-5: (a) intrinsic absorption from the valence to the conduction band; (b) extrinsic absorption from a donor impurity level (n-type doping) to the conduction band; (c) free-carrier absorption inside the conduction band. 40

Figure 2-6: Schematic illustration of broken symmetry and functional form of the density of states in different types of structures and their degree of confinement of the carriers; (a) bulk material with no confinement; (b) quantum well with a 1D confinement; (c) quantum wire with a 2D confinement; (d) quantum dot with a 3D confinement. 41

Figure 2-7: Schematics representation of quantum dots growth using the SK growth mode. From left to right, we can see that below a critical thickness, growth occurs in a 2D regime (layer by layer). However, once the material reaches a critical thickness (1.7 MLs in the case of InAs deposited on top of GaAs), the strained epitaxial layer relaxes and forms a high density of small strained islands surrounded by a wetting layer. 43

Figure 2-8: Schematic diagram of conduction band illustrating the photocurrent generation process in InAs/GaAs QDIPs under bias. 44

Figure 2-9: Structure of a standard SK-QDIP containing a top and bottom contact layer surrounding the active region consisting of x layers of InAs SK-QDs. 44

Figure 2-10: Schematics of InAs/GaAs submonolayer quantum dots obtained by repeating 4 times a basic cycle consisting of 0.5 ML of InAs (step 1) followed by 2.5 MLs of GaAs (step 2). The black box in image (3) represents a single SML-QD. 46

Figure 3-1: The Varian MBE system of the "Laboratório de Novos Materiais Semicondutores" at the Institute of Physics of the University of Sao Paulo. One can see the entry-exit chamber (access inside the clean room), the buffer chamber, and the growth chamber. 49

Figure 3-2: Side view of the buffer chamber showing the two transfer rods and the rail on top of which the trolley (in the back) can be moved with an external magnet (on top). 49

Figure 3-3: The opened door of the entry-exit chamber located in the clean room where the trolley is ready to be removed for changing the samples. 50

Figure 3-4: (a) Main components of the growth chamber of the Gen II MBE system; (b) Top view of the growth chamber of the Gen II MBE system at LNMS. 52

Figure 3-5: (a) Typical MBE solid effusion cell with a crucible; (b) Typical valved cracker for Arsenic; (c) Schematic drawing of the valved cracker. 54

Figure 3-6: (a) The trolley with several Mo blocks (substrate holders); the small samples were fixed with Indium melted at 200 ºC, and the large samples (1/4 of a wafer) were fixed with clips; (b) The trolley with the new samples is loaded into the entry-exit chamber whose hatch door is located in the clean room. 55

Figure 3-7: RHEED setup inside the growth chamber of the MBE system: the electron beam is reflected/diffracted by the surface of the sample and then observed by a CCD camera on a phosphor screen. 56

Figure 3-8: RHEED pattern of a GaAs(001) surface; (a) immediately after oxide removal (spotty pattern); (b) after the deposition of 30 nm of GaAs (streaky pattern with specular spot). 57

Figure 3-9: Diagram and interpretation of the RHEED oscillations. The left image shows the intensity of the specular spot as a function of time, where one period (a, b, c, and d) of the oscillation corresponds to the deposition of a single monolayer. The right image relates the physical evolution of the surface (nucleation of 2D GaAs islands) to each RHEED intensity. 58

Figure 3-10: (a) Typical RHEED oscillation obtained during calibration of a Ga cell. The Ga and As cells were simultaneously opened, and the growth rate is given by dividing the number of oscillations by the respective time. (b) RHEED oscillations obtained during calibration of the As flux. First, the As shutter was closed and the Ga shutter was opened to deposit the equivalent to 8 MLs of material. Then, the As shutter was opened to allow the As molecules to react with the Ga atoms and form 8 GaAs layers, as can be confirmed by the number of oscillations. 60

Figure 3-11: Comparison of the 3 growth methods. (a) Frank-van der Merwe; (b) Volmer-Weber; (c) Stranski-Krastanov. 61

Figure 3-12: (a) RHEED pattern of an atomically flat GaAs surface at 515 °C in a c(4×4) surface reconstruction just before InAs deposition; (b) just after deposition of 1.7 MLs of InAs and nucleation of the first InAs SK-QDs. 62

Figure 3-13: Scheme of the formation of SML-QDs: (a) Deposition of an InAs submonolayer (0.5 ML) on top of GaAs to nucleate small 2D InAs islands; (b) Coverage of the InAs islands with GaAs material (2.5 MLs); (c) Vertical alignment of the islands of consecutive InAs submonolayers; (d) InGaAs SML-QDs (blue box) formed by repeating 4 times the basic deposition cycle. 63

Figure 3-14: (a) RHEED pattern of an atomically flat GaAs surface before starting to grow InAs SML-QDs, (b) just after the deposition of 0.5 ML of InAs to nucleate small 2D InAs islands (Figure 3-13-a), and (c) just after deposition of 2.50 MLs of GaAs to cover the 2D islands (Figure 3-13-b). 64

Figure 3-15: Atomic representation of bulk GaAs(001) in the zincblende structure. Ga and As planes alternate along the [001] direction with a spacing of 1.41 Å. 65

Figure 3-16: Reconstruction phase diagram of the arsenic-rich GaAs(001) surface as measured using RHEED. The solid lines indicate the transitions between the three reconstructions as indicated. The dotted lines indicate the transitions between the three sub-phases of the (2×4) reconstruction. 66

Figure 3-17: Model of the atomic structure of the different types (α, β, γ) of As-rich GaAs(001)-(2×4) surface reconstructions. The upper part of the figure represents a top view of the surface reconstruction, while the bottom part is a side view of the same surface. Filled (open) circles denote As (Ga) atoms. 67

Figure 3-18: Top and side views of the Ga–As dimer and As–As dimer structures of the As-stabilized GaAs(001)-c(4×4) surface. Closed (open) circles denote As (Ga) atoms. 68

Figure 3-19: RHEED patterns of the GaAs surface before the growth of the SML-QDs at 500°C along (a) the [110] direction with a high As flux (c(4×4) reconstruction); (b) the [110] direction with a low As flux ((2×4) reconstruction); (c) the [010] direction with a high As flux (c(4×4) reconstruction); (d) the [010] direction with a low As flux ((2×4) reconstruction). After the growth of the SML-QDs, the patterns were very similar to the initial ones. (e) Periodicity of some surface reconstructions along several directions. RHEED measurements are usually performed along [110] to calibrate the materials. 70

Figure 4-1: Main physical processes involved in a photoluminescence experiment. 72

Figure 4-2: Schematics of a PL experiment. (a) solid-state laser; (b) chopper and (b´) its controller; (c) small mirror; (d) first focusing lens; (e) cryostat with samples; (f) second focusing lens; (g) monochromator; (h) Ge/Si detector at the exit slit; (i) lock-in amplifier; (j) computer. 72

Figure 4-3: Typical PL spectrum at 77 K of a sample containing SML-QDs. The FWHM is obtained by calculating the difference in energy on both sides of the emission peak, where the intensity is half of the maximum intensity. 73

Figure 4-4: Structure of samples containing different types of In(Ga)As nanostructures to be analyzed by PL; sample #A contains 2.2 MLs of InAs to form conventional SK-QDs; sample #B contains a basic cycle of 0.5/2.5 MLs of InAs/GaAs repeated six times to form SML-QDs; sample #C contains a 5.1 nm wide $In_{0.17}Ga_{0.83}As$/GaAs quantum well. 74

Figure 4-5: Samples fixed on the cold finger of a liquid-nitrogen optical cryostat. 75

Figure 4-6: PL spectra of samples #A, #B, and #C; the measurements were performed at 77 K with a slit of 0.4 mm. The emission of sample #C saturated the detector, and its maximum was estimated to be at the center of the peak. 75

Figure 4-7: Schematic diagram of a typical AFM. During scanning of the surface by the tip, a laser beam is reflected from the back of a micro-fabricated cantilever to which the sharp tip is attached to measure its deflection. 77

Figure 4-8: The three most common modes of AFM operation: contact mode, tapping mode, and non-contact mode. 78

Figure 4-9: (a) Full AFM system at LNMS equipped with an anti-vibration table, a sound-insulation box (also for controlled ambient), control units, and a computer to acquire and process images; (b) The AFM itself—that is normally installed inside the white sound-insulation box of figure a—with its scanning head (top), camera (left) and 6” sample holder (bottom). 79

Figure 4-10: Structure of different types of samples, two of them containing InGaAs nanostructures, to be checked by AFM. Sample #A1: 2.2 MLs of InAs SK-QDs (similar to sample #A but without GaAs cap layer); Sample #B1: 0.5 ML of InAs (half of the first cycle of sample #B used to form SML-QDs); Sample #C1: 200 nm-thick GaAs buffer to be used as a reference. The structures of samples #A1 and #B1 were also grown on top of a 200 nm-thick GaAs buffer. 80

Figure 4-11: 1×1 μm^2 AFM images showing the surface of (a) 2.2 MLs of InAs SK-QDs deposited on the buffer layer; (b) 0.5 ML of InAs material (first layer of the basic cycle of a SML-QD) deposited on the buffer layer, and (c) a 200 nm-thick GaAs buffer deposited at 570 °C. 81

Figure 4-12: (a) JEM-2100F TEM of the Brazilian Nanotechnology National Laboratory (LNNano) that was used in this study, (b) TEM schematic diagram. 82

Figure 4-13: (a) TEM image of sample #D, which consists of ten AlGaAs/GaAs quantum wells containing each a single layer of InAs/GaAs SML-QDs in the well, consisting of 6 repetitions of 0.35 ML of InAs followed by 2.65 MLs of GaAs. The AlGaAs barriers appear as wide dark stripes with, between them, narrow brighter regions related to the wells containing the SML-QDs. (b) High-resolution image of the inner part of one QW containing SML-QDs. The InAs material appears as darker regions. (c) Filtered and processed image of Figure b. Many 1-3 nm-large dark regions appear but seem more related to image-processing effects than to the presence of SML-QDs. 84

Figure 4-14: (Left) TEM image of 5 layers of SML-QDs separated by 50 nm of AlGaAs. (Right) Colored compositional maps of the rectangular region are shown on the left. Ga, As, and In atoms are shown in green, blue, and red, respectively. The red map shows that most of the In atoms are concentrated in a 5-10 nm wide region of the map (due to segregation), and no clear clustering or periodic structure is observed, as would be expected in well-formed SML-QDs. The two larger red images on the right are simply a magnification of the two small regions shown on the main In 85 map. Again, very small 1-3 nm wide clusters may be observed but are more likely due to lack of resolution (noise average during processing).

Figure 4-15: (a) Scheme of the working mechanism of a STM, showing the tip, sample, piezoelectric scanner for x-y-z tip motion, feedback system, and the computer control system; (b) Two main operation modes of an STM: constant-current and constant-height scanning modes. 86

Figure 4-16: Illustration of the principle of (a) top-view scanning tunneling microscopy (usual STM technique) and (b) cross-sectional scanning tunneling microscopy. To image semiconductors successfully at the atomic scale, both techniques must be operated in ultra-high vacuum. 87

Figure 4-17: Schematic structure of the samples grown by MBE for X-STM experiments; sample #A2 contained 2.2 MLs of InAs SK-QDs; sample #B2 contained SML-QDs formed by repeating six times 0.5/2.5 MLs of InAs/GaAs. All the layers were doped to 10^{18} cm^{-3}, except the QDs and 40 nm of GaAs below and above them. Actually, both samples #A2 and #B2 contained other layers, but only the ones of interest (similar to samples #A and #B but grown on a Si-doped substrate) are shown here. 88

Figure 4-18: X-STM filled-state topographic image of sample #A2 containing 2.2 MLs of InAs. From dark to bright, the color contrast corresponds to a difference in the height of 0 to 250 pm out of the cleaved surface. Bright regions have more In atoms than dark ones. The scale bar has a length of 10 nm, and the white arrow indicates the growth direction [001]. 88

Figure 4-19: Filled-state images (80 × 25 nm^2) of the SML-QDs of sample #B2 taken at bias a voltage of –2.1 V and a tunneling current of It = 50 pA. The arrow indicates the growth direction [001]. (a) filled-state image allowing to observe As atoms; (b) empty-state image allowing to observe In and Ga atoms. 89

Figure 5-1: Typical structure of a SML-QDs sample to be analyzed by PL measurements. Here, the basic cycle of 0.5/2.5 MLs of InAs/GaAs was repeated 4 times. 92

Figure 5-2: PL spectra of SML-QDs consisting of 0.5 ML of InAs and 2.5 MLs of GaAs repeated 4 times. Each sample had a different As flux (BEP) during SML-QDs formation. 93

Figure 5-3: PL spectra of SML-QDs consisting of 0.5 ML of InAs and 2.5 MLs of GaAs repeated 4 times. Each sample had a different growth rate for the GaAs interlayer. 95

Figure 5-4: PL spectra of SML-QDs consisting of 0.5 ML of InAs and 2.5 MLs of GaAs repeated 4 times. Each sample had a different InAs growth rate. The FWHM values are 10.5 meV and 16.4 meV for high and low growth rates, respectively. 96

Figure 5-5: PL spectra of SML-QDs consisting of n ML of InAs and 3-n MLs of GaAs repeated 4 times, where n=0.35, 0.5, or 0.65 ML. The FWHM values are 5.6 meV, 14.5 meV, and 19.7 meV for n=0.35, 0.5, or 0.65 ML, respectively. 97

Figure 5-6: PL spectra of SML-QDs structures consisting of 0.5 ML of InAs and 2.5 MLs of GaAs repeated N times. FWHM values are 13.9 meV, 14.5 meV, and 16.0 meV for N=4, 7, or 10 repetitions, respectively. 98

Figure 5-7: Specific conducting sample #E for the X-STM measurements. All five SML-QDs layers were grown under different growth conditions to check their influence on the formation of SML-QDs. Layers #1, #3, and #4 differed only by the As flux (6×10^{-8}, $2\times10^{-7,}$ and 7×10^{-7} Torr (BEP), respectively). Layer #2 had SML-QDs built from 10 repetitions instead of 6, and layer #5 was grown using high growth rates of InAs and GaAs typically used for SK-QDs. 100

Figure 5-8: Filled-state images (80×25 nm^2) of the SML-QDs of layers #1 – #5 (illustrated in Figure 5-7) taken at bias voltage V_b = –2.1 V and tunneling current I_t = 50 pA. The arrow indicates the growth direction [001]. The bright (yellow) spots represent In-rich regions, while the rest of the images consists of the crystalline GaAs matrix (blue lines). 103

Figure 5-9: PL spectra at 77K of the InAs/GaAs SML-QDs samples differing only by the growth temperature. 108

Figure 5-10: structure of InAs/GaAs SML-QDs containing the same InAs fraction (0.5 ML) but different GaAs spacers. (a) 2.5MLs, (b) 1.5MLs, and (c) 0.5ML. The black rectangle shows an individual SML-QD. The average In content of the layers is shown. The average In content of each individual SML-QD is twice that of the layers. 110

Figure 5-11: Structure of set of samples #F1 consisting of X cycles of 0.3 ML of InAs + 0.7 ML of GaAs—with X= 5, 7, 8, 9, or 11—to be checked by AFM (no cap layer). 110

Figure 5-12: 1×1 μm^2 AFM images showing the surface of the set of samples shown in Figure 5-11, consisting of X cycles of 0.3 ML of InAs + 0.7 ML of GaAs, with X= 5, 7, 8, 9, or 11. The last sample (named SKQDs) contains 10.6 MLs of $In_{0.3}Ga_{0.7}As$ deposited on GaAs using the 111

SK growth mode to produce conventional SK-QDs. The critical thickness of $In_{0.3}Ga_{0.7}As$ deposited on top of GaAs was measured to be 9.30 MLs using the RHEED technique.

Figure 5-13: Structure of set of samples #F consisting of X cycles of 0.3 ML of InAs + 0.7 ML of GaAs—with X= 5, 7, 8, 9, or 11—covered with 150 nm of GaAs to be analyzed by PL. 112

Figure 5-14: PL spectra at 77 K of the set of samples of Figure 5-13 containing X repetitions of 0.3/0.7 InAs/GaAs with X= 5, 7, 8, 9, or 11. Above 8 repetitions, the spectra are much wider, redshifted, and compatible with the formation of SK-QDs detected in Figure 5-12. 113

Figure 5-15: PL spectra of the set of samples of Figure 5-13 with 7 and 8 repetitions compared to conventional $In_{0.3}Ga_{0.7}As$ SK-QDs and a 6 MLs-wide $In_{0.3}Ga_{0.7}As$ QW measured at 77K. 113

Figure 6-1: Clean room (ISO 6) of the “Laboratório de Novos Materiais Semicondutores”. On the left side, the mask aligner can be seen, while on the right side, there are two chemical hoods for photoresist handling (spinning and baking) and chemical etching of the samples. 116

Figure 6-2: The main steps of the processing of a photodetector: (I) sample and its structure, (II) photoresist spinning, (III) mesa mask and exposure, (IV) positive development, (V) etching down to the bottom contact, (VI) removal of photoresist (stripping), (VII) photoresist spinning, (VIII) contact mask and exposure, (IX) development, (X) metallization, (XI) lift-off, (XII) wire bonding. 117

Figure 6-3: (a) E-beam deposition system with the deposition chamber (right), turbomolecular vacuum pump (center), control computer (left), and power + control units of the electron beam (bottom, in black). (b) Illustration of the e-beam evaporation process. 118

Figure 6-4: (a) Rapid thermal annealing system with a quartz tray and 3" Si wafer to lay the samples on. (b) RTA model AccuThermo AW 610 without its cover, showing top and bottom banks of 1 kW halogen lamps in the oven unit. 119

Figure 6-5: (a) Probe station equipped with four probes controlled by mechanical xyz translators, a microscope, and a CCD camera. The equipment is installed inside a grounded metallic box to reduce noise and allow measurements in the dark. The semiconductor parameter analyzer is connected to the four probes via low-noise triaxial cables enabling high-sensitivity I×V curves. (b) Testing a mesa (black squares have an area of 120

400×400 μm^2) with two probes. One probe touches the top contact (gold squares have an area of 100×100 μm^2) while the other touches the bottom contact common to all mesas.

Figure 6-6: (a) Commercial chip carrier with a sample fully processed and connected. (b) Wire bonder used to connect the mesas to the chip carrier with thin Au wires (ϕ= 25 μm). 120

Figure 6-7: (a) Optical cryostat for 12-300 K operation with a Ge window; (b) Processed sample installed on the cold finger. 121

Figure 6-8: Experimental setup for the absorption measurements using FTIR spectroscopy; (a) FTIR spectrometer; (b) Cryostat with a photodetector to be tested; (c) Transimpedance amplifier; (d) Computer. 122

Figure 6-9: The experimental setup for photocurrent measurements (black-body responsivity). (a) Optical cryostat with the photodetector to be tested; (b) Black body at 800 °C; (c) Transimpedance amplifier; (d) Chopper; (e) Chopper controller; (f) lock-in. 123

Figure 6-10: The main components of the dark current in a photoconductive photodetector: (a) thermally excited electrons above the barrier; (b) field-assisted tunneling; (c) direct tunneling. 124

Figure 6-11: Experimental setup for the I-V curve experiment (dark current). (a) Cryostat fully mounted with a dark shield surrounding the sample; (b) Source-measure unit with attoampere sensitivity; (c) computer. 124

Figure 6-12: On the left is the experimental setup for the noise-current measurements. (a) Cryostat with a dark shield around the device under test; (b) Low-noise transimpedance amplifier; (c) Dynamic signal analyzer. On the right is a typical frequency spectrum of the total current obtained by the dynamic signal analyzer, showing the 1/f noise, the harmonics of the network, the noise from the cryogenic system, and the intrinsic noise from the device (white noise). The signal of the photocurrent (in red) is only observed when the noise measurements are performed together with the photocurrent measurements—i.e., no longer in the dark. 126

Figure 6-13: Experimental setup for simultaneous measurement of photocurrent and noise. (a) Optical cryostat with the photodetector under test; (b) Black body at 800 °C; (c) Transimpedance amplifier; (d) Chopper; (e) Chopper controller; (f) Dynamic signal analyzer. The noise is measured in the flat region of the spectrum, and the photocurrent corresponds to the intensity of the sharp peak in the noise spectrum at the chopper frequency, as shown in Figure 6-12. 127

Figure 6-14: Two methods of measuring the photocurrent are shown in Figures 6-9 (using lock-in) and 6-13 (using a dynamic signal analyzer). 128

Figure 7-1: (top) Structure of infrared photodetectors based on InAs/GaAs SML-QDs. The black rectangle shows a single SML-QD formed by repeating six times the deposition of 0.5 ML of InAs followed by 2.5 MLs of GaAs:Si. (bottom) Phase diagram of the reconstruction of the arsenic-rich GaAs(001) surface where the red line indicates the transitions between the (2×4) and c(4×4) reconstructions as measured in our MBE system. The green dots indicate approximately the As flux and sample temperature used to grow the SML-QDs of devices #1 - #6, as shown in Table 7-1. 131

Figure 7-2: Sample installed on the cold finger of an optical cryostat having a Ge window (95% transmission in the 3-12 μm range) with the radiation reaching the mesas from (a) the top (normal incidence) or (b) with 45° incidence. 133

Figure 7-3: (a) Spectral response (photocurrent) of SML-QDIP #1 (devices #2 and #3 follow the same trend) at 12 K for bias voltages of 0.2-0.5V. (b) Band structure of the same device, and the possible electronic transitions. 135

Figure 7-4: Normalized spectral response of SML-QDIPs #1, #2, and #3 obtained by FTIR in normal incidence at 12 K with a bias of +1.1 V. 135

Figure 7-5: (a) Black-body responsivity of SML-QDIPs #1, #2, and #3 as a function of bias at 12 K. (b) Responsivity of SML-QDIP #1 as a function of bias voltage at different temperatures. 136

Figure 7-6: (a) Current versus voltage (I-V) curves in the dark (dark current) as a function of bias voltage for SML-QDIPs #1, #2, and #3 obtained at 12 K using a dark+cold shield. (b) Dark current of SML-QDIP #1 as a function of bias voltage at different temperatures. 137

Figure 7-7: (a) Noise-current spectral density of SML-QDIPs #1, #2, and #3 as a function of bias voltage at 12 K with a dark+cold shield. (b) Noise density of the dark current of SML-QDIP #1 as a function of bias voltage for different temperatures. 138

Figure 7-8: Specific detectivity (D*) of SML-QDIPs #1, #2, and #3 as a function of bias voltage at 12 K. 139

Figure 7-9: (a) Grinding and polishing of the sample facet with a 45° angle; (b) Geometry of samples used for optical measurements performed at 45° with s- and p-polarized radiation. 142

Figure 7-10: Normalized spectral response of SML-QDIPs #4 and #5 obtained by FTIR in normal incidence at 12 K. 145

Figure 7-11: Black-body responsivity of SML-QDIPs #4 and #5 under normal incidence as a function of bias at 12 K. 145

Figure 7-12: (a) Current versus voltage (I-V) curves in the dark (dark current) as a function of bias voltage for SML-QDIPs #4 and #5 obtained at 12 K using a dark+cold shield. (b) The dark current as a function of temperature is presented in an Arrhenius plot to calculate the activation energy for SML-QDIPs #4 and #5 at a bias close to 0 V (actually 0.05V). 146

Figure 7-13: Noise-current spectral density of SML-QDIPs #4 and #5 as a function of bias voltage at 12 K with a dark+cold shield. 147

Figure 7-14: Specific detectivity (D*) of SML-QDIPs #4 and #5 as a function of bias voltage at 12K. 148

Figure 7-15: (a) Normalized spectral response of SML-QDIPs #4 and #6 obtained by FTIR under normal incidence at 12 K for a bias voltage of 1.8V. (b) Band structure of device #6 and the possible electronic transitions. 152

Figure 7-16: Black-body responsivity of SML-QDIPs #4 and #6 under normal incidence as a function of bias at 12K. 152

Figure 7-17: (a) I-V curves in the dark (dark current) as a function of bias voltage for SML-QDIPs #4 and #6 obtained at 12 K; (b) Arrhenius plot of the dark current as a function of temperature to calculate the activation energy of SML-QDIPs #4 and #6 at a bias of 0.05V. 153

Figure 7-18: Noise-current spectral density of SML-QDIPs #4 and #6 at 12K. 154

Figure 7-19: Specific detectivity of SML-QDIPs #4 and #6 at 12K. 154

Figure 8-1: Structure of a sample consisting of $In_{1-x}Al_xAs$ QDs ($x \leq 0.65$) to check their density and morphology by AFM (no cap layer). 159

Figure 8-2: Band gap and lattice constant for various III–V alloys and materials of group IV. 160

Figure 8-3: 1×1 μm^2 AFM images of the $In_{1-x}Al_xAs$ layers mentioned in Table 8-1 (first set of samples), showing the surface of a single layer of (a) InAs QDs; (b) $In_{0.85}Al_{0.15}As$ QDs; (c) $In_{0.70}Al_{0.30}As$ QDs; (d) $In_{0.50}Al_{0.50}As$ QDs; (e) $In_{0.35}Al_{0.65}As$ QDs. (f) QDs density (cm^{-2}) of the $In_{1-x}Al_xAs$ samples shown in Figures (a) to (e). 162

Figure 8-4: 1×1 μm^2 AFM images of the second set of samples showing the surface of a single layer of $In_{0.7}Al_{0.3}As$ QDs (a), (b), (c), and of $In_{0.5}Al_{0.5}As$ QDs (d), (e), (f) with a total thickness equivalent to 105%, 125% and 140% of their critical thickness, respectively (from top to bottom). 163

Figure 8-5: QDs density of $In_{1-x}Al_xAs$ layers (shown in Figure 8-4) with 30% and 50% of Al content for different total thicknesses (critical thickness +5%, +25%, and +40%). 164

Figure 8-6: Structure of InAlAs/InAs QD bilayers, consisting of InAlAs QDs, serving as a seed, followed by InAs QDs. Both QD layers were separated by 4 nm of GaAs. 165

Figure 8-7: 1×1 μm^2 AFM images of the third set of samples consisting of (a) 2.1 MLs of InAs only, to serve as a reference; (b) 2.1 MLs of InAs on top of $In_{0.7}Al_{0.3}As$ QDs, separated by 4 nm of GaAs; (c) the same sample as in (b) but with $In_{0.5}Al_{0.5}As$ QDs. The large white spots in Figures (b) and (c) indicate that some InAs QDs have relaxed. (d) InAs QDs density of AFM Figures (a) to (c) as a function of Al content. The first result represents the QDs density of a single 2.1 ML-thick InAs layer (reference sample). 166

Figure 8-8: Structure of a sample of the fourth set consisting of bilayers of $In_{0.7}Al_{0.3}As$/InAs QDs. Both QDs layers were separated by X nm of GaAs, where X = 2, 4, or 8 nm. The structure of interest was duplicated and separated from the bottom one by 100 nm of GaAs to allow AFM measurements on the top and PL measurements on the bottom layers. 168

Figure 8-9: 1×1 μm^2 AFM images of the top layer of samples #a to #g listed in Table 8-2. (a) 1.40 MLs of InAs and (b) 2.30 MLs of $In_{0.7}Al_{0.3}As$. For these 2 samples, deposition was stopped before the critical thickness was reached and therefore no QDs are observed (only the flat 2D layer). (c) 2.1 MLs of InAs QDs and (d) 3.50 MLs of $In_{0.7}Al_{0.3}As$ QDs. $In_{0.7}Al_{0.3}As$/InAs QDs bilayers with a GaAs spacer of (e) 2 nm, (f) 4 nm, and (g) 8 nm. 170

Figure 8-10: Structure of the X-STM sample #h grown on a Si-doped GaAs(001) substrate. Layers #1 to #7 are the same as in samples #a to #g, respectively, and were grown in the same conditions. 172

Figure 8-11: X-STM filled-state topographic images comparing the initial formation of the 2D InAs layer (layer #1) and $In_{0.7}Al_{0.3}As$ layer (layer #2), as well as their quantum dots (layers #3 and #4). The white arrow indicates the growth direction [001]. The two white spots in layer #2 indicate some 173 contaminants or tip related artifacts. The red arrow shows the atomic plane where the Al atoms are located. The color scale represents the height of the relaxed surface outward of the cleaved plane.

Figure 8-12: X-STM filled-state topographic images showing the effect of the GaAs spacer on the formation of InAs QDs in layers #5, #6, and #7. The InAs QDs are deposited on top of the InAlAs QDs seed layer. The intermixing and strain-induced stacking can be seen for X= 2nm and X= 4nm, respectively. The two QDs layers in layer #7 are already uncoupled for a GaAs spacer of 8 nm. The white arrow shows the growth direction [001]. 175

Figure 8-13: PL spectra at 77K of the samples from Figure 8-9 containing different combinations of InAs and $In_{0.7}Al_{0.3}As$ layers (Table 8-2). Sample #b, simulating the $In_{0.7}Al_{0.3}As$ WL, showed no signal at all. 178

List of Tables

Table 7-1: Growth conditions of the InAs/GaAs SML-QDs used in groups 1, 2, and 3 of QDIPs analyzed in this chapter, whose structure is shown in Figures 7-1. Bold numbers refer to parameters that were changed in each group. 132

Table 8-1: Critical and deposited thicknesses (MLs) of the individual $In_{1-x}Al_xAs$ layers as a function of their Al content. 160

Table 8-2: Description of the fourth set of samples. The QDs density (cm^{-2}) in the top layer and the value of the thin GaAs spacer in the InAlAs/InAs bilayers are also given where relevant. 167

Nomenclature

1- List of abbreviations

IR	Infrared or infrared radiation
MBE	Molecular beam epitaxy
MOCVD	Metalorganic chemical vapor deposition
QWIP	Quantum-well infrared photodetector
QDIP	Quantum-dot Infrared Photodetector
QW	Quantum well
QD	Quantum dot
SK	Stranski-Krastanov
SK-QDs	Stranski-Krastanov quantum dots
ML	Monolayer
SML	Submonolayer
SML-QD	Submonolayer quantum dot
FPA	Focal plane array
BEP	Beam-equivalent pressure
PL	photoluminescence
AFM	Atomic force microscopy (or microscope)
TEM	Transmission electron microscopy (or microscope)
X-STM	Cross-sectional scanning tunneling microscopy
NIR	Near infrared
SWIR	Short-wavelength infrared
MWIR	Mid-wavelength infrared
LWIR	Long-wavelength infrared
VLWIR	Very-long-wavelength infrared
FIR	Far infrared
LPE	Liquid-phase epitaxy
CVD	Chemical vapor deposition
UHV	Ultra-high vacuum
CAR	Continuous azimuthal rotation
RHEED	Reflection high-energy electron diffraction

FM	Frank-Van der Merwe (growth mode)
VW	Volmer-Weber (growth mode)
SML-QDIP	Submonolayer quantum dot infrared photodetector
STM	Scanning tunneling microscopy (or microscope)
FWHM	Full width at half maximum
RTA	Rapid thermal annealing
FTIR	Fourier-transform infrared (spectroscopy)
MEE	Migration enhanced epitaxy
SPM	Scanning probe microscopy (or microscope)

2- List of samples and devices

Sample #A	2.2 MLs of InAs SK-QDs at 515 °C in the presence of a c(4×4) surface reconstruction.
Sample #B	6 × (0.50 ML/2.50 MLs) of InAs/GaAs SML-QDs at 490 °C in the presence of a c(4×4) surface reconstruction.
Sample #C	5.1 nm wide $In_{0.17}Ga_{0.83}As$/GaAs QW at 515 °C in the presence of a c(4×4) surface reconstruction.
Sample #A1	2.2 MLs of InAs SK-QDs deposited at 515 °C without any cap layer using the same growth conditions as sample #A.
Sample #B1	0.5 ML of InAs deposited at 490 °C without any cap layer using the same growth conditions as sample #B.
Sample #C1	200 nm-thick GaAs buffer deposited at 570 °C to compare it with sample #B1.
Sample #D	10 × (45nm $Al_{0.1}Ga_{0.9}As$/GaAs) QWs containing each a single layer of (6 × (0.35 ML/2.65 MLs)) InAs/GaAs SML-QDs.
Sample #A2	2.2 MLs of InAs SK-QDs deposited at 515°C and covered by 40 nm of undoped GaAs grown at the same temperature, followed by 120 nm of Si-doped GaAs deposited at 570°C.
Sample #B2	6 × (0.50 ML/2.50 MLs) of InAs/GaAs SML-QDs deposited at 490°C in the presence of a c(4×4) surface reconstruction and covered by 40 nm of undoped GaAs grown at the same temperature, followed by 120 nm of Si-doped GaAs deposited at 570°C.
Sample #E	Five SML-QDs layers were grown under different growth conditions (see Figure 5-7) for the X-STM measurements.
Set of samples #F	Five SML-QDs samples containing X cycles of 0.3 ML of InAs + 0.7 ML of GaAs, with X= 5, 7, 8, 9, or 11. With cap layer for PL.
Set of samples #F1	Five SML-QDs samples containing X cycles of 0.3 ML of InAs + 0.7 ML of GaAs, with X= 5, 7, 8, 9, or 11. Without cap layer for AFM.
Device #1	SML-QDIP containing 6 × (0.50 ML/2.50 MLs) of InAs/GaAs SML-QDs deposited at 490°C with a (2×4) surface reconstruction before InAs deposition (very low As flux).
Device #2	SML-QDIP containing 6 × (0.50 ML/2.50 MLs) of InAs/GaAs SML-QDs deposited at 490°C with a slightly higher As flux and a c(4×4)

	reconstruction (just above the transition from (2×4) to c(4×4) which occured at 1.1×10^{-7} Torr).
Device #3	SML-QDIP containing 6 × (0.50 ML/2.50 MLs) of InAs/GaAs SML-QDs deposited at 490°C with a c(4×4) reconstruction but with a much higher As flux generally used for SK-QDs.
Device #4	SML-QDIP containing 6 × (0.50 ML/2.50 MLs) of InAs/GaAs SML-QDs grown at 490 °C with the usual growth parameters of SK-QDs (i.e., c(4×4) surface reconstruction, high As flux, and moderate InAs and GaAs rates).
Device #5	SML-QDIP containing 6 × (0.50 ML/2.50 MLs) of InAs/GaAs SML-QDs grown at 525 °C with the usual growth parameters of SK-QDs (i.e., c(4×4) surface reconstruction, high As flux, and moderate InAs and GaAs rates), to compare it with device #4.
Device #6	SML-QDIP containing 6 × (0.30 ML/0.7 ML) of InAs/GaAs SML-QDs grown at 490 °C in the presence of a c(4×4) surface reconstruction and moderate InAs and GaAs rates to compare it with device #4.
Set of samples #1	125% of the critical thickness of $In_{1-X}Al_XAs$ QDs (x= 0.15, 0.30, 0.50, or 0.65) without cap layer to check its morphology by AFM.
Set of samples #2	105%, 125%, or 140% of the critical thickness of $In_{1-X}Al_XAs$ QDs (x = 0.30 or 0.50) without cap layer to check its morphology by AFM.
Set of samples #3	125% of the critical thickness of $In_{1-X}Al_XAs$ QDs (x = 0.30 or 0.50) and 2.1 MLs of InAs QDs on top of them, separated by only 4 nm of GaAs.
Set of samples #4	(sample #a) 1.40 MLs of InAs, (sample #b) 2.30 MLs of $In_{0.7}Al_{0.3}As$, (sample #c) 2.1 MLs of InAs QDs, (sample #d) 3.50 MLs of $In_{0.7}Al_{0.3}As$ QDs, and finally, bilayers of 3.50 MLs of $In_{0.7}Al_{0.3}As$/ 2.1 MLs of InAs QDs with a GaAs spacer of 2 nm, 4 nm, or 8 nm in samples #e, #f, and #g, respectively.
Sample #h	It was grown specifically for X-STM measurements and contained a layer or bilayer of the seven different types of samples #a to #g.

Table of contents

1: Introduction 29

1-1 Historical introduction 29

1-2 Infrared photodetectors: present and future 32

1-3 Motivations and objectives 34

2: Infrared radiation and photodetectors 36

2-1 Infrared radiation 36

2-2 Infrared detectors 38

2-2-1 Thermal detectors 38

2-2-2 Photodetectors 39

2-3 Quantum-well infrared photodetectors 41

2-4 Quantum-dot infrared photodetectors 42

2-5 Challenges of InAs/GaAs SK-QDIPs 45

3: Growth of InAs/GaAs quantum dots by molecular beam epitaxy 47

3-1 Molecular beam epitaxy 47

3-2 Varian molecular beam epitaxy system 48

3-2-1 Entry-exit chamber 50

3-2-2 Buffer chamber 51

3-2-3 Growth chamber 51

3-2-4 Effusion cells and Arsenic cracker 53

3-3 MBE operation 55

3-3-1 Sample preparation 55

3-3-2 Reflection high-energy electron diffraction 56

3-3-3 Growth rates and compositions 58

3-4 Quantum dots 61

3-4-1 Self-assembled quantum dots 61

3-4-2 Submonolayer quantum dots 63

3-5 Reconstructed surfaces of GaAs(001) 65

4: In(Ga)As SML-QDs optical and structural characterization techniques 71
4-1 Optical characterization 71
4-1-1 Photoluminescence 71
4-2 Structural characterization 77
4-2-1 Atomic force microscopy 77
4-2-2 Transmission electron microscopy 81
4-2-3 Cross-sectional scanning tunneling microscopy 85
5: Growth optimization of InAs/GaAs SML-QDs 91
5-1 SML-QDs samples growth 91
5-2 Influence of the surface reconstruction 92
5-3 Influence of the Ga and In growth rates 94
5-4 Influence of the InAs coverage 96
5-5 Influence of the number of repetitions 98
5-6 X-STM experimental results 99
5-7 Influence of the growth temperature 108
5-8 SML-QDs with a thinner GaAs interlayer 109
6: Processing and electro-optical characterization 115
I – Processing 115
6-1 Photolithography 115
6-2 Metallization and packaging 118
II -Electro-optical characterization 121
6-3 Spectral response 121
6-4 Photocurrent measurements and black-body responsivity 122
6-5 Dark current 123
6-6 Noise current 125
6-7 Noise equivalent power and specific detectivity 128
7: Optimization of InAs/GaAs submonolayer quantum dots infrared photodetectors 130

7-1 Design, growth, and processing 130
7-2 Group 1: Influence of the As flux and surface reconstruction at low temperature 133
7-2-1 Discussion of the results of the 1st group of samples 139
7-3 Group 2: (2×4) surface reconstruction achieved with other growth conditions 143
7-3-1 Discussion of the results of the 2nd group of samples 148
7-4 Group 3: Influence of the thin GaAs interlayer 150
7-4-1 Discussion of the results of the 3rd group of samples 155
8: Increasing the density of InAs quantum dots by using InAlAs SK-QDs as a seed 158
8-1 High density of InAlAs QDs 158
8-2 Growth optimization of InAlAs QDs 159
8-3 Influence of the pre-deposited InAlAs layer on the InAs SK-QDs density 164
8-4 Influence of the GaAs-separator thickness on the InAs SK-QDs density 166
8-4-1 AFM results 169
8-4-2 X-STM results 171
8-4-3 PL experimental data 177
9: Conclusion 179
10: Publications 182
10-1 Published papers 182
10-2 Papers to be submitted 183
10-2 Participation in conferences 183
Bibliography 186

Chapter 1: Introduction

1-1 Historical introduction

"What is light?" has been a topic of study for philosophers, astronomers, and physicists since ancient times. Over a thousand years have passed since Ibn Al-Haytham published his seminal work on Optics in 1015 [1]. More than two hundred years since Fresnel's description of the wave nature of light in 1815, Maxwell's electromagnetic theory in 1865, Einstein's photoelectric effect in 1905 [1], and the discovery of infrared radiation (IR) in the early 19th century when Herschel's experiment with a thermometer and prism was first reported [2] as he measured the temperature of each color in the spectrum of sunlight with a prism. The detector consisted of a glass thermometer containing a liquid and a specially blackened bulb for radiation absorption. To measure the energy distribution in sunlight, Herschel constructed a crude monochromator that used a thermometer as a detector; he found that the highest temperature was in a region just beyond the red (invisible to the human eye)—which is now called infrared—taking its name from the Latin word infra (meaning below) and the English word red [3].

In the mid-19th century, Macedonio Melloni was the first to develop an IR detector that was practical [4]. The detectors were thermopiles that operated by thermal conduction, relying on the differences in thermal expansion between two dissimilar metals. Theodore Case developed the first modern photodetector in 1917 [5] searching for materials that exhibited variable resistance depending on whether or not they were irradiated with light [6]. In his quest, he noted that several materials, such as lead sulfide, exhibited a response in the IR region; this was the first practical IR detector operating with quantum effects rather than conductive ones. The device was sensitive up to a wavelength of 3 µm, and this technology established the field of IR detectors as we know them today [7].

IR detectors have become increasingly important since World War II, as long-term applications such as night vision, missile tracking, and environmental monitoring require fast, highly sensitive, and low-noise sensors [8]. In the early 1950s, the first extrinsic photoconductive detectors with photon energies smaller than the bandgap of the host material were developed [9, 10]. Their development followed the discovery of the transistor in 1958, which spurred advances in growth and material purification techniques. Copper, mercury, zinc, and gold doping in germanium produced extrinsic photoconductive responses that enabled devices to operate in the 8–30 μm region [11]. However, to achieve performance comparable to that of intrinsic detectors, these devices must be operated at very low temperatures, as a result of the small energy values involved.

During the early 1960s, there was a significant development in narrow-gap III-V semiconductor alloys (such as $InAs_{1-x}Sb_x$), IV-VI semiconductors (such as $Pb_{1-x}Sn_xTe$), and II-VI semiconductors (such as $Hg_{1-x}Cd_xTe$). These material systems offered a remarkable level of flexibility in the design of IR detectors [12, 13] and were based on optical interband transitions from the valence band to the conduction band of bulk narrow-band semiconductors. InSb- and HgCdTe-based detectors were the two dominant IR systems at the end of the last millennium, which were well developed and available commercially [11]. But, the difficulties in epitaxial crystal growth and processing of these materials, leading to spatial non-uniformities, low yield, and high cost, prompted the search for an alternative. In contrast, well-established material growth techniques for III-V compound semiconductors, such as molecular beam epitaxy (MBE) and metalorganic chemical vapor deposition (MOCVD) could produce sizable wafers with accurate control of composition and film thicknesses, which paved the way for quantum-based detectors such as quantum-well (QWIPs) and quantum-dot (QDIPs) infrared photodetectors.

In 1987, Levine *et al.* [14] demonstrated the success of quantum-well structures for infrared-detection applications. QWIPs have shown excellent imaging performance [15]; due to their higher thermionic emission rates, they required lower operating temperatures to achieve performance similar to HgCdTe detectors [16, 17]. However, QWIPs also had serious drawbacks: they couldn't detect radiation with normal incidence due to their polarization selection rules [3, 17] that inhibit intraband transitions, and they showed a high dark current that limited their operation to low temperatures [18]. All the QWIP detectivity data with cutoff wavelength around 9 μm is clustered between 10^9 and 10^{10} cm $Hz^{1/2}$/W when operating at 77 K. At the same temperature, the detectivity of bulk HgCdTe photodetectors reaches up to 10^{12} cm $Hz^{1/2}$/W, explaining why its TRL value of 9—the Technology Readiness Level measures the maturity of a technology and is a number ranging from 0 to 10—is one of the highest on the market along with micro bolometers, while QWIPs have a TRL of 8 [3].

Quantum-dot infrared photodetectors (QDIPs) have recently emerged as a possible alternative to HgCdTe and QWIPs. The beginning of the interest in quantum dot (QD) research can be traced back to a suggestion by Arakawa and Sakaki in 1982 [19], and the first QDIP was demonstrated by J. Phillips in 1998 [20]. The motivation for this interest is based on two characteristics of QDs: they are sensitive to normal incident infrared radiation (when intraband transitions are involved), a consequence of the 3D confinement of electrons in QDs [21, 22], and they show a weak thermionic coupling between the ground state and the excited states. This should lead to lower thermal excitation and, thus, lower dark current and higher operating temperatures [11, 23].

In general, QDIPs are based on self-assembled InAs QDs grown on a GaAs(001) substrate using the Stranski-Krastanov (SK) growth mode [24, 25]. One of the primary drawbacks of Stranski-Krastanov quantum-dots infrared photodetectors (SK-QDIPs) is the large inhomogeneous linewidth of their optical spectra caused by the variation of dot size due to their self-assembling nature [21]. This leads to a reduction in the absorption for a specific wavelength, which negatively affects the performance of QDIPs [26]. A further disadvantage of SK-QDs is that they are surrounded by a 1 ML-thick InGaAs wetting layer that does neither contribute to normal-incidence absorption nor 3D confinement of the carriers [27]. As a result, QDIPs have limitations that need to be addressed to improve their performance.

A more flexible approach to growing QDs with enhanced lateral confinement and without a wetting layer is the submonolayer (SML) technique [28]. With SML quantum dots (SML-QDs), only a fraction of a monolayer (ML) of material (typically 30-50%) is deposited onto the substrate to nucleate a high density of small two-dimensional InAs islands (i.e., 1ML thick) on the GaAs surface. These islands are then covered with a few MLs of GaAs material, and the process is repeated at will to get stacks of InAs islands acting as individual quantum dots, resulting in enhanced lateral confinement [29]. Over the past few years, submonolayer quantum-dot infrared photodetectors (SML-QDIPs) have emerged as a new technology for detecting IR radiation [30]. When compared to more conventional photodetectors (SK-QDIPs), their advantages originate from the small base width, control of their vertical size, and absence of the wetting layer which lead to improved 3D quantum confinement [31, 32]. So far, SML-QDs have been successfully used in lasers [33], vertical cavity surface-emitting lasers [34], infrared photodetectors [30], and solar cells [35]. Being a more recent technology, QDIPs have a much lower TRL (1–2) and have only recently reached the market [3]. However, in the laboratory, they clearly overcame QWIPs and several groups already reported QDIPs showing a specific detectivity above 10^{11} cm $Hz^{1/2}$/W at 77K [23, 30].

1-2 Infrared photodetectors: present and future

In the field of infrared imaging, a complete IR camera system typically includes various components such as optics, a focal plane array (FPA) made of IR detectors, a cooling system, and electronics for image processing [36]. However, traditional cooling systems like liquid-nitrogen dewars or stirling coolers (77 K) can be bulky, expensive, and heavy. To overcome these challenges, there has been a push towards using thermoelectric coolers, which require IR photodetectors able to operate at higher temperatures (150 K or above). QDIPs are a promising technology that can offer improved detector array performance at elevated temperatures [37], which can lead to significant cost savings and reductions in size and weight of IR camera systems. IR imaging is a rapidly growing field of research and development, with applications ranging from security and surveillance to medical imaging and environmental monitoring. Today, with the manufacture of IR detectors having a high sensitivity, high-quality IR cameras are now available for use in various strategic fields such as medicine, engineering, science, agriculture, environment, and energy. Figure 1-1 shows several examples of thermal images. In 2021, the global market for IR detectors reached US$ 463 million. Looking ahead, the Fact.MR group expects the market to reach US$ 968 million by 2031 [41], with a growth rate of 7.7% over the period 2021-2031 as shown in Figure 1-2. The market growth is largely attributed to a significant

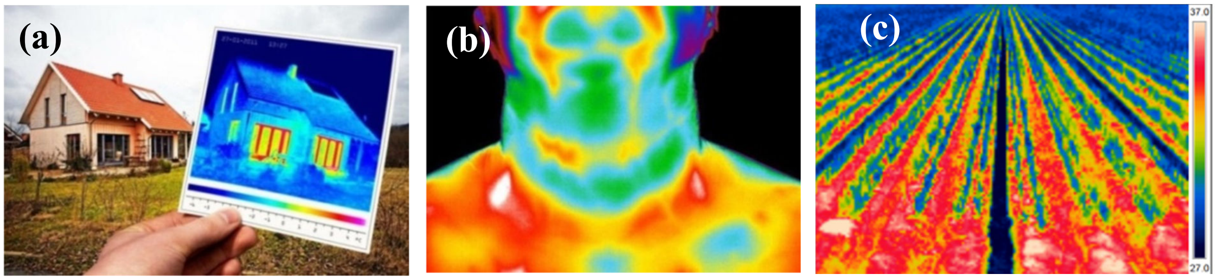

Figure 1-1: Thermal imaging (infrared) illustrating (a) the thermal insulation faults of a house [38]; (b) the frontal neck thermogram showing a hot pattern over the region of the right side of the thyroid [39]; (c) the monitoring of an onion crop. The legend on the right side represents the temperature color ramp in ℃ [40].

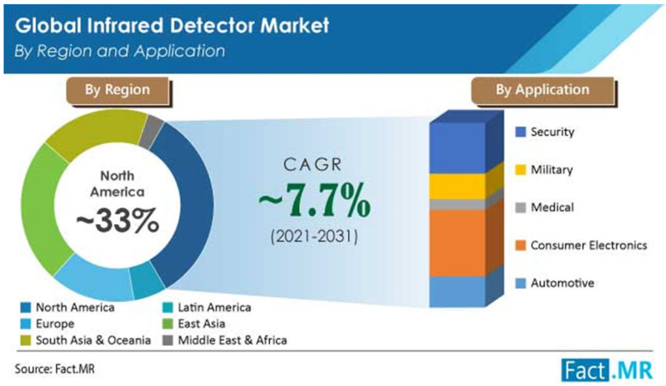

Figure 1-2: The global market for infrared detectors by region and application. During the period 2021-2031, it is expected to grow 7.7% (CAGR, compound annual growth rate) [41].

rise in the demand for devices capable of detecting motion and people. Retail shops, residential buildings, museums, and libraries use IR detectors for intrusion alarms, security cameras, safety lighting, and garage doors. In addition, compact size and ability to detect light from a distance are favoring the market growth in the military and defense sectors. As the level of information required by society becomes more complex, the demand for devices that require QDIPs with enhanced performance is increasing. When extremely high performance is required (fast response, high resolution, multicolors), regardless of cost, detectors containing nanostructures such as SML-QDIPs might become relevant to the market in the future. The SML-QDs have demonstrated superior performance in various devices, such as, solar cells [35] and photodetectors [30], even without fully optimized growth conditions, and this is exactly where this work fits in.

1-3 Motivations and objectives

Recently, SML-QDs have become more popular as a result of their advantages over conventional SK-QDs, such as high areal density, on-demand vertical size and composition control, and the absence of a wetting layer [31, 32]. As a consequence, they are expected to provide excellent performance when used for IR photodetectors. However, a mandatory growth condition to have real SML-QDs is to be sure that the small 2D InAs islands, which are the building blocks of such nanostructures, are successfully nucleated on the GaAs surface to allow the alignment of the 2D islands of the next InAs submonolayers along the vertical direction.

The first paper on InAs/GaAs SML-QDIPs was published in 2009 by Ting *et al.* [43]. Although InAs SML-QDs have been successfully used in several devices since then, we believe that the growth conditions reported in the literature are not the best ones, as SML-QDs appear as irregular InGaAs agglomerates and don't develop their full size [44]. It seems that, for the sake of simplicity, growers always use the same growth conditions for SK-QDs and SML-QDs [43-46], i.e., a high As flux ($4\text{-}8\times10^{-6}$ Torr BEP (beam equivalent pressure)), a low InAs growth rate (0.05-0.1 ML/s), and a sample temperature around 480-515 °C). The high As flux and low sample temperature always yield a c(4×4) surface reconstruction of the GaAs surface under static conditions (no growth) before deposition of the InAs SML. Some papers published more than two decades ago clearly demonstrated with scanning tunneling microscopy (STM) that [47, 48], in such conditions, the In adatoms are preferentially incorporated randomly into the trenches of the c(4×4) reconstruction, thus yielding an InGaAs alloy instead of 2D InAs islands. They also showed that real 2D InAs islands could only be nucleated on the GaAs surface when its reconstruction was of the (2×4) type [48]. Therefore, in this work, I focused on optimizing the growth conditions of InAs SML-QDs with a (2×4) surface reconstruction, compared such nanostructures with those obtained in the presence of the usual c(4×4) reconstruction, and used them in infrared photodetectors in an attempt to get devices with better performance.

This thesis is divided into the following sections: in the next chapter (second), I give an overview of the main principles of infrared radiation and the different types of photodetectors. In the third chapter, I present the basic features of molecular beam epitaxy and then of the growth of quantum dots obtained by self-assembly and using the submonolayer method. Several experimental techniques such as photoluminescence (PL), atomic force microscopy (AFM), transmission electron microscopy (TEM), and cross-sectional scanning tunneling microscopy (X-STM) will be discussed in the fourth chapter to evaluate the optical and structural properties of both types of InAs/GaAs QDs and eventually compare them with QWs. Particular attention is paid to the X-STM study as it provides a clear picture of the shape and composition of the nanostructure at the atomic level and was determinant to better understand the properties of In(Ga)As SML-QDs. Then, in chapter five, PL and X-STM experiments were carried out on various samples of InAs/GaAs QDs grown under different growth conditions to investigate and optimize their properties. Chapter six shows the main steps for processing the samples into photodetectors, their electro-optical characterization, as well as the major procedures and calculations performed to obtain reliable measurements. Then, in chapter seven, several QDIPs containing SML-QDs grown in different conditions were tested at low temperatures to study how the growth conditions investigated by PL and X-STM affect the performance of the devices, with a special focus on the (2×4) reconstruction reached by increasing the sample temperature (with high As flux) that led to highly performant SML-QDIPs. Finally, since one goal of SML-QDs was to increase the density of nanostructures, chapter eight will present an alternative method of increasing the density of InAs SK-QDs using InAlAs QDs as a seed, which is very important to produce good optoelectronic devices. Then I will draw a conclusion on the experimental work performed here, followed by a list of my publications.

Chapter 2: Infrared radiation and photodetectors

This chapter reviews the main principles of infrared radiation and the different types of photodetectors.

2-1 Infrared radiation

The electromagnetic spectrum is the distribution of electromagnetic waves as a function of their wavelength or energy. From gamma rays to radio waves, it includes all types of radiation that are used in different fields [49], as shown in Figure 2-1. Infrared, micro, and radio waves are usually less harmful to the human eye than radiation with higher photon energy or shorter wavelength, such as γ-rays, X-rays, and ultraviolet. The human eye is only sensitive to the section of the electromagnetic spectrum ranging from 0.35 µm (violet) to 0.74 µm (red), which is therefore called the visible spectrum.

Unlike visible light, infrared radiation (0.74 µm - 1000 µm) can't be seen by the human eye, but it can be sensed as heat by nerve endings inside the skin or using specific thermal sensors [50]. All the objects with a temperature above zero Kelvin (K) spontaneously emit electromagnetic radiation in the IR region [51]. It means that any object is a spontaneous source of IR and can be directly observed with an IR camera (even in the absence of any visible light), unlike the human eyes which can only perceive objects when they are irradiated with visible radiation which is then scattered back to our eyes.

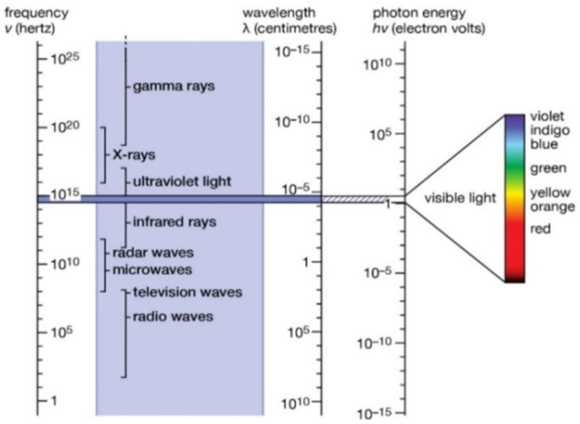

Figure 2-1: Schematics of the electromagnetic spectrum showing the range of the visible and IR spectra [49].

IR radiation differs from visible light by its longer wavelength and lesser scattering and absorption by dense gaseous or dusty regions. Therefore, it is possible to identify people, cars, boats, and planes on a foggy day with an IR camera or even to observe celestial objects in the universe using special telescopes coupled with such cameras. The IR spectrum is generally divided into six parts, depending on the wavelength [52]: near-infrared radiation (NIR) corresponding to wavelengths from 0.74 to 1.3 µm; short-wavelength infrared radiation (SWIR) with wavelengths from 1.4 to 3 µm, medium-wavelength infrared radiation (MWIR) ranging from 3 to 5 µm, long-wavelength infrared radiation (LWIR) corresponding to wavelengths from 8 to 12 µm, very-long-wavelength infrared radiation (VLWIR) with wavelengths of 12 to 30 µm, and far infrared (FIR) with wavelengths from 30 up to 1000 µm. In this work, the regions of interest are in the 3 to 5 µm and 8 to 14 µm, which are the best windows for producing thermal images on Earth.

IR radiation can be emitted during molecular transitions in covalent compounds that also absorb at the same wavelengths. Since several gases in the Earth's atmosphere exhibit these types of transition (H_2O, CO_2, methane (CH_4), etc.), the atmosphere becomes diffuse or opaque in the spectral regions corresponding to the wavelengths of these transitions, enabling practical applications but also affecting the use of IR radiation in other cases [53]. The atmospheric transmission spectrum at different wavelengths is shown in Figure 2-2: the high-transmission bands are called atmospheric windows and range mainly from 3 to 5 µm and from 8 to 14 µm, allowing the use of IR detectors and cameras for terrestrial applications [51].

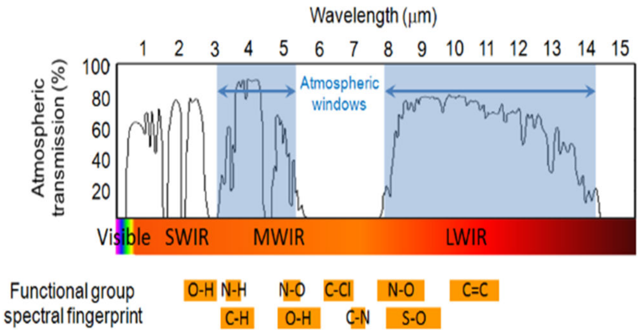

Figure 2-2: Atmospheric transmission spectrum showing two IR windows at 3-5 µm and 8-14 µm regions [54].

2-2 Infrared detectors

There are basically two types of IR detectors [3]: thermal detectors, which detect small temperature changes due to the absorption of IR light by monitoring a specific physical property, and photon detectors (also called photodetectors), which are directly sensitive to electronic transitions.

2-2-1 Thermal detectors

The first class of detectors is composed of thermal detectors, as shown schematically in Figure 2-3. The incident radiation is absorbed by the device and changes the material temperature which, in turn, modifies the value of the parameter of the detector that is monitored (electrical resistance, thermoelectric effect, pyroelectric effect) [55]. In a thermal detector, the incident radiation is absorbed and the resultant change in some physical properties is used to generate an electrical output. The detector is often suspended with small legs (to minimize heat transfer) that are connected to the heat sink and some electronics, as shown in Figure 2-3. The output signal is independent of the photonic nature of the incident radiation. Consequently, thermal effects are generally wavelength independent (Figure 2-4) and the output signal of thermal detectors mainly depend on the radiant power. Depending on the property to be monitored (resistance, electric polarization), they have different names (bolometer, pyrometer) [3]. Although they are usually slower, larger, and less sensitive than photon detectors, they have the huge advantage of operating at room temperature [56].

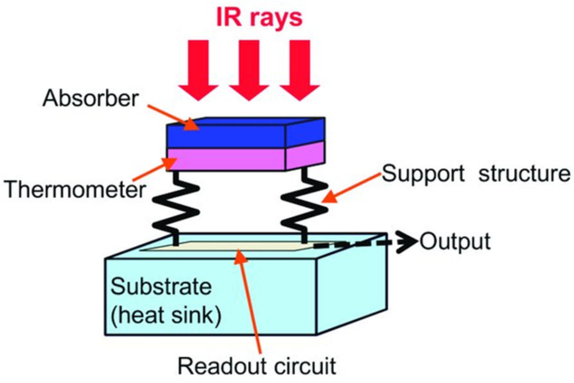

Figure 2-3: Schematic diagram of how thermal IR detectors operate [55].

2-2-2 Photodetectors

Photodetectors are a special type of detector based on the absorption of photons by electrons of the device that are promoted to higher energy levels and can generate an electrical current (called photocurrent) which can be measured by an external circuit [3]. Photodetectors show a selective wavelength dependence of their response, as shown in Figure 2-4. They are generally more sensitive than thermal detectors and can be fabricated with smaller sizes, but, depending on their operating wavelength (as they are wavelength sensitive), they require low temperatures to perform adequately—especially at longer wavelengths, as the energy values involved are small—which can make them bulky and heavy. They are divided into two classes depending on the absence (or not) of doping [57]: intrinsic and extrinsic photodetectors, respectively.

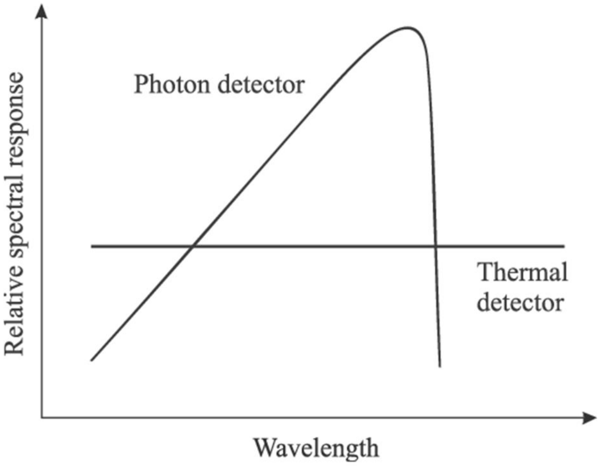

Figure 2-4: Relative spectral response of a photon and thermal detector [3].

Intrinsic photodetectors consist of semiconductors that have no intentional doping. Their basic operation is shown in Figure 2-5-a. In this case, the incident photons must have an energy larger than the bandgap of the bulk material (which is the difference between the energy of the valence and conduction bands) to generate an electron-hole pair whose components will transit in opposite directions toward the electrical contacts. They don't require any intentional doping as they operate with electronic transitions through the bandgap of the bulk material. It means that changing their operating wavelength requires a different material (with a different bandgap) or an alloy whose composition can be easily varied. The most successful example of an intrinsic photodetector is surely $Hg_{1-x}Cd_xTe$, which can be obtained with a wide range of compositions absorbing in a broad range of wavelengths [12]. InSb and HgCdTe are narrow bandgap semiconductors that feature interband transitions that are widely used for IR detection through the atmospheric transparency windows of 3–5 µm and 8–13 µm [58, 59].

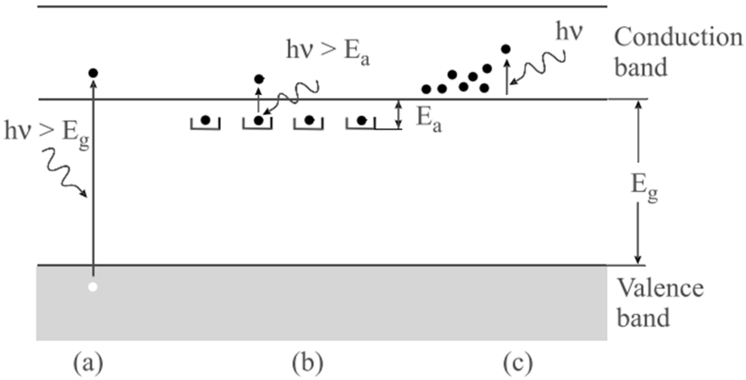

Figure 2-5: (a) intrinsic absorption from the valence to the conduction band; (b) extrinsic absorption from a donor impurity level (n-type doping) to the conduction band; (c) free-carrier absorption inside the conduction band [3].

An extrinsic photodetector consists of intentionally doped semiconductor materials where the dopant elements generate an impurity level inside the host material [60, 61], such as silicon (Si) doped with an appropriate impurity, like arsenic (As) atoms [62]. The dopant impurity levels (which can broaden into bands at high doping levels) are generally located within the bandgap; in the case of arsenic-doped silicon, the impurity band is located right below the conduction band, as shown in Figure 2-5-b, providing n-type doping. Thus, when a photon hits the surface of the detector, it can excite an electron from the impurity level to the conduction band which can contribute to the photocurrent. Here again, changing their operating wavelength requires the use of different impurity levels, which is not always easy due to compatibility issues with the host material. Moreover, the impurity levels of most compatible impurities are generally shallow, meaning that very low temperatures are often required for proper operation. Therefore, many attempts were made to find new types of extrinsic photodetectors able to be easily tuned and possibly work at higher temperatures. A high level of maturity has now been reached with quantum-well infrared photodetectors (QWIPs) utilizing intersubband transitions for IR absorption [63].

2-3 Quantum-well infrared photodetectors

QWIPs rely on quantum-scale physical effects (quantum confinement), while bulk photodetectors rely on electronic transitions across the material's bandgap. Therefore, the latter don't require any extrinsic doping, while QWIPs are based on intraband transitions (generally involving energy levels inside the conduction band) and need extrinsic doping to perform properly. QWIPs are based on quantum wells which, in their simplest form, are a periodic deposition of layers of two materials with dissimilar bandgaps. The material with the lower energy bandgap is commonly referred to as the well layer—it is generally extremely thin and surrounded by a thicker layer of the other material, like a sandwich— while the material with a higher-energy bandgap is referred to as the barrier layer. Since the well is generally a few nm thick, the carriers are confined along one direction of space and free in the QW plane (Figure 2-6-b), and their energy is quantized.

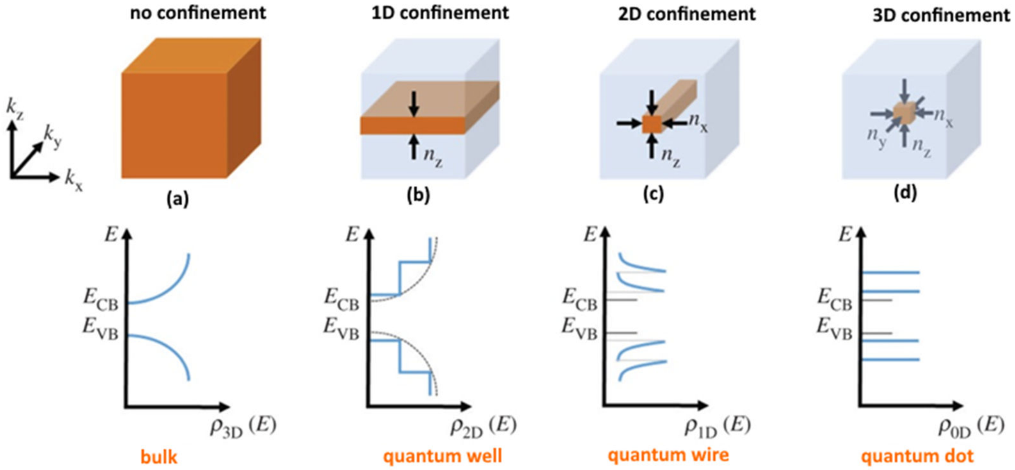

Figure 2-6: Schematic illustration of broken symmetry and functional form of the density of states in different types of structures and their degree of confinement of the carriers; (a) bulk material with no confinement; (b) quantum well with a 1D confinement; (c) quantum wire with a 2D confinement; (d) quantum dot with a 3D confinement [64].

Although QWIPs are simpler to grow using available epitaxial techniques and provide an easy way to tune the operation wavelength of the devices (by varying the width of the well), they suffer from 2 main problems: they are not sensitive to normal incident radiation [65] (due to polarization rules for the electronic intraband transitions) and have high values of thermally generated dark current. To solve these problems, the quantum-well layers of QWIPs were later replaced by quantum-dot layers. Indeed, based on their carrier confinement in all three directions of space (Figure 2-6-d), it was expected that QDIPs would not suffer from the normal-incidence limitation and might have a lower dark current, as well as a longer lifetime of the photoexcited carriers [66]. Although the size and composition of QDs are more difficult to vary than those of QWs, QDs can also be inserted in QWs to broaden the wavelength range of the devices and solve simultaneously the incidence problem of QWIPs [67, 68].

2-4 Quantum-dot infrared photodetectors

Although QDs were proposed in 1982 as a way to reduce or eliminate the temperature dependence of quantum well lasers, they were only experimentally demonstrated in a practical way 11 years later [69, 70]. In the last two decades, detecting IR radiation based on QDIPs has emerged as a new technology [26, 71, 72]. In 1999, researchers at the University of Michigan performed the first extensive QDIP characterization [73]. Since then, several research groups around the world [74-79] have examined these devices in an effort to push the boundaries of technology performance, particularly within the mid-IR wavelength range [80]; low dark current [74], multi-spectral response [81], high detectivity [82], high-temperature photodetection [83], and IR imaging [84] have been demonstrated in QDIPs.

Generally, QDIPs contain self-assembled InAs QDs deposited on a GaAs(001) substrate using the SK growth mode. Above a critical thickness of 1.7 monolayers (MLs), the thin InAs layer—which is under biaxial compressive strain due to the difference in lattice parameter between InAs and GaAs—relaxes and spontaneously forms a high density of small and rather homogeneous InAs islands (Figure 2-7). By controlling the material composition (using $In_xGa_{1-x}As$

instead of GaAs for the barriers, or $In_yGa_{1-y}As$ instead of InAs for the QDs, with y>x) and QD sizes (by varying the amount of InAs or InGaAs material deposited beyond the critical thickness), it is possible to control in some way the spectral response of the devices [71, 81].

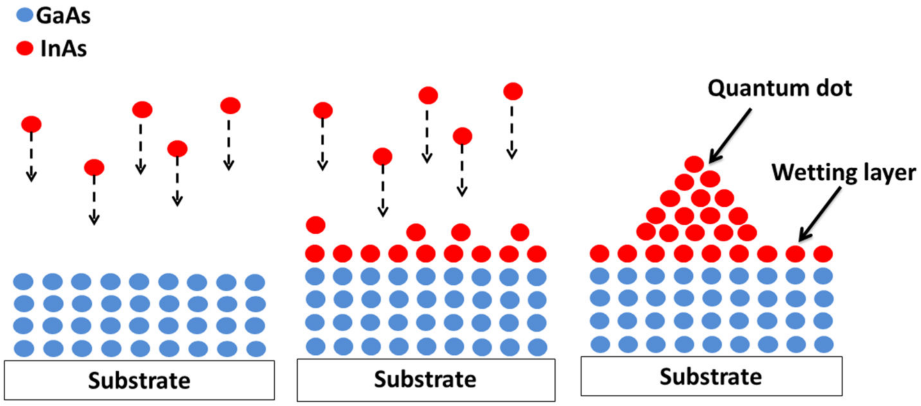

Figure 2-7: Schematics representation of quantum dots growth using the SK growth mode. From left to right, we can see that below a critical thickness, growth occurs in a 2D regime (layer by layer). However, once the material reaches a critical thickness (1.7 MLs in the case of InAs deposited on top of GaAs), the strained epitaxial layer relaxes and forms a high density of small strained islands surrounded by a wetting layer.

When InAs QDs are embedded in a wider-bandgap matrix material (e.g., GaAs), potential barriers appear in the conduction and valence bands, providing a mechanism for quantum confinement resulting from the nanoscale QD size. Confining carriers along the three directions of space leads to discrete energy levels which are expected to provide devices with an intrinsic sensitivity to normal incidence radiation, a lower dark current, a longer lifetime of the carriers in the excited states, a higher photoconductive gain, and consequently higher operating temperatures. A typical InAs/GaAs QD conduction band diagram is shown in Figure 2-8. QDIPs employ a detection method that relies on intraband photoexcitation due to 3D quantum confinement in the active region of the photodetector, allowing for the absorption of photons with an energy lower than the bandgap. The QDs are doped (in the case of InAs/GaAs QDs, Si atoms are used for n-type doping) in such a way as to fully populate the ground state of all the QDs present in the active region of the device.

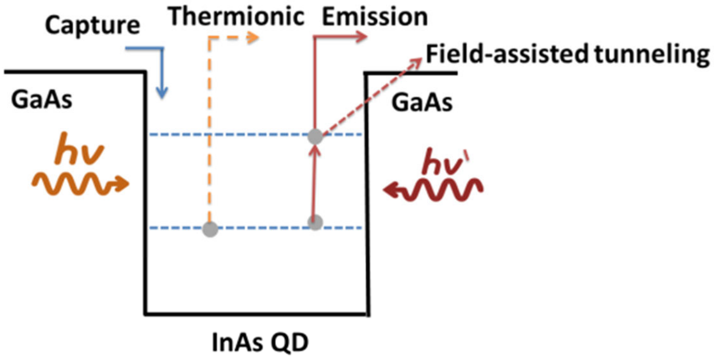

Figure 2-8: Schematic diagram of conduction band illustrating the photocurrent generation process in InAs/GaAs QDIPs under bias.

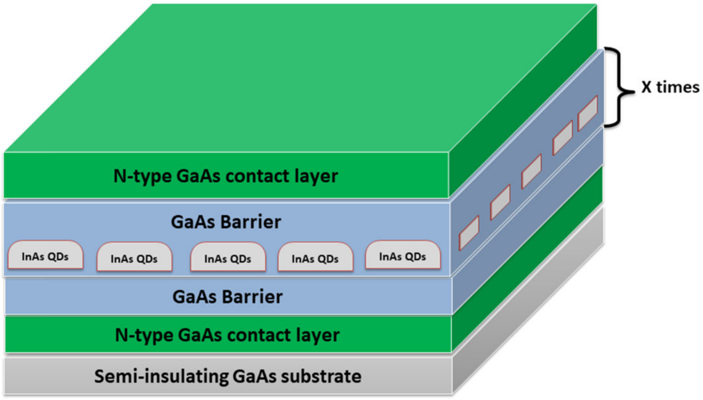

Figure 2-9: Structure of a standard SK-QDIP containing a top and bottom contact layer surrounding the active region consisting of x layers of InAs SK-QDs.

When IR photons with the right energy impinge on the QDIP surface, they excite electrons from the QDs ground state to a higher energy level—where from they can escape by thermal excitation or field-assisted tunneling—or to the continuum above the barriers. After photoexcited carriers enter the continuum, they may undergo several additional processes, including (i) drifting within the continuum due to the influence of an electric field, (ii) capture into the excited state of either the same QD or a different one, and (iii) collection at a device contact. Figure 2-9 shows the structure of a standard InAs/GaAs SK-QDIP consisting of an active region, with a certain number (x) of QD layers, surrounded by a top and bottom n-type doped contact layer.

2-5 Challenges of InAs/GaAs SK-QDIPs

Although 3D quantum confinement in QDs is anticipated to offer various benefits, SK-QDIPs have been shown to perform less than expected due to their self-assembling nature. A fine tuning of their properties is more difficult to achieve than in the case of QWs, as the density of QDs and their size can only be varied in a narrow range of values. Another drawback is that their size distribution is relatively wide and they are surrounded by an InGaAs wetting layer (Figure 2-7) which doesn't contribute to the 3D confinement of carriers nor the normal-incidence absorption, but increases the quantity of strained material in the system.

Although SK-QDIPs performance might be further improved (higher operating temperature and high specific detectivity) using more sophisticated structures or improving some of the growth conditions, the scientific community realized that most limitations due to the self-assembling process itself would be difficult to overcome and started to search for substitutes. This is why lately SML-QDs have emerged as a new technique for growing QDs—although it was known for more than two decades but was rarely used as SK-QDs were much easier to grow [28, 85]. Compared to conventional SK-QDs, their advantages originate from the higher areal density of nanostructures, their smaller aspect ratio (base/height), the more flexible control of their height and composition, and the absence of a wetting layer [31, 32]. SML-QDs can be obtained by depositing a fraction of a monolayer of InAs material to nucleate a high density of small two-dimensional (2D) islands on the GaAs substrate, and then by covering them with a few GaAs monolayers [29]. The sequence of InAs/GaAs SML-QDs formation is schematically shown in Figure 2-10. By repeating that sequence at will, the internal strain field (due to the different lattice parameters of GaAs and InAs) will contribute to vertically aligning the small 2D islands of adjacent InAs submonolayers and form stacks that will behave as individual QDs [43, 86]. In this way, it is possible to grow a very high density of nanostructures in a more flexible way that should be able to improve the performance of infrared photodetectors and other optoelectronic devices.

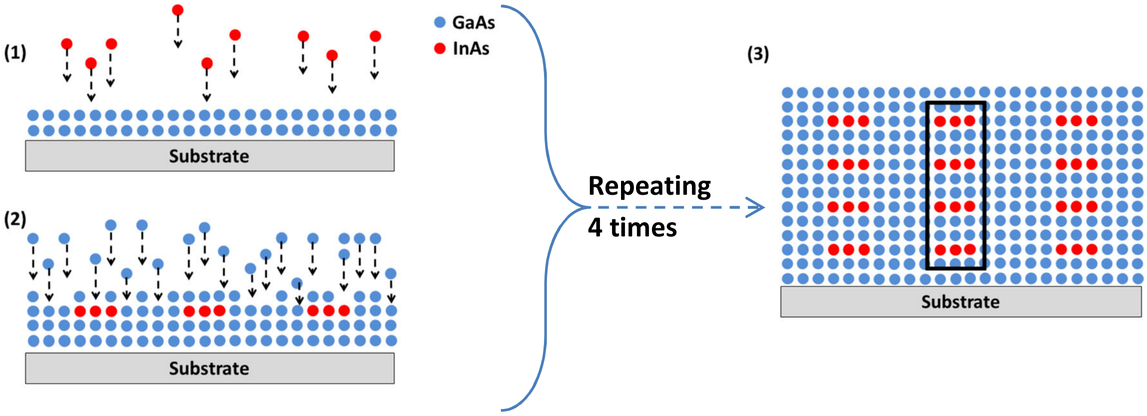

Figure 2-10: Schematics of InAs/GaAs submonolayer quantum dots obtained by repeating 4 times a basic cycle consisting of 0.5 ML of InAs (step 1) followed by 2.5 MLs of GaAs (step 2). The black box in image (3) represents a single SML-QD.

Chapter 3: Growth of InAs/GaAs quantum dots by molecular beam epitaxy

This chapter discusses the main experimental techniques that were used to grow the samples, with a focus on the Varian molecular beam epitaxy system that we have in our laboratory, as well as the growth itself of both SML-QDs and SK-QDs.

3-1 Molecular beam epitaxy

Several techniques can be used to produce thin films like the ones that are needed to fabricate the type of detectors that will be investigated here. Among them, we can cite thermal or electron-beam evaporation, sputtering, liquid-phase epitaxy (LPE), chemical vapor deposition (CVD), and molecular beam epitaxy (MBE). However, only the three last ones are able to provide single crystalline materials that are necessary to reach the desired performance. The MBE method uses atoms or molecules originating from high-purity (99.9999%) solid materials contained in cells that can be heated individually. Since the process occurs under ultra-high vacuum, the atoms and molecules move in a straight line (molecular regime) toward the sample and form real beams of material which are shaped according to the geometry of the crucibles. Growth can be started or stopped using individual shutters, which can interrupt the beams in a fraction of a second (0.1 s). Epitaxy—which comes from the Greek words "epi" (on top) and "taxis" (order)—is a deposition technique where a thin film is deposited on top of a crystalline substrate and copies its lattice parameter and crystal structure. Epitaxy is made possible in MBE due to the low growth rates (commonly between 0.1 and 1.0 monolayer per second (ML/s)) and the possibility of heating the substrate in such a way that the species arriving at the surface are mobile enough to incorporate into the right sites of the crystal. MBE was invented in the 1970s [87] to produce epitaxial layers under ultra-high vacuum conditions to obtain heterostructures of semiconductor compounds of high purity, high crystalline quality, and having sharp interfaces. Compared with metalorganic chemical vapor deposition (MOCVD) and LPE, MBE is a more expensive and slower deposition technique, but the growth is simpler and provides high precision control of the layer composition, doping, and thickness [88].

Generally, MBE systems consist of three chambers: entry-exit, buffer (intermediate), and growth chamber. The first chamber has the worst vacuum as it is frequently ventilated to allow the samples to be entered into or removed from the system. It is also used to bake the samples together to remove contamination from outside and eventual cleaning residues. In the second chamber, the wafers can be stored together (it has the best vacuum) and can eventually be outgassed individually at a higher temperature. The last chamber contains all the cells and most of the monitoring equipment necessary for the growth. MBE works under ultra-high vacuum (UHV, pressure lower than 7.5×10^{-9} Torr) conditions, which can be achieved by using cryogenic or ion pumps, with eventually an auxiliary titanium-sublimation pump. Each chamber has its own pumping system, pressure gauge (and possibly other types of equipment or monitoring tools), and is separated from the other chambers by a gate valve.

3-2 Varian molecular beam epitaxy system

Figure 3-1 shows the Varian (model Gen II) MBE system installed at the Institute of Physics of the University of Sao Paulo. This system consists of three chambers. The growth chamber (the largest one in the center) contains the effusion cells, which are visible in the backside. The buffer chamber (in the front) contains two long transfer rods to transfer the samples to the growth chamber or heating station (Figure 3-2). The entry-exit chamber (on the right side) has its access flange in the clean room (on the other side of the wall) as can be seen in Figure 3-3. The whole system is controlled by a computer, other pieces of equipment, and power supplies located in the rack (on the left side)

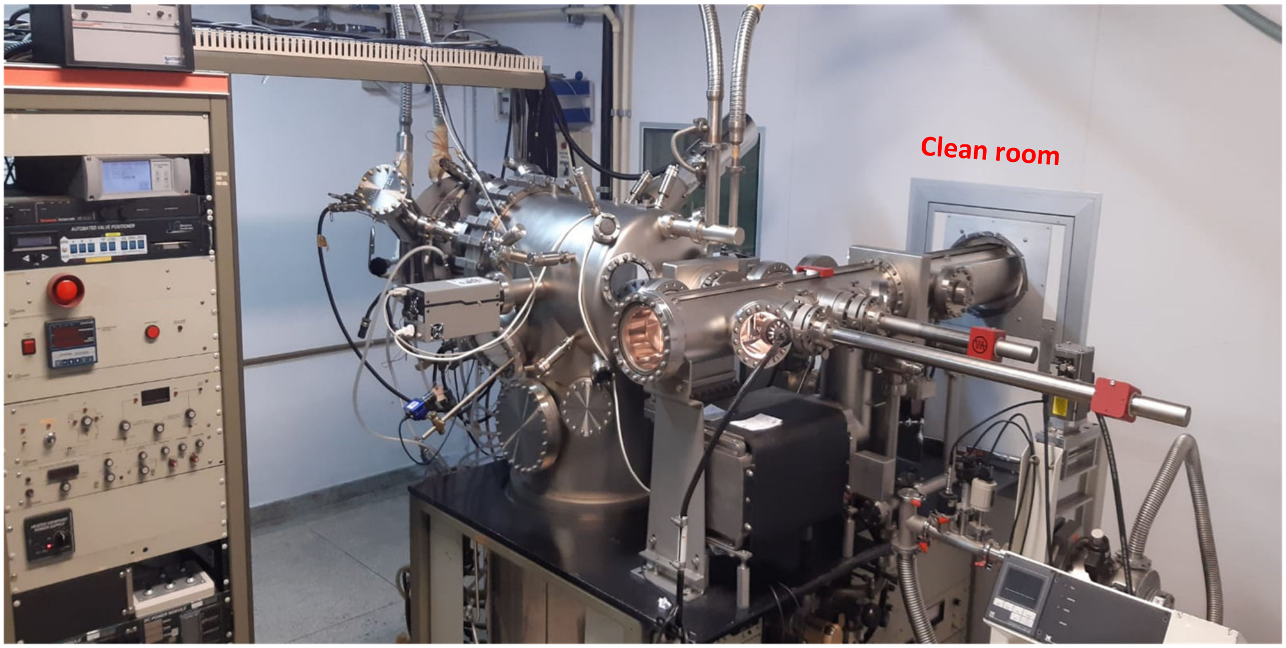

Figure 3-1: The Varian MBE system of the "Laboratório de Novos Materiais Semicondutores" at the Institute of Physics of the University of Sao Paulo. One can see the entry-exit chamber (access inside the clean room), the buffer chamber, and the growth chamber.

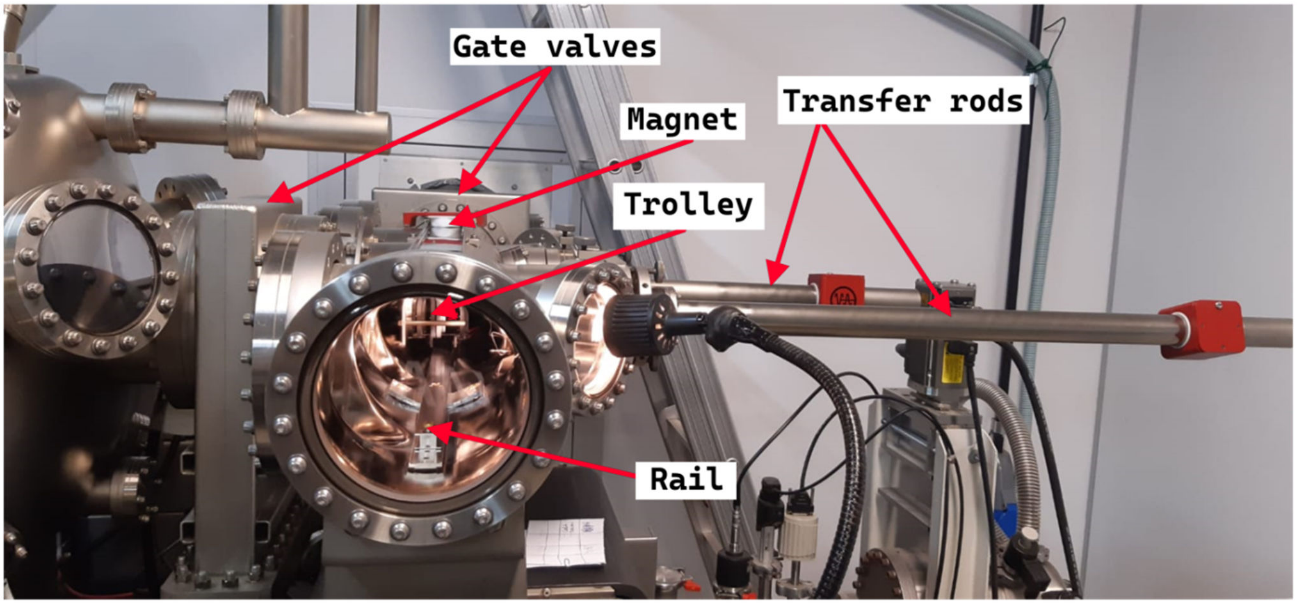

Figure 3-2: Side view of the buffer chamber showing the two transfer rods and the rail on top of which the trolley (in the back) can be moved with an external magnet (on top).

3-2-1 Entry-exit chamber

The entry-exit chamber is used to load and remove the samples. It may be exposed to air during sample exchanges, so its access flange needs to be inside a clean room (preferentially). Typically, MBE systems are located completely within a large clean room, but since IFUSP's clean room was built later and is quite small (about 18 m^2), only the extremity of the entry-exit chamber was included in the clean room, which is sufficient for the growth routine. Figure 3-3 shows the hatch door of the chamber wide open (for sample removal) in the clean room. A trolley with 16 slots for 3-inch Molybdenum (Mo) blocks can be loaded into the chamber. It can be pumped from the atmosphere to 10^{-8} Torr using a turbo pump and an ion pump. Next, the trolley with all the Mo blocks and samples can be baked for at least one hour at 200 ˚C using quartz lamps to remove all contamination introduced during sample handling and loading.

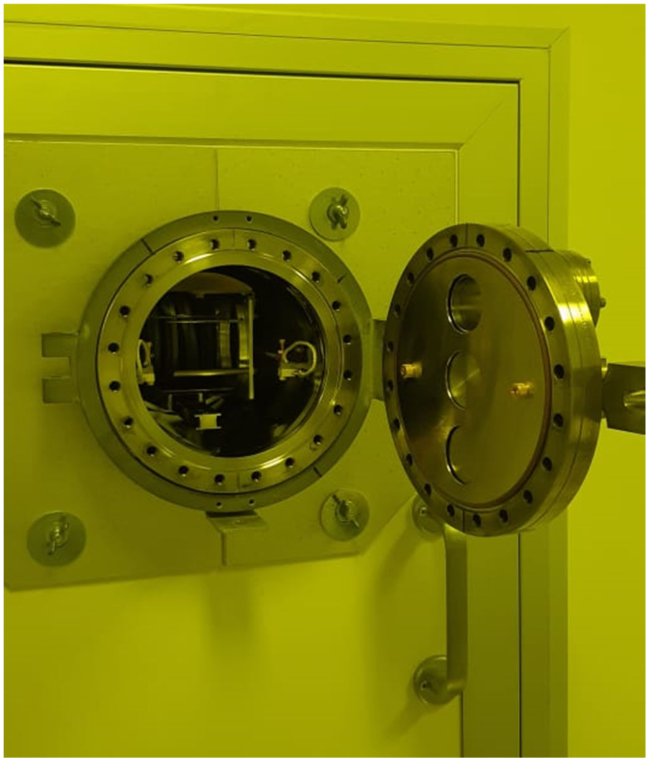

Figure 3-3: The opened door of the entry-exit chamber located in the clean room where the trolley is ready to be removed for changing the samples.

3-2-2 Buffer chamber

The buffer chamber or pre-growth or intermediate chamber is the chamber connected to both the growth and entry-exit chambers, where samples are stored and can be outgassed individually to a higher temperature before their transfer to the growth chamber. It protects the growth chamber from possible contamination introduced through the entry-exit chamber, especially when that latter is opened to the air during sample loading/removal. It can also be used to store degassed wafers and grown samples as its pressure is generally in the 10^{-10} - 10^{-11} Torr range. The trolley can be transferred from the entry-exit chamber to this chamber (and vice versa) rolling on a rail with an external magnet after opening the gate valve separating both chambers (Figure 3-2). Fresh substrates introduced into the buffer chamber should be outgassed at 350 °C for more than 30 min before being transferred to the growth chamber.

3-2-3 Growth chamber

Figure 3-4-a shows a schematic of the growth chamber, which consists of a vacuum chamber with a sample holder that can be heated to allow the species arriving on the sample to diffuse and incorporate into the right sites and provide the best crystalline quality. The samples can be moved from the trolley inside the buffer chamber to the front of the cells using the long arm of the buffer chamber and the sample holder that can rotate around two orthogonal axes (Figure 3-4-a). The cells contain high-purity materials (6N-7N5) that will be used during epitaxy and need to be controlled individually to reach the right temperature and provide the desired growth rate of each material.

In the Varian MBE system of LNMS, eight flanges can accommodate cells (see Figure 3-4-b). Currently, there are two with gallium (Ga), one with arsenic (As), one with indium (In), one with aluminum (Al), and two dopant cells: one with silicon (Si) for n-type doping and another with two carbon (C) filaments for p-type doping. Each cell has a shutter that can be opened or closed whenever needed to allow deposition of a specific material. In addition, the cells and sample

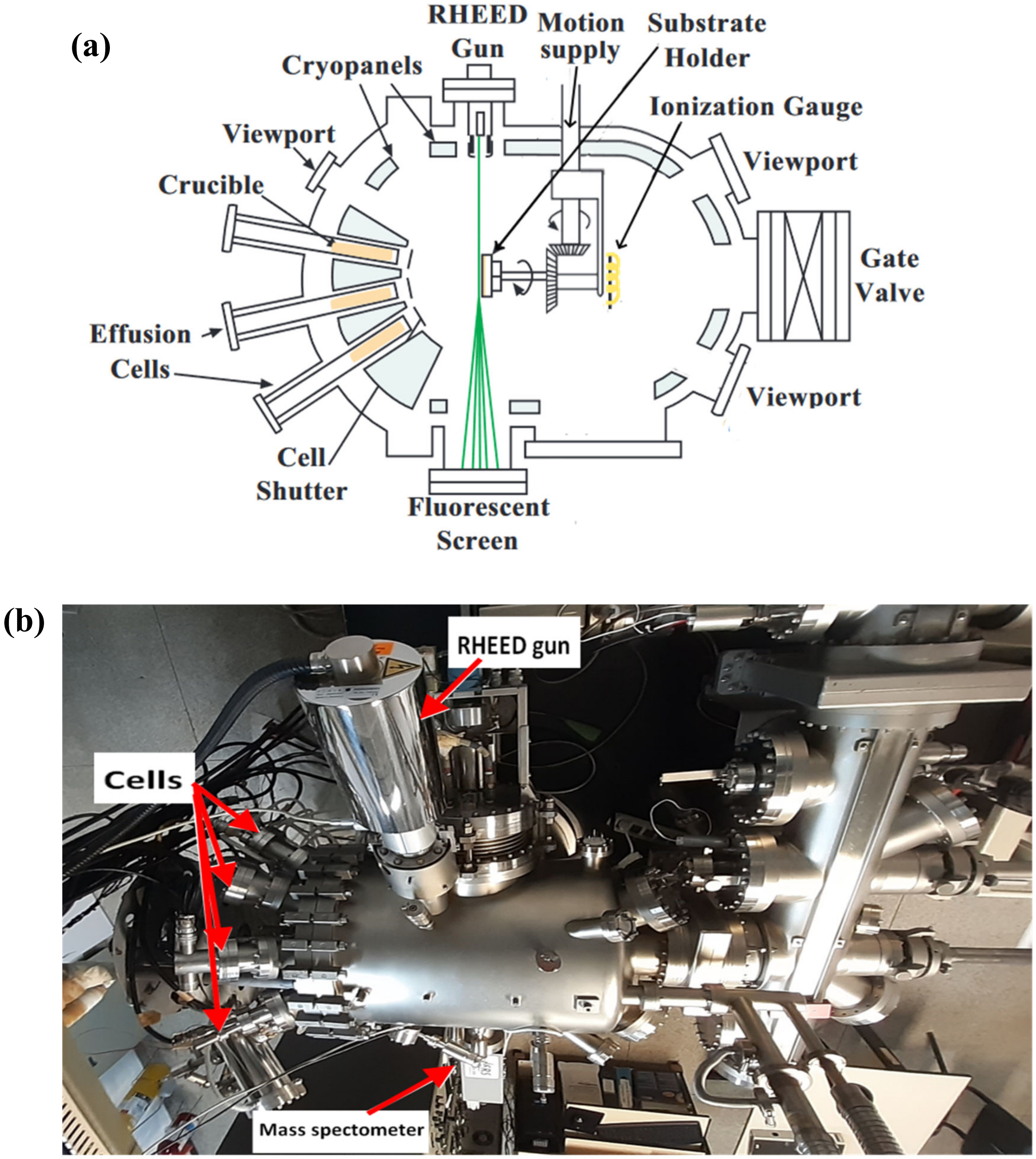

Figure 3-4: (a) Main components of the growth chamber of the Gen II MBE system [89]; (b) Top view of the growth chamber of the Gen II MBE system at LNMS.

holder are surrounded by a panel containing liquid nitrogen that acts as an extra cryogenic pump to reduce further the pressure inside the chamber and allow better quality and higher purity of the samples. Some *in-situ* characterization techniques are also available (Figure 3-4-b): several Bayard-Alpert vacuum gauges are responsible for the measurement of the flux of elements and the pressure inside the chamber, a mass spectrometer allows analysis of the residual atmosphere, and an infrared pyrometer detects the substrate temperature (in the 400 ˚C – 1200 ˚C range), which is also independently monitored by a thermocouple (located in the sample holder, just behind the Mo block) used for its stabilization. A RHEED (reflection high-energy electron diffraction) system consisting of an electron gun and a fluorescent screen (Figure 3-4-b), allows in-situ measurements of the growth rates and alloy composition in real-time, as well as the monitoring of the atomic reconstruction of the sample surface as a function of the growth conditions. The sample holder consists of a heater (with the thermocouple in its center) and a mechanism to fix the Mo blocks and allow a continuous azimuthal rotation motion (this is why that system is called CAR) of the samples during growth to achieve a high homogeneity (of thickness and composition). Finally, a mass spectrometer (RGA, residual gas analyzer) allows to analyze the composition of the residual gas in the chamber, but can also be used to check desorbed species, growth issues, vacuum leaks, etc.

3-2-4 Effusion cells and Arsenic cracker

Effusion cells are important key components of the MBE system as they must provide excellent flux stability and homogeneity, as well as material purity. There are 7 cells (there is still one blank flange) symmetrically placed on the main 18-inches source flange and facing the substrate heater to optimize flux uniformity. The instability of the material flux is within 1% during short periods, with variations of less than 5% during a full day [90]. In our group, we calibrate the growth rates before every growth day to ensure the accuracy of their value. Figure 3-5-a shows a typical MBE solid effusion cell that consists of (1) a crucible, which is usually made of pyrolytic boron nitride (but can also be made of tantalum, titanium, beryllium, or quartz depending on the element to be deposited) to resist temperatures up to ~1300 ºC without appreciable degassing. Its size is determined by the material to be evaporated, and it must be large enough to last many depositions before relevant depletion occurs; (2) a Ta or W filament, which is responsible for heating the crucible and the pure element inside; (3) a thermocouple, which is located in an appropriate position (but always with a very good mechanical and thermal contact) to accurately measure the crucible's temperature; (4) a pneumatic shutter placed in front of the cell to trigger (i.e., to start or stop) the flux of material emitted from the cell. The shutter's reaction time must be as low as possible (typically less than 0.1 s) and should be computer-controlled to provide reproducible layer thicknesses and growth cycles. They must also be designed not to outgas when heated by the cells, nor to constitute an appreciable heat shield, giving rise to flux transients after opening (i.e., they should not be too close to the cell). In our MBE system at LNMS, all the group-III materials are contained in standard effusion cells (Figure 3-5-a) in a looking-up position, while the Arsenic material (group V) is in a valved cracker effusion cell (Figure 3-5-b). A large reservoir (with a W crucible) of solid As material is thermally heated, allowing the material to sublime in the tetrameric form As_4 (As has an extremely high vapor pressure). The As_4 molecules then pass through a microvalve, which allows changing the flux of material by one order of magnitude within a few seconds, and finally through a cracking zone (Figure 3-5-c). There, depending on the temperature of this region, the As_4 molecules can be cracked into two As_2 dimers (at high temperatures) or cross the whole zone and come out as As_4 (at low temperatures). The bulk-zone crucible can hold an As charge of up to 2 kg which is enough for several years of growth.

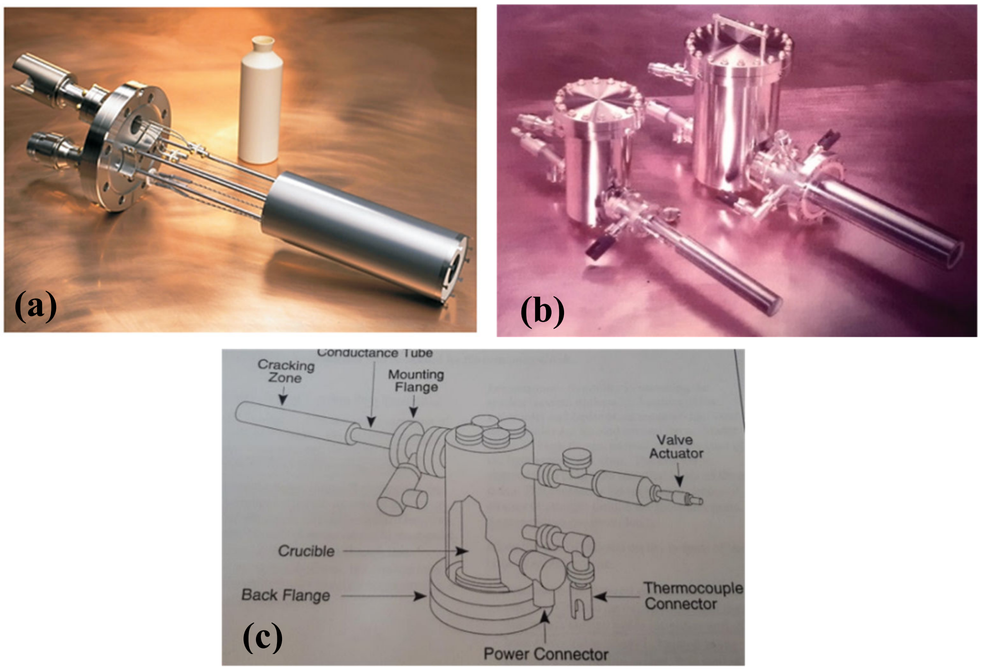

Figure 3-5: (a) Typical MBE solid effusion cell with a crucible; (b) Typical valved cracker for Arsenic; (c) Schematic drawing of the valved cracker [91].

3-3 MBE operation

3-3-1 Sample preparation

Clean substrates are essential for epitaxial growth since their oxidation and contamination due to atmospheric exposure may result in crystal defects that degrade both their optical and electrical properties. Nowadays, vendors provide 'epi-ready' wafers that are pre-cleaned and oxidized in a controlled environment so that the thin oxide protective layer can be thermally removed inside the growth chamber without damaging the crystalline surface. Fresh substrates should be handled in a clean room or under a laminar flux, using gloves and clean tools (tweezers, scissors, etc.).

A sample-preparation process begins by cleaving the substrate (3 inches) into smaller pieces depending on the purpose: test samples are usually small squares (~1–2 cm^2) fixed with melted In on a Mo block, while devices are grown on a quarter of a wafer (~11 cm^2) which is fixed with small clips (Figure 3-6-a). Then the new samples are loaded on the trolley which is in turn introduced into the entry-exit chamber of the MBE system (Figure 3-6-b), where it is outgassed at 200 ºC for at least one hour and then transferred to the buffer chamber to outgas each block individually at 350 ºC for 30 min. Following the opening of the gate valve that separates the buffer and growth chambers, the sample is moved to the sample holder (CAR) inside the growth chamber, where it undergoes oxide removal and outgassing at 615 °C for 5 min.

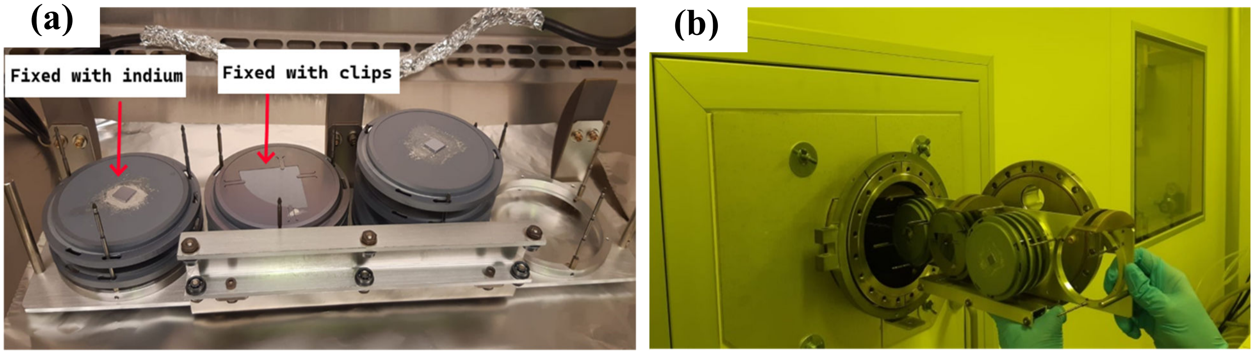

Figure 3-6: (a) The trolley with several Mo blocks (substrate holders); the small samples were fixed with Indium melted at 200 ºC, and the large samples (1/4 of a wafer) were fixed with clips; (b) The trolley with the new samples is loaded into the entry-exit chamber whose hatch door is located in the clean room.

3-3-2 Reflection high-energy electron diffraction

Several instruments are used in the growth chamber to determine and control parameters during the growth of the samples. For instance, the sample temperature is remotely measured by a pyrometer and controlled by a thermocouple which is used as feedback for the power supply that controls the sample temperature. The beam equivalent pressure (BEP) of each material can be measured by a Bayard-Alpert pressure gauge located on the backside of the sample holder. When the sample holder faces the cells, the pressure gauge measures the background pressure; however, when it is in the transfer position (i.e., facing the buffer chamber), the pressure gauges face the cells and can measure their BEP, which is proportional to the flux of material. A mass spectrometer can be used to perform a compositional analysis of the residual gas in the growth chamber to detect leaks or check the release of specific species at different stages of the growth or during any other process. An electron gun and a fluorescent screen compose the RHEED system, which is the main *in-situ* tool used to determine most growth parameters.

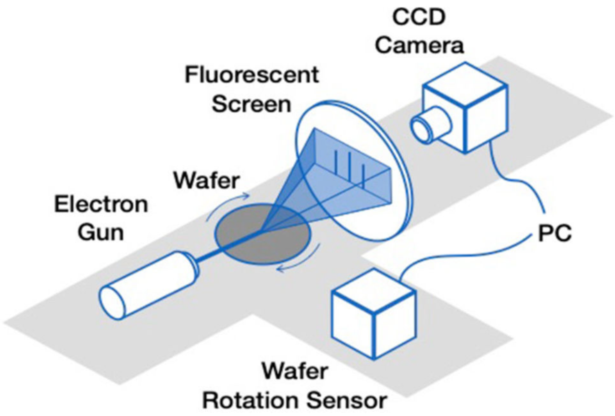

Figure 3-7: RHEED setup inside the growth chamber of the MBE system: the electron beam is reflected/diffracted by the surface of the sample and then observed by a CCD camera on a phosphor screen [92].

Figure 3-7 shows a typical RHEED system consisting of an electron gun that shoots high-energy electrons at a grazing incidence—typically at an angle of 1 degree—onto the sample surface. The electrons are reflected and diffracted by the sample and can be observed on a phosphor screen where they form a typical pattern that can be recorded using a CCD (charge-coupled device) camera connected to a computer. Due to the grazing incidence, the electrons can only enter the very first monolayers of the sample and thus provide information almost exclusively about the surface. RHEED is the most helpful way for accurately monitoring the growth process, providing information about the epilayers thickness, growth rate, composition of the alloys, as well as surface roughness and reconstruction. Since it is extremely sensitive to the state of the surface, it is also used to monitor the sample before, during, and after growth. After the GaAs sample is loaded into the growth chamber, its temperature is increased up to 610 °C—measured with a calibrated pyrometer—to remove the oxide film that naturally formed on the GaAs surface since the moment it was produced at the factory. As the oxide layer is amorphous and a few nm thick, the electron beam is randomly scattered and the pattern on the fluorescent screen is diffuse. When the sample is heated above 580°C, the oxide slowly evaporates and the GaAs surface can be probed by the electron beam. Since this oxide layer is not homogeneous, its removal forms pits in the GaAs surface, and this roughness appears on the RHEED screen as a spotty pattern (Figure 3-8-a) resulting from the 3D diffraction of the electron beam by the rough surface. After the deposition of 30 nm of GaAs, an atomically flat and crystalline surface of GaAs is recovered, as can be seen by the streaky RHEED pattern typical of a flat 2D surface in Figure 3-8-b. In that case, most of the incident electron beam is specularly reflected and an intense spot dominates the pattern. It is only when the surface is flat (and streaky as shown in Figure 3-8-b) that the RHEED system can be fully utilized to provide growth rates and compositions as well as a detailed investigation of the surface reconstruction.

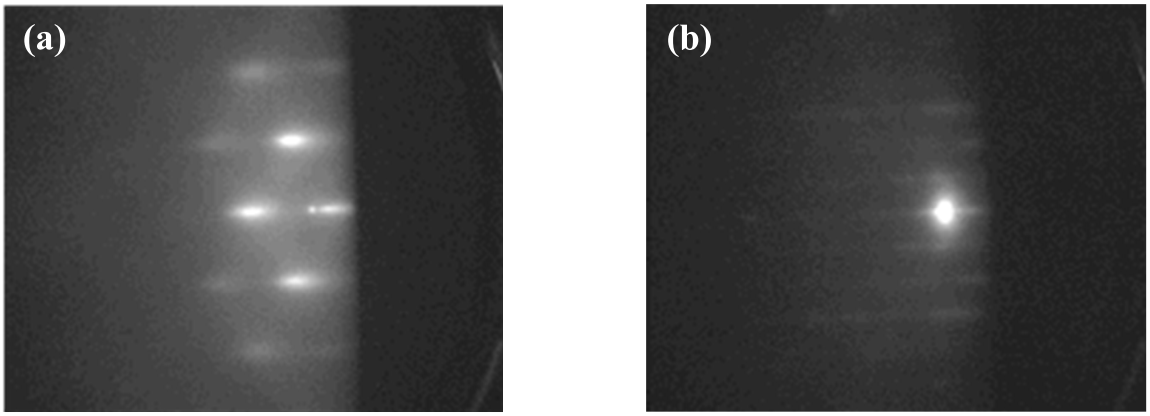

Figure 3-8: RHEED pattern of a GaAs(001) surface; (a) immediately after oxide removal (spotty pattern); (b) after the deposition of 30 nm of GaAs (streaky pattern with specular spot).

3-3-3 Growth rates and compositions

The MBE growth of GaAs must occur in well-defined conditions to provide an epitaxial layer of excellent crystalline quality with specific properties. Consequently, the sample temperature, material growth rate, and As flux must be in a specific range to provide the best material quality. The growth rates can be determined directly at the beginning of the growth run using the RHEED system, while the As flux is usually monitored indirectly, but in real-time, with Bayard-Alpert pressure gauges (although it can also be measured by RHEED, as will be shown later). As already explained earlier, one of the pressure gauges is located at the backside of the sample heater and can be placed just in front of the cells to measure the flux of material coming directly from each of them (actually, it measures the BEP, which can be transformed into a flux value when necessary). When the sample is placed in front of the cells for the growth, the pressure gauge looks in the opposite direction and operates as a standard pressure gauge, indicating the background pressure in the chamber, which depends on the flux of each material (Figure 3-4-a). However, since the As pressure vapor is much larger than that of the other materials in usual growth conditions, the background pressure is mostly due to the As material.

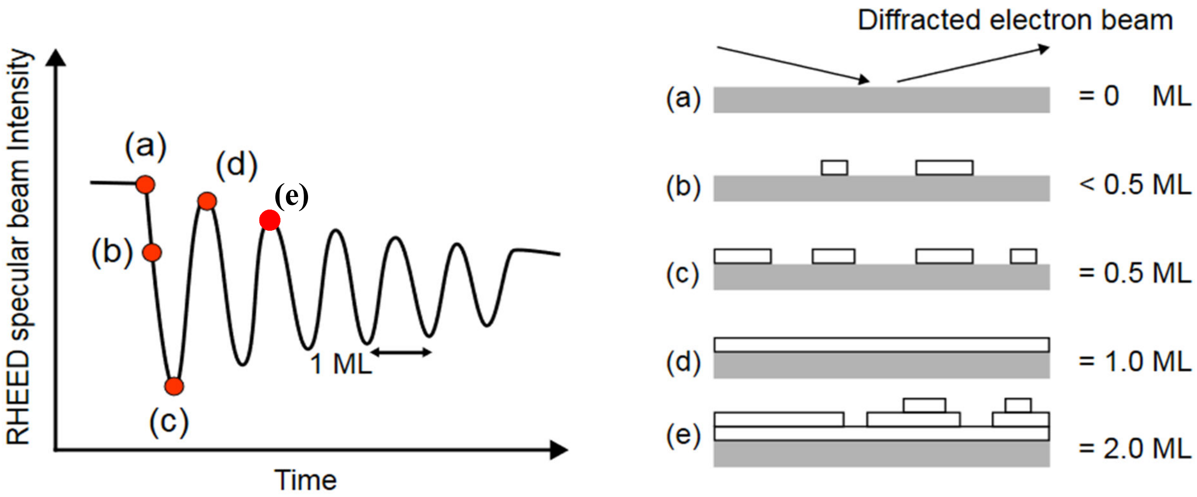

Figure 3-9: Diagram and interpretation of the RHEED oscillations. The left image, shows the intensity of the specular spot as a function of time, where one period (a, b, c, and d) of the oscillation corresponds to the deposition of a single monolayer. The right image relates the physical evolution of the surface (nucleation of 2D GaAs islands) to each RHEED intensity [93].

The growth rate of the materials is calibrated using the RHEED system by monitoring the intensity of the specular beam on the fluorescent screen with a CCD camera and a program that allows measurement of the light intensity in a narrow window of the image. A smooth surface provides a streaky pattern (diffracted part of the beam) and an intense specular spot (reflected part of the beam), as shown in Figure 3-8-b. When the growth starts from a flat surface (point a in Figure 3-9), 2D islands are nucleated and therefore increase the scattering of the electron beam (due to the higher density of steps), meaning that the reflected beam (specular spot) loses intensity (point b in Figure 3-9). The roughness of the surface keeps increasing until half of a monolayer is deposited, providing thus the maximum scattering and minimum intensity of the specular spot observed in Figure 3-9 (point c). Beyond that value, the holes of the layer start to be filled with material and the roughness decreases gradually, until a full layer is deposited (point d). As a consequence, when depositing a material on the surface, the roughness of the growth front varies periodically, yielding an oscillation of the specular-spot intensity, as shown in Figure 3-9. The deposition rate of the materials can be determined accurately by dividing the number of oscillations (i.e., of monolayers) by the corresponding elapsed time. The maximum intensity of the oscillation keeps decreasing slowly with time because a new layer generally starts before the previous one can be completed (i.e., it is not completely flat and some scattering is already present, as we can see in point e of Figure 3-9).

In our MBE system, we have one cell with Al, one with In, and two with Ga, whose flux can be calibrated as explained above. Each cell can be heated individually, and the flux coming out of them is a function of that temperature. Therefore, each cell must be set at a specific temperature to produce the flux that will provide the desired growth rate. Good growth conditions of III-As compounds usually require an As/III flux ratio between 1-3 to get an As-stabilized surface (i.e., the top crystalline layer of the GaAs substrate consists of only As atoms) [94, 95]. The calibration of a material consists in opening the III and V shutter simultaneously and recording the RHEED oscillations (Figure 3-10-a). Actually, the As shutter is always kept open as the usual growth temperature (between 500 and 600°C) is such that As atoms continuously desorb from the GaAs surface and must therefore be replaced by extra material coming from the As cell to maintain its stoichiometry. For this reason, the As/III flux ratio must always be larger than 1.

The sticking coefficient of As is zero on an As-stabilized surface, while it is 1.0 only when the GaAs surface is group-III rich. Therefore, when the As shutter is open, the As molecules don't stick on the surface unless the shutter of a group-III cell is open. The sticking coefficient of the group-III elements is 1.0 on the GaAs surface, which means that the growth is controlled by the arrival of the group-III elements. Another consequence is that, when two group-III materials are simultaneously deposited (e.g., InAs and GaAs), their growth rates (R_{GaAs} and R_{InAs}, respectively) add, and the growth rate of the $In_xGa_{1-x}As$ alloy is $R_{InGaAs}=R_{GaAs} + R_{InAs}$. Therefore, one can easily estimate the composition of the ternary alloy, as the In content x is simply given by $x= R_{InAs} / R_{InGaAs}$.

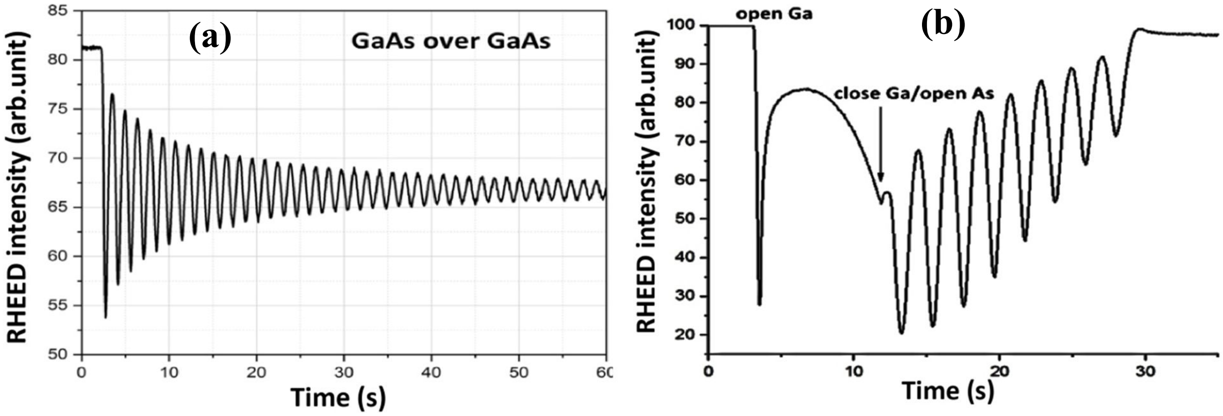

Figure 3-10: (a) Typical RHEED oscillation obtained during calibration of a Ga cell. The Ga and As cells were simultaneously opened, and the growth rate is given by dividing the number of oscillations by the respective time. (b) RHEED oscillations obtained during calibration of the As flux. First, the As shutter was closed and the Ga shutter was opened to deposit the equivalent to 8 MLs of material. Then, the As shutter was opened to allow the As molecules to react with the Ga atoms and form 8 GaAs layers, as can be confirmed by the number of oscillations.

The calibration of the As flux with the RHEED system is different because the sticking coefficient of As is zero unless a population of group-III elements is present on the surface. As a consequence, to calibrate the As flux, a few MLs of Ga are generally deposited on the surface without any As (the As shutter remains closed), and then the shutter of the As cell is open (and the Ga shutter is closed). The As material will react with the Ga population to grow crystalline GaAs that will roughen the surface (as explained above) and yield RHEED oscillations similar to the ones shown in Figure 3-10-b.

3-4 Quantum dots

There are basically three different growth modes to produce a thin film [96]: The Frank-van der Merwe (FM) growth mode is the one that is used for the epitaxy of semiconductor materials, where the atomic layers are deposited one after each other in a two-dimensional way to produce an atomically flat surface (Figure 3-11-a). In the Volmer-Weber (VW) growth mode, which typically occurs when a metal is deposited on top of a semiconductor, large islands are formed on the surface and merge to cover the substrate with a continuous film (Figure 3-11-b) that is not flat and has a specific structure and roughness. Finally, in the Stranski-Krastanov (SK) growth mode, which is used to grow self-assembled QDs (Figure 3-11-c), the deposition starts in the FM growth mode, where a 2D layer is formed, and then switches to the VW growth mode due to an instability of the system, generally related to the accumulation of elastic energy due to the stress between the material and the substrate related to their lattice mismatch. The remaining of the initial 2D layer after formation of the 3D islands is called wetting layer.

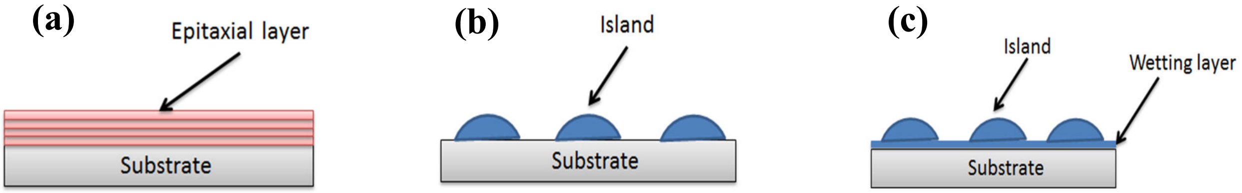

Figure 3-11: Comparison of the 3 growth methods. (a) Frank-van der Merwe; (b) Volmer-Weber; (c) Stranski-Krastanov.

3-4-1 Self-assembled quantum dots

The usual type of InAs quantum dots is obtained by self-assembling using the SK growth mode which consists in depositing a thin InAs layer on top of a GaAs substrate that will relax beyond a critical thickness and form small 3D islands on the surface of the epitaxial film. InAs SK-QDs are generally grown below 520°C (generally between 500 and 515°C) using a growth rate of InAs around 0.1 ML/s to limit In desorption that starts to be relevant above 520°C. Above a critical thickness of 1.7 MLs, the thin 2D InAs layer—that is under compressive biaxial strain due to the difference in lattice parameter between InAs

(6.0585 Å) and GaAs (5.6534 Å)—relaxes and spontaneously forms a high density of small and rather homogeneous InAs islands that can confine the carriers along the three directions of space, and thus behave as quantum dots. Since such nanostructures are self-assembled, they can only be controlled in a very limited way. SK-QDs usually are lens-shaped, have a density in the 10^{10} cm^{-2} range [97], and have a base and height of the order of 10-20 nm and 3-7 nm, respectively. The nucleation of the first SK-QDs on the GaAs surface can be easily monitored *in situ* with the RHEED system, as the diffraction pattern switches from a streaky configuration (initial deposition of the 2D InAs layers) to a spotty one (formation of the first SK-QDs that generate some roughness), resulting from the transition from a 2D to a 3D diffraction of the electron beam (Figure 3-12). This transition can be used to calibrate the InAs growth rate by dividing the InAs critical thickness (1.7 MLs) by the growth time elapsed to observe the transition.

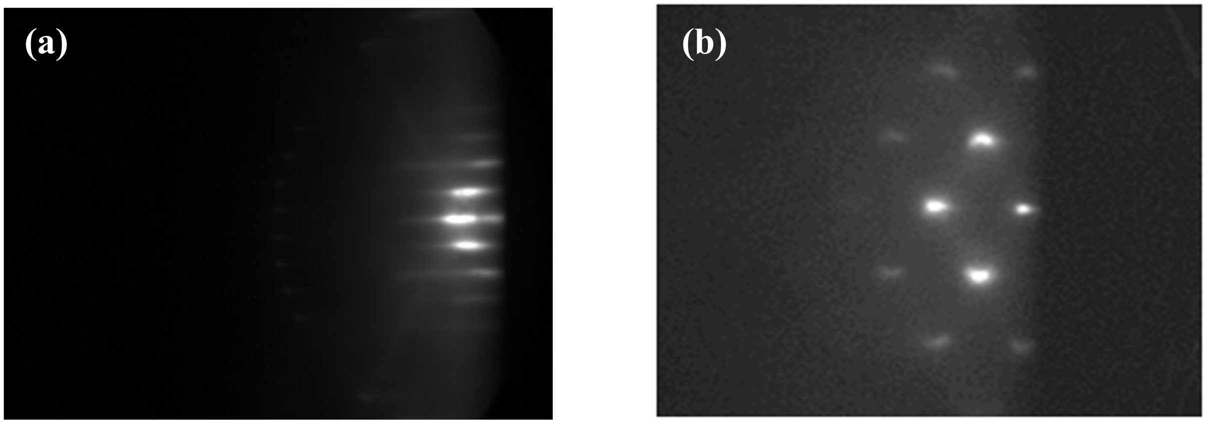

Figure 3-12: (a) RHEED pattern of an atomically flat GaAs surface at 515 °C in a c(4×4) surface reconstruction just before InAs deposition; (b) just after deposition of 1.7 MLs of InAs and nucleation of the first InAs SK-QDs.

Although the use of SK-QDs has already improved the performance of optoelectronic devices compared to QWs, further improvement is currently more difficult due to the lack of control of their size, composition, and density, and to the presence of the wetting layer that reduces the 3D confinement of the carriers. Many research groups have worked on methods to improve the performance of devices based on SK-QDs, either by changing their composition (InAs, InGaAs, InAlGaAs) [98, 99], size and density (varying the growth temperature) [100], or by changing the design of the structure using, for example, quantum dots in a well

(DWELL) [101], quantum dots in a double well (DDWELL) [102], or confinement-enhanced dots-in-a-well (CE-DWELL) [103]. In parallel, a new way to grow the QDs was also proposed and is based on a submonolayer deposition technique.

3-4-2 Submonolayer quantum dots

Over the past few years, the submonolayer deposition technique has arisen as a possible solution to grow quantum dots and solve the problems of low areal density, lack of control, and presence of a wetting layer that are typical of SK-QDs [31, 32, 104]. In(Ga)As submonolayer quantum dots (SML-QDs) are made by depositing a fraction of a monolayer (usually between 0.3 and 0.65 ML) of InAs material—to nucleate an extremely high density of small 2D islands on the GaAs substrate (up to 10^{12} cm^{-2} [44])—followed by a specific number of GaAs monolayers (generally between 1 and 3 MLs) to cover the islands, as shown in Figures 3-13-a and 3-13-b. Repeating that sequence as many times as needed, one expects to get a high density of stacks of small 2D InAs islands, whose height and composition can be obtained in a more controllable way. Indeed, due to the elastic strain present in the InAs/GaAs system, the small 2D islands from each InAs SML will tend to nucleate above the ones of the previous InAs SML (Figure 3-13-c), thus forming stacks of 2D InAs islands, separated by GaAs material, that will behave as individual InGaAs quantum dots (Figure 3-13-d).

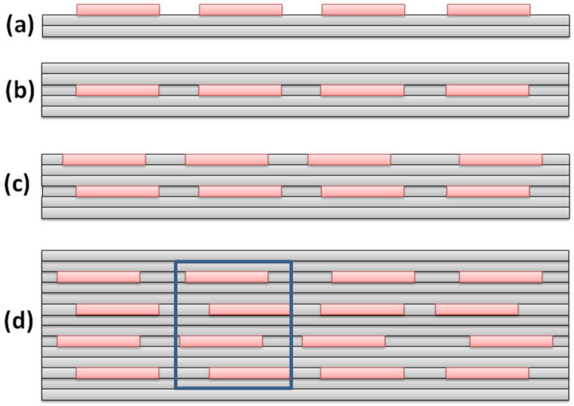

Figure 3-13: Scheme of the formation of SML-QDs: (a) Deposition of an InAs submonolayer (0.5 ML) on top of GaAs to nucleate small 2D InAs islands; (b) Coverage of the InAs islands with GaAs material (2.5 MLs); (c) Vertical alignment of the islands of consecutive InAs submonolayers; (d) InGaAs SML-QDs (blue box) formed by repeating 4 times the basic deposition cycle.

The evolution of the RHEED pattern during the growth of InAs/GaAs is shown in Figure 3-14. Since deposition proceeds the whole time in the VW growth mode, the RHEED pattern is always streaky (Figure 3-14) and never becomes spotty, as was the case for SK-QDs (Figure 3-12-b). However, the pattern becomes fuzzy after the first cycle, most probably because of the strong segregation of In atoms that keep floating on the surface and promote a diffuse scattering of the electron beam.

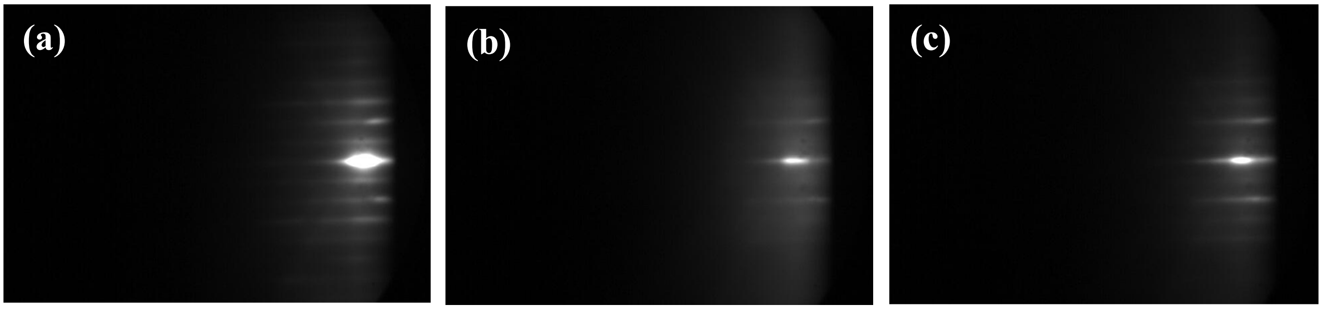

Figure 3-14: (a) RHEED pattern of an atomically flat GaAs surface before starting to grow InAs SML-QDs, (b) just after the deposition of 0.5 ML of InAs to nucleate small 2D InAs islands (Figure 3-13-a), and (c) just after deposition of 2.50 MLs of GaAs to cover the 2D islands (Figure 3-13-b).

Since In strongly segregates during GaAs capping, the InAs material of the 2D islands will be diluted in the stacks and form SML-QDs with an average InGaAs composition that will depend on the amount of InAs and GaAs material deposited in each cycle. This new type of QD has already shown excellent results in lasers [33], solar cells [35], and QDIPs, compared to conventional SK-QDs [105-107]. However, it seems that their growth conditions still need to be improved. Indeed, as we mentioned previously in Chapter 1, all the results of the literature involving SML-QDIPs have been obtained under growth conditions similar to those used for SK-QDs, which provide a c(4×4) surface reconstruction of the GaAs(001) surface. However, in-situ STM data already showed that 2D InAs islands (which are the building blocks of SML-QDs) can only be nucleated on a GaAs(001) surface in the presence of a (2×4) reconstruction [47, 48]. As a consequence, the investigation of the right surface reconstruction to be used to get the best SML-QDs is extremely important.

3-5 Reconstructed surfaces of GaAs(001)

A detailed understanding of the atomic configuration of the compound semiconductor surface, especially after reconstruction, is very important for device fabrication and performance. After the first successful demonstration of MBE on GaAs(001) [108], it has been reported that a variety of reconstructions were formed depending on the surface stoichiometries, ranging from c(4×4)—the most As-rich surface—through (2×4), (6×6), and c(8×2), to (4×6)—the less As-rich surface (i.e., the most Ga-rich one). The atomic structures of all these reconstructions have been extensively studied [109, 110], but only the c(4×4) and (2×4) phases are generally used in the MBE growth of GaAs—as the other ones usually lead to poor crystalline quality—and, therefore, will be detailed here.

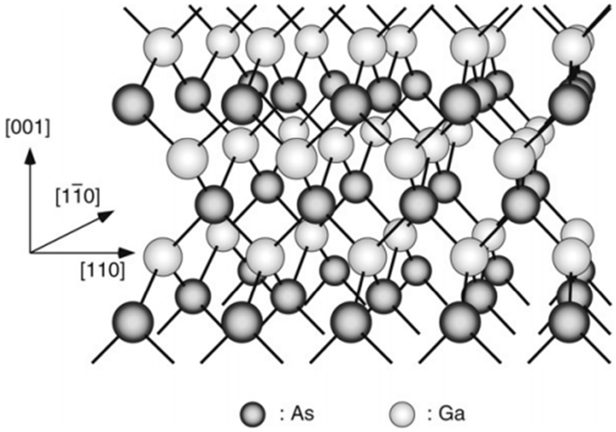

Figure 3-15: Atomic representation of bulk GaAs(001) in the zincblende structure. Ga and As planes alternate along the [001] direction with a spacing of 1.41 Å [111].

The bulk crystalline structure of GaAs is of the zincblende type and consists of 2 face-centered cubic structures—one with only Ga atoms and the other with only As atoms—that are shifted by ¼ of the long diagonal of the cube. As a consequence, the (001) surface of the zincblende structure of GaAs can be terminated by either As or Ga atoms, as shown in Figure 3-15. At the surface, the crystal is interrupted, and there are two dangling bonds for each surface atom. In addition, due to the symmetry breaking, the surface atoms can adopt different positions from the ones in the bulk to minimize the surface energy, leading to surface reconstructions. Figure 3-16 shows that the reconstruction of a GaAs(001) surface can usually be changed in two different ways: by changing the As flux (which is relatively easy with a valved cracker, see Figure 3-5-c) or by changing the sample temperature, which gives more energy to the surface atoms to break the symmetry of the bulk structure. Therefore, depending on the sample temperature and the delivery of Ga and As atoms from the cells, a Ga-rich or As-rich surface can be obtained, and different surface reconstructions (with different stoichiometries) can be observed.

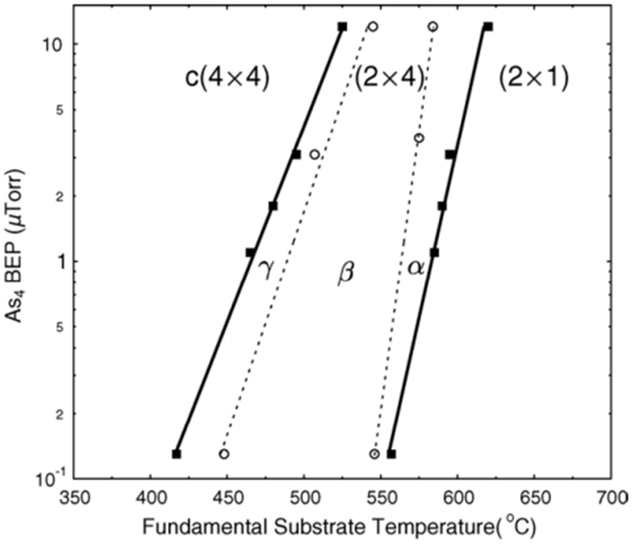

Figure 3-16: Reconstruction phase diagram of the arsenic-rich GaAs(001) surface as measured using RHEED. The solid lines indicate the transitions between the three reconstructions as indicated. The dotted lines indicate the transitions between the three sub-phases of the (2×4) reconstruction [110].

The growth of high-quality GaAs crystals for optoelectronic devices always occurs in the arsenic-rich (2×4) surface reconstructions around 570–600 °C. This As-rich surface appears whenever a clean GaAs(001) surface is heated above 525 °C under a high arsenic flux. Due to the low In-As binding energy, deposition of InAs is typically carried out at a temperature below 520 °C to avoid the evaporation of In atoms from the surface. As the temperature of the GaAs(001) surface is reduced from 570-600 °C down to 520 °C in the presence of a high As flux, the surface switches from the (2×4) to the c(4×4) reconstruction, which has the largest number of As atoms at the surface. It is this c(4×4) reconstruction that is used to obtain conventional SK-QDs, as well as all the SML-QDs reported in the literature. Figure 3-16 shows that if one wishes to recover the (2×4) reconstruction at such a low temperature, a reduction of the As flux is necessary. Analyzing the differences between both reconstructions of the GaAs(001) surface at the atomic scale is important to better understand how it may affect the growth of InAs.

The atomic structure of the (2×4) surface has been a subject of continuing interest over the past four decades. Cho first reported that the (2×4) reconstructions could form on both As- and Ga-stabilized surfaces prepared by MBE [112]. Since good epitaxial layers can only be obtained in As-rich conditions, only the As-stabilized surface reconstruction will be analyzed here. The (2×4) reconstruction has a twofold periodicity along [110], which is the direction parallel to the As dangling bonds of the As-terminated GaAs(001) surface (Figure 3-17), and a four-fold periodicity along the orthogonal direction ([1$\bar{1}$0]). It is associated with three different atomic configurations (α, β, and γ) that can be obtained by varying the As flux (or substrate temperature).

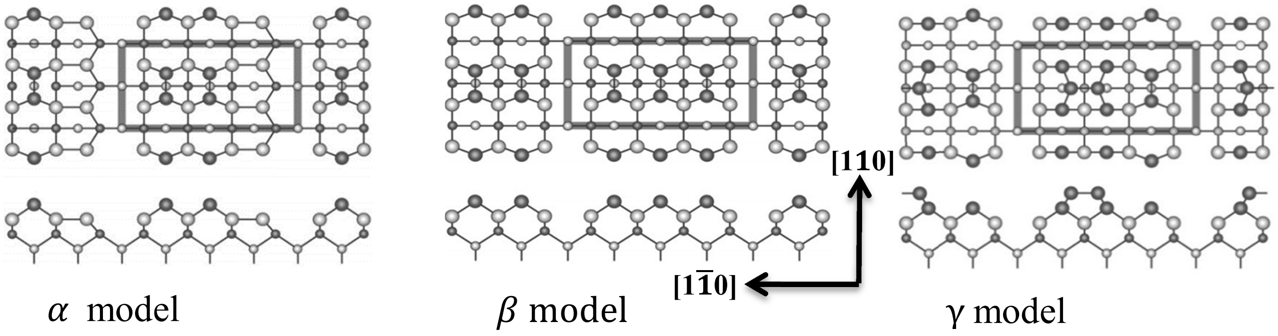

Figure 3-17: Model of the atomic structure of the different types (α, β, γ) of As-rich GaAs(001)-(2×4) surface reconstructions. The upper part of the figure represents a top view of the surface reconstruction, while the bottom part is a side view of the same surface. Filled (open) circles denote As (Ga) atoms [113].

According to the model of Chadi *et al.* [114], the β-(2×4) structure contains three As dimers in the uppermost atomic layer, while the α-(2×4) has two As dimers in the top layer, and the γ-(2×4) is similar to the β-(2×4) structure with an extra As dimer on the top. One can see from Figure 3-17 that the number of As atoms increase from 4 to 6 to 8 per unit cell of the reconstructed surface when one goes from the α to the β and then the γ phase, respectively. For a fixed As_2 flux, the GaAs(001)-(2×4) surface reconstruction can be easily changed by reducing the substrate temperature a few tens of degrees Celsius. For our usual growth condition (BEP of As close to 10 μTorr), Figure 3-16 shows that $T_{(2\times1)\rightarrow\alpha-(2\times4)} \approx 620°\mathrm{C}$, $T_{\alpha\rightarrow\beta} \approx 580°\mathrm{C}$, $T_{\beta\rightarrow\gamma} \approx 545°\mathrm{C}$, $T_{\gamma-(2\times4)\rightarrow c(4\times4)} \approx 525°\mathrm{C}$. However, once the c(4×4) reconstruction is reached at a lower temperature, the only way to recover the original (2×4) reconstruction is by considerably decreasing the As BEP [110].

Akihiro Ohtake *et al.* [113] showed that the c(4×4) surfaces are classified into two phases: the α phase has a Ga-As dimer structure, and the β phase has an As-As dimer structure, depending on the preparation conditions. While the c(4×4)-α structure is usually obtained by cooling the (2×4) surface under As flux, the c(4×4)- β structure can only be formed when the c(4×4)- α surface is covered with amorphous As layers and then is thermally annealed under an As flux.

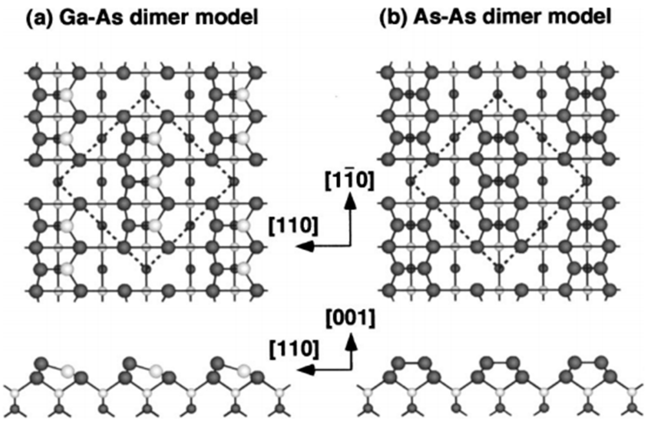

Figure 3-18: Top and side views of the Ga–As dimer and As–As dimer structures of the As-stabilized GaAs(001)-c(4×4) surface. Closed (open) circles denote As (Ga) atoms. [113].

The usual growth conditions of GaAs and AlGaAs layers generally consist of a substrate temperature around 570-600 °C, an As background BEP around 5-7×10^{-7} Torr (equivalent to an As-flux BEP of 8-10×10^{-6} Torr when the gauge is facing the As cell), and a growth rate of 1 ML/s (roughly equivalent to 1 μm/h) that lead to a (2×4) surface reconstruction. The growth conditions of the InAs material are similar, except for the substrate temperature, which is generally below 520 °C to avoid re-evaporation of the In atoms due to the lower binding energy of InAs. The GaAs(001) surface is generally c(4×4) reconstructed in such conditions. Since the thickness of the InAs layer needs to be very small to get good SK-QDs (usually between 1.7 and 3.0 MLs), the deposition rate is often reduced to 0.1 ML/s to have a higher accuracy over the thickness. For SML-QDs, the quantity of InAs is even smaller (0.3-0.7 MLs), and the growth rate is often reduced further to achieve a better accuracy over the thickness. If the other growth conditions are kept the same as for SK-QDs, the surface reconstruction will be c(4×4), which, according to previous STM works, should not lead to the nucleation of 2D InAs islands on the GaAs(001) surface. Although several papers published so far clearly show that the nanostructures grown in such conditions do improve somehow the performance of devices compared to QWs or SK-QDs [30, 35]—we will discuss why later—one might expect (for the reasons already explained earlier) SML-QDs deposited in the presence of a (2×4) reconstruction to provide even better results [47, 48]. Recovering a (2×4) reconstruction from usual growth conditions adopted for SK-QDs requires a strong reduction of the As flux, as can be seen in Figure 3-16. In our case, the As background BEP value has to be lowered from 8×10^{-7} to below 1.5×10^{-7} Torr, which is equivalent to an As arrival rate of 0.3 ML/s. When the As flux is so low, the GaAs and InAs growth rates need to be drastically reduced too for the growth to remain under As-rich conditions (Ga or In-rich conditions lead to the presence of many structural defects).

Both surface reconstructions have a different atomic structure (Figures 3-17 and 3-18) and, when they are observed with the RHEED system, they have some similarities and differences which make them sometimes difficult to be identified, especially when one starts to change into the other one. This is because RHEED experiments are usually performed with the electron beam pointed along the [110] direction, as it is the one that provides the best oscillations of the specular spot needed to calibrate the growth rates and determine the composition of the ternary alloys. However, along that direction, both (2×4) and c(4×4) surface reconstructions have the same periodicity (2-fold symmetry), and the exact transition from one pattern to the other one is not straightforward, although the intensity of some diffractions spots is clearly different far from the transition, as can be seen in Figure 3-19-a and 3-19-b. Yet, along the [010] direction (located at 45° from the usual [110] direction), the (2×4) and c(4×4) reconstructions have a 1-fold and 4-fold symmetry, respectively, which makes the transition from one pattern to the other one much easier to detect (Figure 3-19-c and 3-19-d).

Therefore, it is more practical to reduce the As flux by monitoring the RHEED pattern along the [010] direction to observe when the 4-fold symmetry switches to a one-fold symmetry. At that precise moment, the system is back to the (2×4) surface reconstruction, which is supposed to be more adequate to get better SML-QDs.

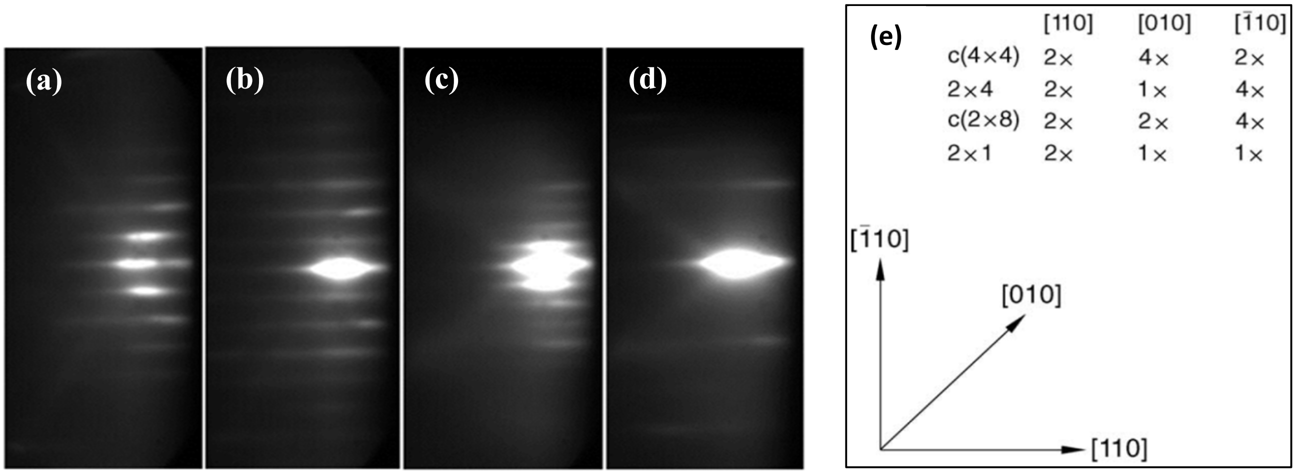

Figure 3-19: RHEED patterns of the GaAs surface before the growth of the SML-QDs at 500°C along (a) the [110] direction with a high As flux (c(4×4) reconstruction); (b) the [110] direction with a low As flux ((2×4) reconstruction); (c) the [010] direction with a high As flux (c(4×4) reconstruction); (d) the [010] direction with a low As flux ((2×4) reconstruction) [115]. After the growth of the SML-QDs, the patterns were very similar to the initial ones. (e) Periodicity of some surface reconstructions along several directions [110]. RHEED measurements are usually performed along [110] to calibrate the materials.

As mentioned before, the growth must always occur in As-rich conditions and, consequently, the growth rates of the GaAs and InAs materials should always be lower than the deposition rate of As. Usually, the ratio between the As to Ga or As to In growth rate should be at least 1.3 to provide good crystalline quality. The large reduction of the As flux, the careful recovery of the (2×4) surface reconstruction at low temperature, and the much lower growth rates make the growth of SML-QDs with a (2×4) reconstruction much more difficult and longer than with the c(4×4) reconstruction. Therefore, such special growth conditions would only be worth it if they lead to a real improvement of the SML-QDs, manifesting itself in better devices. This has become the main objective of this thesis throughout the past few years, and the fruits of this effort will be presented in the following chapters.

Chapter 4: In(Ga)As SML-QDs optical and structural characterization techniques

In this chapter, I describe the experimental techniques employed for analyzing the optical and structural characterization of In(Ga)As SK-QDs and determining their usefulness for characterizing In(Ga)As SML-QDs; these techniques include photoluminescence, atomic force microscopy, transmission electron microscopy, and scanning tunneling microscopy.

4-1 Optical characterization

4-1-1 Photoluminescence

In a photoluminescence (PL) experiment, light is spontaneously emitted from materials after they are optically excited. It provides valuable information about the material's bandgap, the presence of discrete energy levels, sample composition, quantum-well thickness and roughness, or quantum-dot size homogeneity. In this kind of experiment—our setup is simple and only allows us to perform a quick optical characterization of the structures—the sample is fixed inside a cryostat having a cold finger kept at liquid-nitrogen temperature (77 K) and irradiated with a laser that will excite the electrons from the valence band to the conduction band of the semiconductor, as illustrated in Figure 4-1. These hot electrons will thermalize and decay to the fundamental state of the bulk material (or nanostructures), where they will finally recombine with holes left behind in the valence band (that also moved to the top of the valence band), thus emitting photons having an energy equal to the difference of energy between both levels. These photons are collected by a lens and focused by a second lens into the entrance slit of a monochromator. A germanium (Ge) or silicon (Si) detector is located at the exit slit of the monochromator and detects the wavelengths that are present in the luminescence signal produced by the sample. A computer controls the wavelength selected by the monochromator and reads the signal of the detector via a lock-in coupled to a chopper (Figure 4-2).

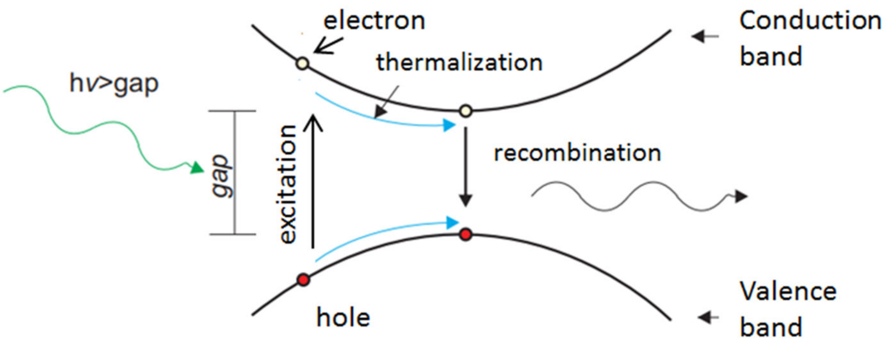

Figure 4-1: Main physical processes involved in a photoluminescence experiment [116].

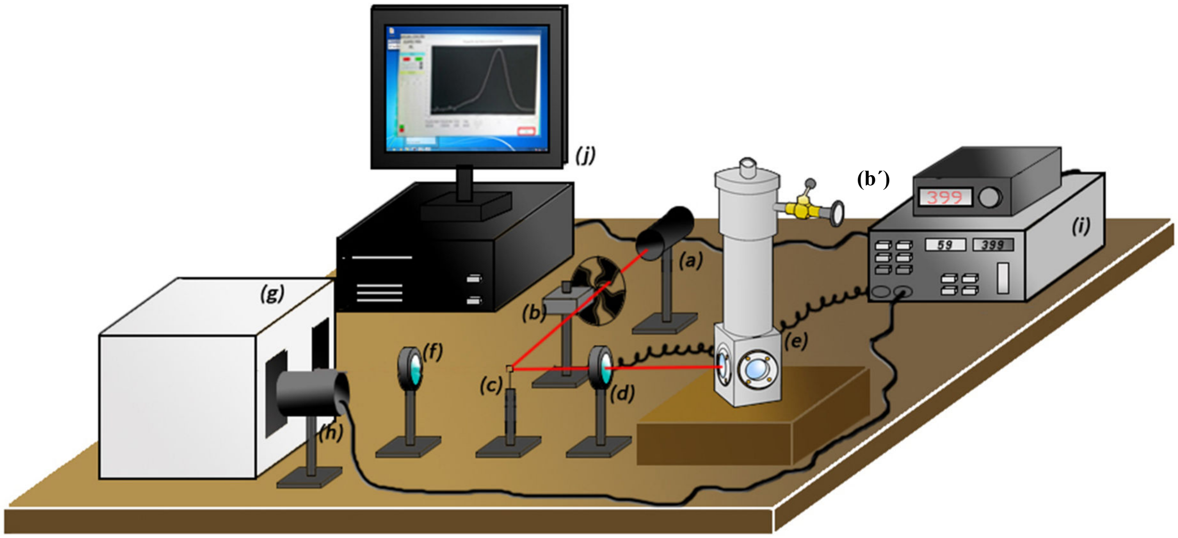

Figure 4-2: Schematics of a PL experiment. (a) solid-state laser; (b) chopper and (b´) its controller; (c) small mirror; (d) first focusing lens; (e) cryostat with samples; (f) second focusing lens; (g) monochromator; (h) Ge/Si detector at the exit slit; (i) lock-in amplifier; (j) computer.

Usually, one expects the PL spectrum to provide information about the growth quality, the presence of defects in the epitaxial layers, the width of compositional interfaces, the size of the nanostructures, and their energy levels. The large intensity of the signal is a clue that the crystalline quality is good and that there are only a few defects or impurities in the epitaxial layers, while the energy of the emission peak is generally related to the transition between the ground states of electrons and holes in the nanostructures that mainly depend on the size and composition of the nanostructure. The full width at half maximum (FWHM) is a parameter deduced from the PL spectrum to describe the width of the emission peaks (Figure 4-3). It is usually given in units of energy (meV) and is mainly a function of the size distribution of the nanostructures in the sample, but it may also be due to alloy fluctuations at the interfaces or inside the nanostructures themselves.

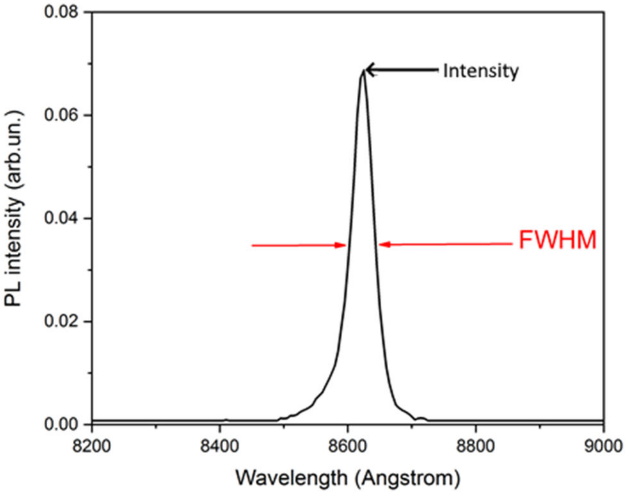

Figure 4-3: Typical PL spectrum at 77 K of a sample containing SML-QDs. The FWHM is obtained by calculating the difference in energy on both sides of the emission peak, where the intensity is half of the maximum intensity.

The optical characterization of SML-QDs could be performed using this photoluminescence setup (Figure 4-2), and the results were compared to those of SK-QDs and QWs. Figure 4-4 shows three samples containing different types of In(Ga)As nanostructures that were grown by MBE on epi-ready GaAs(001) substrates. After oxide removal and outgassing at 615°C for 5 min, a 200 nm-thick GaAs buffer was deposited at 570 °C. Then, the temperature of the sample was lowered to 515°C to deposit the In(Ga)As/GaAs nanostructures of the samples (#A, #B, and #C), which were followed by 15 nm of GaAs grown at the same temperature to prevent evaporation of the In atoms. Finally, 85 nm of GaAs were deposited at 570 °C.

Sample #A contained conventional SK-QDs obtained by depositing 2.2 MLs of InAs at 515 °C, sample #B consisted of six consecutive repetitions of 0.5 ML of InAs followed by 2.5 MLs of GaAs deposited under the same growth conditions as sample #A (i.e., in the presence of a c(4×4) surface reconstruction), and sample #C was a 5.1 nm wide $In_{0.17}Ga_{0.83}As$/GaAs quantum well (QW) having the same thickness (6 × (0.5 ML + 2.5 MLs) = 18 MLs ≈ 5.1 nm) and average composition as the SML-QDs of sample #B (0.5/3.0 = 16.7% of InAs).

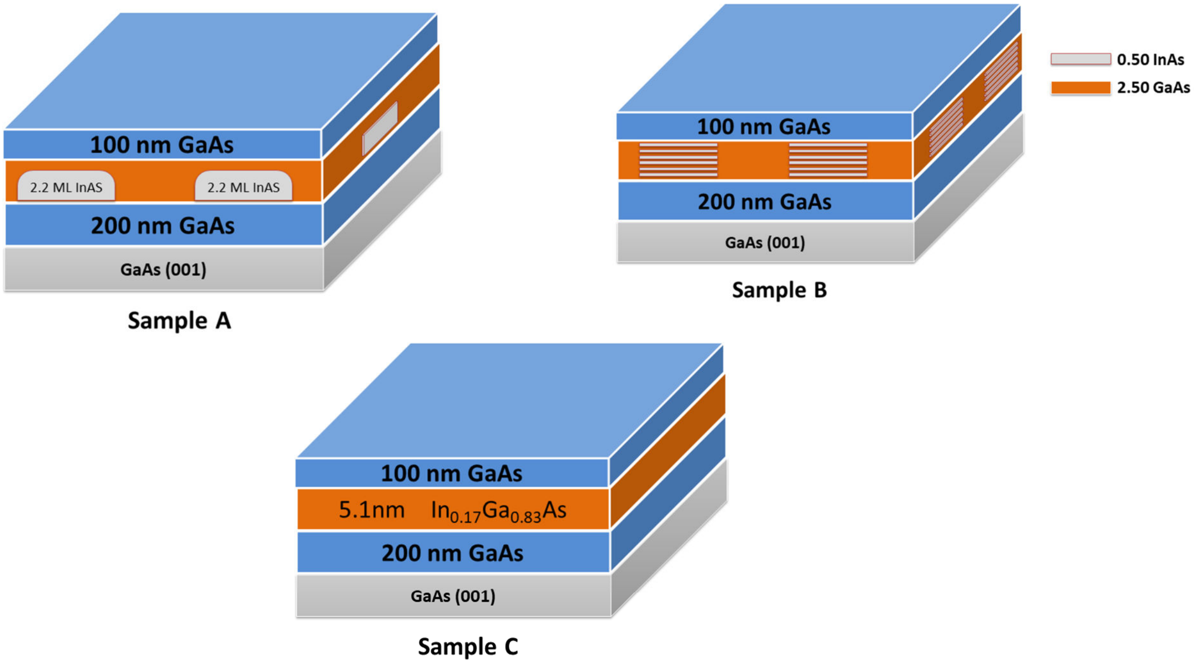

Figure 4-4: Structure of samples containing different types of In(Ga)As nanostructures to be analyzed by PL; sample #A contains 2.2 MLs of InAs to form conventional SK-QDs; sample #B contains a basic cycle of 0.5/2.5 MLs of InAs/GaAs repeated six times to form SML-QDs; sample #C contains a 5.1 nm wide $In_{0.17}Ga_{0.83}As$/GaAs quantum well.

After growth, each sample was cleaved into a small piece (1.0 × 0.5 cm^2), fixed inside the cryostat (Figure 4-5), and measured at liquid-nitrogen temperature (77 K). The PL measurements were performed with the setup shown in Figure 4-2 using a 50 cm monochromator equipped with a 1200 l/mm diffraction grating and a diode laser emitting at 660 nm with a power of 100 mW.

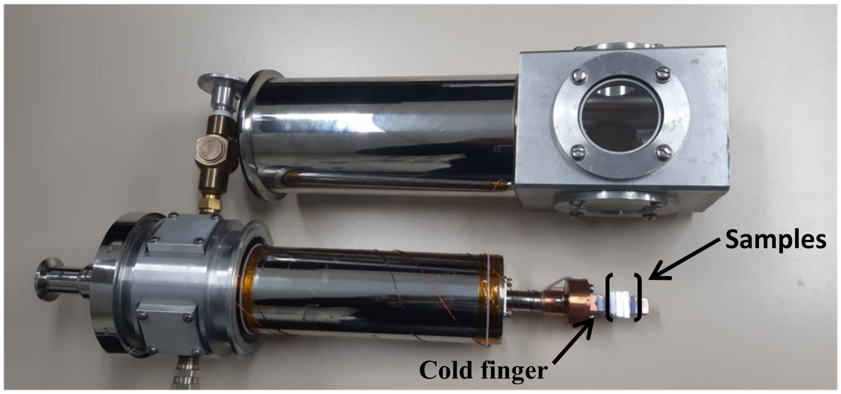

Figure 4-5: Samples fixed on the cold finger of a liquid-nitrogen optical cryostat.

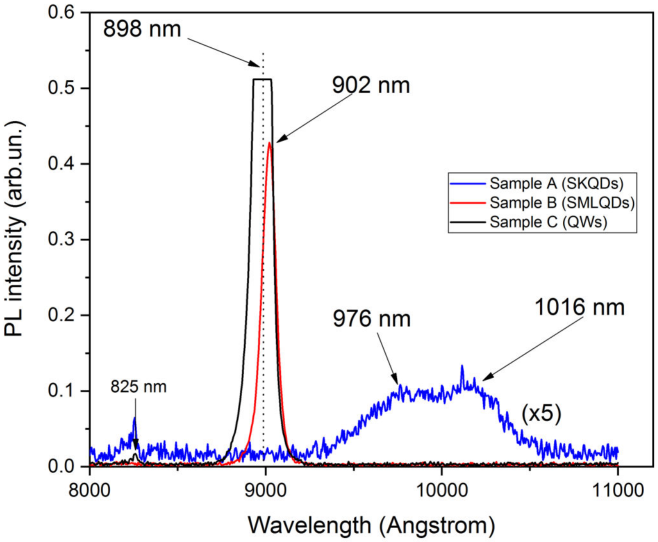

Figure 4-6: PL spectra of samples #A, #B, and #C; the measurements were performed at 77 K with a slit of 0.4mm. The emission of sample #C saturated the detector, and its maximum was estimated to be at the center of the peak.

Figure 4-6 shows the PL spectrum of samples #A, #B, and #C at low temperatures (77K). Each spectrum shows clear PL emission peaks corresponding to the band-to-band transition of the bulk GaAs material (825 nm) and the transitions from the In(Ga)As nanostructures at higher wavelengths, depending on their structure (QDs or QW). The SK-QDs (sample #A) have a weak and broad spectrum (FWHM=37.2 meV) with two emission bands, while the SML-QDs (sample #B) have a single sharp and intense peak. The SK-QDs spectrum is weaker and has a peak at a higher wavelength ($\lambda = 976\,nm$, $\lambda = 1016\,nm$) compared to the SML-QDs sample. These characteristics are common to SK-QDs;

the lower intensity is related to the presence of a higher density of structural defects at the SK-QDs interface, resulting from the fact that these 4-7 nm high structures need to be covered later by GaAs. The capping process leads to point defects at the interface between InAs and GaAs [117, 118] due to the 7.2% lattice mismatch between the two materials.

PL spectrum of sample #B (Figure 4-6) shows a much narrower emission (FWHM=9.7 meV) than that of sample #A, with peaks at a lower wavelength ($\lambda = 902\, nm$) than those of as-grown SK-QDs. The lower wavelength is generally attributed to the smaller size of the 2D islands in SML-QDs compared to SK-QDs but is also attributable to their lower In content due to their nominal InAs/GaAs periodic structure. The narrower emission is often (but erroneously) associated with higher size homogeneity of SML-QDs. However, Harrison *et al.* [119] have shown instead that this characteristic is due to the very small size of the nanostructures that provide effective confinement of holes but only very weak confinement of electrons. Due to the overlap of the electron wave functions with the closest SML-QDs, a narrow PL emission is produced due to an average of the local composition fluctuations (PL actually senses the InGaAs QW surrounding the SML-QDs, as will be shown later).

Sample #C exhibits optical properties similar to those of sample #B (SML-QDs), with a narrow emission (FWHM=7.2 meV) peaking at a low wavelength ($\lambda = 898\, nm$), but with an even higher intensity (saturated) than sample #B (Figure 4-6). Several studies have reported that SML-QDs exhibit optical properties similar to those of InGaAs quantum wells, suggesting they may actually not be formed or are optically inactive [120]. The tiny differences between the spectra of samples #B and #C would thus originate from small fluctuations in the growth parameters or measurement conditions. However, this hypothesis can be easily ruled out when such SML-QDs are inserted in the active region of an infrared photodetector, as we will show later (Chapter 7). Sample #B must indeed contain zero-dimensional nanostructures that differentiate them from the QW of sample #C—as will be confirmed in the structural characterization—to explain the very strong signal measured in photodetectors.

4-2 Structural characterization

4-2-1 Atomic force microscopy

The atomic force microscope (AFM) is the most famous member of the scanning probe microscope (SPM) family [121]. SPM is a branch of microscopy that uses a nanoscale probe to produce images by scanning it over a surface. It can provide high-resolution images of both conductive and insulating samples at the nanometer scale; usually, the images consist of a local topography of the surface, but they can also provide thermal, electrical, hardness, compositional, and magnetic maps. A typical AFM system consists of [122] a cantilever with a sharp tip mounted to a piezoelectric actuator and a position-sensitive photodetector for receiving a laser beam reflected by the end-point of the cantilever to provide deflection feedback, as shown in Figure 4-7.

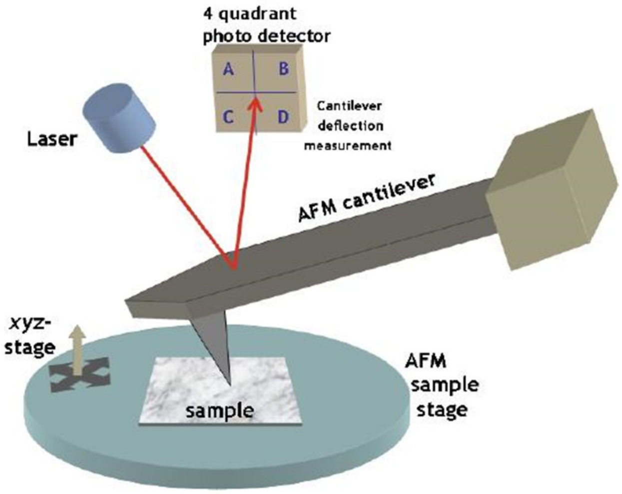

Figure 4-7: Schematic diagram of a typical AFM. During scanning of the surface by the tip, a laser beam is reflected from the back of a micro-fabricated cantilever to which the sharp tip is attached to measure its deflection [123].

In AFM, the tip is scanned over the surface of the sample; the sample surface and the tip are caused to bend the cantilever by atomic forces, and the laser beam reflected from the back of the cantilever is detected by a four-quadrant photodiode. In most operating modes, a feedback circuit connected to the cantilever deflection sensor keeps the interaction between the tip and the sample at a fixed value and controls the tip-sample distance by acting on the vertical component of a piezoelectric system that can move the tip along the three directions of space. A computer records the feedback signal to reconstruct a 3D image of the surface topography [124].

Figure 4-8 shows the three most common modes of an AFM: contact, intermittent (tapping), and non-contact mode, which are usually chosen depending on the intensity of the forces between the sample and probe [125, 126]. The contact mode provides the highest resolution but also results in a strong interaction between the tip and the sample that can eventually destroy both, considerably reducing the tip's lifetime. It is used for hard materials when the highest resolution is required. For softer materials or when a longer tip lifetime is desired, the intermittent mode is better and is most often used. In this mode, the tip oscillates over the sample and gently touches it at its bottom position, considerably reducing the tip-sample forces. For extreme cases of very soft materials or materials weakly adsorbed on a substrate, the non-contact mode is recommended but has the lowest resolution as the tip has to sense and monitor the attraction-repulsion atomic forces of the sample from a distance.

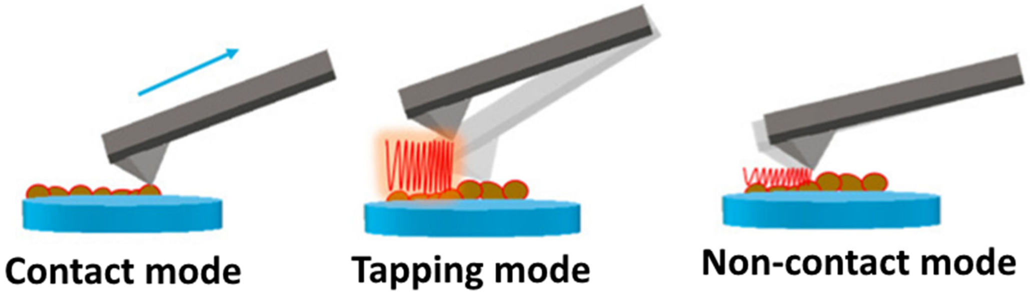

Figure 4-8: The three most common modes of AFM operation: contact mode, tapping mode, and non-contact mode [127].

The characteristics of the AFM technique make it extremely useful for the investigation of insulators and semiconductors (which are often covered by an oxide layer in air and, therefore, behave like insulators). In addition to measuring the atomic forces on solid surfaces, it can also measure in liquids. Nowadays, AFM is widely used in biology, e.g., for imaging DNA molecules [128], and in chemistry to image and manipulate atoms. Unlike a scanning tunneling microscope (STM), it doesn't require a metallic tip and sample to measure the tunneling current between both. The AFM technique is widely used for the *ex-situ* characterization of SK-QDs since an analysis of QDs density and size can still be easily performed even after the sample is oxidized in the air [129].

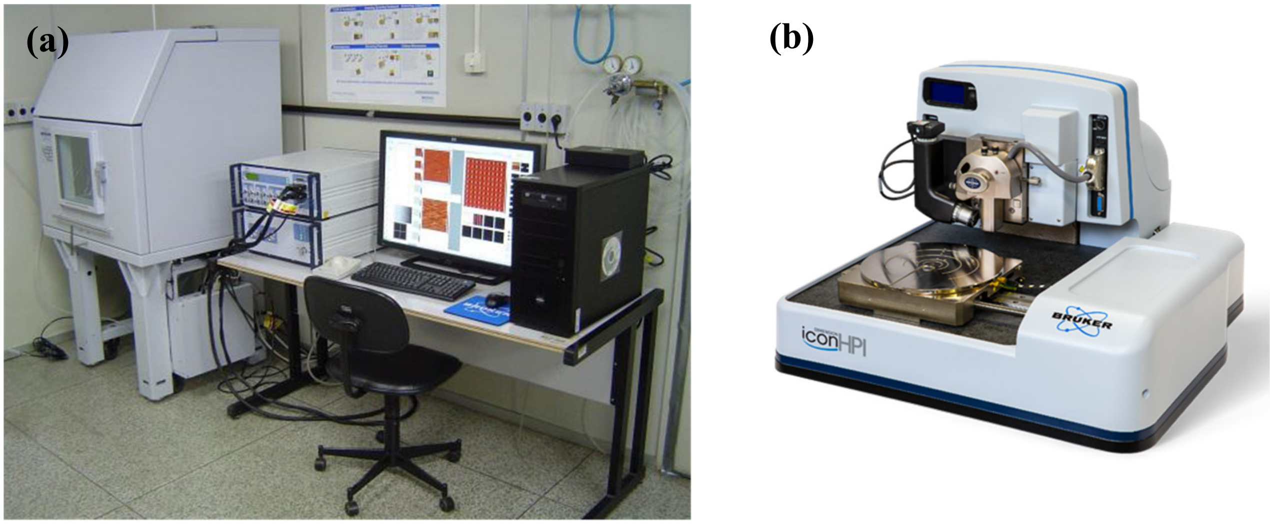

Figure 4-9: (a) Full AFM system at LNMS equipped with an anti-vibration table, a sound-insulation box (also for controlled ambient), control units, and a computer to acquire and process images; (b) The AFM itself—that is normally installed inside the white sound-insulation box of figure a—with its scanning head (top), camera (left) and 6” sample holder (bottom).

To examine the morphology of the QDs samples, the tapping mode was used (Figure 4-8), as it combines high resolution with low sample-tip interaction required to minimize tip deterioration. As an attempt to analyze and compare the morphology of InAs SK-QDs and SML-QDs (or at least the small 2D InAs islands that are nucleated and will be staked later), we analyzed the morphology of three samples #A1, #B1, and #C1. Their structures are shown in Figure 4-10. Sample #A1 contains 2.2 MLs of InAs material that went through the 2D-3D transition (SK mode) around 1.7 MLs, and was grown with the same growth conditions of sample #A. Sample #B1 contains only 0.5 ML of InAs deposited on the buffer layer using the same growth conditions as those of sample #B. Finally, sample #C1 was just a 200 nm-thick GaAs buffer deposited at 570 °C to compare it with sample #B1. All the samples were grown on an epi-ready GaAs(001) substrate;

after oxide removal and outgassing at 615 °C for 5 min, a 200 nm-thick GaAs buffer was deposited at 570 °C, and the temperature was lowered to 515 °C or 490 °C to grow 2.2 MLs or 0.5 ML of InAs in samples #A1 and #B1, respectively.

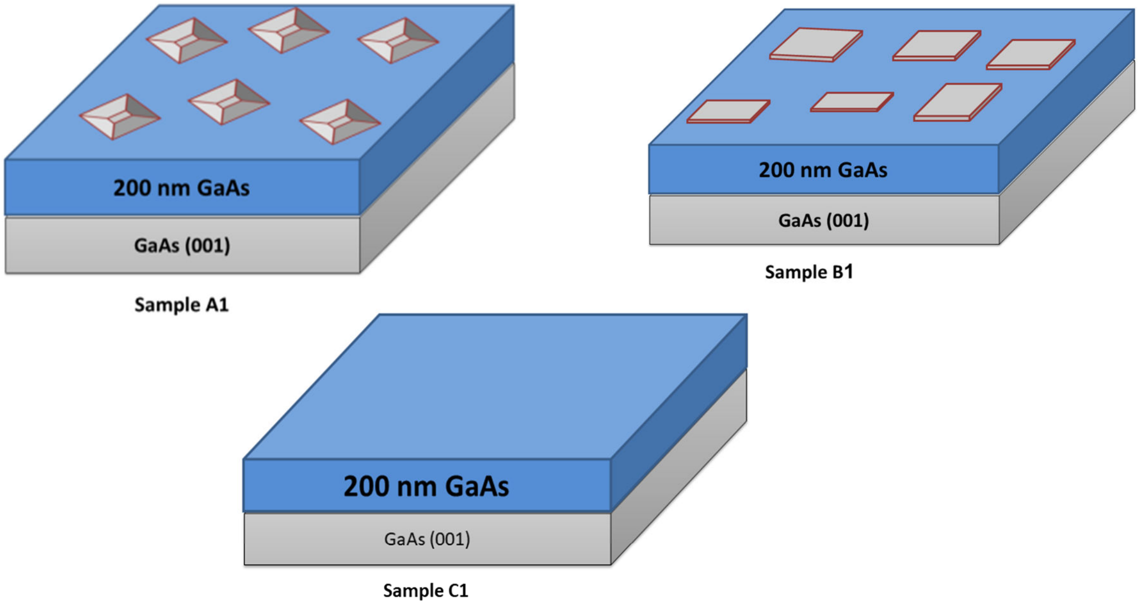

Figure 4-10: Structure of different types of samples, two of them containing InGaAs nanostructures, to be checked by AFM. Sample #A1: 2.2 MLs of InAs SK-QDs (similar to sample #A but without GaAs cap layer); Sample #B1: 0.5 ML of InAs (half of the first cycle of sample #B used to form SML-QDs); Sample #C1: 200 nm-thick GaAs buffer to be used as a reference. The structures of samples #A1 and #B1 were also grown on top of a 200 nm-thick GaAs buffer.

We can see from Figure 4-11 that AFM is useful for analyzing the morphology of SK-QDs, as it provides information about the size and density of the QDs, while nothing can be said in the case of the InAs submonolayer (sample #B1). There are no visual differences between the AFM images of the GaAs buffer (sample #C1) and the fractional deposition of InAs (sample #B1), suggesting that the technique cannot distinguish the high density of very small 2D InAs islands (which may not form on a c(4×4) reconstructed surface and thus would lead to random incorporation of the In atoms) from the lower density of large 2D GaAs islands nucleated during the growth of the buffer layer.

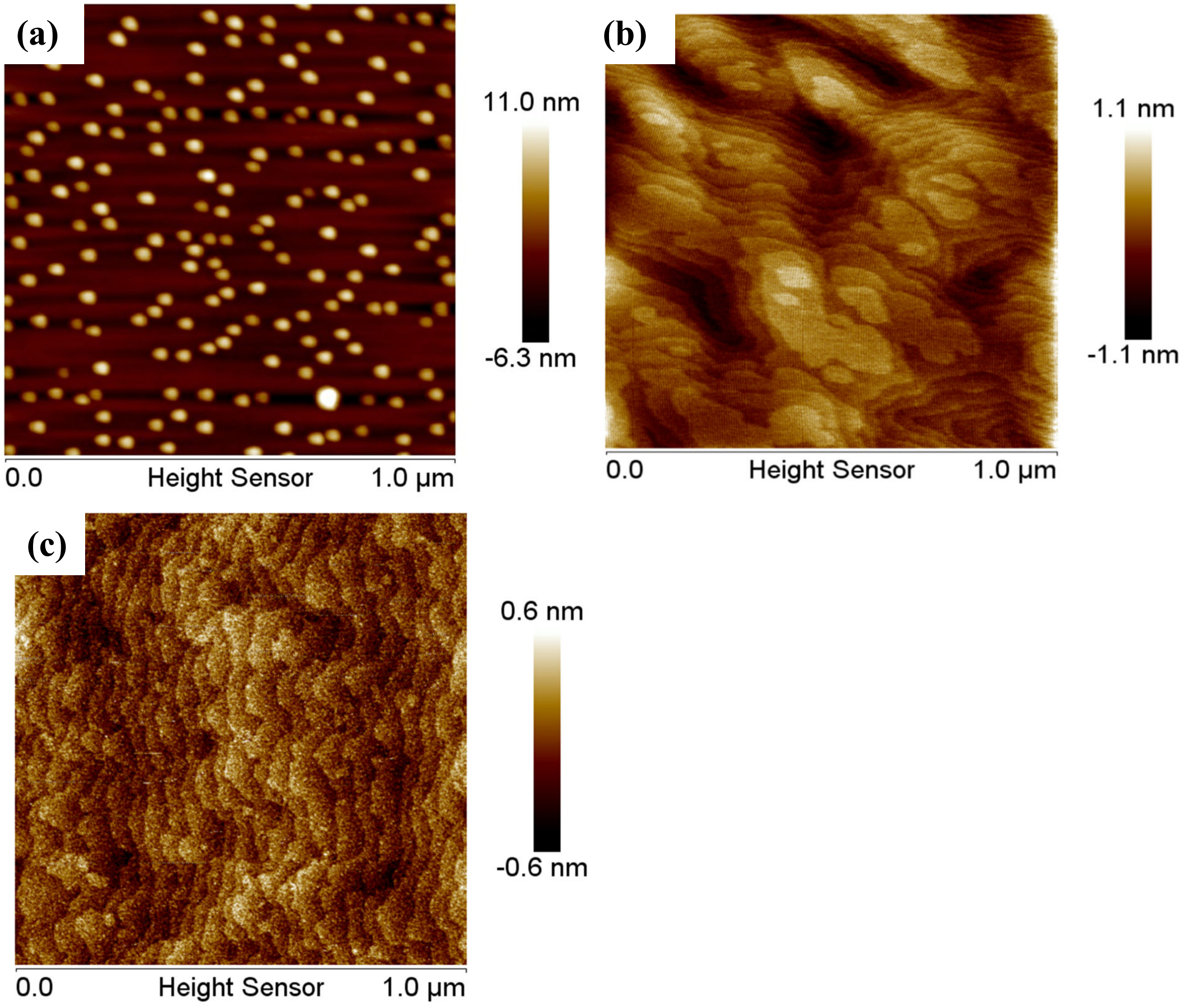

Figure 4-11: 1×1 μm^2 AFM images showing the surface of (a) 2.2 MLs of InAs SK-QDs deposited on the buffer layer; (b) 0.5 ML of InAs material (first layer of the basic cycle of a SML-QD) deposited on the buffer layer, and (c) a 200 nm-thick GaAs buffer deposited at 570 °C.

4-2-2 Transmission electron microscopy

The principle of transmission electron microscopy (TEM), as suggested by its name, is to use a beam of electrons and make it pass through a very thin slab of material to analyze it on the other side. Thus, TEM provides valuable information about a sample's inner structure, such as its crystal structure, morphology, composition, and stress state. The image is formed by the interaction (scattering) of electrons and atoms. In general, TEM can provide an image resolution better than 0.2 nm and is very capable of resolving nanoparticles at the atomic scale [130]. However, it is a very expensive technique, and sample preparation is long (can take several days) and also requires other expensive preparation tools. TEM can be used in two modes [131], namely dark field and bright field. The sample is usually placed within the objective lens, and the position of the sample relative to the objective aperture determines the available imaging modes. The electron beam passes through the sample before reaching the objective aperture, so that electrons scattered from the sample can be selected for imaging (Figure 4-12-b). Bright-field images (BF) are obtained when the objective aperture is positioned to include the unscattered light from the thin sample, while dark-field images (DF) are obtained when the objective aperture excludes the unscattered light from the incident beam [132].

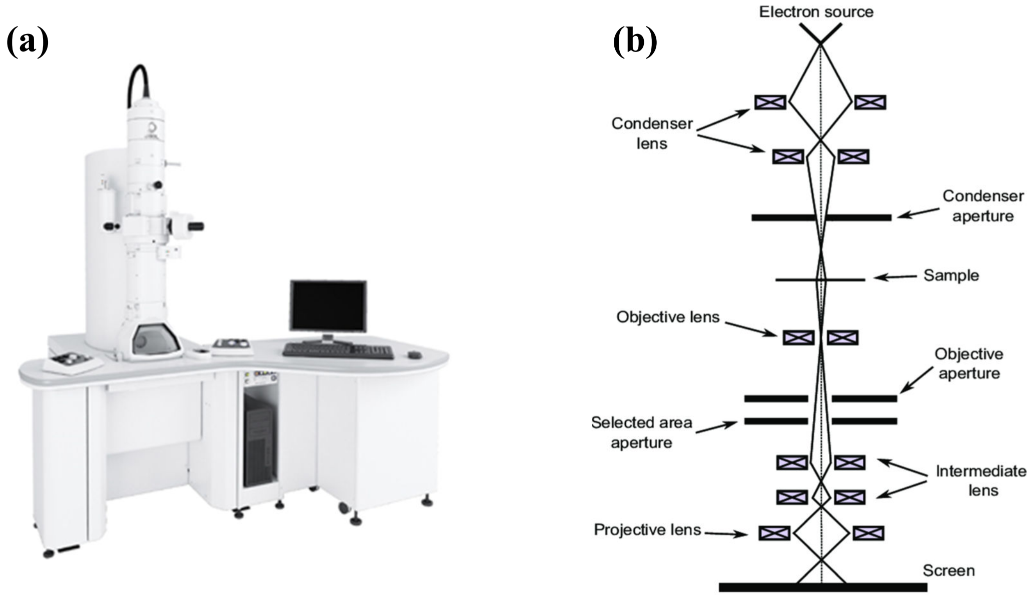

Figure 4-12: (a) JEM-2100F TEM of the Brazilian Nanotechnology National Laboratory (LNNano) that was used in this study [133], (b) TEM schematic diagram [132].

As an attempt to investigate the morphology of the SML-QDs, one of our samples (#D) containing SML-QDs deposited in the presence of a (2×4) reconstruction of the GaAs(001) surface was imaged using the JEOL JEM 2100F TEM of the Brazilian Nanotechnology National Laboratory (LNNano/CNPEM), located in Campinas (Figure 4-12-a). The JEM-2100F is a multipurpose, 200 kV field-emission (FE) analytical electron microscope. FE electron guns produce highly stable and bright electron probes that conventional thermionic electron guns cannot produce; this feature is essential for ultrahigh resolution in TEM and for nanoscale analysis of the sample. A computer controls the microscope by integrating analytical instruments or cameras, such as energy-dispersive X-ray spectrometers, electron energy loss spectrometers, or even CCD cameras. Unfortunately, neither the 2D InAs islands nor the SML-QDs themselves could be clearly observed in the measurements (Figures 4-13 and 4-14), probably due to the strong segregation of the In atoms leading to significant intermixing with the spacer layers—Cantalice *et al.* [134] found a segregation coefficient R = 0.81 for InAs/GaAs SML-QDs grown under the same conditions. Despite this strong segregation, Niermann *et al.* [135] were able to get good TEM images of InAs/GaAs SML-QDs. Although their samples were obtained using a different epitaxial technique (MOCVD), the quality of their images suggests that the sample preparation is very important. TEM samples must be extremely thin (generally less than 150 nm and, whenever possible, less than 30 nm) when high-resolution imaging is needed as a result of the requirement for transmitted electrons. Also, our inability to obtain a clear image of our SML-QDs could be due to partial amorphization of the surface during the FIB (focus ion beam) preparation of the samples. Although we were unable to identify the SML-QDs in the matrix, even so we performed a compositional study of the same layers to eventually detect clusters of a specific element that could be related to the nanostructures. However, as can be seen in Figure 4-13, we were unsuccessful as well. Consequently, this technique was not useful for extracting valuable structural information from our samples containing InAs/GaAs SML-QDs.

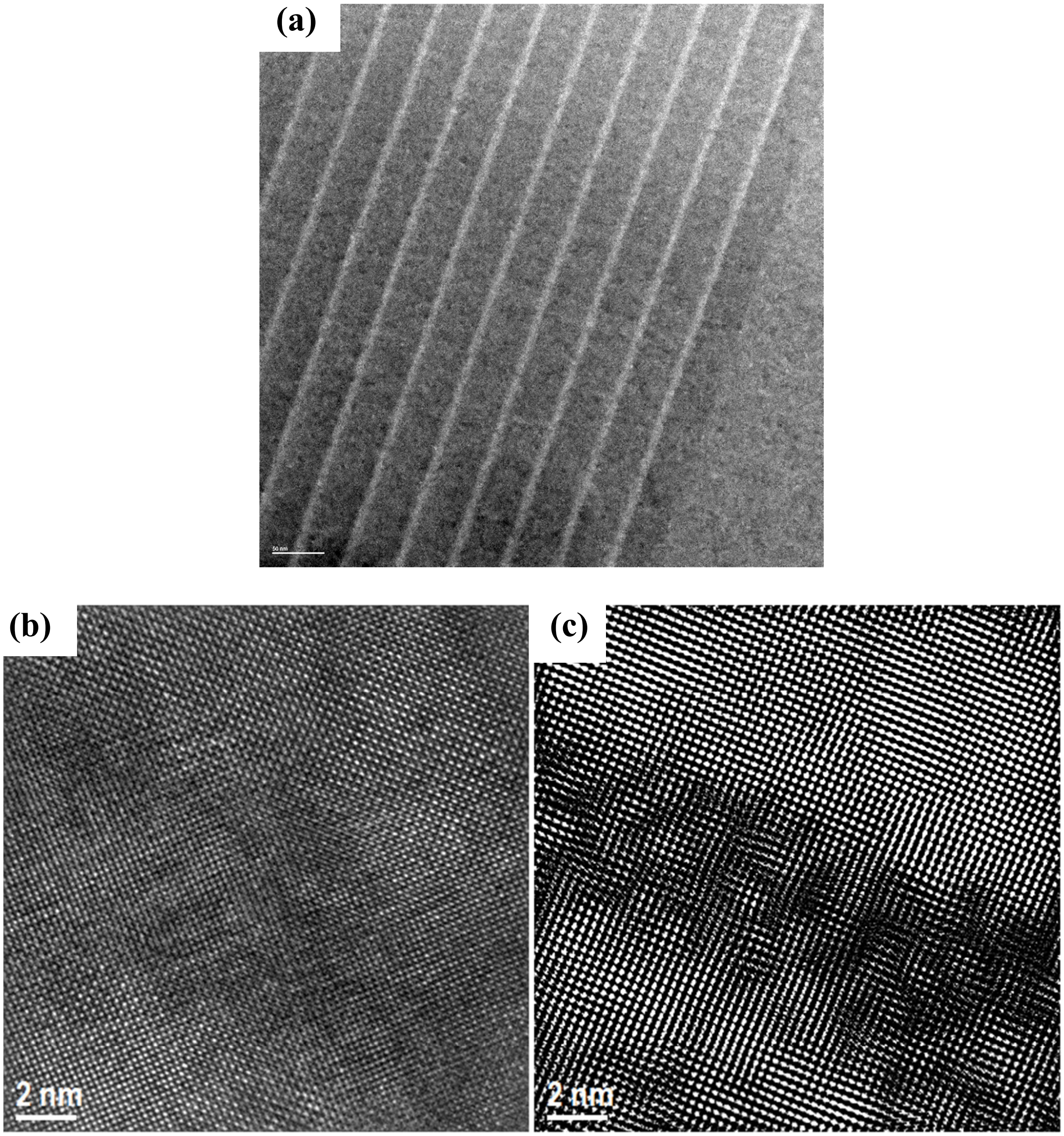

Figure 4-13: (a) TEM image of sample #D, which consists of ten AlGaAs/GaAs quantum wells containing each a single layer of InAs/GaAs SML-QDs in the well, consisting of 6 repetitions of 0.35 ML of InAs followed by 2.65 MLs of GaAs. The AlGaAs barriers appear as wide dark stripes with, between them, narrow brighter regions related to the wells containing the SML-QDs. (b) High-resolution image of the inner part of one QW containing SML-QDs. The InAs material appears as darker regions. (c) Filtered and processed image of Figure b. Many 1-3 nm-large dark regions appear but seem more related to image-processing effects than to the presence of SML-QDs.

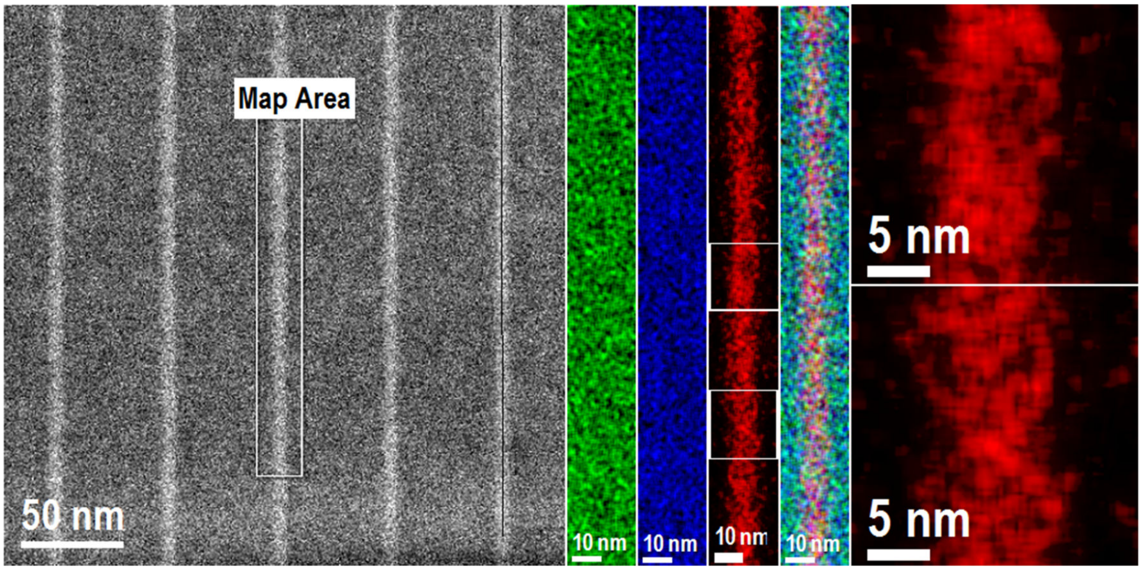

Figure 4-14: (Left) TEM image of 5 layers of SML-QDs separated by 50 nm of AlGaAs. (Right) Colored compositional maps of the rectangular region are shown on the left. Ga, As, and In atoms are shown in green, blue, and red, respectively. The red map shows that most of the In atoms are concentrated in a 5-10 nm wide region of the map (due to segregation), and no clear clustering or periodic structure is observed, as would be expected in well-formed SML-QDs. The two larger red images on the right are simply a magnification of the two small regions shown on the main In map. Again, very small 1-3 nm wide clusters may be observed but are more likely due to lack of resolution (noise average during processing).

4-2-3 Cross-sectional scanning tunneling microscopy

Scanning tunneling microscopy (STM) was used for the first time by Binnig *et al.* in 1981 [136]. Since then, STM has become the most important tool for analyzing the surface structural properties of conducting samples at the atomic scale. The principle of the experiment is based on a sharp conducting tip that is brought into a distance of only a few Angstrom from the surface that must also be conductive, as shown in Figure 4-15-a. A voltage difference (bias) is applied between the tip and the sample that, when close enough, allows electrons to tunnel through the very narrow gap (around 1 nm) between both, creating a very tiny current (typically in the pA to nA range) resulting from the quantum mechanical tunneling effect. As for AFM, a x-y-z piezoelectric system allows the tip to scan the surface, and at each point of the grid the tunneling current is evaluated and kept constant by a feedback system acting on the z component of the piezoelectric motion system. Finally, the measured signals feedback electronics are transferred to a computer to create a topographic image of the sample's surface.

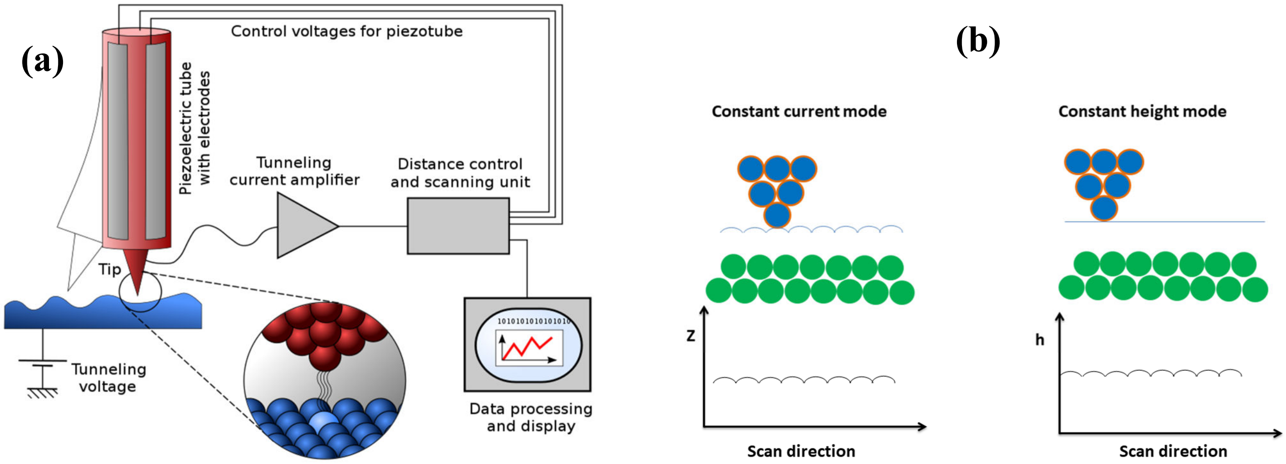

Figure 4-15: (a) Scheme of the working mechanism of a STM, showing the tip, sample, piezoelectric scanner for x-y-z tip motion, feedback system, and the computer control system; (b) Two main operation modes of a STM: constant-current and constant-height scanning modes [137].

Usually, STM is operated in two modes [138]: constant-current and constant-height modes, as shown in Figure 4-15-b. In constant-current mode, the tunneling current is kept constant while the tip is scanning the surface by adjusting the distance between the tip and the sample with the feedback system. The tip height signal at each scanning point results in a map of the surface topography. It is the most widely used mode because it allows analysis of smooth and rough surfaces, but it is slower as the scanning speed is limited by the response time of the feedback system. In contrast, in constant-height mode, the tip height is always kept constant during scanning, which means that the tunneling current changes according to the topography of the surface. Thus, recording the current directly reflects the changes in topography. Since there is no electronic feedback involved, the scanning can be much faster, but only very flat samples can be imaged to avoid current saturation (and tip crashing), as it depends exponentially on the tip-to-sample distance.

Unlike conventional STM, which measures the sample surface, cross-sectional scanning tunneling microscopy (X-STM) measures the sample's cross-sectional surface to provide some structural information about the inner part of the sample [139]. Analyzing the cross-section of a sample is useful because it allows direct observation of capped nanoscale structures at the atomic scale that would, otherwise, be impossible, as shown in Figure 4-16. However, sample preparation is more complex as the sample must be cleaved in-situ (under vacuum) to obtain a fresh and atomically flat surface. Moreover, the tip must be brought just above the sample cross section and the nanostructures that need to be investigated, which generally require an extra monitoring system (like a scanning electron microscope).

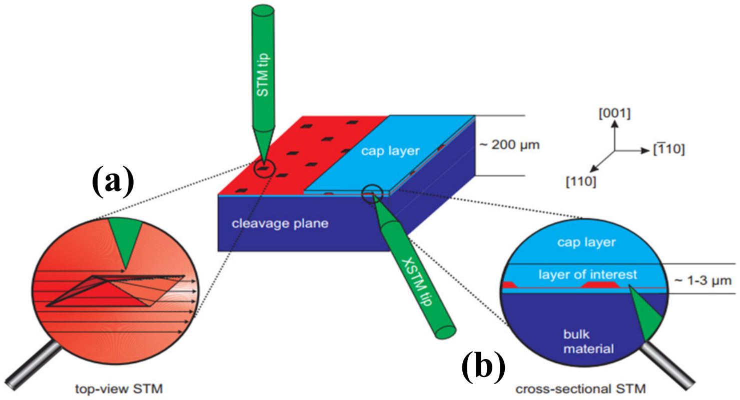

Figure 4-16: Illustration of the principle of (a) top-view scanning tunneling microscopy (usual STM technique) and (b) cross-sectional scanning tunneling microscopy [140]. To image semiconductors successfully at the atomic scale, both techniques must be operated in ultra-high vacuum.

Since conventional techniques such as AFM and TEM cannot be used to check the properties of SML-QDs samples, we tried to investigate the structure of our InAs/GaAs SML-QDs using X-STM and compare their formation with that of conventional SK-QDs. Therefore, two specific samples (#A2 and #B2) were grown on a Si-doped GaAs(001) substrate ($n=1\times10^{18}$ cm^{-3}), and all the layers were also doped (except the QDs themselves and 40 nm of GaAs above and below them) to allow the tiny tunneling current to flow through the sample and provide high-quality X-STM measurements. Figure 4-17 shows that sample #A2 consisted of 2.2 MLs of InAs SK-QDs, deposited at 515 °C, and covered by a 40-nm thick undoped GaAs layer (15 nm grown at 515 °C and the rest at 570 °C) followed by a

120-nm thick doped GaAs cap deposited at 570 °C. Sample #B2 was similar but contained SML-QDs obtained by repeating six times a basic cycle consisting of 0.50 ML /2.50 MLs of InAs/GaAs deposited at 490 °C with growth conditions similar to those of sample #A2, in the presence of a c(4×4) surface reconstruction. Then the samples were cleaved under ultra-high vacuum and measured by X-STM at 77K on a freshly obtained {110} surface.

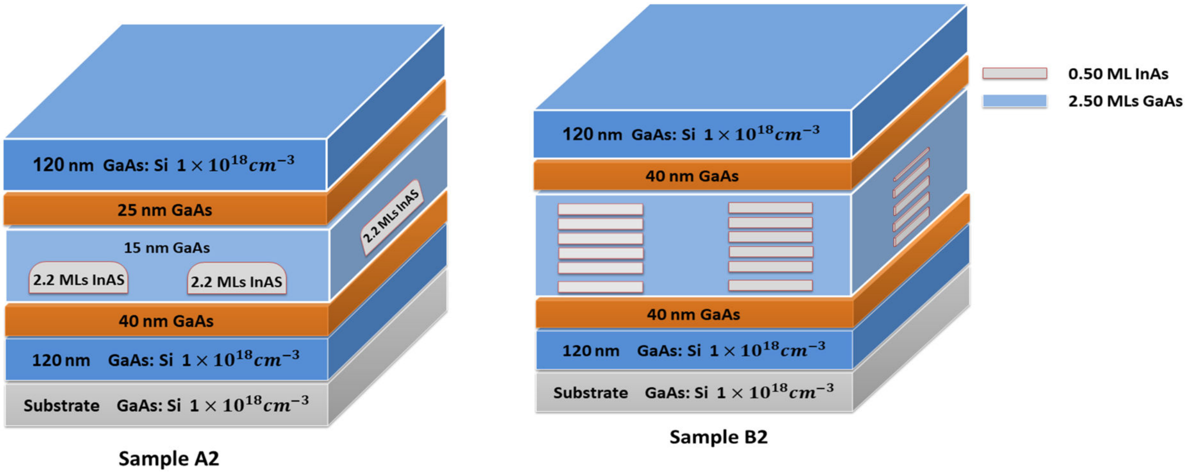

Figure 4-17: Schematic structure of the samples grown by MBE for X-STM experiments; sample #A2 contained 2.2 MLs of InAs SK-QDs; sample #B2 contained SML-QDs formed by repeating six times 0.5/2.5 MLs of InAs/GaAs. All the layers were doped to 10^{18} cm^{-3}, except the QDs and 40 nm of GaAs below and above them. Actually, both samples #A2 and #B2 contained other layers, but only the ones of interest (similar to samples #A and #B but grown on a Si-doped substrate) are shown here.

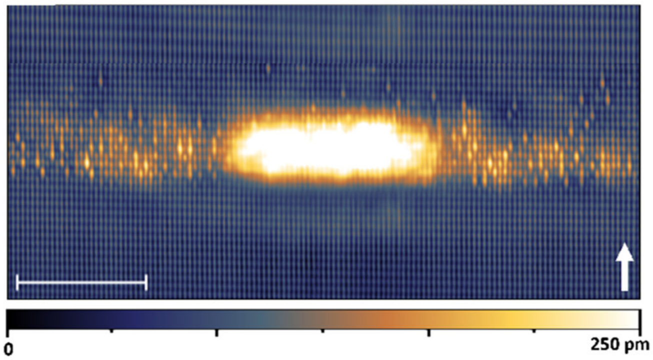

Figure 4-18: X-STM filled-state topographic image of sample #A2 containing 2.2 MLs of InAs. From dark to bright, the color contrast corresponds to a difference in the height of 0 to 250 pm out of the cleaved surface. Bright regions have more In atoms than dark ones. The scale bar has a length of 10 nm, and the white arrow indicates the growth direction [001].

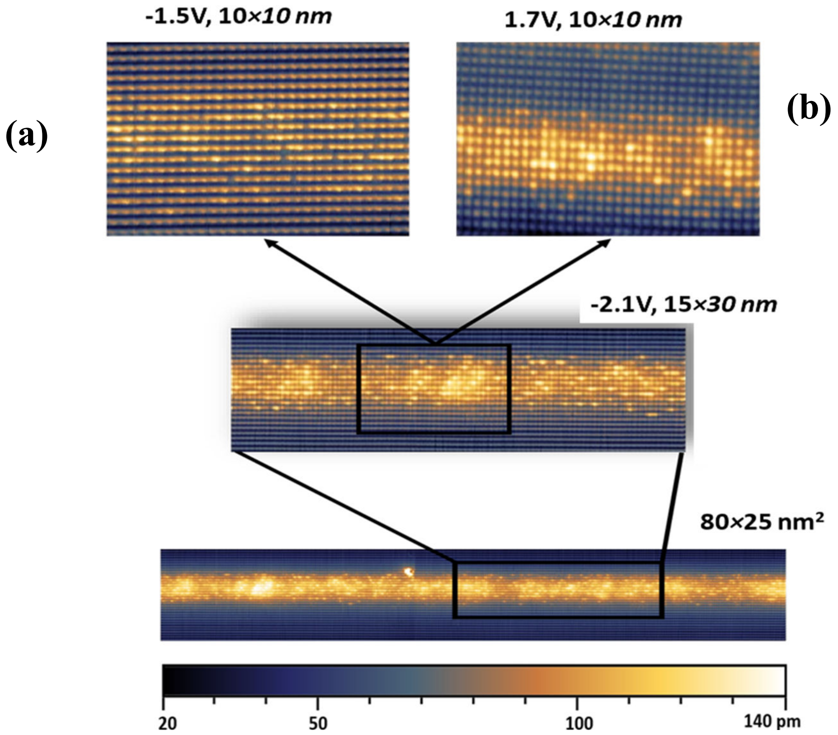

Figure 4-19: Filled-state images (80 × 25 nm^2) of the SML-QDs of sample #B2 taken at bias a voltage of –2.1 V and a tunneling current of It = 50 pA. The arrow indicates the growth direction [001]. (a) filled-state image allowing to observe As atoms; (b) empty-state image allowing to observe In and Ga atoms.

Figure 4-18 shows a high-resolution X-STM image of sample #A2, where we can see a single InAs SK-QD and the surrounding wetting layer. It has a base length of 18.0 ± 0.8 nm and a height of 4.0 ± 0.5 nm [141]. In segregation can be observed in the atomic layers around the QD, where the In content decreases from bottom to top. Figure 4-19 shows filled-state images of sample #B2, where the contrast represents the relative height of the atoms out of the cleaved surface, which is a function of the In concentration. Filled-state images are obtained at high negative bias voltages and allow to observe group-V atoms (As), while empty-state images are obtained at high positive bias voltages and allow to observe group-III atoms (Ga, In). The latter is used mainly when accurate counting of In-atoms is required (e.g., when evaluating the In-segregation coefficient R). According to these X-STM images, there is no evidence that SML-QDs consist of stacks of 2D InAs islands, as suggested in the schematics of Figure 4-17, indicating that the 2D islands were never formed or were dissolved at a later stage. Instead, one can observe small agglomerates of In-rich material—without any internal periodic structure—scattered in a thick InGaAs QW with lower In content, probably resulting from the strong In segregation. The density of these clusters can reach

$5–6 \times 10^{11}$ cm^{-2} in some samples (depending on the growth conditions), which is roughly ten times the usual SK-QDs density [142].

Based on the information provided, it appears that AFM is a useless technique for analyzing the morphology of InAs/GaAs SML-QDs. This is because these structures are 2D islands that do not exhibit surface profiles and are also very small and buried beneath the surface of the sample. Additionally, we also concluded that TEM is not suitable for extracting valuable structural information from samples containing InAs/GaAs SML-QDs. We could not obtain a clear image to identify the 2D structure of our InAs/GaAs SML-QDs in the matrix due to our limited ability to prepare a very thin sample using FIB, which is required for TEM measurements. As a result, X-STM is probably the most effective method in examining buried structures, as it can analyze their structure and composition at the atomic scale. It will therefore be used in the next chapter along with PL (which also proved to be useful to optically investigate SML-QDs) to optimize the growth conditions of InAs/GaAs SML-QDs for infrared photodetectors.

Chapter 5: Growth optimization of InAs/GaAs SML-QDs

In this chapter, the PL and X-STM techniques were employed to investigate and optimize the growth conditions of InAs/GaAs SML-QDs, such as the influence of the surface reconstruction, growth rate, InAs coverage, and the number of repetitions. The main idea was to change a single growth parameter at a time to always be able to compare its influence unambiguously.

5-1 SML-QDs samples growth

Figure 5-1 shows the typical structure of a SML-QDs sample that was grown for PL measurements. After removing the native oxide layer of the GaAs substrate at 580 °C in the growth chamber and degassing at 610 °C for 5 min, the temperature was lowered to 570 °C, and a 150 nm-thick GaAs buffer layer was deposited. Then, the substrate temperature was lowered to the required temperature (490 – 525 °C), the As flux was adjusted to the adequate value, and a sequence of a fraction of InAs monolayer followed by a few monolayers of GaAs was deposited a certain number of times. As a final step, 3 nm of GaAs were deposited at the same temperature to prevent evaporation of In from the surface before increasing the sample's temperature to 570 °C for the growth of the top 147 nm–thick GaAs cap. Since we had some contamination problems with Al-containing epitaxial layers, we couldn't use an AlGaAs confinement layer commonly used to enhance the PL intensity, and the SML-QDs were consequently covered with GaAs only.

After the growth, a small piece of each sample (1.0 × 0.5 cm^2) was cleaved and glued with carbon paint to get good thermal contact with the cold finger of the optical cryostat (see Figure 4-5). PL measurements were performed at 77 K with two main goals for optimizing the growth parameters. The first goal was to obtain the highest possible PL intensity, indicating the excellent structural and optical quality of the samples. The second goal was to achieve the lowest possible FWHM, generally related to a more uniform size distribution.

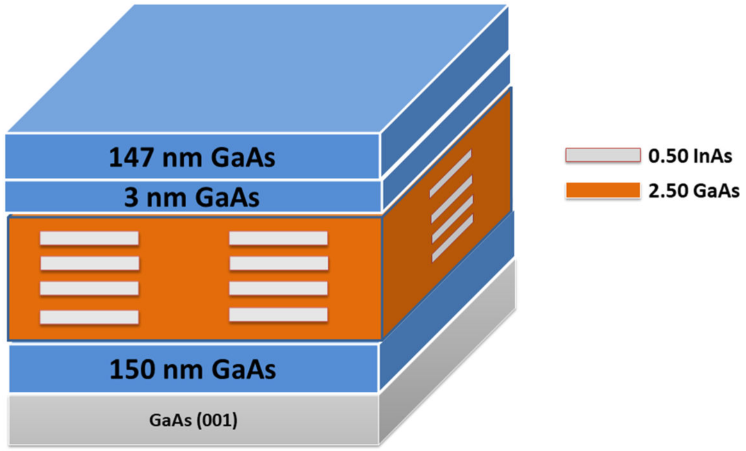

Figure 5-1: Typical structure of a SML-QDs sample to be analyzed by PL measurements. Here, the basic cycle of 0.5/2.5 MLs of InAs/GaAs was repeated 4 times.

5-2 Influence of the surface reconstruction

InAs QDs are often deposited at 480-515 °C to minimize desorption of In from the surface [143]. When the sample temperature is lowered from 570 °C—which is necessary to grow good-quality GaAs material—to 480-515 °C, the surface morphology undergoes a change around 520 °C, switching from a (2×4) reconstruction at high temperature to a c(4×4) reconstruction at low temperature. To recover the (2×4) reconstruction at the low temperature needed to allow nucleation of true 2D InAs island on the surface [47, 48], the As flux must be considerably decreased (roughly by a factor of 10) [110]. However, this large reduction in the As flux is also expected to limit In incorporation [142, 144]. So, to determine whether or not SML-QDs would be better with a (2×4) reconstruction, we investigated the influence of the surface reconstruction, which mainly depends on the As flux and the growth temperature (see Figure 3-16).

Five samples with the same structure as that of Figure 5-1 were grown at a fixed temperature (T=490 °C) but with a different BEP value of the As flux ranging from 6.0×10^{-8} to 6.5×10^{-7} Torr. Since, above an As BEP of 1.2×10^{-7} Torr (at T=490 °C), the surface reconstruction changes from (2×4) to c(4×4), we might expect the samples grown with a higher As pressure to be eventually different from the others. Indeed, as shown earlier in Figure 4-19, there should be random incorporation of the In atoms into the GaAs surface, leading to the formation of an InGaAs alloy instead of SML-QDs.

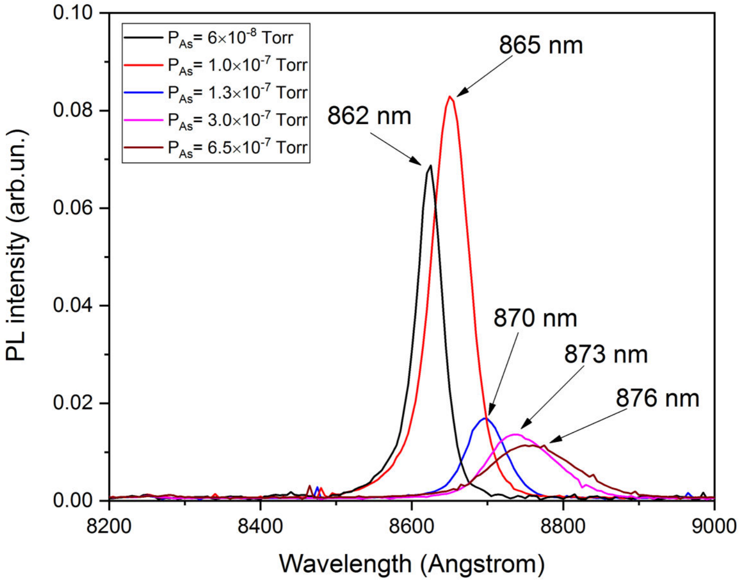

Figure 5-2: PL spectra of SML-QDs consisting of 0.5 ML of InAs and 2.5 MLs of GaAs repeated 4 times. Each sample had a different As flux (BEP) during SML-QDs formation.

Figure 5-2 shows the PL spectra of the samples where only the As flux was changed during deposition of the SML-QDs. The spectra of the two samples grown with a (2×4) reconstruction (As BEP lower than 1.2×10^{-7} Torr) have more or less the same intensity, which is also true for the samples grown with a c(4×4) reconstruction (As BEP larger than 1.2×10^{-7} Torr), although their intensity is much lower. This difference in intensity could be due to the formation of the SML-QDs at low As pressure, which could lead to stronger carrier confinement and, consequently, to stronger PL intensity. On the other hand, at higher As flux, the SML-QDs might not be formed due to the presence of the c(4×4) reconstruction, yielding the growth of an InGaAs QW, which causes weaker confinement of the carriers. When looking at the FWHM of the emission peaks, one can see that the ones of the samples grown with a (2×4) reconstruction are smaller than the others, and indeed it appears that their values increase with the As flux (6.7, 9.9, 10.3, 17.5, and 21.9 meV). The narrow value obtained for the SML-QDs is surprising, especially when compared to SK-QDs, which typically exhibit a very broad PL emission (as shown in Figure 4-6) related to their size distribution and to the fact that millions of nanostructures are sampled at the same time [100]. If we suppose that an InGaAs QW is formed instead of SML-QDs at higher As flux, then the increase of the FWHM could be due to the rougher interface related to the lower surface mobility of the adatoms with increasing As flux. Another striking feature is the systematic redshift of the emissions with increasing As flux. This observation is usually related to the size of the nanostructures or the composition of their material. We will see later in the X-STM section that, although there might be a small variation in the average size of the SML-QDs (a QW should not show any net variation of its width), there is indeed a reduction of the In concentration when the As flux is decreased.

5-3 Influence of Ga and In growth rates

Usually, InAs/GaAs SK-QDs are grown under As-rich conditions at high V/III ratios (c(4×4) reconstruction) using growth rates of 1.0ML/s and 0.1ML/s for GaAs and InAs, respectively [100]. This is actually true for the growth of any arsenide to get high crystalline quality. Since a (2×4) reconstruction—and consequently a low As flux—is required for the nucleation of true 2D InAs islands on the GaAs(001) surface, we had to lower both growth rates to keep growing the SML-QDs under As-rich conditions as well. Thus, the second growth parameter investigated is the growth rate of the fractional InAs layer and GaAs material deposited between two InAs submonolayers. Four samples with the same structure as in Figure 5-1 were grown in the presence of a (2×4) reconstruction (T= 490 °C and a BEP value of 1×10^{-7} Torr equivalent to 0.2 ML/s). Initially, we varied the growth rate of the GaAs interlayer from 0.05 to 0.2 ML/s and kept the InAs growth rate constant (0.014 ML/s).

Figure 5-3 shows that the sample grown with the highest GaAs rate (0.2 ML/s) showed no PL signal at all due to the fact that the As and Ga fluxes were similar. The growth of this sample probably occurred under Ga-rich conditions that are known to cause structural defects, which reduce the PL signal. Among the other samples, the one grown with a GaAs rate of 0.1 ML/s showed the narrowest (FWHM = 7.3 meV) and most intense spectrum, suggesting higher optical quality. Since In segregation is strong in the InAs/GaAs system ($R\approx0.8$) [144], it is always better to choose growth conditions that limit its effects. From this point of view, a GaAs growth rate of 0.15 ML/s might be better—it has also a narrow value of the FWHM (7.6 meV)—as confirmed by the redshift of its emission. However, the V/III ratio is still close to the limit of the Ga-rich condition, and the PL intensity is not the highest one. For this reason, the GaAs growth of 0.1 ML/s rate was preferred for the next optimization steps.

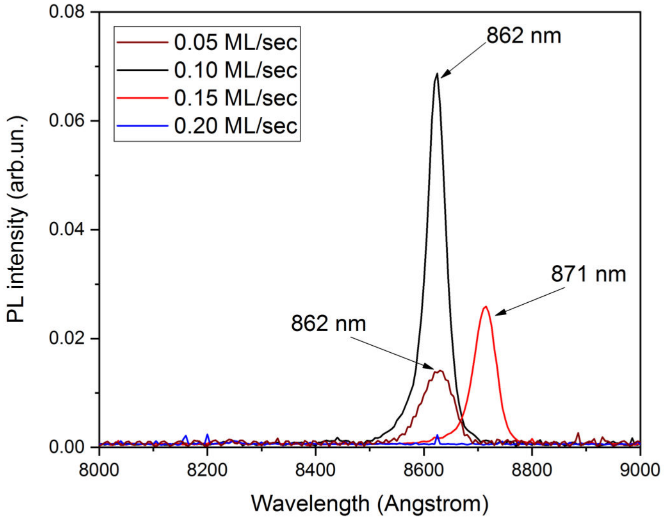

Figure 5-3: PL spectra of SML-QDs consisting of 0.5 ML of InAs and 2.5 MLs of GaAs repeated 4 times. Each sample had a different growth rate for the GaAs interlayer.

To check the influence of the InAs growth rate on the PL result of InAs/ GaAs SML-QDs, two samples were grown with different InAs growth rates (0.014 and 0.117 ML/s). Figure 5-4 shows that the SML-QDs sample grown at 0.014 ML/s has a higher and broader signal that is redshifted compared to the sample grown at 0.12 ML/s. STM and AFM studies of thin InAs layers or of uncapped SK-QDs have shown that a lower InAs growth rate leads to larger 2D InAs islands or 3D quantum dots with more uniform size distribution [145, 146], both of which are consistent with improved optical line widths. The features of Figure 5-4 are partly in agreement with these observations, and the lowest growth rates probably provide a lower density of slightly wider SML-QDs yielding the redshift. One might perhaps expect a larger redshift as a result of the large difference between the two growth rates. However, a lower InAs growth rate also increases In segregation and therefore reduces the In content, leading to a blueshift of the emission competing with the previous size effect. The cause of the larger

FWHM is not clear, as a lower growth rate usually leads to more homogeneous structures resulting in a narrower emission.

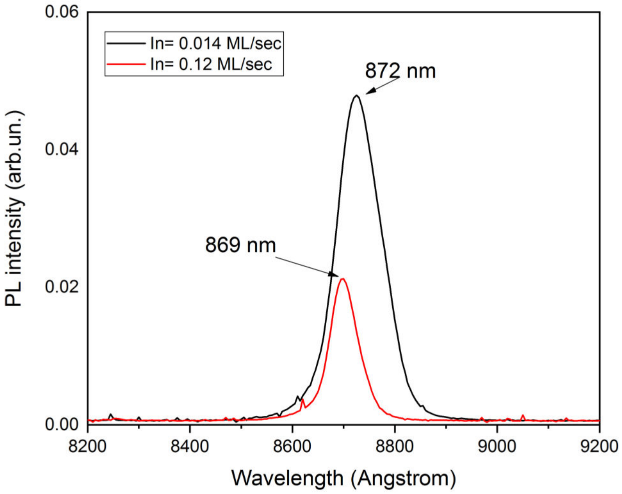

Figure 5-4: PL spectra of SML-QDs consisting of 0.5 ML of InAs and 2.5 MLs of GaAs repeated 4 times. Each sample had a different InAs growth rate. The FWHM values are 10.5 meV and 16.4 meV for high and low growth rates, respectively.

5-4 Influence of the InAs coverage

SML-QDs are supposed to be formed by stacking small 2D InAs islands separated vertically by a few monolayers of GaAs. Therefore, SML-QDs are expected to have approximately the lateral size and areal density of these 2D InAs islands. So, the third structural parameter investigated was the InAs coverage (fraction) deposited in each submonolayer to check its influence on the properties of SML-QDs. One expects low fractions to create a high density of narrow islands, while larger fractions should lead to a lower density of wider islands. Three samples were grown using three different fractions of InAs material (0.35, 0.50, and 0.65 ML) covered by a thin GaAs layer (2.65, 2.50, and 2.35 MLs, respectively) to keep the same period.

Figure 5-5 shows that the PL emission is redshifted and has a higher intensity with a rising InAs fraction. In general, low InAs coverage leads to narrower 2D islands, whose density increases with increasing amounts of material. After a certain amount of material is deposited, the density decreases as the small islands start to merge, yielding wider 2D islands. Since the sample with the lowest InAs fraction has only 35% of its surface covered by InAs material, we can expect it to have a high density of narrow 2D islands and, therefore, very small SML-QDs, which can hardly confine charge carriers—due to their ground state being close to the top of the GaAs barriers. Moreover, smaller islands are easier to be dissolved by In segregation, which could reduce their density and size or reduce their In composition. As a consequence, their PL signal is expected to be weaker and blueshifted. When the InAs fraction increases, the size, number, and the In content of the SML-QDs increase as well, yielding stronger confinement and PL emission at higher wavelengths. For the largest fraction (0.65 ML), more than half of the GaAs surface is covered by InAs, and some large islands start to merge in an attempt to complete a full InAs monolayer. Although the PL intensity is even stronger (due to larger 2D structures containing more In atoms), such large and probably irregular islands may not be suited to form homogeneous SML-QDs. Therefore, we preferred to use a fraction of 0.5 ML for the rest of the optimization process.

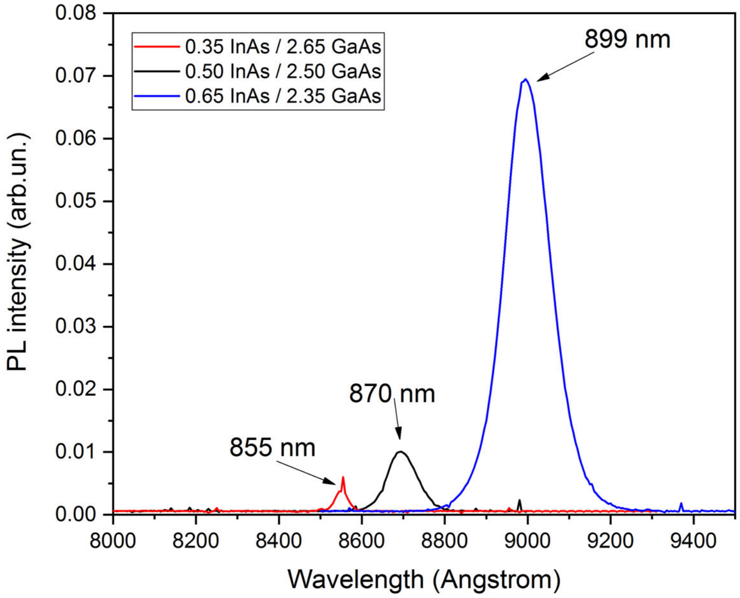

Figure 5-5: PL spectra of SML-QDs consisting of n ML of InAs and 3-n MLs of GaAs repeated 4 times, where n=0.35, 0.5, or 0.65 ML. The FWHM values are 5.6 meV, 14.5 meV, and 19.7 meV for n=0.35, 0.5, or 0.65 ML, respectively.

5-5 Influence of the number of repetitions

Finally, we investigated the number of repetitions of the InAs/GaAs cycle to change the height of the nanostructures. Figure 5-6 shows the PL spectra of three 0.5/2.5 InAs/GaAs SML-QDs samples with a number of repetitions varying from 4 to 10, corresponding thus to a height of the structures ranging between 12 and 30 MLs, i.e., between 3.4 and 8.5 nm. It can be seen that the peaks shift significantly to higher wavelengths (i.e., lower energies) when the height of the structures increases, which is consistent with the fact that the vertical size of the structures dominates the confinement energies (i.e., their lateral size is larger or comparable). The higher intensity of the larger structures is due to their lower energy levels that provide better confinement of the carriers (the ground state is deeper inside the potential well) and, thus, a stronger overlap of their wave functions. There also appears to be a slight increase in the FWHM as the number of repetitions rises, which might be due to the fact that large SML-QDs might be more inhomogeneous. Indeed, it has been suggested [120] that, since the amount of InAs material is much less in SML-QDs than in usual SK-QDs, the strain field might be weaker in the former type of nanostructures, and therefore the alignment of the 2D islands may not be as effective as expected, leading to more disordered

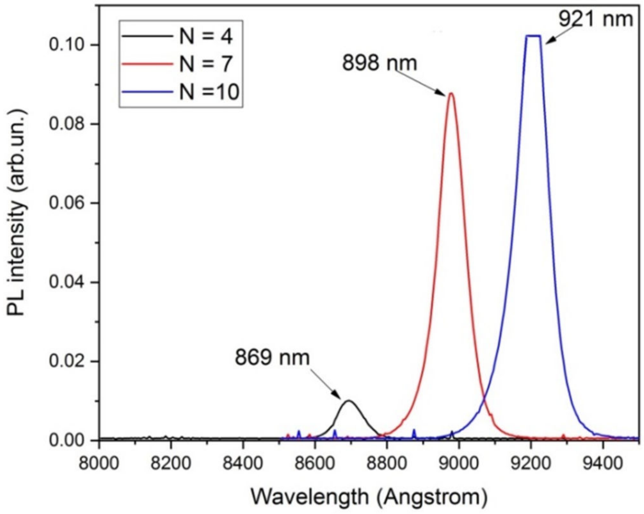

Figure 5-6: PL spectra of SML-QDs structures consisting of 0.5 ML of InAs and 2.5 MLs of GaAs repeated N times. FWHM values are 13.9 meV, 14.5 meV, and 16.0 meV for N=4, 7, or 10 repetitions, respectively.

stacks and, consequently, to a broader PL spectrum. Since the growth of SML-QDs using (2×4) reconstruction is complex and time-consuming, and, furthermore, 10 repetitions seemed to only slightly improve the optical quality of the samples, a 6-fold repetition was adopted to obtain SML-QDs with a height similar to that of SK-QDs.

This first phase of optimization process has come to a conclusion that, in order to grow such nanostructures in the presence of a (2×4) surface reconstruction, we had to use a 0.5/2.5 InAs/GaAs basic cycle repeated 6 times and a growth rate of 0.015 ML/s and 0.1 ML/s for InAs and the thin GaAs interlayers, respectively, in the presence of an As BEP around 1.0×10^{-7} Torr (slightly below 0.2 ML/s). These optimized growth conditions will be used to grow a sample for the X-STM measurements in the second phase of optimization.

5-6 X-STM experimental results

As we demonstrated in the previous chapter, X-STM is probably the most effective way for investigating SML-QDs, as it allows the structural and compositional investigation of buried structures at the atomic scale. However, it is still a surface-related technique that can only probe a few nanostructures at a time due to its very high resolution. Figure 5-7 shows the very specific structure (sample #E) that was grown on a Si-doped GaAs(001) substrate ($n=1\times10^{18}$ cm^{-3}) to perform X-STM measurements. It contains five layers of InAs/GaAs SML-QDs grown in different conditions to measure all of them at the same time, with the same tip, and under the same experimental conditions, in order to compare all measurements without any ambiguity. These five layers were designed to check the influence of some of the growth parameters studied above (i.e., As flux, surface reconstruction, number of repetitions, and growth rate) on the structural properties of the SML-QDs. Each layer was surrounded by 40 nm of undoped GaAs and separated from the next SML-QDs layer by 120 nm of GaAs: Si ($n = 1 \times 10^{18}$ cm^{-3}) to provide a good conductivity for the X-STM measurements without having Si atoms inside or close to the nanostructures themselves to avoid any influence of the Si dopant on the topographic measurements. The goal of this sample was to evaluate the influence of the main growth conditions, but not all of them, because the technique is complex and time-consuming, and we were only able to analyze a single sample. The growth parameters of the 5 layers were chosen to allow several types of comparisons between some of the layers. With layers #1, #3, and #4 we could check the influence of the As flux; with layers #1 and #3, the influence of the surface reconstructions (but their As fluxes are similar); with layers #1 and #2 the influence of the number of repetitions, and with layers #3 and #5 the influence of the growth rates (layer #5 was grown using conditions similar to those of SK-QDs).

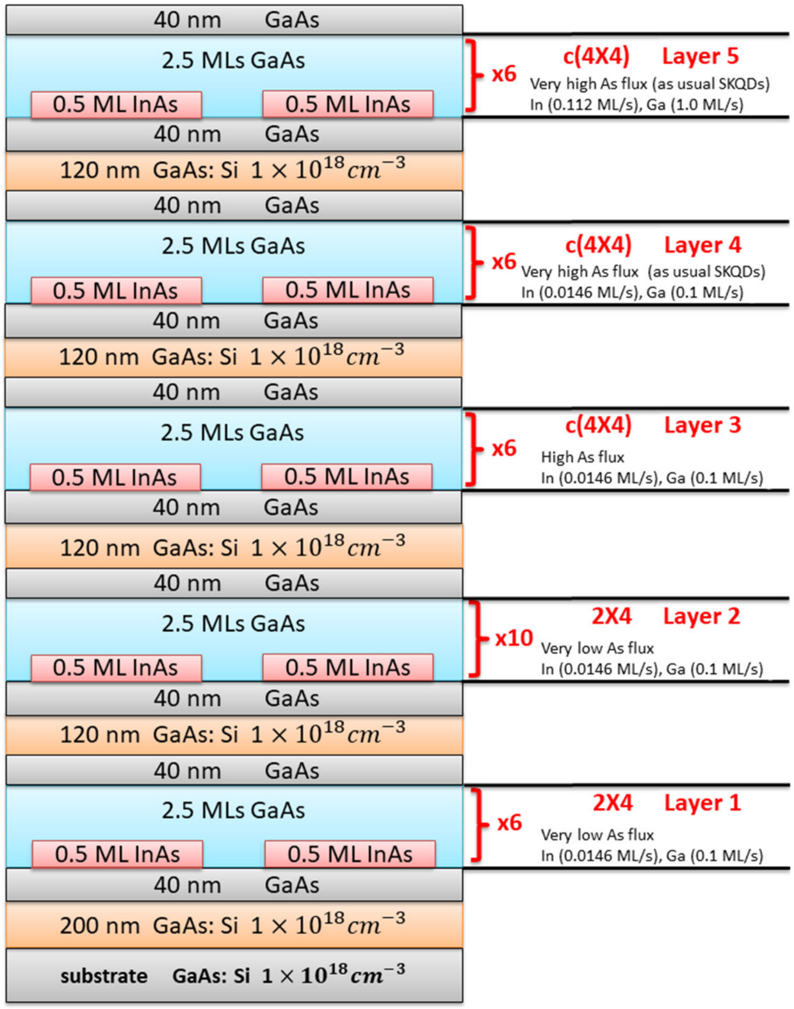

Figure 5-7: Specific conducting sample #E for the X-STM measurements. All five SML-QDs layers were grown under different growth conditions to check their influence on the formation of SML-QDs. Layers #1, #3, and #4 differed only by the As flux (6×10^{-8}, $2\times10^{-7,}$ and 7×10^{-7} Torr (BEP), respectively). Layer #2 had SML-QDs built from 10 repetitions instead of 6, and layer #5 was grown using high growth rates of InAs and GaAs typically used for SK-QDs.

All the five SML-QDs layers of the sample contained six repetitions of a basic cycle consisting of 0.5 ML of InAs followed by 2.5 MLs of GaAs (except for layer #2, which contained ten repetitions). Only one growth parameter or feature of the structure was varied at a time in any of the five SML-QDs layers, as shown in Figure 5-7. Since the STM technique is based on an electric current between a sharp metallic tip and the sample surface, the sample needed to be conductive. For this reason, we used a doped GaAs:Si ($n=1.0\times10^{18}$ cm^{-3}) substrate, and all SML-QDs layers were separated by 120 nm thick doped GaAs:Si layers with the same doping level as the substrate.

A small sample with dimensions of 4×8 mm^2 was cut from the wafer, and its backside was mechanically polished to reduce the thickness from 350 μm to 120-150 μm. Typically, thinner samples provide better cleaving to obtain atomically flat surfaces for X-STM measurements. The sample was then clamped on a special holder after making a small scratch (1 mm) on the back side to aid the cleaving. The sample was then loaded into the STM preparation chamber and baked for 30 min to remove any contaminants. All the X-STM measurements presented here were performed in a conventional Liquid-Nitrogen-cooled Omicron STM at the Eindhoven University of Technology by Dr. Raja Gajjela (from the group of Prof. Paul Koenraad). These measurements were carried out on a fresh {110} surface obtained by cleaving the sample in ultra-high vacuum (UHV). The polycrystalline tungsten wire used for the STM tip was electrochemically etched, baked, and sputtered using Ar in the STM preparation chamber under UHV. All the X-STM images were acquired in constant-current mode. Due to the atomic arrangement of the {110} surfaces of Zinc blende crystals, only every 2nd ML along the growth direction is visible in the X-STM images. Therefore, in the present case, either the group-III or the group-V atoms can be observed at a time. When scanning the surface at positive bias voltage, an empty-state image is obtained—i.e., only the group-III sublattice (Ga, In, Al) is visible—while, at negative bias voltage, only the group-V sublattice (i.e., As) is detected (filled-states images, Figure 4-19) [147].

Figure 5-8 provides high-resolution X-STM images of each SML-QDs layer of the sample. Comparing the first group of layers (#1, #3, and #4), where only the As flux was varied, it is clear that layer #1 has fewer In atoms—the relaxation outwards the surface is smaller and the contrast (brightness) is weaker—than layer

#3, which in turn also has less In than layer #4. This is because InAs has a larger lattice parameter than GaAs and, consequently, applies a tensile stress on the sample which pushes the atoms out of the cleaved surface. Since the structures of these three layers were nominally identical and all layers received exactly the same amount of InAs material (only the As flux was changed during the formation of SML-QDs), this is most probably due to the fact that In incorporation is less than unity at low As flux [142]. Under these conditions, part of the In atoms deposited in layer #1 was not incorporated. Instead, they remained "floating" on the surface as adsorbed species (this effect is different from In segregation that will be discussed below) and were desorbed later when the substrate temperature was increased to grow the thick GaAs separation layer (400 nm + 1200 nm + 400 nm).

When comparing layers #1 and #3, which have the closest As fluxes but were deposited under a different surface reconstruction—(2×4) and c(4×4), respectively —we can see that both have In rich InGaAs clusters, although they have different sizes, densities, and compositions. This is, of course, in contradiction with previous STM studies [47], which predicted that a c(4×4) surface reconstruction would not be able to nucleate 2D InAs islands and, therefore, should not allow the formation of SML-QDs. However, these agglomerates have indeed already been observed by several groups [119, 148] and found to behave like quantum dots, even when deposited in the presence of a c(4×4) reconstruction resulting from growth conditions similar to those of SK-QDs. However, it is clear from Figure 5-8 that none of these clusters show any internal periodicity related to the vertical stacking of small 2D InAs islands, as usually sketched and represented in Figure 5-7. In addition, it has already been pointed out that a lower As flux should increase In segregation [149]. That was also confirmed in our sample by taking empty-states images of the same layers at positive bias. In this case, the In atoms can be directly imaged and counted, and their number can be determined in consecutive atomic layers along the growth conditions [142]. Using the semi-empirical segregation model of Muraki *et al.* [144], we inferred the segregation coefficient R of the In atoms to be 0.83±0.02, 0.79±0.01, and 0.72±0.02 for layers #1, #3, and #4, respectively. These values were independently confirmed using *in-situ* RHEED measurements to monitor In segregation during the growth of InGaAs layers deposited in conditions similar to those of layers #1 to #5 [134]. Therefore, in addition to lower In incorporation, SML-QDs deposited with a (2×4) reconstruction also suffer from stronger In segregation, and both effects together result in a much lower In content than with the usual c(4×4) reconstruction.

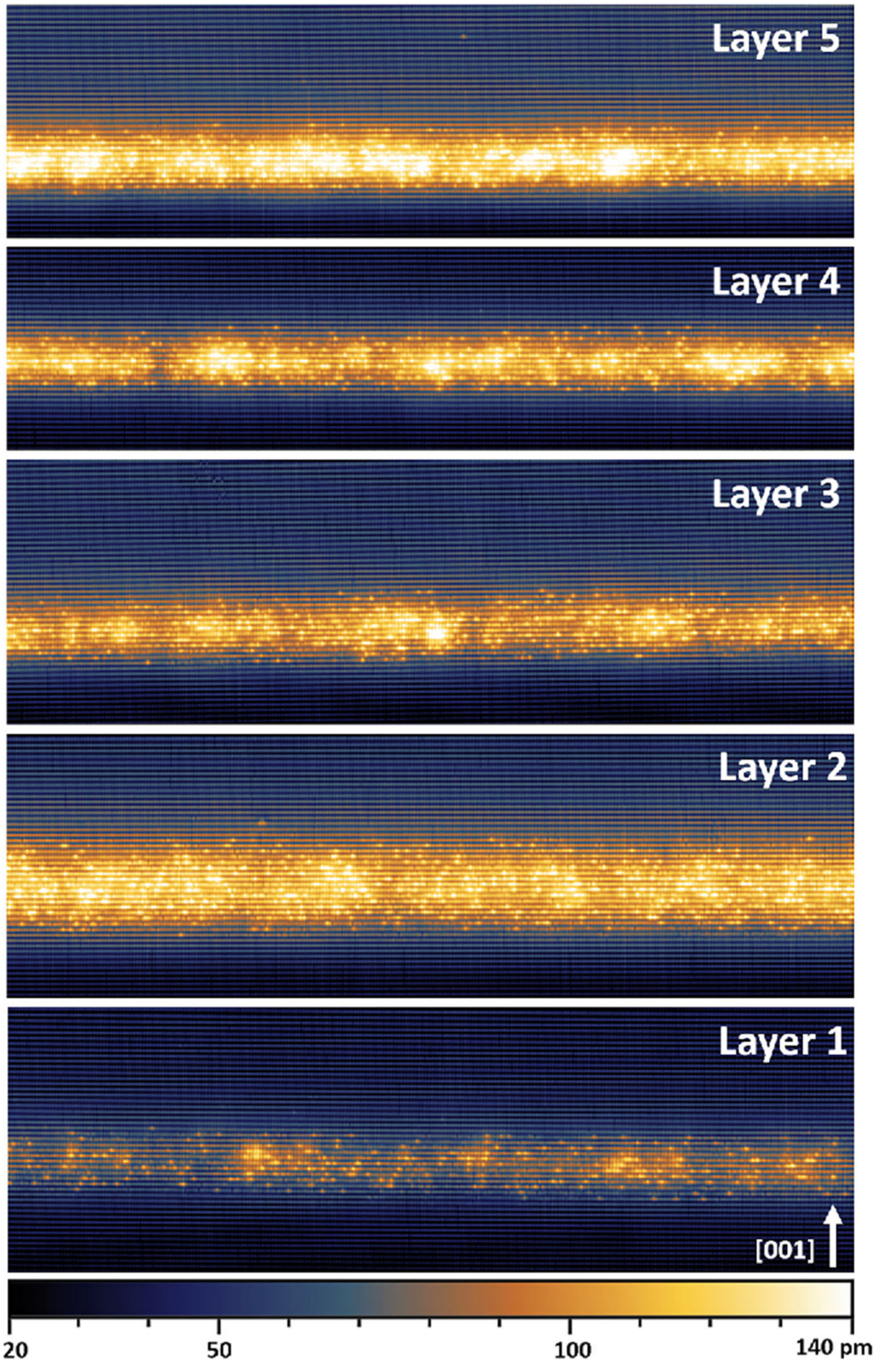

Figure 5-8: Filled-state images (80×25 nm^2) of the SML-QDs of layers #1 – #5 (illustrated in Figure 5-7) taken at bias voltage V_b = –2.1 V and tunneling current I_t = 50 pA. The arrow indicates the growth direction [001]. The bright (yellow) spots represent In-rich regions, while the rest of the images consists of the crystalline GaAs matrix (blue lines).

Layer #2 is much broader than the others due to the larger number of repetitions of the basic cycle (10 instead of 6). It appears much brighter than layer #1, even though it was deposited under exactly the same conditions. Indeed, the X-STM data show that the In content and In segregation are similar in both layers, but the contrast is higher in layer #2 due to the enhanced surface relaxation resulting from the larger number of repetitions (the section of a wide surface may relax outward more than a narrow one). However, no relevant differences can be observed concerning the number, composition, or size of the nanostructures, suggesting that something prevents SML-QDs from developing their full height.

Finally, layer #5 was grown using the same parameters as layer #4 (high As flux), except that higher InAs and GaAs growth rates were used to get typical growth conditions of SK-QDs (i.e., 0.1 ML/s and 1 ML/s for InAs and GaAs). These are actually the growth conditions (or very similar ones) used in all reports about SML-QDs found so far in the literature. Layer #5 shows the highest density of all the layers—5–6 × 10^{11} cm^{-2} compared to 2–3 × 10^{11} cm^{-2} for layer #4, which is roughly ten times the usual SK-QDs density [150]—as well as a larger amount of In atoms (higher contrast). Both features are due to the higher InAs growth rate—which is known to increase the density of the small 2D InAs islands as a consequence of the smaller diffusion length of the adatoms—and to the higher GaAs rate, which reduces In segregation. We can see in Figure 5-8 that the SML-QDs generally have a base length of 4–6 nm and a height of 3–3.5 nm, which leads to a smaller aspect ratio than for SK-QDs [151] that might contribute to enhancing the efficiency of devices.

It is clear from our X-STM images that 2D InAs islands are not consistently nucleated (or, if they are, they don't survive capping), that stacks of such islands are not formed, that the nanostructures actually look like In-rich agglomerates embedded in a wider InGaAs QW with a lower In content, and that these clusters are shorter than expected (compared to the number of repetitions involved in the structure) [105]. In addition, it seems that both surface reconstructions allow the formation of nanostructures (although with different sizes and densities), while nothing was expected for the c(4×4) case (according to previous STM reports). These features are most probably due to the presence of In segregation which seems to have a much stronger influence in SML-QDs than

SK-QDs. Segregation can occur during the growth of the In(Ga)As alloy or during its capping by another material (e.g., GaAs), and its consequences can be effectively observed during the growth of the first 10 MLs of material (very thin layers are extremely affected). It consists in substituting the In atoms of the surface with Ga atoms to reduce the strain in the InAs/GaAs system. Thus, it is exclusively a surface phenomenon that can occur only during growth—only the growth front is affected, and it should not be confused with bulk diffusion or intermixing that can occur after growth and may involve layers well below the surface. In thick layers, the main consequence is a strong composition change during the first 10 MLs, which appears as a broadening of the interface. The In atoms that are not readily incorporated keep floating on the surface, as adsorbed species, and will be incorporated later in order to reach the desired nominal composition.

InAs SK-QDs consist of large 3D InGaAs lens- or pyramid-shaped islands containing up to 85% of In because, during their formation and capping, segregation and strain forced part of the In atoms to leave the original InAs material to lower the total elastic energy of the system. On the other hand, the building blocks of SML-QDs are narrow 2D InAs islands (let's assume for now that they can be formed somehow) which are covered by a few MLs of GaAs. Since the segregation coefficient for our structures is 0.70-0.85, it means that, after the deposition of the first fraction of InAs ML, between 70% and 85% of the In atoms deposited will migrate to the next layer during GaAs capping, destroying most of the 2D InAs islands. These In atoms will remain adsorbed on the surface and, again, part of them will eventually incorporate, while the rest will continue to migrate upward during deposition of the next layers. This late incorporation can take place anywhere on the surface and is responsible for the thick InGaAs layer (acting as an InGaAs QW) surrounding the observed In-rich clusters.

One might question why none of layers #1 to #5 showed any vertical stacking of small 2D InAs islands as it is well known to happen when several layers of SK-QDs are deposited sequentially and separated by a short distance. Indeed, Xie *et al.* [152] developed a semi-empirical model able to evaluate the strain field around InAs SK-QDs embedded in a GaAs matrix and its ability to influence the nucleation of SK-QDs in the next InAs layer close by. They found that SK-QDs of consecutive InAs layers were always vertically aligned whenever the GaAs spacer was thinner than a certain value z_0 which mainly depends on the size of the SK-QDs, their average lateral separation, the lattice parameters of InAs and GaAs, as well as several elastic constants of both materials. They calculated that typical SK-QDs should stack vertically with a probability larger than 95% whenever their vertical separation was smaller than 10 nm, and should be completely uncoupled for distances larger than 50 nm, in excellent agreement with their experimental observations. Because of the very thin GaAs spacer existing between consecutive InAs submonolayers, one usually expects such a vertical alignment of the small 2D InAs islands to occur as well and allow the formation of SML-QDs. This is why these nanostructures are invariably sketched as stacks of 2D InAs islands separated by thin layers of GaAs material.

However, one should be aware that there are at least two fundamental differences between InAs/GaAs SK-QDs and SML-QDs. First, SK-QDs are much larger 3D InAs structures that can induce higher strain in the surrounding matrix, allowing thus to vertically align nanostructures over longer distances. Second, In segregation is more effective in SML-QDs due to the very thin GaAs layer separating consecutive InAs submonolayers. Therefore, most In atoms are removed from the 2D islands that are actually made (whenever they survive to the capping process) of InGaAs material with a low In content (15-30%), which further reduces the strength of the strain field around the islands. When these major differences—together with other ones that are, individually, less relevant—are taken into account in the model of Xie *et al.*, one can show that, for more realistic SML-QDs, the value of Z_0 can drop below 2 MLs, suggesting that the internal strain is indeed no longer strong enough to align the 2D islands [153], resulting in the formation of irregular In rich InGaAs clusters scattered inside the wide InGaAs QW. An indirect way to show that the strain is much weaker in SML-QDs is to apply a rapid thermal annealing (RTA) to the samples [120]. When SK-QDs are submitted to a RTA, their optical properties change drastically: their emission increases, narrows, and blueshifts. This is due to the large strain in the sample that, during RTA, allows a strong intermixing between the In atoms of the QDs and the Ga atoms of the cap or bottom layer, yielding more homogeneous structures (narrowing) having a lower In content (blueshift) and less structural defects (increase). When SML-QDs are submitted to the same process, their optical properties are barely modified, confirming that their internal strain is indeed much lower and is no longer sufficient to activate any relevant intermixing.

As a consequence, one can understand why SML-QDs look like In-rich agglomerates instead of vertical stacks of small 2D InAs islands, but it may not be very clear why both types of surface reconstructions allow the formation of that kind of clusters when only the (2×4) reconstruction should be able to nucleate the 2D InAs islands. However, since the effects of In segregation are extremely strong for SML-QDs (due to the very thin layers involved), most of the InAs material is dissolved and the In atoms are randomly incorporated later, giving rise to the In-rich clusters, as is the case for the c(4×4) reconstruction where the In atoms are initially randomly incorporated. The (2×4) surface reconstruction has several drawbacks when considering the growth of SML-QDs: the growth conditions are more difficult to achieve, they lead to longer growth times, In segregation is stronger at lower As flux, and In incorporation as well. Since both surface reconstructions clearly allow the formation of those In-rich clusters, it is then obviously easier to use the c(4×4) surface reconstruction, unless one could find another way to keep the (2×4) reconstruction at a low temperature and overcome the problems mentioned above.

There is actually another way to maintain the (2×4) reconstruction and grow the SML-QDs at low temperatures. Since the surface morphology changes from a (2×4) reconstruction to a c(4×4) reconstruction around 520 °C (at high As flux) when the temperature decreases from 570 to 515-490 °C, one way to avoid this problem would be to keep the sample temperature slightly above 520 °C to keep the original (2×4) reconstruction in the presence of a high As flux. Therefore, instead of growing the SML-QDs at 490 °C with an extremely low As (which has the drawbacks mentioned above), we used a growth temperature of around 525 °C and a high As flux, as usual. It is clear that In segregation should be slightly larger and the In atoms should desorb slightly more than at 490 °C, but the other drawbacks (lower In incorporation, longer growth times, complex growth conditions) would disappear. So, the next growth parameter that was investigated is the growth temperature, but keeping the high As flux fixed.

5-7 Influence of the growth temperature

Two samples containing SML-QDs (0.5/2.5 InAs/GaAs) were grown with the same growth conditions and As flux (7.0×10^{-7} Torr, equivalent to 2.5 ML/s), except for their growth temperature. One was grown with a (2×4) surface reconstruction and a high growth temperature (528 °C)—just before the transition to the c(4×4) reconstruction that occurs at approximately 520 °C—whereas the other was grown at the usual temperature for SML-QDs (490 °C), i.e., in the presence of a c(4×4) reconstruction.

Figure 5-9 shows that SML-QDs grown at high temperature (528 °C) with a (2×4) reconstruction exhibits a blueshift compared to those grown at low temperature (490 °C) with a c(4×4) reconstruction. This may be attributed to the lower In content resulting from the stronger In segregation and desorption (or eventually to smaller QDs). Furthermore, the FWHM of the (2×4) sample was smaller (9.5 meV) than that of sample c(4×4) (14.7 meV), and its emission was five times higher. This probably means that the 2D InAs islands are more homogeneous at higher growth temperatures (528 °C) and contain less structural defects than the c(4×4) sample grown at low temperatures.

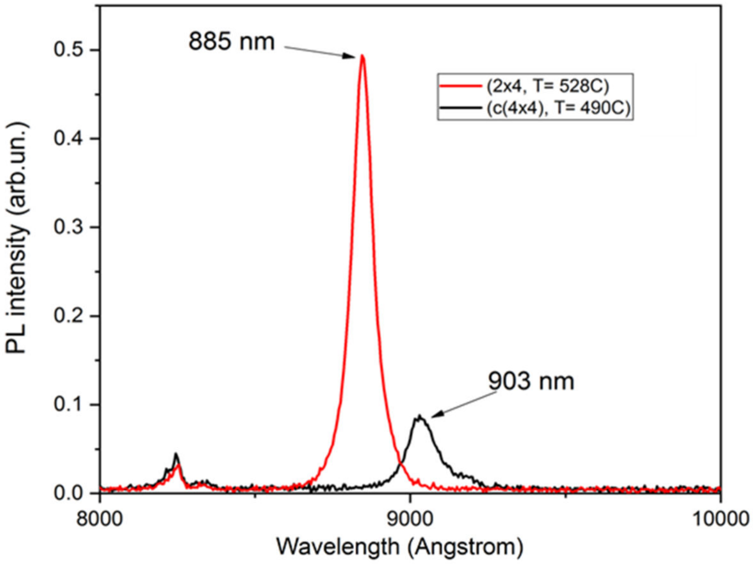

Figure 5-9: PL spectra at 77K of the InAs/GaAs SML-QDs samples differing only by the growth temperature.

Another sample was grown for X-STM measurements to determine whether the growth of SML-QDs at higher temperatures and higher As flux indeed leads to better nanostructures. However, the results of the experiment are still unavailable as the sample is being measured by another research group, led by Professor Rachel S. Goldman at the University of Michigan, that is currently having problems with the X-STM equipment.

5-8 SML-QDs with a thinner GaAs interlayer

Until now, we have mainly considered SML-QDs consisting of six repetitions of a basic cycle containing 0.5 ML of InAs followed by 2.5 MLs of GaAs. As a consequence, the average nominal In composition in those layers is 16.7% (0.5/3.0), but the nominal In concentration in the individual SML-QDs (see Figure 5-10) is 33% (1 ML of InAs and 2 MLs of GaAs). Since we used six repetitions, the total thickness of the layers containing SML-QDs was 18 MLs (around 6 nm), a value that is much lower than the critical thickness of $In_{0.17}Ga_{0.83}As$ deposited on top of GaAs (around 18 nm). For this reason, such SML-QDs can be grown without any relaxation of the epitaxial layers. However, real SML-QDs are very different from those outlined in Figure 5-7. Indeed, due to strong In segregation, most of the In atoms from the 2D InAs islands (when they are ever formed) are scattered in the epitaxial layers, and the strain field required to align the 2D islands from the next InAs submonolayers is too weak to do so, yielding the formation of small and irregular In-rich clusters. Therefore, a simple way to strengthen that strain field would be to increase the In content of the nominal structure by reducing the thickness of the GaAs interlayer (which is currently 2.5 MLs). However, when the GaAs spacer is reduced down to 1.5 MLs or even 0.5 ML, the average In composition of the layers increases to 25% and 50% (Figure 5-10), and their critical thickness is reduced accordingly—to around 10 nm and 4 nm, respectively—as can be checked on the RHEED screen when the diffraction pattern changes from a streaky to spotty figure. Therefore, it would be impossible, for example, to grow 6 nm-high SML-QDs consisting of cycles containing 0.5 ML of InAs + 0.5 ML of GaAs. To increase the In content as much as possible and check the relaxation of the layers, we used a basic cycle consisting of 0.3 ML of InAs + 0.7 ML of GaAs and varied the number of repetitions. It means that, nominally, there was no GaAs material between 2 successive InAs submonolayers (Figure 5-10), and all the deposited GaAs material was actually used to fill the spaces between the InAs islands of the same layer.

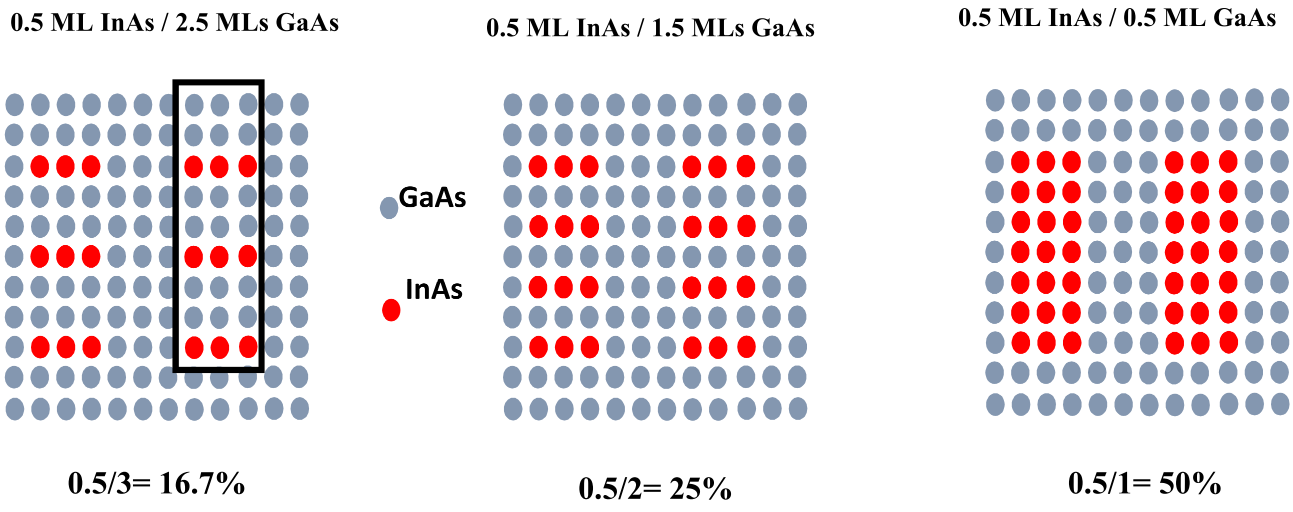

Figure 5-10: structure of InAs/GaAs SML-QDs containing the same InAs fraction (0.5 ML) but different GaAs spacers. (a) 2.5MLs, (b) 1.5MLs, and (c) 0.5ML. The black rectangle shows an individual SML-QD. The average In content of the layers is shown. The average In content of each individual SML-QD is twice that of the layers.

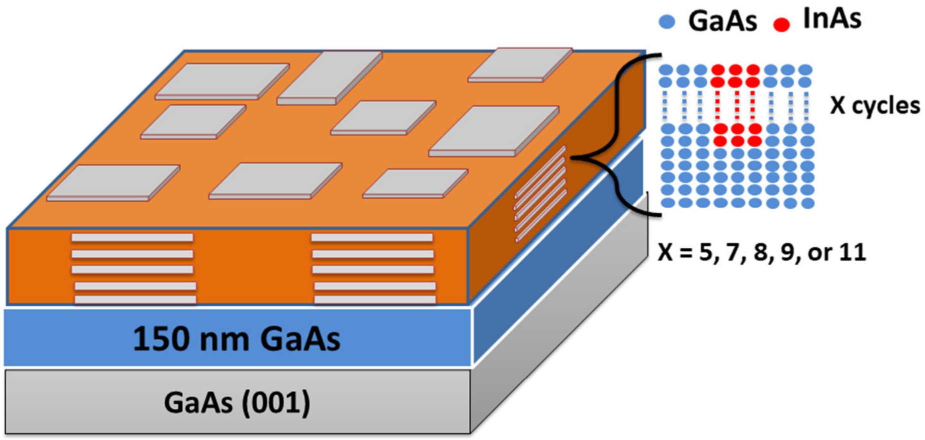

Figure 5-11: Structure of set of samples #F1 consisting of X cycles of 0.3 ML of InAs + 0.7 ML of GaAs—with X= 5, 7, 8, 9, or 11—to be checked by AFM (no cap layer).

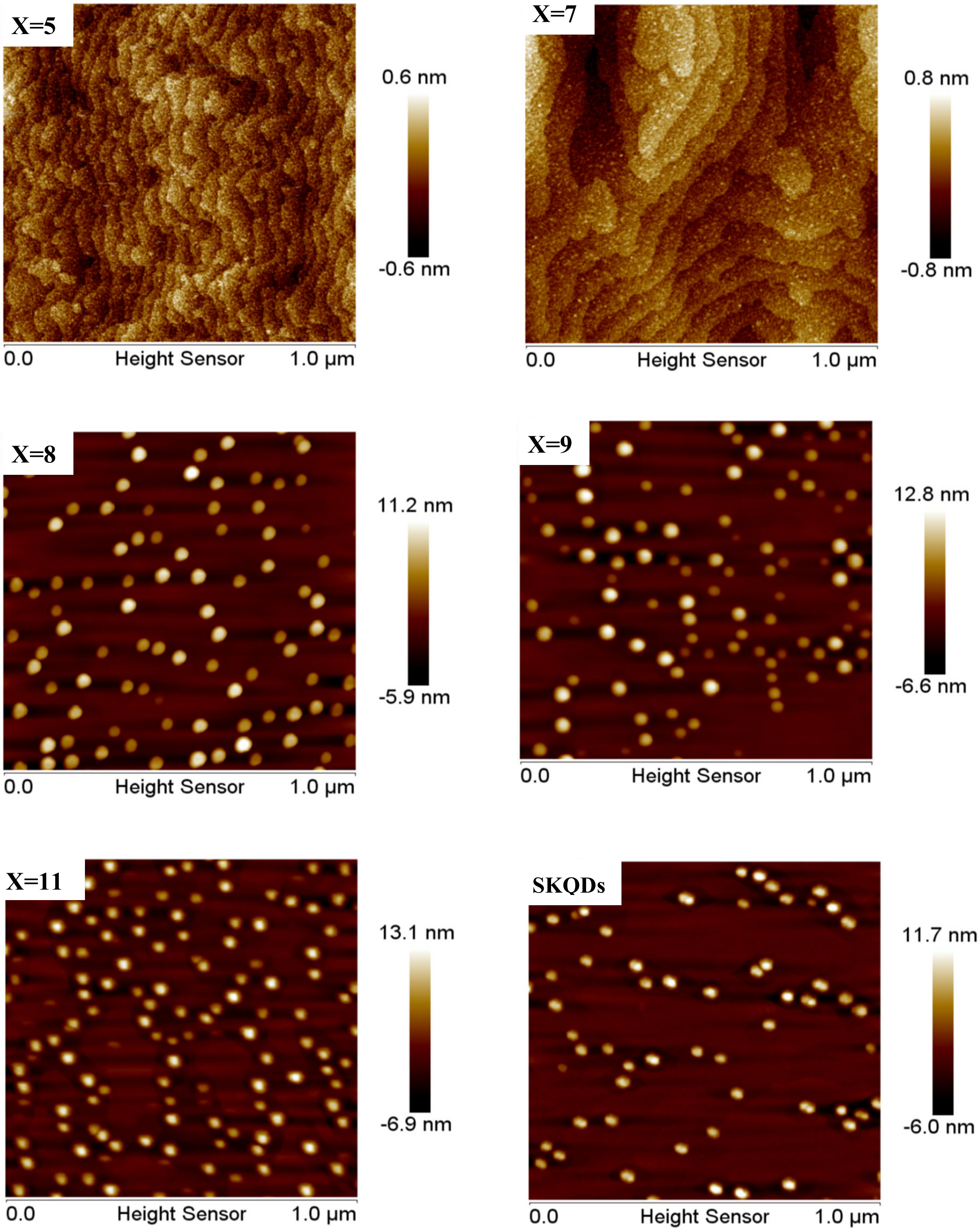

Figure 5-12: 1×1 μm^2 AFM images showing the surface of the set of samples shown in Figure 5-11, consisting of X cycles of 0.3 ML of InAs + 0.7 ML of GaAs, with X= 5, 7, 8, 9, or 11. The last sample (named SKQDs) contains 10.6 MLs of $In_{0.3}Ga_{0.7}As$ deposited on GaAs using the SK growth mode to produce conventional SK-QDs. The critical thickness of $In_{0.3}Ga_{0.7}As$ deposited on top of GaAs was measured to be 9.30 MLs using the RHEED technique.

We grew several samples with cycle repetitions ranging from 5 to 11 in order to determine when relaxation occurs and how the optical properties of such quantum dots evolve. One set of samples was grown with structures capped by 100 nm of GaAs for PL measurements, while another set, identical to the first one, was grown without a cap layer to allow AFM analysis. Figure 5-12 shows the AFM images of the set without any cap layer. One can see that the surface is atomically flat below 8 repetitions, indicating that the SML-QDs can be formed normally. Above 8 repetitions, SK-QDs are clearly visible, indicating that the accumulated strain energy was too large and induced the morphological transformation of the epitaxial layer. Even though these SK-QDs were grown using a different technique, they have a size, shape, and density that are similar to those of $In_{0.3}Ga_{0.7}As$ QDs obtained using the usual SK technique. More specifically, the sample containing 8 cycles has a density of 8.7×10^{9} cm^{-2}, and this value increases with the number of repetitions until it reaches 1.2×10^{10} cm^{-2} in the case of 11 cycles. The same structures were covered with 150 nm thick of GaAs (figure 5-13) and then investigated by PL at 77 K to check their optical quality and the presence (or absence) of SML-QDs below 8 cycles.

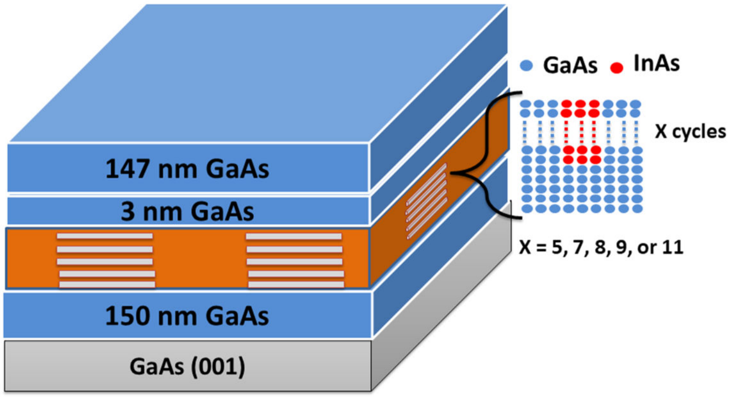

Figure 5-13: Structure of set of samples #F consisting of X cycles of 0.3 ML of InAs + 0.7 ML of GaAs—with X= 5, 7, 8, 9, or 11—covered with 150 nm of GaAs to be analyzed by PL.

Figure 5-14 shows that the structures obtained with 5 and 7 repetitions behave as SML-QDs, as can be seen from their intense and narrow PL emission that peaks at low wavelength values, resulting from their small size. The other 3 samples have a much broader spectrum peaked at larger wavelengths, due to their larger size and broad size distribution, typical of SK-QDs, confirming the characteristics of Figure 5-12. As the number of repetitions increases, the emission redshifts, and the intensity decreases. This is due to the larger amount of strained material that increases the QDs size but also the number of structural defects.

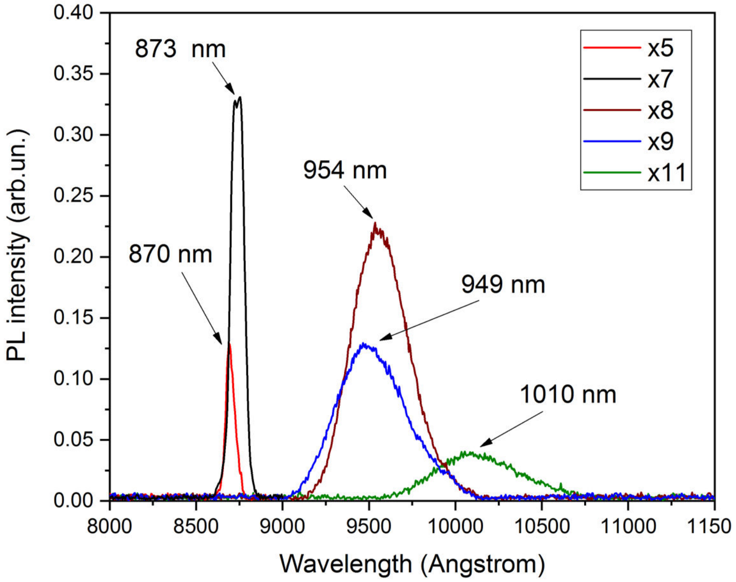

Figure 5-14: PL spectra at 77 K of the set of samples of Figure 5-13 containing X repetitions of 0.3/0.7 InAs/GaAs with X= 5, 7, 8, 9, or 11. Above 8 repetitions, the spectra are much wider, redshifted, and compatible with the formation of SK-QDs detected in Figure 5-12.

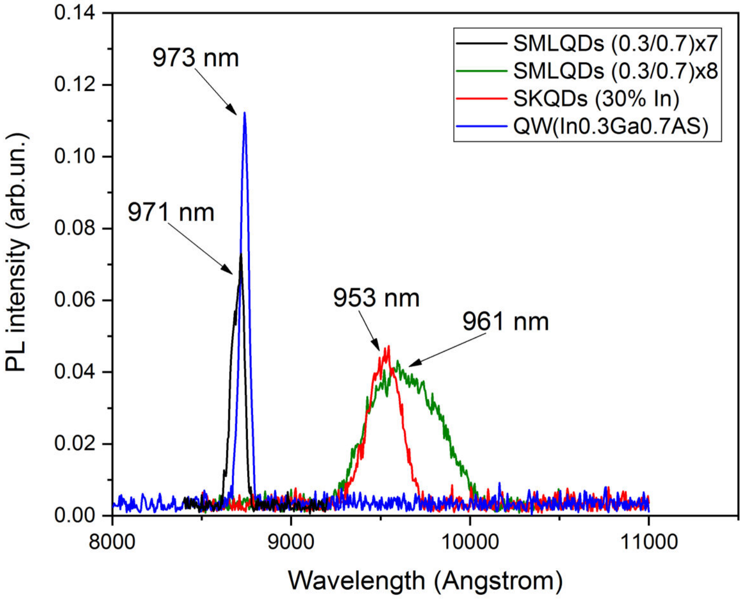

Figure 5-15: PL spectra of the set of samples of Figure 5-13 with 7 and 8 repetitions compared to conventional $In_{0.3}Ga_{0.7}As$ SK-QDs and a 6 MLs-wide $In_{0.3}Ga_{0.7}As$ QW measured at 77K.

Figure 5-15 shows that, as was already detected in the AFM pictures of Figure 5-12, the SML-QDs sample with 8 repetitions has optical properties similar to those of $In_{0.3}Ga_{0.7}As$ SK-QDs grown in conventional conditions. On the other hand, the optical properties of the SML-QDs sample with 7 repetitions are very similar to those of an $In_{0.3}Ga_{0.7}As$ QW having a width of 7 MLs equivalent to the full height of the SML-QDs. This is why some reports [119] suggest that the SML-QDs may actually not form at all, and a QW is obtained instead. However, as will be shown in the next chapters, this is inconsistent with the excellent performance of infrared photodetectors obtained with such SML-QDs. The similar optical properties of SML-QDs and equivalent InGaAs QWs are due to the fact that actual SML-QDs are smaller than expected and, although the wave function of the holes is indeed confined in individual structures, that of the electrons is strongly delocalized and is able to overlap the closest QDs and sense the interfaces of the wider InGaAs layer (acting as a QW) surrounding them [119].

So far, we have optimized the main growth conditions of InAs/GaAs SML-QDs using PL as a guide to maximizing their optical properties, and we performed X-STM and AFM measurements to check some of their structural characteristics that are not optically accessible. However, the main goal of this work is to produce high-performance infrared photodetectors and check whether the new conditions analyzed here to grow SML-QDs—mainly those involving the (2×4) surface reconstruction—can provide better devices than those currently found in the literature (using the c(4×4) reconstruction only). It is only then that we will know for sure whether the optimization process was successful. That will be done in Chapter 7, where SML-QDs with some of the best growth conditions in the active region of such devices will be used. Before that, in the next chapter (Chapter 6), we will see how to process photodetectors and obtain their main figures of merit.

Chapter 6: Processing and electro-optical characterization

In this chapter, I describe the main techniques used to process the samples into photodetectors, including photolithography, metallization, and packaging, along with the setup of experiments used to test the devices such as photocurrent, responsivity, and noise current, followed by a discussion of how reliable results can be obtained using a series of procedures and calculations.

I – Processing:

6-1 Photolithography

All the samples in the next chapter were processed in the ISO 6 clean room of our laboratory (Figure 6-1) into small squared photodetectors using photolithography. Each sample was placed in a spinner, covered with a few drops of photoresist (AZ5214) (Figure 6-2-I and 6-2-II), and rotated at 4000 rotations per minute (rpm) during 30 s to produce a uniform layer of photoresist with a thickness of approximately1.4 µm. The sample was then heated (soft bake) at 90 °C during 4 min on a hot plate to remove most of the solvent present in the photoresist and provide some mechanical resistance to the layer. After the soft bake, the sample was placed in a mask aligner with the mesa mask on top of it (Figure 6-2-III). The mask consists of a glass or quartz plate covered with a thin metallic film containing the pattern to be transferred to the sample. This metallic pattern locally protects the photoresist from the ultraviolet (UV) radiation that is generated by the mask aligner during the exposure process. In the case of a positive photoresist, the regions of the photoresist layer exposed to UV light (during 7 sec at 14.8 mW/cm^2) react and can be removed during the development phase, while the regions that were protected by the metallic pattern of the mask remain intact on the surface of the sample. After the development (Figure 6-2-IV), which consists in dipping the sample in a developer (AZ400) for around 18 s, the sample is rinsed in deionized (DI) water, blown out with dry nitrogen, and heated again (hard baking) at 120 °C for 20 min to prepare the photoresist patterns that remained on the sample for the chemical etching (Figure 6-2-V), which will attack the regions of the sample that were not covered by photoresist. The etching solution that was chosen

(H_2O_2:H_2SO_4:H_2O (1:8:40)) is known to etch GaAs at a rate close to 1.2 µm/min. The actual etching rate was checked with a profiler on the sample itself, and all etchings were done in two steps (after checking each step with the profiler to calibrate the etching rate) to reach precisely the middle of the bottom contact. After removing the photoresist pattern from the surface (stripping) using acetone, the sample was rinsed in isopropanol and blown out with dry N_2. At this stage, the sample contains a large number of small squared mesas having a lateral size of 400 µm × 400 µm and a height that depends on the structure of the sample and on the etching time (Figure 6-2-VI). The same steps mentioned in Figures 6-2- II, III, and IV were repeated once more to open a small window in the photoresist layer overlying all mesas using another (contact) mask (Figure 6-2- VII, VIII, and IX). This small window (Figure 6-2-IX) shows the place where the small electrical contacts will be deposited in the next step (metallization). It is worth mentioning here that we use photoresist AZ5214 as a positive resist, while it is mostly used for reverse processes using a flood and extra reversal bake. However, the procedure described above works well when the contacts are deposited by e-beam and allow us to skip the extra image-reversal process that is more delicate.

Figure 6-1: Clean room (ISO 6) of the "Laboratório de Novos Materiais Semicondutores". On the left side, the mask aligner can be seen, while on the right side, there are two chemical hoods for photoresist handling (spinning and baking) and chemical etching of the samples.

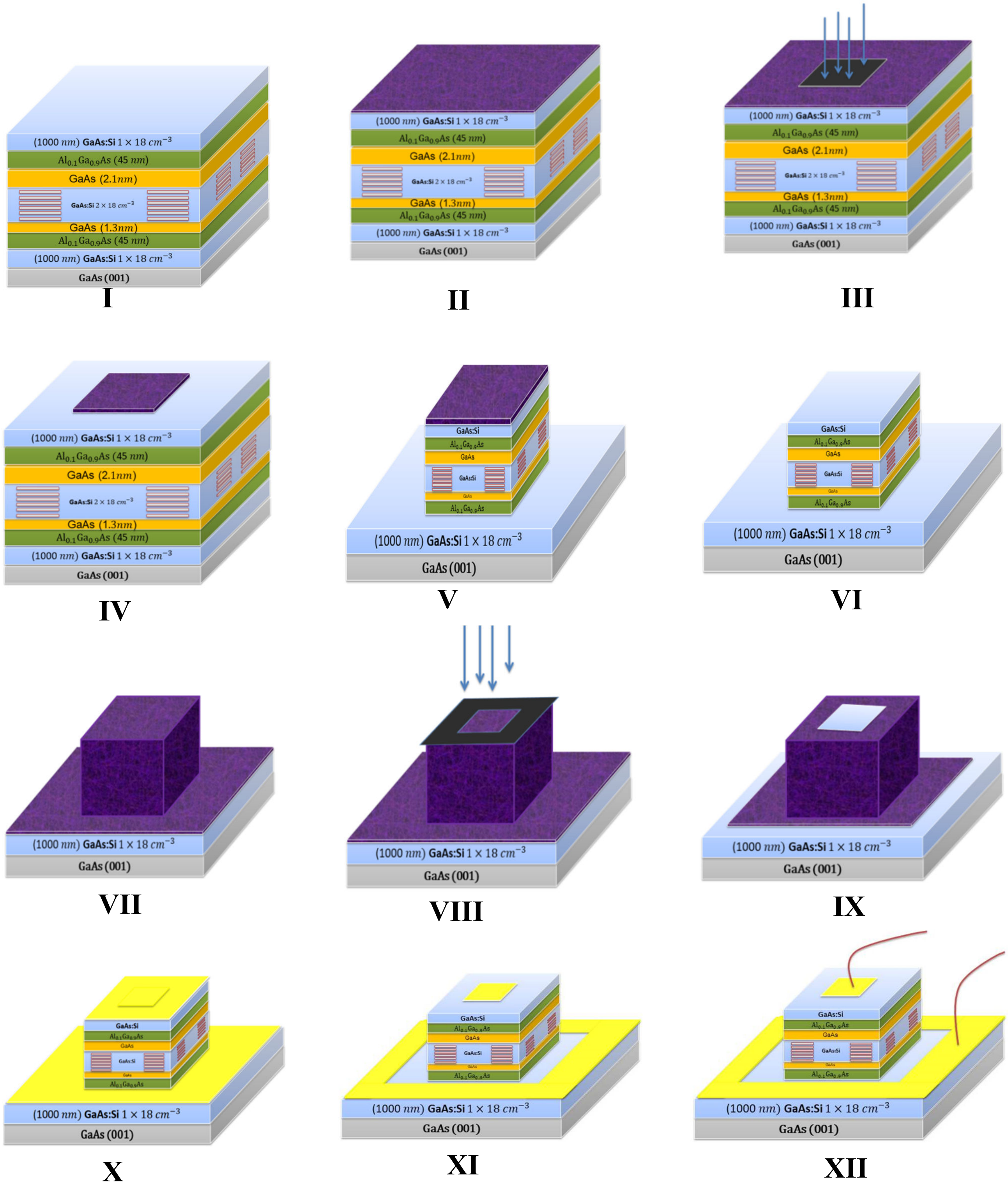

Figure 6-2: The main steps of the processing of a photodetector: (I) sample and its structure, (II) photoresist spinning, (III) mesa mask and exposure, (IV) positive development, (V) etching down to the bottom contact, (VI) removal of photoresist (stripping), (VII) photoresist spinning, (VIII) contact mask and exposure, (IX) development, (X) metallization, (XI) lift-off, (XII) wire bonding.

6-2 Metallization and packaging

Electron-beam (e-beam) metallization and RTA allowed the fabrication of small Ohmic contacts, while wire bonding with thin Au wires was used to connect the devices to the chip carrier. During an e-beam evaporation process (Figure 6-3-a), as the current passes through a tungsten filament, Joule heating occurs and electrons are released (Figure 6-3-b). A high voltage is applied to the filament to accelerate and deflect these electrons with the help of a magnetic field toward the crucible containing the pure material to be deposited. Upon arrival, the energy of the beam is transferred to the material in the crucible, causing it to evaporate (or sublimate) locally and deposit on the substrate. A carousel containing several crucibles and materials allows the deposition of consecutive layers of different nature. Since the heating is localized and defined by the size of the e-beam, the source of the material is close to a point, and the flux of material is more unidirectional than with other deposition methods, making e-beam deposition more adequate for contact metallization and posterior lift-off process.

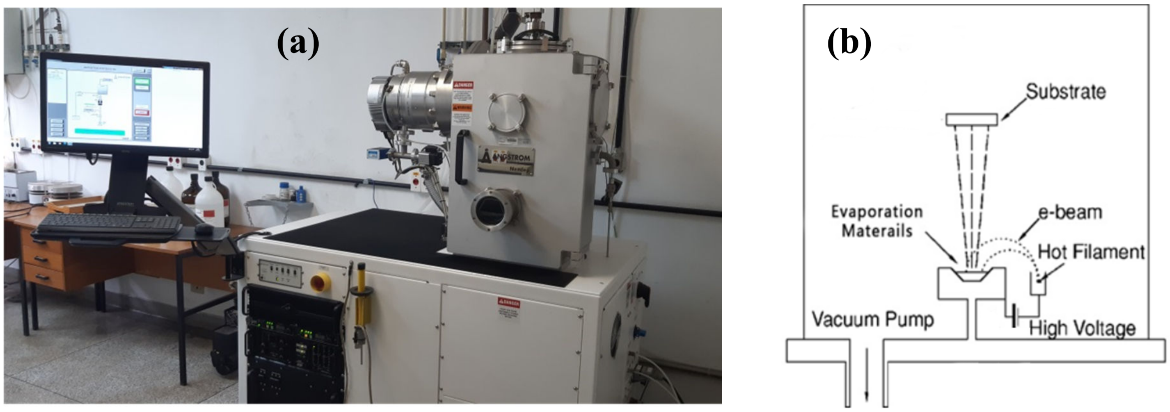

Figure 6-3: (a) E-beam deposition system with the deposition chamber (right), turbomolecular vacuum pump (center), control computer (left), and power + control units of the electron beam (bottom, in black). (b) Illustration of the e-beam evaporation process [154].

Good Ohmic contacts on n-type GaAs are usually obtained by deposition of thin metallic films of Ni, Ge, and Au. These metals were deposited sequentially with a respective thickness of 25, 50, and 150 nm (Figures 6-2-X) using the e-beam evaporator. The sample was then soaked in acetone to dissolve the photoresist pattern and remove the excess metal outside the original small windows (this step is called lift-off, Figure 6-2-XI) that were defined in the second lithography step. At the end of the process, all mesas have a small top contact and a common bottom contact between them (Figure 6-2-XII). To avoid formation of a Schottky barrier, which usually occurs when a metal is deposited directly on top of a semiconductor, the sample was then annealed in a RTA system (Figure 6-4-a) which consists basically of an oven—wherein the temperature can be ramped quickly—and a control computer. Since our samples are small, they are placed on a Si wafer resting on a quartz tray that slides into a quartz chamber in the oven unit. Two banks of 1 kW halogen lamps (Figure 6-4-b), eleven above the quartz chamber and ten below it, serve as a source of energy to heat the samples very quickly, allowing temperature ramps up to 200 °C per second. For our GaAs devices, the samples were heated to 520 °C at a rate of 100 °C/s, kept at this temperature for 30 s to get good Ohmic contacts, and then cooled as quickly as possible to stop further diffusion of the metals.

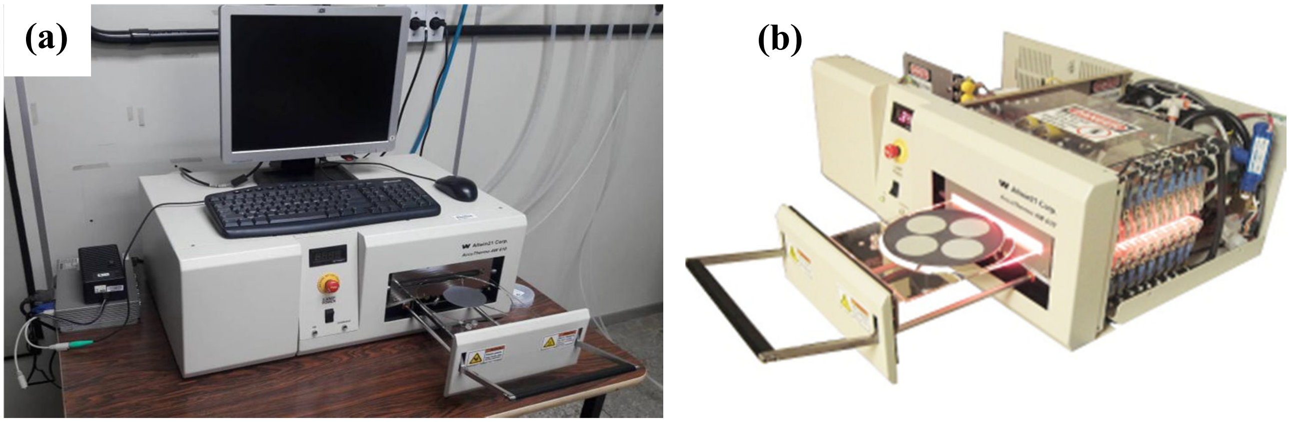

Figure 6-4: (a) Rapid thermal annealing system with a quartz tray and 3" Si wafer to lay the samples on. (b) RTA model AccuThermo AW 610 without its cover, showing top and bottom banks of 1 kW halogen lamps in the oven unit [155].

Using a probe station (Figure 6-5-a) connected to a semiconductor-parameter analyzer, the quality of each device was quickly checked (Figure 6-5-b) to decide which devices would be measured in more detail at lower temperatures. Finally, the sample was fixed in a commercial chip carrier (Figure 6-6-a) with a drop of liquid carbon paint to establish good thermal contact between the sample and the chip carrier. Then the best mesas were connected to the pads of the chip carrier with thin Au wires (diameter ϕ= 25 μm) using a wire bonder (Figure 6-6-b).

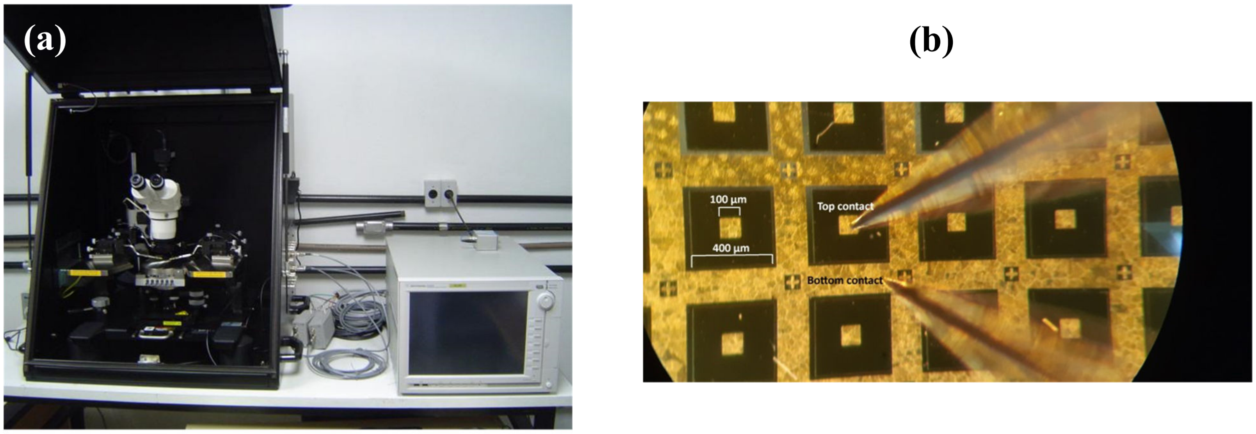

Figure 6-5: (a) Probe station equipped with four probes controlled by mechanical xyz translators, a microscope, and a CCD camera. The equipment is installed inside a grounded metallic box to reduce noise and allow measurements in the dark. The semiconductor parameter analyzer is connected to the four probes via low-noise triaxial cables enabling high sensitivity I×V curves. (b) Testing a mesa (black squares have an area of 400×400 μm^2) with two probes. One probe touches the top contact (gold squares have an area of 100×100 μm^2) while the other touches the bottom contact common to all mesas.

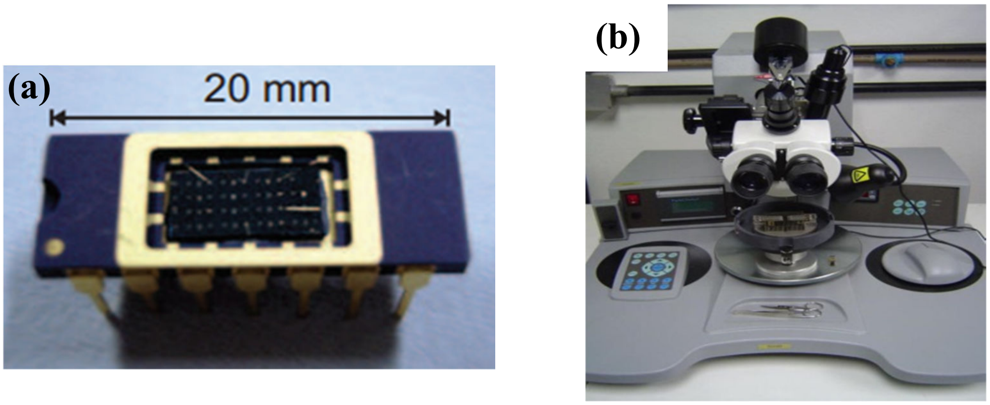

Figure 6-6: (a) Commercial chip carrier with a sample fully processed and connected. (b) Wire bonder used to connect the mesas to the chip carrier with thin Au wires (ϕ= 25 μm).

Finally, the chip carrier was installed on the cold finger of an optical cryostat (Figure 6-7) operating between 12 and 300 K with a closed-loop He circuit. After evacuating the cryostat and cooling the head to 12 K (everything takes around three hours), the device is ready for electro-optical characterization.

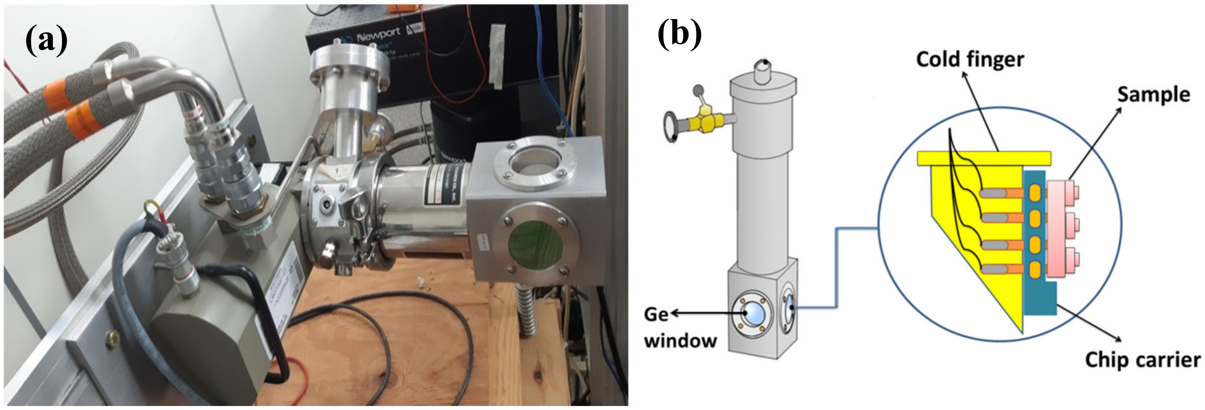

Figure 6-7: (a) Optical cryostat for 12-300 K operation with a Ge window; (b) Processed sample installed on the cold finger.

II -Electro-optical characterization:

6-3 Spectral response

Fourier-transform infrared (FTIR) spectroscopy is a technique for analyzing the optical response of photodetectors. The basic elements of an FTIR spectrometer are the infrared source, the Michelson interferometer (Figure 6-8), and the internal detector. To analyze the properties of our devices, the standard detector of the FTIR system is replaced by one of our fully processed samples (mounted inside the cryostat), but the rest of the internal system of the FTIR spectrometer is used normally. First, a source of infrared light is properly collimated to obtain a highly directional light beam which is then split into two beams using a beam splitter (Figure 6-8). One of these beams is reflected back on a fixed mirror, and the other one is reflected back on a moving mirror. When the two beams interfere, a modulated beam (called interferogram) is produced, which is then directed toward the window of the cryostat. The device under test absorbs a portion of the radiation, that depends on its internal composition and structure, and generates a photocurrent that is processed by the hardware and software of the spectrometer. The final step is to perform an inverse Fourier transform of this output interferogram to obtain the absorption spectrum of the device as a function of wavelength for different bias voltages. The transimpedance amplifier is used to apply an external bias voltage to the photodetector to be tested in the cryostat, to collect the current that is generated, and to feed it into the hardware of the FTIR system to be processed accordingly.

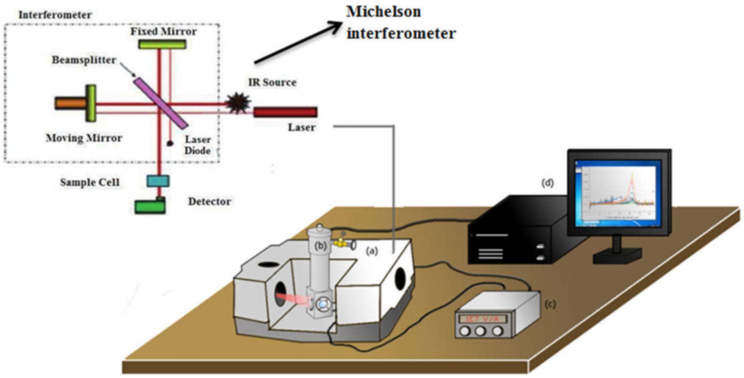

Figure 6-8: Experimental setup for the absorption measurements using FTIR spectroscopy [156]; (a) FTIR spectrometer; (b) Cryostat with a photodetector to be tested; (c) Transimpedance amplifier; (d) Computer.

6-4 Photocurrent measurements and black-body responsivity

Photodetectors are sensors able to convert an optical signal into an electrical signal and are made from a photoconductive material, i.e., generally a semiconductor. The efficiency of a photodetector is determined by calculating the ratio between its electrical output (photocurrent generated in the device) and optical input (number and energy of photons hitting the device per unit of time, generally coming from a calibrated black body), which is called black-body responsivity and is given by Equation 6-1 [157].

$$\mathrm{R} = I_{ph} / \int_{\lambda_1}^{\lambda_2} M_f \times T_{Ge} \times \frac{\Omega}{\pi} \times \epsilon \times (A_d - A_c) \times M_e(T,\lambda)\ d\lambda \qquad (6-1)$$

where I_{ph} is the measured photocurrent, M_f is the chopper modulation factor, T_{Ge} is the transmission of the Ge window of the cryostat, Ω is the solid angle sustained by the exit hole of the black body, A_d is the detector area, A_c is the top-contact area, $M_e(T,\lambda)$ is the black-body radiance, and λ_1 and λ_2 are the two wavelengths defining the FWHM of the spectral response (obtained by FTIR spectroscopy, as explained above). The photocurrent is generally measured using lock-in techniques that allow automatic subtraction of the dark current from the total current, leaving as the signal only the real photocurrent generated by the IR radiation hitting the device and originating from the black body set at 800 °C, as shown in Figure 6-9. Here, again, the transimpedance amplifier is used to set a bias on the device and collect the current that will be fed into the lockin.

The responsivity is the main parameter related to the efficiency of a photodetector, but it isn't enough when we want to compare two different photodetectors (of different nature or size) because it is then necessary to take account of some physical, geometrical, and technical factors which strongly influence the final performance of the devices.

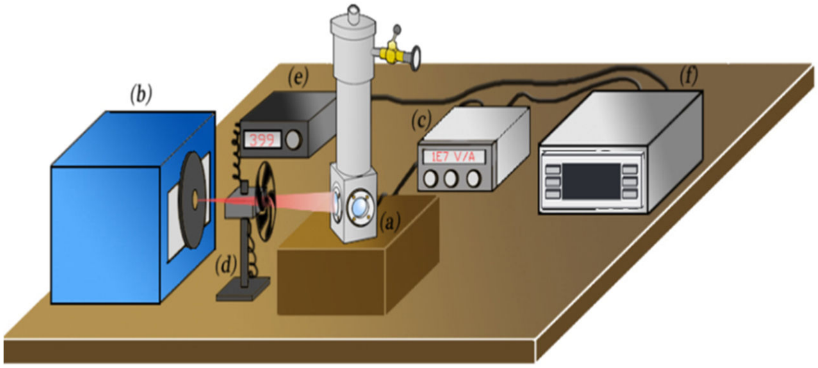

Figure 6-9: The experimental setup for photocurrent measurements (black-body responsivity) [156]. (a) Optical cryostat with the photodetector to be tested; (b) Black body at 800 °C; (c) Transimpedance amplifier; (d) Chopper; (e) Chopper controller; (f) lock-in.

6-5 Dark current

The dark current of a photodetector is the electrical signal measured in the device without the presence of any external IR (the device is kept in the dark). This current is a source of noise and usually determines the limitations of the performance of QDIPs [158, 159]. For most intersubband photodetectors, the dark current is generally much larger than the photocurrent itself, so the noise of such devices comes mainly from the fluctuations of the dark current. There are basically three sources of dark current: the first consists of electrons that are thermally excited to continuum states above the barrier (Figure 6-10-a). This effect depends exponentially on temperature and is usually the dominant component at temperatures above 50 K. The second source of dark current is field-assisted tunneling, where carriers are thermally excited to a higher excited state just below the top of the barrier, where they can tunnel through the triangular tip of the barrier into the continuum states (Figure 6-10-b). It is dominant at higher bias voltage, as the internal electric field—due to the applied bias—is able to bend the barrier potential and considerably reduce its width, allowing thus the carriers to tunnel through the tip. The last source of dark current is direct tunneling through the full width of the barriers, like in mini bands (Figure 6-10-c), which is more important at low temperatures and low bias voltage when the other mechanisms are weak (and if the barriers are not too thick).

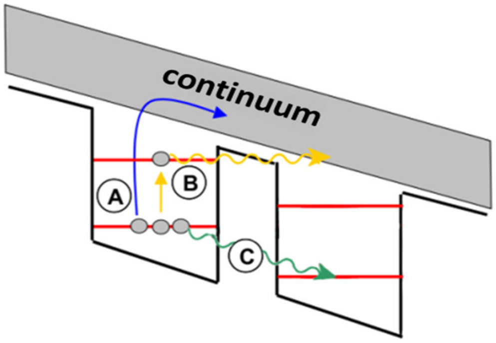

Figure 6-10: The main components of the dark current in a photoconductive photodetector: (a) thermally excited electrons above the barrier; (b) field-assisted tunneling; (c) direct tunneling. [156]

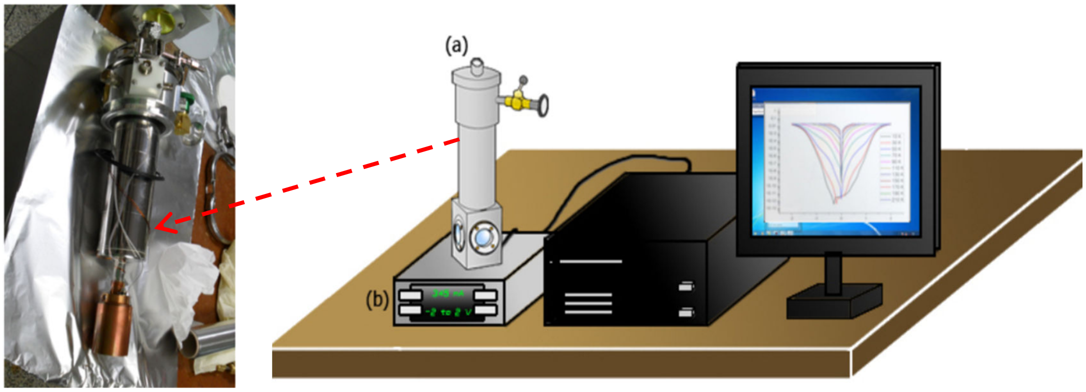

Figure 6-11: Experimental setup for the I-V curve experiment (dark current). (a) Cryostat fully mounted with a dark shield surrounding the sample; (b) Source-measure unit with attoampere sensitivity; (c) computer.

Figure 6-11 shows the setup for the dark-current measurements; the chip carrier containing the device was plugged into the socket of a cold-finger cryostat and surrounded by a copper shield to allow measurements in the dark. Since the dark shield was in thermal contact with the sample, it also served as a cold shield. The I-V curves were acquired by a sub-femto ampere source-measurement unit (Keithley 6430) remotely controlled by a computer running a homemade software developed with LabView.

6-6 Noise current

The noise current (noise of the device expressed as a current value) can be divided into several components, such as 1/f noise, shot noise, Johnson-Nyquist noise (also called thermal noise), and generation-recombination noise (also called GR noise). In general, in a QDIP, the first two types of noise are much smaller than thermal and GR noise and are therefore neglected, especially when the noise is measured far from the low-frequency region (the 1/f component is weak) and when the IR signal is strong enough (the shot noise can be neglected). In our case (photoconductive photodetectors), the total noise is usually dominated by the GR noise of the dark current, which is due to the random absorption of the background photons and to the random generation of thermally-excited electrons. Thermal noise is present in every resistive element and is caused by thermal agitation of the charge carriers. As a consequence, it is also present in a photoconductive device but is usually dominant only in photovoltaic photodetectors—as quantum-cascade detectors [160] where no external bias voltage is required and, therefore, the dark current is very weak.

The total noise current i_n measured in a QDIP contains both thermal and GR noise contributions [157] and is therefore given by Equation 6-2:

$$i_n^2 = i_{GR}^2 + i_{th}^2 = 4eg_nI_{dark}\,\Delta f + \frac{4kT\Delta f}{R} \qquad (6\text{-}2)$$

where k is Boltzmann's constant, Δf is the bandwidth used to measure the noise (i.e., the frequency span of the noise spectrum divided by the number of points), R is the resistance of the photodetector, T is the absolute temperature, e is the electron charge, g is the photoconductive gain, and I_{dark} is the dark current.

Although it would be more correct to measure the noise current during normal operation of the device (i.e., in the presence of the external IR of interest), since the dark current is usually much larger than the real photocurrent, the noise-current measurements of the literature are generally performed in the dark. Therefore, we will proceed in the same way, and a dark shield will be used around the devices, as was done for evaluating the dark current. For the noise measurements in the dark, the device is biased by a low-noise transimpedance amplifier, and its response (the dark current converted into a voltage by the transimpedance amplifier) is fed into a dynamic signal analyzer, which provides a frequency spectrum in real-time by calculating the Fourier transform of the input signal (Figure 6-12). The noise is analyzed in a frequency range of 100 – 1000 Hz to stay far from 1/f noise and to be in a flat and horizontal region of the spectrum that provides a good estimate of the noise.

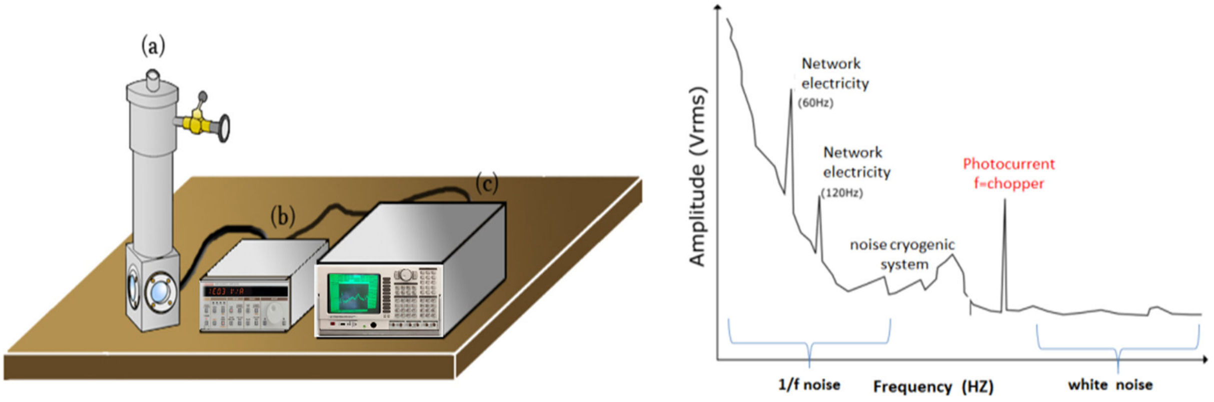

Figure 6-12: On the left is the experimental setup for the noise-current measurements. (a) Cryostat with a dark shield around the device under test; (b) Low-noise transimpedance amplifier; (c) Dynamic signal analyzer. On the right is a typical frequency spectrum of the total current obtained by the dynamic signal analyzer, showing the 1/f noise, the harmonics of the network, the noise from the cryogenic system, and the intrinsic noise from the device (white noise). The signal of the photocurrent (in red) is only observed when the noise measurements are performed together with the photocurrent measurements—i.e., no longer in the dark.

The noise experiment can actually also be performed during photocurrent measurements—i.e., no longer in the dark—by combining some of the equipment shown in Figures 6-9 and 6-12 to measure the real noise during the exposure to the IR. The advantage is that the photocurrent and noise can be measured simultaneously, which provides a simple and direct way to observe when the signal becomes comparable to the noise. This can be done with the black body, transimpedance amplifier, and chopper of the conventional photocurrent setup (Figure 6-9), and with the signal analyzer of the noise measurements (Figure 6-12), as shown in Figure 6-13. The noise can still be measured in the flat region of the frequency spectrum provided by the signal analyzer, as before, but now the photocurrent appears as a sharp peak at the chopper frequency superposed upon the noise spectrum (see right image of Figure 6-12). The intensity of the peak provides a direct reading of the photocurrent. Since the noise measurement of a signal depends on the frequency range used, it is generally more practical to measure the noise spectral density instead of just the noise. This is easily done on a dynamic signal analyzer by choosing the spectral-density option. In this case, the square of the noise is divided by the bandwidth Δf, and the unit of the noise current measured in such a way is $A/\sqrt{Hz}$. Two different measurements of noise-current spectral density can be unambiguously compared since they are already normalized by their respective noise bandwidth.

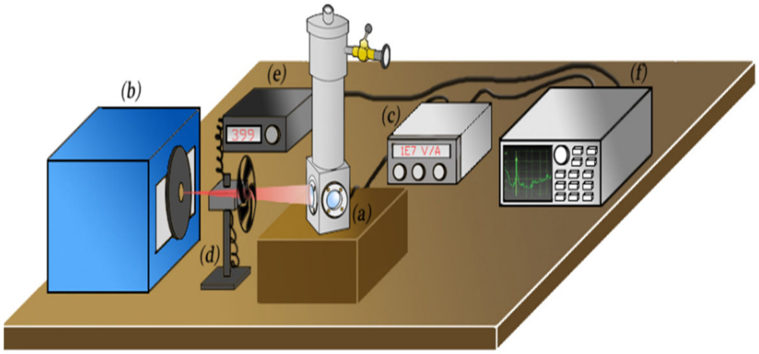

Figure 6-13: Experimental setup for simultaneous measurement of photocurrent and noise [156]. (a) Optical cryostat with the photodetector under test; (b) Black body at 800 °C; (c) Transimpedance amplifier; (d) Chopper; (e) Chopper controller; (f) Dynamic signal analyzer. The noise is measured in the flat region of the spectrum, and the photocurrent corresponds to the intensity of the sharp peak in the noise spectrum at the chopper frequency, as shown in Figure 6-12.

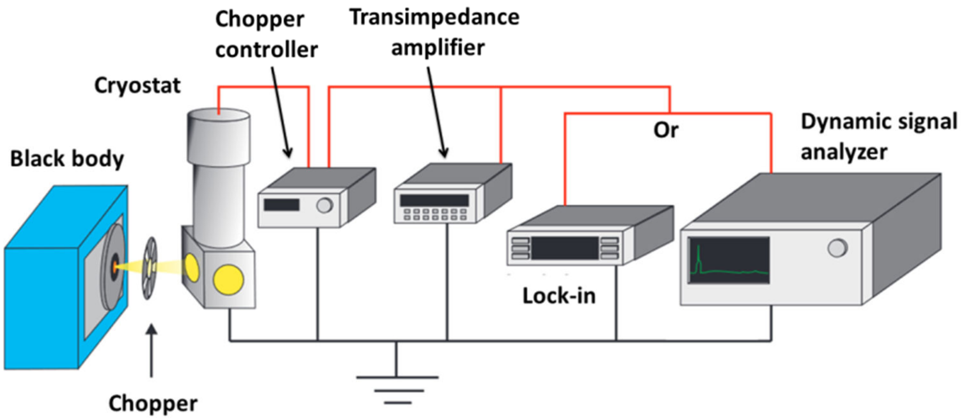

Figure 6-14: Two methods of measuring the photocurrent are shown in Figures 6-9 (using lock-in) and 6-13 (using dynamic signal analyzer).

6-7 Noise equivalent power and specific detectivity

The noise equivalent power (NEP) of a photodetector is the power of the optical signal impinging of the device that is required to get a signal-to-noise ratio of 1 [161]. NEP characterizes the smallest optical signal power that can be separated from a photodetector's noise, and is therefore associated to its sensitivity. The concept of detectivity was developed by Jones in 1958 [162] as a way to grade detectors, and was defined as the reciprocal of NEP. Thus, larger detectivities suggest superior detectors instead of using smaller NEPs—i.e., the change only represents a psychological benefit. Jones prefers the term "detectivity" because it avoids the word "sensitivity" which has multiple meanings in technical language. Detectivity, then, is the signal-to-noise ratio and therefore provides the final performance of the device given by Equation 6-3

$$D = R / i_n \qquad (6-3)$$

where R and i_n are the responsivity and noise current, respectively, of the device.

The detectivity of a photodetector depends on the noise bandwidth (Δf) of the measurement system and the detector's effective optical area (A) [161]. As a consequence, comparing the performance of various photodetectors based on their NEP or D only can be challenging. To address this issue, the specific detectivity (D*) is the figure of merit used to evaluate the ultimate performance of

IR photodetectors because it mitigates the impact of varying effective areas or noise bandwidth and takes account of several characteristics of the devices and experimental setups [163]. D* is generally used to compare detectors of different sizes and natures. Basically, it is calculated as [157, 164]:

$$D^{*} = R\sqrt{A}\Delta f / i_{n} \qquad (6-4)$$

where A is the effective optical area of the mesa (i.e., substracting the top-contact area) and Δf is the noise bandwidth. When the noise-current spectral density is provided instead of the noise current, Δf in the above formula must be set to 1. In that case, equation 6-4 can be written as:

$$D^{*} = R\sqrt{A} / i_{n} \qquad (6-5)$$

This equation was used to compare the performance of the six InAs/GaAs SML-QDIPs shown in the following chapter after they were processed and tested using the techniques and series of procedures and calculations described in this chapter.

Chapter 7: Optimization of InAs/GaAs submonolayer quantum dots infrared photodetectors

Infrared photodetectors based on InAs/GaAs SML-QDs grown in different growth conditions of temperature, As flux, and InAs coverage—previously examined by PL and X-STM—are tested in this chapter to determine how they influence the performance of QDIPs, especially when InAs/GaAs SML-QDs are grown with a (2×4) surface reconstruction achieved either at low temperatures with a low As flux or at high temperatures with a high As flux. For this reason, this set of 6 devices was divided into three groups—with a single parameter changed in each group, as presented in Table 7-1—to better understand their respective influence.

7-1 Design, growth, and processing

Molecular beam epitaxy was used to grow a full QDIP structure containing InAs/GaAs SML-QDs on top of an epi-ready undoped GaAs(001) substrate. Figure 7-1 shows the basic SML-QDIP structure that consists of two 1 μm-thick Si-doped GaAs layers (doping concentration $n=1\times10^{18}$ cm^{-3}) grown at 570 °C, acting as bottom and top contacts. Between them, the active region was formed by ten GaAs QWs, each surrounded by 45 nm-wide $Al_{0.1}Ga_{0.9}As$ barriers deposited at 580 °C. The inner part of each well was grown at 490 °C (except for sample #5, which was grown at 525 °C, as shown in Table 7-1) and started with 1.3 nm of GaAs followed by the SML-QDs—composed of six repetitions of a basic cycle formed by 0.5 ML of InAs and 2.5 MLs of GaAs—which were covered by 2.1 nm of GaAs. Each 2.5 MLs-thick GaAs spacer was Si-doped at 2×10^{18} cm^{-3} to provide the correct doping to the SML-QDs—to have two electrons in the ground state of each QDs—whose density was estimated from our X-STM measurements [142] to be around $4.3\times10^{11}\ \mathrm{cm}^{-2}$. Therefore, by doping each 2.50 MLs of GaAs at $2\times10^{18} cm^{-3}$, the equivalent 2D electron density is thus $6\times(2\times10^{18} cm^{-3}\times2.50\times2.83\times10^{-8}\,cm)=8.5\times10^{11}\,cm^{-2}$, which is twice the density of the SML-QDs. For sample #6 the basic cycle was 0.3 ML of InAs followed by 0.7 ML of GaAs.

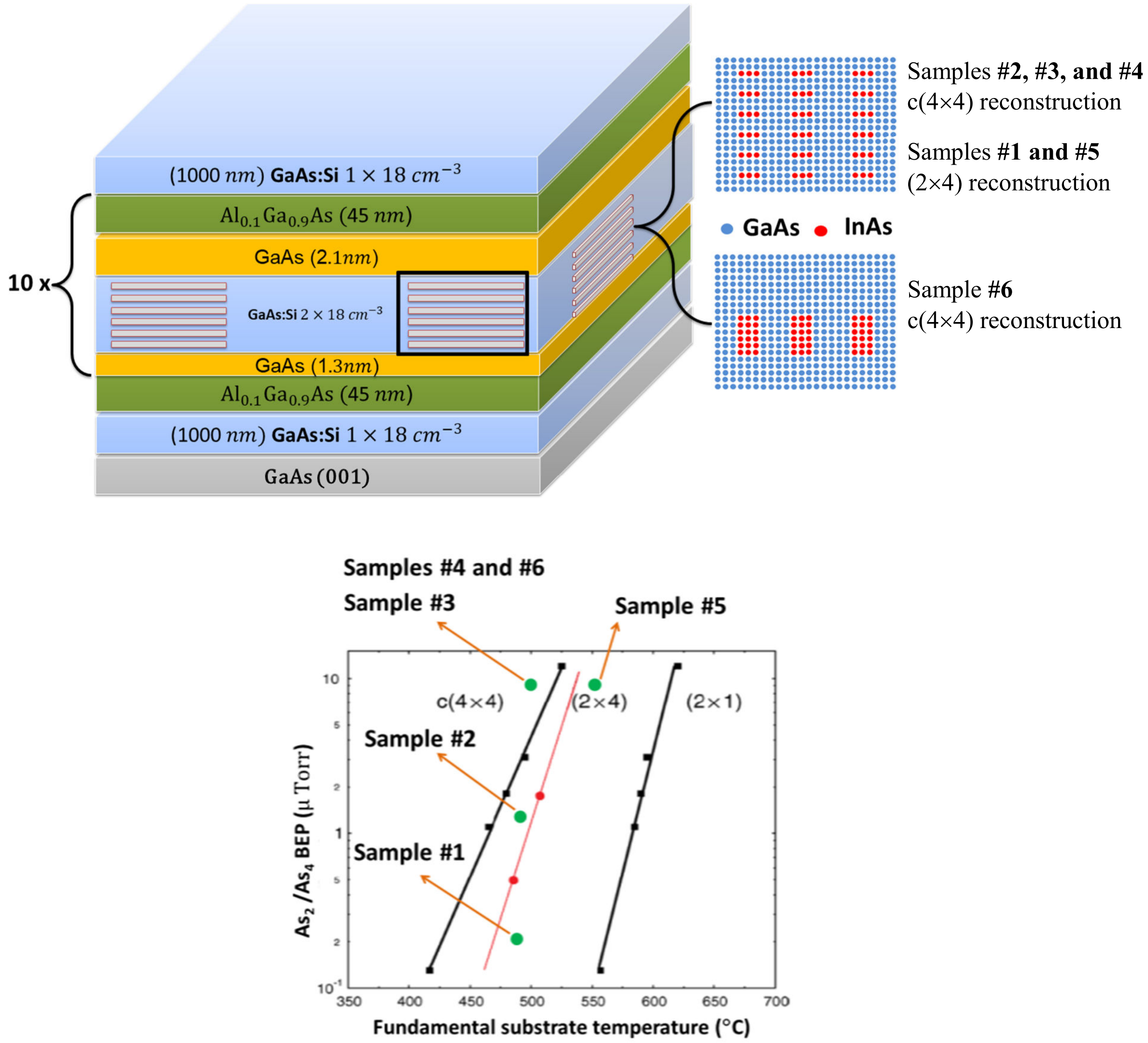

Figure 7-1: (top) Structure of infrared photodetectors based on InAs/GaAs SML-QDs. The black rectangle shows a single SML-QD formed by repeating six times the deposition of 0.5 ML of InAs followed by 2.5 MLs of GaAs:Si. (bottom) Phase diagram of the reconstruction of the arsenic-rich GaAs(001) surface where the red line indicates the transitions between the (2×4) and c(4×4) reconstructions as measured in our MBE system. The green dots indicate approximately the As flux and sample temperature used to grow the SML-QDs of devices #1 - #6, as shown in Table 7-1.

To minimize In desorption from the surface, the deposition of InAs has to occur at low temperature, generally below 515 °C [100]. So, after growing the AlGaAs barriers, the sample temperature was cooled to 490 °C, and the transition from the (2×4) to the c(4×4) surface reconstruction was observed around 520 °C.

For this reason, the As flux had to be significantly reduced to around 0.15 ML/s to recover the (2×4) surface reconstruction at low temperature for one of the samples [110]. In that specific case, since the growth must still occur under As-rich conditions to provide layers of good quality, the growth rate of InAs and GaAs in the samples of the first group—where only the As flux was changed—was set to 0.015 ML/s and 0.1 ML/s, respectively. Since the samples of the second and third groups were grown with a high As flux (see Table 7-1), the usual growth rates of InAs and GaAs for SK-QDs were used (i.e., 0.1 ML/s and 1.0 ML/s, respectively). *In-situ* RHEED was used to calibrate the growth rates of all materials and to accurately determine the transition between the c(4×4) and (2×4) surface reconstructions as a function of As flux and sample temperature.

	Device	**GR $_{\text{InAs}}$** (ML/s)	**GR $_{\text{GaAs}}$** (ML/s)	**As flux** (Torr)	**Growth T** (°C)	**SML-QDs cycle of InAs/GaAs** (MLs)	**Reconstruction**
Group 1	#1	0.015	0.1	**8.0E-8**	490	0.5/2.5	(2×4)
	#2	0.015	0.1	**1.3E-7**	490	0.5/2.5	c(4×4)
	#3	0.015	0.1	**7.0 E-7**	490	0.5/2.5	c(4×4)
Group 2	#4	0.1	1.0	7.0 E-7	**490**	0.5/2.5	c(4×4)
	#5	0.1	1.0	7.0 E-7	**525**	0.5/2.5	(2×4)
Group 3	#4	0.1	1.0	7.0 E-7	490	**0.5/2.5**	c(4×4)
	#6	0.1	1.0	7.0 E-7	490	**0.3/0.7**	c(4×4)

Table 7-1: Growth conditions of the InAs/GaAs SML-QDs used in groups 1, 2, and 3 of QDIPs analyzed in this chapter, whose structure is shown in Figures 7-1. Bold numbers refer to parameters that were changed in each group.

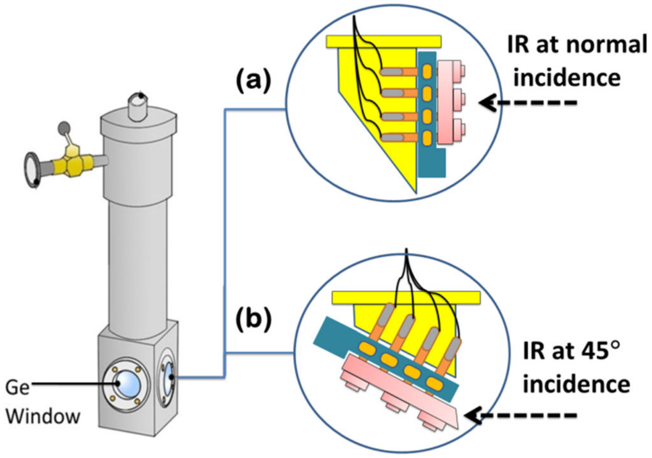

Figure 7-2: Sample installed on the cold finger of an optical cryostat having a Ge window (95% transmission in the 3-12 μm range) with the radiation reaching the mesas from (a) the top (normal incidence) or (b) with 45° incidence.

After growth, we processed the samples into small squared (400×400 μm^2) mesas using conventional lithography techniques, wet etching, e-beam metallization (Ni/Ge/Au, 25/55/150 nm), and RTA at 520 °C for 30 s to obtain good Ohmic contacts. Then the devices were glued on a commercial chip carrier (Figure 6-6-a), and the mesas were connected to the pads with thin Au wires (diameter = 25 μm) using a wire bonder (Figure 6-6-b). Finally, the chip carrier was installed on the cold finger of a closed-loop He cryostat having a Ge window (Figure 7-2) and operating between 12 and 300 K.

7-2 Group 1: Influence of the As flux and surface reconstruction at low growth temperature

The first group of photodetectors we will analyze consists of devices #1, #2, and #3, whose SML-QDs were grown under the same conditions as those of layers #1, #3, and #4 of sample #E, respectively, described in the X-STM and PL samples reported in Chapter 5. Therefore, we will refer to these results from time to time to interpret the experimental data obtained with these three SML-QDIPs. They have exactly the same structure as shown in Figure 7-1 and differ only in the value of As flux used during the formation of the SML-QDs (Table 7-1); device #1 was grown with a (2×4) surface reconstruction prior to InAs deposition (i.e., with a very low As flux), device #2 was grown with a slightly higher As flux and a c(4×4) reconstruction (just above the transition from (2×4) to c(4×4) that occurs at 1.2E-7 Torr), and device #3 was also grown with a c(4×4) reconstruction but with the much higher As flux generally used for SK-QDs.

The absorption spectrum was measured with a conventional FTIR spectrometer under normal incidence—i.e., with the radiation reaching the mesas from the top (Figure 7-2-a)—at 12 K and with a bias voltage between -3 V and +3 V. Figure 7-3-a shows that, for all three devices, there are two peaks at low bias. The broad one, at higher energy (lower wavelengths, near to 9.70 μm), is most probably related to a bound-to-continuum transition, from the ground state of the SML-QDs to the continuum above the $Al_{0.1}Ga_{0.9}As$ barrier (Figure 7-3-b). The second peak, which is narrower and located at a higher wavelength (11.57 μm), must be related to the bound-to-bound transition involving two confined states: the ground state of the SML-QDs and the first (and only) excited state of the AlGaAs/GaAs QW (Figure 7-3-b). At low bias voltage (0.2V), the bound-to-bound transition signal is weaker as the excited state of the QW is localized deeper in the potential. Most photocarriers don't have enough thermal energy to overcome the barrier, and the photocurrent under these conditions is dominated by the bound-to-continuum transition. However, as the bias increases, the $Al_{0.1}Ga_{0.9}As$ barrier is tilted (i.e., it becomes thinner), field-assisted tunneling through the tip of the barrier is much easier, and the bound-to-bound transition starts to dominate the spectrum. Considering that our goal in this chapter is to understand how these growth conditions affect the performance of the QDIPs, only their results at 12 K will be shown here to facilitate comparisons, since, at higher temperatures, their properties are dominated by thermal effects and they all follow the same trend of device #1.

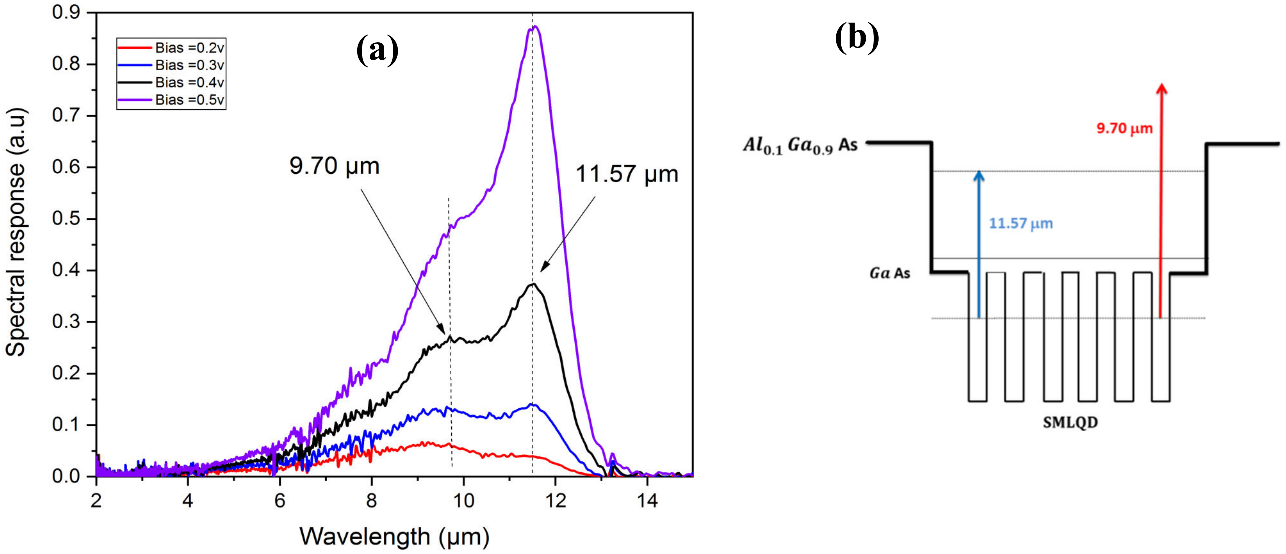

Figure 7-3: (a) Spectral response (photocurrent) of SML-QDIP #1 (devices #2 and #3 follow the same trend) at 12 K for bias voltages of 0.2-0.5V. (b) Band structure of the same device, and the possible electronic transitions.

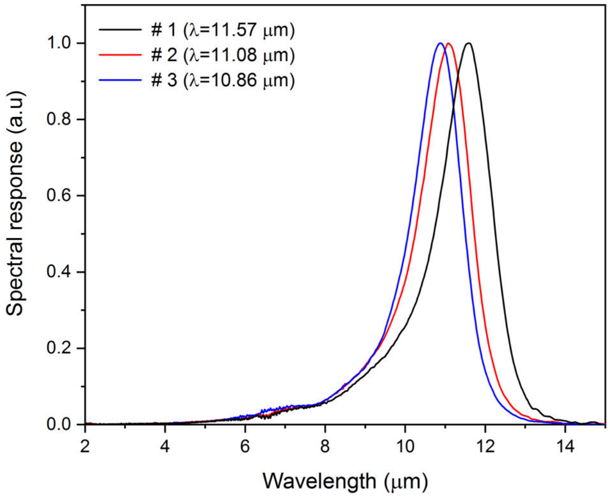

Figure 7-4: Normalized spectral response of SML-QDIPs #1, #2, and #3 obtained by FTIR in normal incidence at 12 K with a bias of +1.1 V.

Figure 7-4 shows the absorption spectrum of SML-QDIPs #1, #2, and #3 at 12 K for a bias voltage of 1.1 V. This bias was chosen because, as will be shown later, the maximum specific detectivity value was obtained at this bias. The three spectra (only one narrow peak for each device) were very similar but systematically blueshifted from device #1 to #3. As $\Delta\lambda/\lambda$ is around 0.13 for all of them, they involve a bound-to-bound transition. Since SML-QDs have a smaller size than conventional SK-QDs, they have only a single confined state [119], and the observed peaks are due to an electronic transition from the ground state of the SML-QDs to the first (and only) excited state of the GaAs quantum well. Going back to the X-STM images (Figure 5-8), they show that increasing the As flux produces larger InGaAs nanostructures with a higher In content, whose combined effect is to lower the energy of the electron ground state in the SML-QDs relative to the excited state of the GaAs quantum well, causing the blueshift shown in Figure 7-4.

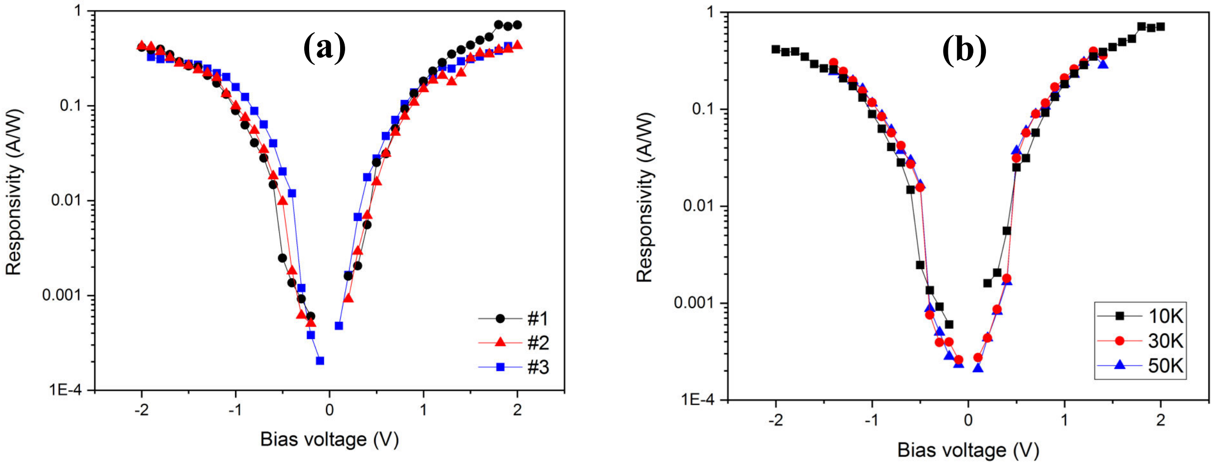

Figure 7-5: (a) Black-body responsivity of SML-QDIPs #1, #2, and #3 as a function of bias at 12 K. (b) Responsivity of SML-QDIP #1 as a function of bias voltage at different temperatures.

Responsivity measurements were used to determine the efficiency of the devices by taking the ratio of their electrical output (photocurrent generated in the mesas) to their optical input (power of the radiation falling on their optically active area). First, the spectral irradiance of the calibrated black-body (set at 800 °C) and the total incident power were estimated. Then, the total photocurrent of the devices facing the calibrated black body was measured using a dynamic signal analyzer (Figure 6-13) and allowed the calculation of the black-body responsivity reported in Figure 7-5-a. It can be seen that the curves of all devices are, once more, very similar and show a responsivity that monotonically increases up to a value of about 0.6-0.8 A/W at a bias voltage of +2V. Figure 7-5-b shows that the responsivity of device #1 (the other two devices follow the same trend) doesn't change much as a function of temperature, confirming that the doping of the structure was correct (2 electrons in each quantum dot in an attempt to get the ground state of all SML-QDs fully occupied).

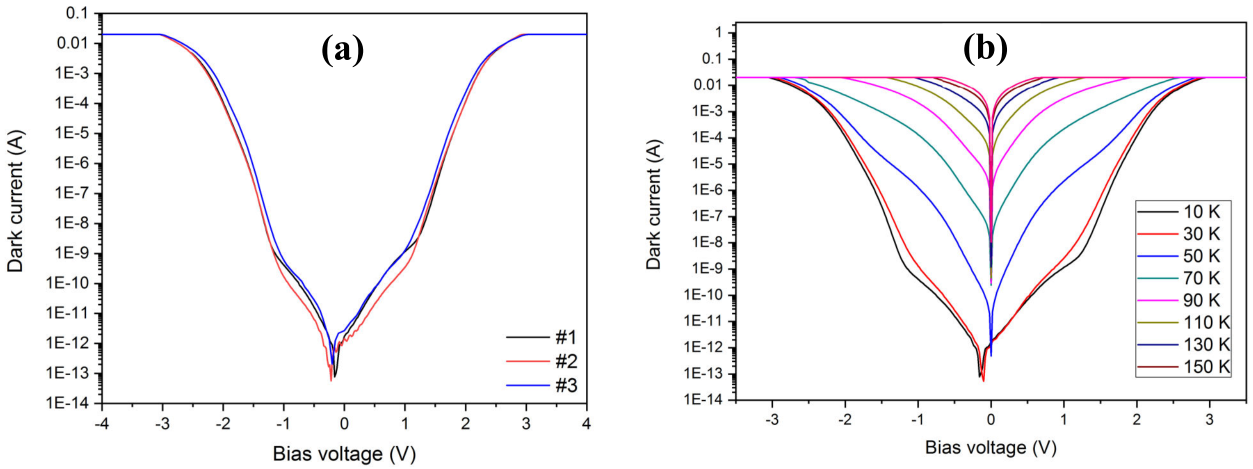

Figure 7-6: (a) Current versus voltage (I-V) curves in the dark (dark current) as a function of bias voltage for SML-QDIPs #1, #2, and #3 obtained at 12 K using a dark+cold shield. (b) Dark current of SML-QDIP #1 as a function of bias voltage at different temperatures.

Figure 7-6 shows the dark current of the three devices as a function of bias voltage at 12 K. Once again, one can observe that they have basically the same trends. At high bias, the exponential dependence of the current is due to field-assisted tunneling through the top of the $Al_{0.1}Ga_{0.9}As$ barriers which are distorted by the applied bias [159]. This is confirmed by the rather linear dependence (on a logarithmic scale) of the current which is due to the decrease in the effective barrier width through which the carriers can tunnel when the bias increases. Temperature-dependent measurements for device #1 (devices #2 and #3 follow the same trends) are reported in Figure 7-6-b, indicating that, at temperatures below 30 K, the dark current doesn't change significantly as a function of temperature. This suggests that the main dark-current mechanism may be related to direct tunneling through the QWs' barriers, since the carriers lack the thermal energy required to be excited over them. As the temperature rises (above 50 K), the carriers have sufficient thermal energy to overcome the $Al_{0.1}Ga_{0.9}As$ barrier directly and can contribute to the dark current, which increases very rapidly with temperature. Thus, above 50 K, the dark current was thermally activated [165], as could be seen by its exponential temperature dependence that yielded activation energies between 62 meV and 71 meV for SML-QDIP devices #1 to #3.

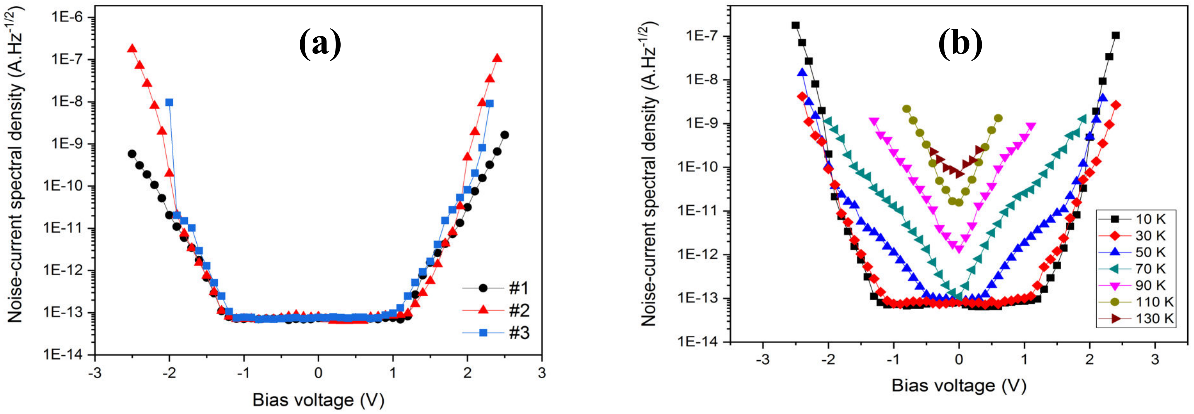

Figure 7-7: (a) Noise-current spectral density of SML-QDIPs #1, #2, and #3 as a function of bias voltage at 12 K with a dark+cold shield. (b) Noise density of the dark current of SML-QDIP #1 as a function of bias voltage for different temperatures.

The noise-current density was calculated by dividing the root-mean-square (RMS) noise current coming from the devices in the dark by the square root of the bandwidth (Δf) of the noise spectrum used by the spectrum analyzer to obtain a noise value that is independent of the experimental parameters (see Equation 6-2). In photoconductive photodetectors, the main source of intrinsic noise usually comes from the generation-recombination (GR) processes associated with the presence of the dark current [161], which is often several orders of magnitude larger than the photocurrent itself. Therefore, the noise curves are expected to show the same features as the dark current. Figure 7-7-a shows the noise current density of SML-QDIPs #1, #2, and #3 as a function of bias voltage at 12 K. The curves are very similar, and the noise is clearly limited at low bias by the intrinsic background noise of the experimental setup, around $7 \times 10^{-14}\ A/\sqrt{Hz}$. Then, as the bias increases, the noise rises considerably as a consequence of the strong increase of the dark current due to field-assisted tunneling through the AlGaAs barriers. When the temperature is increased, the noise curves of all devices are similar and evolve in the same way as the dark current [161, 165]. Figure 7-7-b shows that, below 50 K, the curves don't change significantly as was the case for the dark current. Above 50 K, the noise rises considerably due to the strong increase of the dark current due to thermal excitation of the carriers above the AlGaAs barriers.

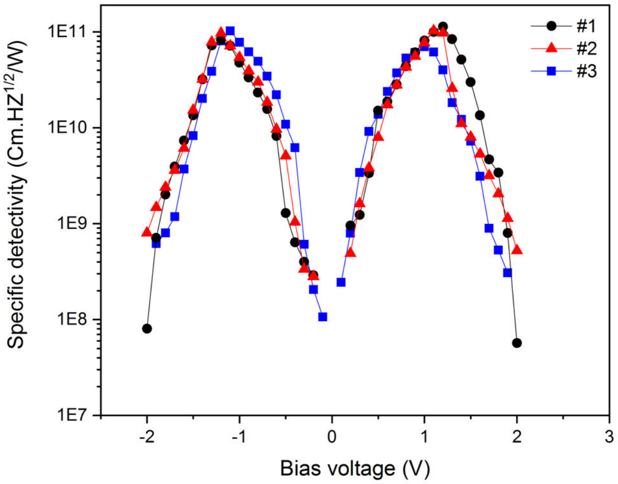

Figure 7-8: Specific detectivity (D*) of SML-QDIPs #1, #2, and #3 as a function of bias voltage at 12 K.

The specific detectivity (signal-to-noise ratio) of the devices was calculated as a function of bias voltage at 12K and is shown in Figure 7-8. Its value is defined as $D^* = R\sqrt{A}/i_n$, where R is the black-body responsivity, A is the optically active area of the mesas, and i_n is the noise-current spectral density. Although the responsivity increases monotonically up to ±2 V (Figure 7-5-a), the specific detectivity has a maximum at around ±1.1 V as a consequence of the strong increase of the noise beyond this bias voltage (Figure 7-7-a). The maximum specific detectivities of 1.13×10^{11} cm Hz$^{1/2}$ W^{-1}, 1.03×10^{11} cm Hz$^{1/2}$ W^{-1}, and 1.03×10^{11} cm Hz$^{1/2}$ W^{-1} were achieved in devices #1, #2, and #3, respectively.

7-2-1 Discussion of the results of the 1st group of samples

In view of the fact that the SML-QDs of devices #1, #2, and #3 were grown under the same conditions as layers #1, #3, and #4 (Figure 5-7) examined in Chapter 5, we will now discuss the device's results using the X-STM data shown in Figure 5-8. There, it can be seen that none of the different types of SML-QDs exhibited any vertical stacking of 2D InAs islands. Rather, small clusters of InGaAs material could be detected in a wider InGaAs QW—containing less In than the agglomerates themselves—but there was clearly no periodicity inside them. This is most probably a consequence of the strong segregation effect of the In atoms (which decreases slightly as the As flux increases), yielding values of R—calculated by counting the In atoms in empty-states X-STM images—equal to 0.83, 0.79, and 0.72 for devices #1, #2, and #3, respectively [142]. These values are in excellent agreement with experimental data from *in-situ* RHEED measurements performed in our group *in situ* during the deposition of InGaAs layers under the same conditions as those used for the SML-QDs investigated here [134].

Let's begin our discussion by determining whether the absorption signal in Figure 7-4 might be coming from the wider InGaAs quantum well and not from the SML-QDs themselves. The answer is very simple: all measurements reported in Figures 7-3 to 7-8 were performed at normal incidence (Figure 7-2-a), and it is well known that, in such conditions, intersubband transitions are prohibited in 2D systems due to polarization rules. This is why QWIPs always require an additional diffraction grating (or any other equivalent mechanism) on top of the devices to operate properly at normal incidence [166]. Because of that, there is no way that such high detectivity in the 10^{11} cm $\text{Hz}^{1/2}$/W range could be attributed to InGaAs QWs. Consequently, the strong signal measured in our SML-QDIPs can only be due to 3D confinement of carriers inside the In-rich clusters observed in the X-STM images (Figure 5-8), and the blueshift of the spectral response must be related to the size variation (or composition changes) of these clusters that behave as quantum dots [167].

Second, why is the performance of devices #1 to #3 similar if they were grown under very different growth conditions? More specifically, it is surprising that they perform similarly even though the density of SML-QDs increases roughly by a factor of ten from device #1 to device #3 [153]. The X-STM images showed that SML-QDs consist of small InGaAs agglomerates that contain slightly more indium than the thick InGaAs layer (but much less than usual SK-QDs) that surrounds them—indeed, the original GaAs material has been transformed into InGaAs precisely because of the presence of In segregation. The ground-state energy of such SML-QDs is therefore very close to the top of the potential barrier (Figure 7-3-b)—which was nominally the bottom of the GaAs conduction band—and the wave function of the confined electrons is only weakly localized. Since SML-QDs can reach extremely high areal densities (up to 10^{12} cm^{-2}) [142], their lateral separation can be very small (only a few nm), allowing their ground-state wave function to overlap the closest nanostructures [119]. Because of the Pauli exclusion principle, when an electron is confined in a specific SML-QD, the closest nanostructures will have a very low probability to be populated (at least by electrons having the same spin). Although an electron with the opposite spin could be accommodated in the ground state of the same SML-QDs, or in one of the closest SML-QDs, the same physical principle applies, and the other SML-QDs around will also have a very low probability to accommodate an electron with an antiparallel spin, leveling off the optical activity (and device performance) of samples having the highest densities of SML-QDs. The only way to solve this problem seems to reduce the In segregation during formation of the SML-QDs. In this way, the 2D InAs islands will hold longer, and the In content of the SML-QDs will increase, as well as their height (due to the stronger internal strain field, which allows a more effective vertical alignment). Consequently, the carriers become more confined, and their wave function will no longer spread outside the nanostructures, allowing us to benefit more from samples with higher densities of SML-QDs.

Another clue of the confinement capability of SML-QDs can be obtained by performing the black-body responsivity measurements with the IR impinging on the mesas with a tilted angle (Figure 7-2-b). A 45° facet was ground and polished on one edge of the samples (Figure 7-9), and the black-body radiation was shone perpendicularly to its surface. Using a linear polarizer, s- and p-polarized light could be selected with their polarization vector being parallel (s) or perpendicular (p) to the epitaxial layers (i.e., the mesas) to probe the carrier confinement along the lateral (s) and vertical (p) directions of the QDs. In our case, the maximum s/p ratio (obtained by measuring the responsivity with each polarization) of devices similar to SML-QDIPs #1 and #3 was between 25% and 40%, which is higher than for conventional SK-QDs (13-15%) and quantum wells (2.8%) [105].

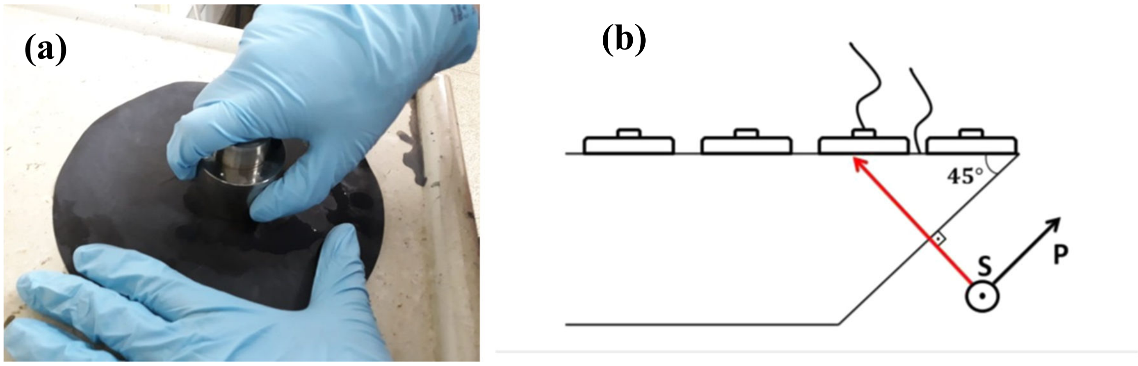

Figure 7-9: (a) Grinding and polishing of the sample facet with a 45° angle; (b) Geometry of samples used for optical measurements performed at 45° with s- and p-polarized radiation [115].

From this, we can conclude that, although these three devices were grown in the presence of a very different As flux which led to very different densities of nanostructures, In incorporations, and In contents, their overall properties are very similar. The simple growth conditions of SML-QDIP #3—similar to those for usual SK-QDs leading to c(4×4) surface reconstruction—were able to provide a high density of nanoscopic InGaAs agglomerates and a device with good performance, despite the fact that such growth conditions should not lead to the formation of 2D InAs islands that are necessary to form SML-QDs. On the other hand, depositing the InAs submonolayers on a (2×4)-reconstructed surface requires much more difficult growth conditions and was expected to form true 2D InAs islands. However, we observed only a lower density of smaller In-rich InGaAs clusters together with a low In content and In incorporation resulting from the very low As flux. Nevertheless, device #1 had properties similar to those of devices #2 and #3. Comparing devices #1 and #2, which had a close As flux but different surface reconstruction, suggests that an additional physical phenomenon is responsible for the fact that both contain In-rich agglomerates dispersed in a wider InGaAs QW, although the former was supposed to nucleate small 2D InAs islands and the latter was not. Therefore, it is reasonable to speculate that In segregation is responsible for partially destroying most 2D InAs islands, allowing the In atoms to be incorporated later in the sample to form the InGaAs QW as well as the In-rich clusters. Consequently, limiting segregation could be a way to keep more In in the

2D islands and form real SML-QDs in the presence of the (2×4) surface reconstruction. Since In segregation in the InAs/GaAs system is a thermally activated process with an activation energy of around 0.1 eV, reducing the sample temperature during growth is the easiest way to limit segregation [144, 168]. Of course, this may also reduce the crystalline quality of the sample, and a compromise will thus be necessary. Only then it may be worth using the more difficult growth conditions of device #1 to achieve better results.

7-3 Group 2: (2 × 4) surface reconstruction achieved with other growth conditions

InAs usually needs to be deposited on GaAs at temperatures below 515 °C to limit the evaporation of In atoms from the surface [169]. Additionally, when the InAs growth rate is very low (e.g., 0.015 ML/s as for device #1 discussed above), the sample temperature is further lowered (below 500 °C) because the evaporation rate can no longer be neglected. For this reason, the growth temperature of the SML-QDs of device #1 was chosen to be 490 °C. At such a low temperature and in the presence of a usual As flux, the surface reconstruction is always c(4×4) and doesn't allow nucleation of small 2D InAs islands required for the formation of SML-QDs. To recover the (2×4) surface reconstruction usually present at higher temperatures, the As flux needs to be significantly reduced. However, it has been shown that, in the presence of such a low As flux, In incorporation is less than unity and In segregation increases [142, 170], resulting in In-rich clusters that are smaller, contain less In, and have a lower areal density than in device #3. In spite of that, devices #1 and #3 show the same performance, and one may wonder whether, under more idealistic conditions, a device obtained with a (2×4) surface reconstruction could outperform the other devices.

There is actually another way to obtain a (2×4) surface reconstruction: instead of lowering the sample temperature from 570 °C to 490 °C, which invariably switches the reconstruction from (2×4) to c(4×4) at around 520 °C, one could keep the sample slightly above this value (around 525 °C) to avoid the change of reconstruction (Figure 3-16). Under such conditions, the As flux and the growth rates of In and Ga wouldn't need to be reduced, and the In incorporation would be unity again [170]. The only drawback is that In segregation and evaporation become larger at higher temperatures [168]. Nothing can be done to prevent the former, but the latter can be taken into account by calibrating the InAs growth rate at the same temperature. SML-QDIPs #4 and #5 form a second group of samples and have exactly the same structures as former devices of group 1 (Figure 7-1). Sample #4 acts as a reference for group 2. It was grown with the usual growth parameters used for SK-QDs (i.e., c(4×4) surface reconstruction, high As flux, and moderate InAs and GaAs rates) but at 490 °C, as for the previous samples. Sample #5 was obtained under the same growth conditions, except that the SML-QDs were grown at a higher temperature (525 °C), as shown in Table 7-1.

Figure 7-10 shows the spectra of SML-QDIPs #4 and #5 at 12 K. The absorption spectrum of device #5 is broader and redshifted (λ_{max}=10.4 µm) compared to device #4 (λ_{max}=8.9 µm). The redshift is probably related to stronger In segregation—and possibly high surface evaporation as well—that decreases the overall In content and increases the bandgap of the material inside the nanostructures [171, 172]. The broader peak might be due to a narrowing of the SML-QDs grown at a higher temperature—which usually increases quantum effects—but this is unlikely because higher sample temperature increases surface diffusion and, consequently, should also increase the lateral size of the 2D InAs islands [100]. Therefore, the broader peak is probably due to a more inhomogeneous size distribution of the In-rich clusters (unfortunately, X-STM images of this sample are not yet available).

Figure 7-11 shows that the black-body responsivity of SML-QDIP #5 is typically ten times higher than that of reference device #4 at the same voltage bias. Since they were measured under the same experimental conditions and have the same geometry, this means that device #5 grown in the presence of the (2×4) reconstruction obtained at higher temperatures produces an output signal ten times higher than the same device obtained with a c(4×4) reconstruction (device #4).

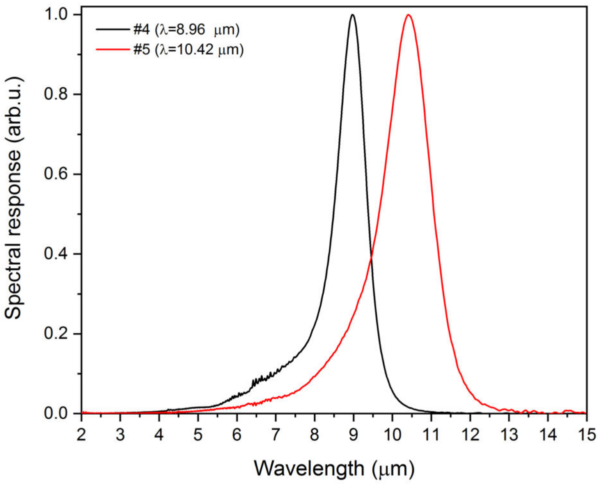

Figure 7-10: Normalized spectral response of SML-QDIPs #4 and #5 obtained by FTIR in normal incidence at 12 K.

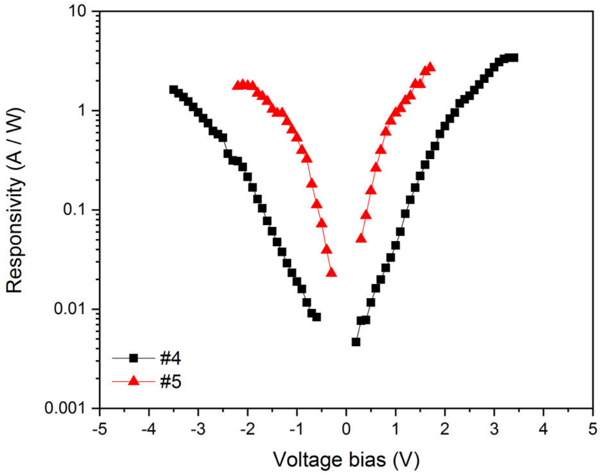

Figure 7-11: Black-body responsivity of SML-QDIPs #4 and #5 under normal incidence as a function of bias at 12 K.

Figure 7-12-a shows that the dark current of SML-QDIP #5 is much higher than that of device #4, which is consistent with the higher ground-state energy of those SML-QDs, as suggested in Figure 7-10. Based on temperature-dependent I-V measurements at a fixed bias (usually close to 0 V), the activation energy was calculated to be 85 and 57 meV for SML-QDIP #4 and #5, respectively, using the Arrhenius equation [173]:

$$I = I_0 \times e^{-E_{activ}/kT} \qquad (7\text{-}1)$$

Taking the log of the equation above, $\log(I) = \log(I_0) - \frac{\log(e) \times E_{activ}}{k} \frac{1}{T}$

Therefore, in a log(I) × 1/T graph (called Arrhenius plot), the slope of the curve will be given by:

$$Slope = -\frac{\log(e) \times E_{activ}}{k}$$

where I is the dark current, I_0 is a constant, k is Boltzmann constant, T is the absolute temperature, and E_{activ} is the activation energy of the process. Since Si doping was the same in both samples and the activation energy is the difference between the Fermi energy (not to be confused with the ground-state energy of the SML-QDs) and the top of the AlGaAs barriers [174], the lower activation energy could be due to a low In content or a smaller size of the SML-QDs of device #5, as mentioned previously. However, it could also result from excessive doping due to a lower density of nanostructures (the doping was calibrated for sample #4) or structural defects compared to sample #4.

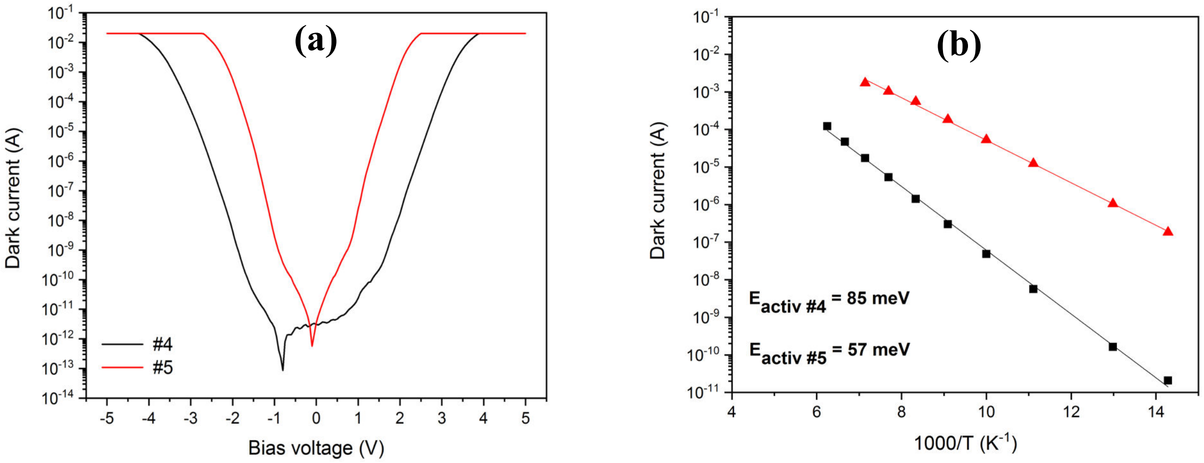

Figure 7-12. (a) Current versus voltage (I-V) curves in the dark (dark current) as a function of bias voltage for SML-QDIPs #4 and #5 obtained at 12 K using a dark+cold shield. (b) The dark current as a function of temperature is presented in an Arrhenius plot to calculate the activation energy for SML-QDIPs #4 and #5 at a bias close to 0 V (actually 0.05V).

The noise-current spectral density ($\frac{i_n}{\sqrt{\Delta f}}$) of both devices as a function of the bias voltage is reported in Figure 7-13. At low bias, the signal was limited by the noise floor of the experimental setup, which prevents any measurement below 4×10^{-14} A $Hz^{-1/2}$. Above this plateau, at higher bias, the noise-current curve follows the same trends as the dark current, since the generation-recombination noise of the dark current is the main noise source in the photodetector (Figure 7-12-a).

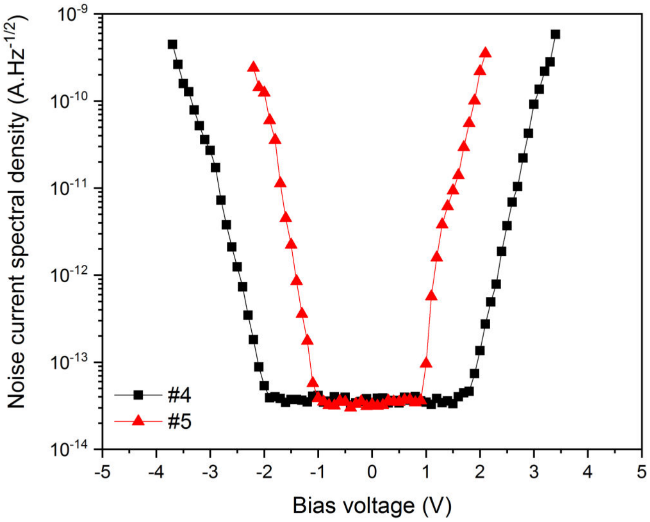

Figure 7-13: Noise-current spectral density of SML-QDIPs #4 and #5 as a function of bias voltage at 12 K with a dark+cold shield.

Figure 7-14 shows that device #5, grown with a (2×4) surface reconstruction at higher temperature, shows a maximum specific detectivity of 8.3×10^{11} cm $Hz^{1/2}$ W^{-1} at 0.9 V, which is 2.5 times higher than that of the reference device SML-QDIP #4 (3.67×10^{11} cm $Hz^{1/2}$ W^{-1} at 1.8 V) that was grown at 490 °C in the presence of a c(4×4) reconstruction. This is mainly because the noise floor of SML-QDIP #5 is twice narrower than that of the other device, and the onset of its noise occurs at a bias (± 1V) where the responsivity of the (2×4) device is much higher than that of the reference c(4×4) device.

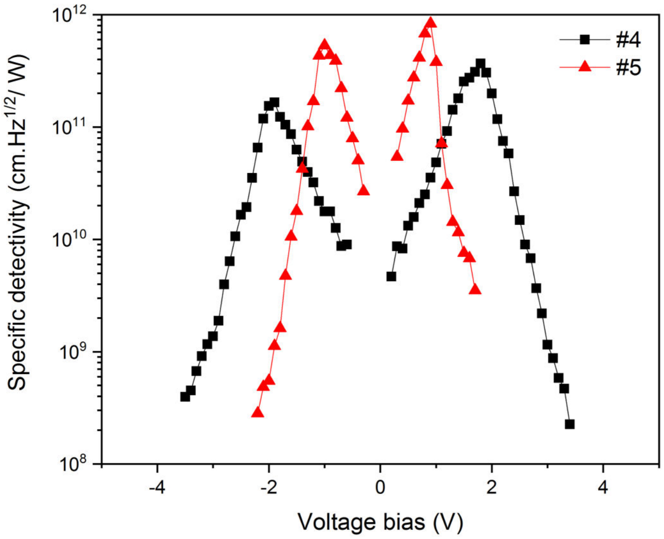

Figure 7-14: Specific detectivity (D*) of SML-QDIPs #4 and #5 as a function of bias voltage at 12 K.

7-3-1 Discussion of the results of the 2nd group of samples

Before discussing the reasons of the better performance of SML-QDIP #5, let's first briefly compare the differences between devices #3 and #4 that were used as references for their respective groups. The SML-QDs of device #4 were deposited with growth parameters commonly used for SK-QDs. The nanostructures of device #3 were grown under almost the same conditions, except that the growth rates of InAs and GaAs were much lower, to compare device #3 with devices #1 and #2. Thus, it can be seen that the simple fact of growing SML-QDs faster was sufficient to improve the performance of device #4 by a factor of 3 (compared to sample #3), while changing the As flux by a factor of 10 had not much influence on the final performance of the first group of devices (#1 to #3), despite the many changes already reported (different surface reconstructions, QD densities, In incorporation, segregation, etc.). This is probably because the growth rates of InAs and GaAs have been shown to influence surface diffusion and segregation, leading to lower segregation as the rate increases [175]. This may indicate that In segregation is indeed the villain to defeat when trying to improve the performance of SML-QDs and related devices. However, we should also not lose sight of the fact that both samples were grown with a high

As flux—i.e., in the presence of a c(4×4) surface reconstruction—and therefore should not lead to the formation of 2D InAs islands and SML-QDs [48, 176].

Comparison of SML-QDIPs #4 and #5 shows that, unlike in group 1 where the (2×4) and c(4×4) devices had similar performance, in group 2 the (2×4) reconstruction provided a superior SML-QDIP. Since both devices have the same As flux and growth rates of InAs and GaAs, this difference could be attributed to the surface reconstruction. Of course, this is not completely correct, as the (2×4) reconstruction could only be achieved by keeping the sample temperature just above the (2×4) to c(4×4) transition, i.e., 525 °C in device #5 instead of 490 °C in device #4. A lower temperature usually creates a higher density of structural defects [143] that act as non-radiative recombination centers and therefore contribute to worsening the optical properties of the nanostructures in device #4. However, the most relevant difference between the two samples is the (2×4) surface reconstruction used in device #5, which is expected to nucleate true 2D InAs islands on the GaAs(001) surface instead of forming a random InGaAs Alloy when the c(4×4) reconstruction is preferred. Although we might expect stronger segregation and In evaporation at higher temperatures [149], In incorporation is back to unity (due to the As flux that is now much higher than in sample #1), and the higher growth rates of InAs and GaAs should contribute to limit the increase of In segregation [177]. As a result, we might expect to have now 2D InAs islands (device #4 doesn't have any) with a higher In content than in device #1, which could contribute to increasing the strain field around the remaining 2D islands and improve their vertical alignment. However, from the redshift observed in Figure 7-10, one can deduce that their average In content is probably still less than in device #4.

Finally, it would be interesting to compare also devices #1 and #5, which were both grown with a (2×4) surface reconstruction—this is actually their only common feature, as all other growth parameters are different. It can be seen that device #5 has a detectivity 8 times higher than the other device. The reasons for this are similar to those already mentioned above: its growth temperature is higher (525 instead of 490 °C), leading to a lower density of structural defects [143]. Such a higher temperature should slightly increase In evaporation and segregation, but higher InAs and GaAs growth rates should contribute to limiting the latter effect.

Last but certainly not least—on the contrary—the high As flux required to achieve the (2×4) reconstruction at a high temperature sets the In incorporation back to unity, increasing considerably the In content of the layers of interest. Hopefully, that should result in the formation of more robust 2D InAs islands able to stack and form more realistic SML-QDs, as usually sketched (Figure 2-10).

SML-QDIP #5 studied here is the first one ever grown with the (2×4) surface reconstruction achieved at high growth temperature, and no optimization of its growth conditions was performed. In spite of this, it has the highest detectivity (8.3×10^{11} cm $Hz^{1/2}$ W^{-1}) among the QDIPs of our group and one of the highest in the literature at such low temperatures; therefore, optimizing the growth conditions may have a positive effect on its performance. Since the detectivity is the ratio of the device responsivity to its noise, any improvement in either characteristic will improve the value of the detectivity.

7-4 Group 3: Influence of the thin GaAs interlayer

We have seen in the previous group of samples that increasing the In content of the small 2D islands is vital to create a stronger strain field and to vertically align the structures from consecutive InAs submonolayers. Instead of trying to increase the In content by controlling In segregation, evaporation, and incorporation, one could find a way to use the existing strain field more effectively—e.g., by reducing the thickness of the GaAs interlayer. For instance, using a basic cycle of 0.5/1.5 MLs of InAs/GaAs instead of 0.5/2.5 (as we did so far, see paragraph 5-8), the 2D islands of the next InAs submonolayer would be twice closer and would thus sense a stronger strain field. Concomitantly, it would also increase the average nominal In content in the layers from 16.6% to 25%, and the In content of the SML-QDs themselves from 33.3% to 50% (see Figure 5-10). A more radical proposal would be to use cycles containing 0.5 ML of InAs followed by 0.5 ML of GaAs, i.e., the InAs islands are stacked on top of each other without any GaAs material in between. In such a case, the average nominal concentration in the layers would be 50% and that inside the SML-QDs would be 100%. Unfortunately, the critical thickness for this type of structure is considerably reduced (due to the much higher In content), and it is no longer possible to grow

18 MLs of such an alloy as before (18×[0.5/0.5] instead of 6×[0.5/2.5]) without relaxing the layers (and creating a high density of structural defects), as seen in Chapter 5. Therefore, we decided to reduce the fraction of InAs deposited in each layer (0.3 ML instead of 0.5 ML), and we kept the same number of repetitions as before (six). As a consequence, the last device, called SML-QDIP #6, was grown in the same conditions as device #4—i.e., at 490 °C in the presence of a c(4×4) surface reconstruction and with a high As flux and higher InAs and GaAs growth rates as shown in Table 7-1—and its structure is shown in Figure 7-1. *In-situ* RHEED and PL measurements showed that, in such conditions, the InAs/GaAs system was kept below the critical thickness, and the layers exhibited excellent optical quality.

The spectral response of devices #4 and #6 was investigated by FTIR spectroscopy and is shown in Figure 7-15. It can be observed that the absorption peak of device #6 is broader and blueshifted when compared to device #4. The broader peak is mainly related to stronger quantum effects due to the smaller size of SML-QDs in device #6. The shorter cycle of 6 MLs (6 × (0.3/0.7)) instead of 18 MLs (6 × (0.5/2.5)) reduces the AlGaAs/GaAs quantum well width from 85 Å to 51 Å, resulting in a QW that does not have any excited state, unlike in device #4. As a consequence, the broader peak is related to a bound-to-continuum transition from the ground state of the SML-QDs to the continuum above the $Al_{0.1}Ga_{0.9}As$ barrier (Figure 7-15-b). Of course, a broader size distribution of the nanostructures could also contribute to a broader absorption spectrum. The blueshift can be explained by the richer In content (nominally, 100% instead of 33% in device #4), which lowers the gap of the SML-QD material and thus increases the transition energy from their ground state to the continuum above the $Al_{0.1}Ga_{0.9}As$ barrier. This effect clearly overcomes the influence of their smaller size—both laterally, due to the smaller InAs coverage, and vertically, due to the shorter period of the basic cycle—which should actually increase their ground-state energy and, consequently, lower their transition energy. It should be noted that, in Figure 7-15, the curves are normalized, for the sake of comparison. Actually, the signal of SML-QDIP #6 is around ten times lower than that of device #4, which is consistent with a bound to continuum transition.

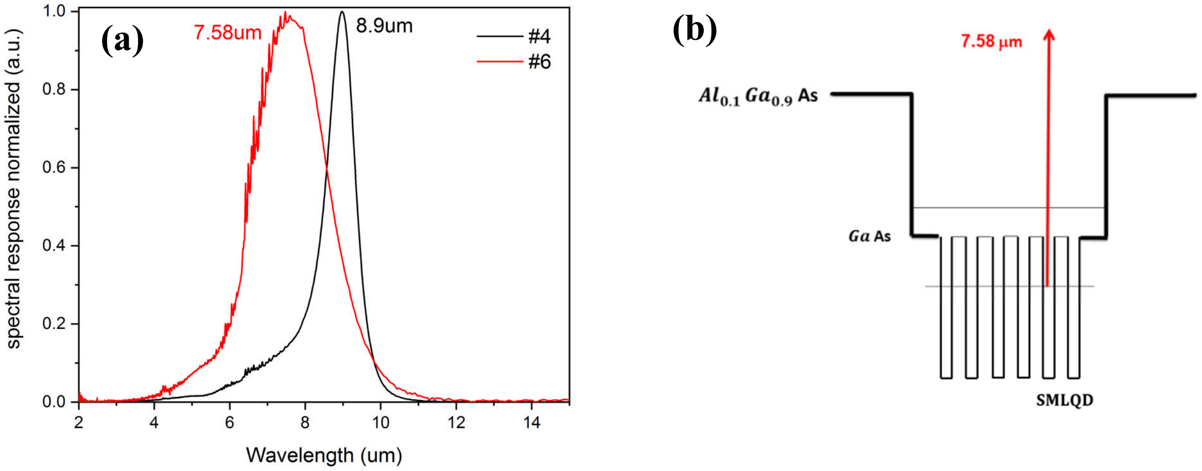

Figure 7-15: (a) Normalized spectral response of SML-QDIPs #4 and #6 obtained by FTIR under normal incidence at 12 K for a bias voltage of 1.8 V. (b) Band structure of device #6 and the possible electronic transitions.

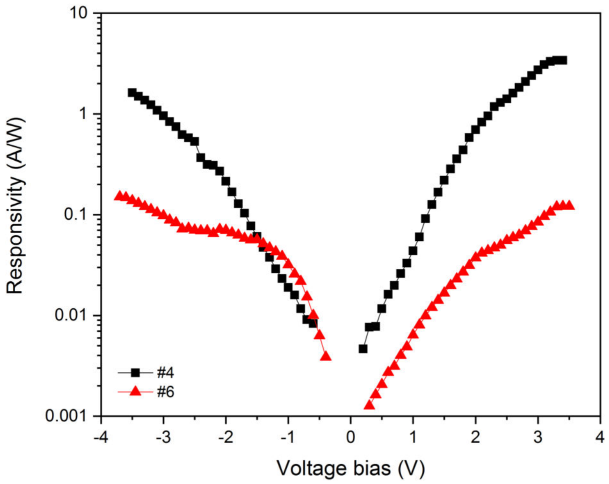

Figure 7-16: Black-body responsivity of SML-QDIPs #4 and #6 under normal incidence as a function of bias at 12 K.

Figure 7-16 shows that, for a given bias, the responsivity of device #6 is generally much lower than that of device #4, which follows the same trends as the intensity of the absorption curves shown in Figure 7-15, wherein the photocurrent of SML-QDIP #6 is ten times lower than that of device #4. It means that device #4 provides a stronger output signal than device #6 under the same experimental conditions.

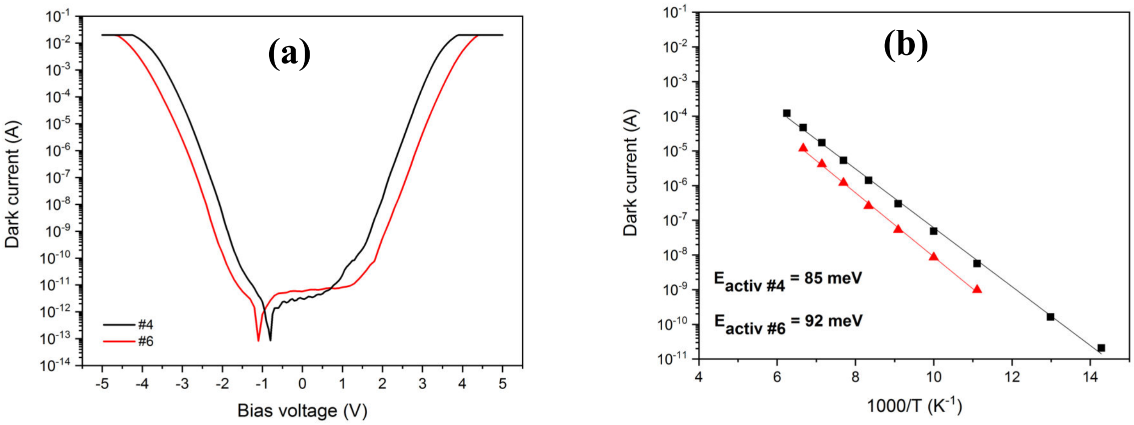

Figure 7-17: (a) I-V curves in the dark (dark current) as a function of bias voltage for SML-QDIPs #4 and #6 obtained at 12 K; (b) Arrhenius plot of the dark current as a function of temperature to calculate the activation energy of SML-QDIPs #4 and #6 at a bias of 0.05V.

Figure 7-17-a shows that the dark current of device #4 is generally higher than that of device #6, which is consistent with the higher ground-state energy of those SML-QDs as suggested in Figure 7-15. To confirm this, I-V curves were measured in the dark as a function of temperature (not shown here), and an Arrhenius plot of the dark current at a fixed bias voltage (Figure 7-17-b) was used to calculate the activation energy, which can be obtained from the slope of the linear section of the data above 70 K. It can be seen that the activation energy of device #4 (85 meV) is smaller than that of device #6 (92 meV), which explains its higher dark current. The plateau at low temperatures and bias is due to direct tunneling through the full thickness of the barriers.

The noise current spectral density ($\frac{i_n}{\sqrt{\Delta f}}$) was measured with a signal analyzer, far from the 1/f noise region, in a region of the spectrum where the noise shows a plateau (white noise). Figure 7-18 shows that both noise curves are similar. At low bias voltage (-2 V to +2 V), the noise is limited by the intrinsic background noise of the experimental setup, around $3 \times 10^{-14}\ \mathrm{A}/\sqrt{\mathrm{Hz}}$. Above -/+ 2V, the noise rises considerably as a consequence of the strong increase of the dark current (Figure 7-17-a) due to field-assisted tunneling through the tip of the $Al_{0.1}Ga_{0.9}As$ barriers of the system. We can also see that the noise current of device #6 is generally lower than that of sample #4, which is in agreement with the lower ground-state energy of device #6 that generates less dark current in the device and, consequently, less noise (the main noise source is the GR noise coming from the dark current).

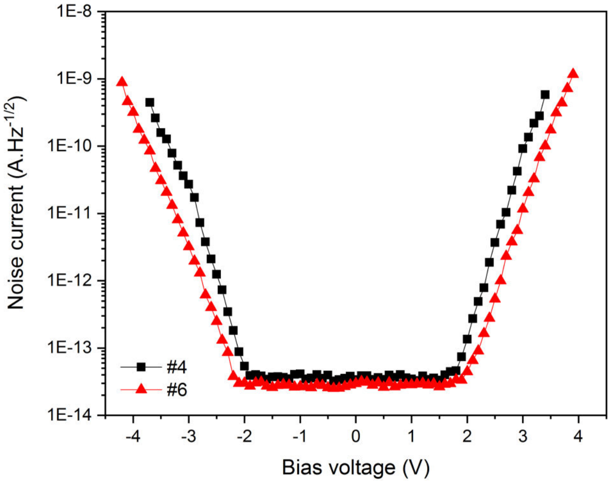

Figure 7-18: Noise-current spectral density of SML-QDIPs #4 and #6 at 12 K.

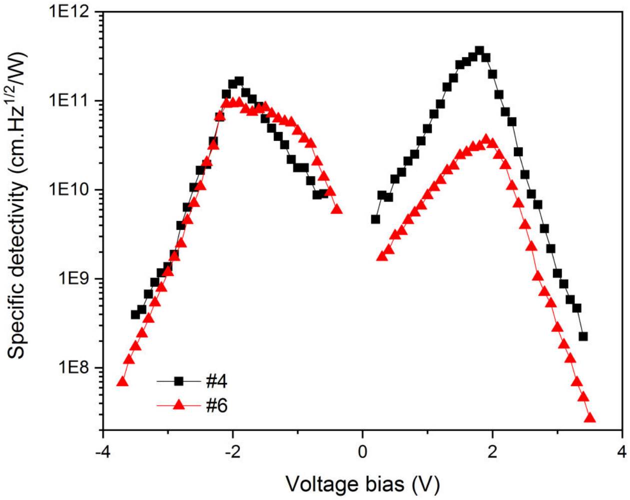

Figure 7-19: Specific detectivity of SML-QDIPs #4 and #6 at 12 K.

Finally, the specific detectivity was calculated as a function of bias voltage at 12 K and is reported in Figure 7-19. It shows that the specific detectivity increases monotonically with bias up to -/+2 V and then decreases abruptly as a consequence of the noise that rises considerably above -/+2V (Figure 7-18).

The maximum specific detectivity of 3.67×10^{11} cm $Hz^{1/2}$ W^{-1} and 9.41×10^{10} cm $Hz^{1/2}$ W^{-1} was achieved (at 12 K) in devices #4 and #6 at a bias of 1.8 V and -1.9 V, respectively. Since the noise curves of both devices are similar, the loss of performance of device #6 mainly comes from its lower responsivity at positive bias.

7-4-1 Discussion of the results of the 3rd group of samples

The activation energy calculated above is actually the difference between the Fermi level of the system and the top of the $Al_{0.1}Ga_{0.9}As$ barrier of the QW (continuum), and not the difference between the ground state of the SML-QDs and the top of the barrier, as is often assumed [174]. Since a lower In fraction (0.3 ML in sample #6 compared to 0.5 ML in all other devices) should result in a higher density of small 2D islands—and consequently also of SML-QDs [178]—the doping of sample #6 may no longer be optimal and could be responsible for its lower absorption and responsivity (Figures 7-15 and 7-16). It is worth noting here that samples #4, #5, and #6 were grown in the same time period; the Si doping was originally adjusted to match the density of SML-QDs of reference device #4—which was initially estimated to be around 4.3×10^{11} cm^{-2}—to have two electrons in the ground state of each nanostructure, and was then kept constant for the other devices. As a result, the Fermi energy of sample #6 is naturally lower than that of sample #4, where all the SML-QDs are supposedly fully doped. In addition, it is well known that the InAs/GaAs system is strained, and each QD introduces a certain density of structural defects that are potentially able to trap carriers. Furthermore , the higher the In content, the higher the strain and density of defects. As a result, the higher density of SML-QDs in sample #6 contributes to further reducing the effective doping of SML-QDs, resulting in lower responsivity.

Although it is generally better to change a single parameter at a time to check its influence on the device performance, in this specific case, it could lead to erroneous conclusions since the constant Si doping used in the present group was originally optimized for sample #4 and was kept constant for the other samples but was probably not ideally suited for sample #6, which probably has a higher density of SML-QDs. Therefore, a study varying the doping of the thin GaAs interlayer should also be performed in sample #6 to confirm that sample #4 is definitely superior.

In segregation continues very strong in sample #6 and still removes most of the In atoms from the 2D islands to form the InGaAs QW around the nanostructures—although, according to some STM studies [48], such islands should not be nucleated on the c(4×4) reconstructed surface that was used in devices #4 and #6. To compensate for this effect, we reduced the distance between consecutive 2D InAs islands to zero, but the strain in the system increased and the SML-QDs became smaller, leading to other problems and limitations. Of course, more testing is necessary to really optimize QDIPs like device #6, but it is very clear that In segregation must be kept as low as possible if one wants to benefit from the full potential of such quantum dots. Since segregation is a thermally activated process, lowering the sample temperature during deposition of the GaAs/InAs cycle is the easiest way to limit its effect. However, the activation energy of this phenomenon is quite small (0.11-0.12 eV), which means that reducing the sample temperature to 350 °C (instead of 490-515 °C) would only decrease the segregation coefficient to around 0.5 (instead of 0.7-0.8 at 490-515 °C) [175, 179]. At such low temperatures, MBE samples usually have a high density of structural defects that act as non-radiative recombination centers and considerably worsen the optical properties of the layers [180]. Therefore, a compromise should be found.

Another way would be to use MEE (migration enhanced epitaxy [181]) instead of MBE. Unlike MBE, where all shutters are simultaneously opened during deposition of an alloy, in MEE they are opened one at a time, consecutively and repeatedly, to deposit exactly a single atomic layer of each material. Under such conditions, the surface mobility of the species is much higher, and lower sample temperatures can be used without loss of crystalline quality [182]. Since such growth is much slower and more difficult than usual MBE growth, it can be used only to deposit or cover the SML-QDs—which are themselves already more difficult to grow than SK-QDs.

Finally, sample #6 was an attempt to improve the quality of the SML-QDs by reducing the GaAs interlayer to increase the average In composition and the strain field within the system to form better stacks of 2D islands. As a result, one might improve the performance of optoelectronic devices by taking advantage of the high SML-QD density, which could reach values up to 10^{12} cm^{-2} that are almost two orders of magnitudes larger than for SK-QDs. Another way would be to further increase the density of InAs SK-QDs themselves using the seed technique. By pre-depositing a high density of 2D InAs islands or InAs/GaAs SML-QDs, the strain field generated by their presence could serve as a seed to nucleate a layer of InAs QDs, just on top of them, to help increasing their density when the separation is kept small. Although we grew several samples of SML-QDs/SK-QDs bilayers (not shown here), we could never enhance the density of SK-QDs using this technique. That's because, as already discussed above, the 2D islands and SML-QDs have a much lower In content than expected and are surrounded by a thick InGaAs layer that considerably weaken the strain field around the nanostructures and turn them into ineffective seeds. Another way to use the seed concept to increase the density of InAs SK-QDs was proposed by Kovsh *et al.* [183] and consists in adding Aluminum to the InAs material used for the seed. Since Al adatoms have a very low surface diffusion, it is believed that they generate more nucleation centers and lead to a high density of InAlAs QDs that can be used as a seed, as it can easily reach the 10^{11} cm^{-2} range. As a consequence, in the next chapter, after optimizing the growth conditions of InAlAs SK-QDs, we will use them as a seed to investigate how much the density of SK-QDs in the top InAs layer can be increased in samples containing InAlAs/InAs SK-QDs bilayers.

Chapter 8: Increasing the density of InAs quantum dots by using InAlAs SK-QDs as a seed

One of the major drawbacks of conventional InAs SK-QDs is their low areal density, which is due to the self-assembling process. From this point of view, SML-QDs are more interesting since their density is expected to reach the 10^{12} cm^{-2} range. In this chapter, we present a way to further increase the density of InAs SK-QDs themselves using the seed concept. Pre-deposition of InAlAs quantum dots—which naturally have higher density than InAs SK-QD due to addition of aluminum (Al) atoms to the alloy—could be an effective way to increase the areal density of InAs SK-QDs grown just on top of them, as the strain field generated by the first layer of high-density QDs can serve as a template to nucleate the QDs of the second layer.

8-1 High density of InAlAs QDs

A high density of QDs is one of the keys to improving the performance of optoelectronic devices. There have been many attempts to increase the overall density of QDs by optimizing the growth conditions such as deposition rate, growth temperature, and film thickness, or by using several layers of vertically coupled QDs, which have been shown to enhance optical gain [100, 184, 185]. However, increasing QDs density is difficult because it results from a self-assembling process over which the grower doesn't have much control, and the number of QDs is limited by strain relaxation and lateral association of neighboring QDs in the upper layers [186].

An interesting technique to increase the QDs density was proposed by Kovsh *et al.* [183] and consists in adding aluminum to the usual InAs material. They used $In_{0.7}Al_{0.3}As$ QDs as a seed to obtain a higher density of In(Ga)As QDs located just above them, and, in this way, they were able to improve the properties of 1.2 µm lasers. Due to the low mobility of Al adatoms that enhances the nucleation of InAlAs islands on the GaAs (001) surface, the InAlAs QDs were used as an effective seed, and a higher density of InAs SK-QDs could be obtained [187].

8-2 Growth optimization of InAlAs QDs

To determine the highest density of InAlAs QDs that can be achieved as a function of their Al content, we optimized this type of QDs by growing several samples containing a single layer of $In_{1-x}Al_xAs$ QDs ($x \leq 0.65$) without a cap layer to check their density and morphology using AFM. All the samples had the same structure and differed only by the Al content in the QDs layer (Table 8-1). They consisted of a 200 nm thick GaAs buffer layer, deposited at 570 °C, followed by an $In_{1-x}Al_xAs$ layer deposited at 510 °C, as shown in Figure 8-1.

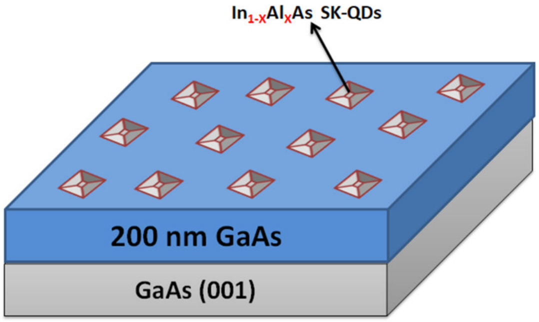

Figure 8-1: Structure of a sample consisting of $In_{1-x}Al_xAs$ QDs ($x \leq 0.65$) to check their density and morphology by AFM (no cap layer).

Generally, in the InAs/GaAs system, the thin epitaxial InAs layer relaxes above a thickness of 1.7 MLs and spontaneously forms small and homogeneous 3D InAs islands (quantum dots). This critical thickness (1.7 MLs for pure InAs deposited on top of GaAs) mainly depends on the difference in lattice parameters between both materials and can be monitored *in situ* (and in real time) in the MBE system using the RHEED technique. Thus, when additional Al is added to the InAs material, the lattice mismatch is reduced (Figure 8-2), as well as the strain, so that the critical thickness increases and strongly depends on the percentage of Al in the $In_{1-x}Al_xAs$ alloy. The critical thickness for each type of $In_{1-x}Al_xAs$ layer was measured to be between 1.7 and 10.4 MLs (depending on the Al content) using the RHEED technique, as shown in Table 8-1.

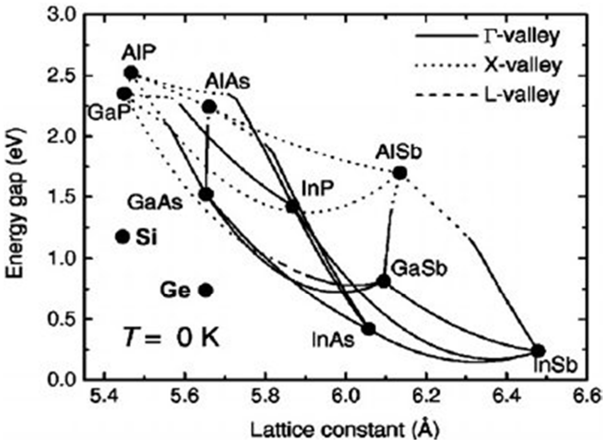

Figure 8-2: Band gap and lattice constant for various III–V alloys and materials of group IV [188].

Sample	$In_{1-x}Al_xAs$	Critical thickness (MLs)	Deposited thickness - Critical thickness +25% (MLs)
#1	x= 0 (reference sample)	1.70	2.1
#2	x=0.15	2.16	2.7
#3	x=0.30	2.90	3.6
#4	x=0.50	4.86	6.1
#5	x=0.65	10.40	13.0

Table 8-1: Critical and deposited thicknesses (MLs) of the individual $In_{1-x}Al_xAs$ layers as a function of their Al content.

In order to limit the number of samples to be grown and still be able to compare them consistently, we had to decide which In content to consider and how much material needed to be deposited for each sample. The reason for this is that the islands close to the critical thickness are very small and their areal density is low. As more material is deposited, they become larger and increase their density, and for even larger film thicknesses they start to coalesce and relax, introducing structural defects into the layer which are detrimental to the optical and electrical properties of the samples. Therefore, it is a good practice to keep the QDs density as high as possible without causing any coalescence. For pure InAs QDs deposited on top of GaAs, the highest density generally occurs between 2.0 and 2.2 MLs [184]. In this study, we used 2.1 MLs for that specific case. Since this corresponds to around 125% of the critical thickness of this particular system (1.7 MLs), we also deposited 125% of the critical thickness for the other $In_{1-x}Al_xAs$ layers, as shown in Table 8-1. Then, all samples were examined by AFM to check the size and density of the QDs, and the possible presence of relaxed structures.

Figure 8-3 shows a 1×1 μm^2 AFM scan of the top surface of all samples. One can see that, initially, the QDs density increases with the Al content and, after reaching a maximum value, it starts to decrease. This effect is usually attributed—but, as we will see later, this is not correct—to the lower migration rate of Al atoms adsorbed on the surface, resulting in a higher density of nucleation centers. Initially, the density of QDs increases with Al content, but the highest Al value (65%) appears to promote a decrease in density and a larger inhomogeneity of the QDs size, along with a worse homogeneity in their spatial distribution. This is probably due to the low In content (only 35%), which considerably reduces the strain in the system and makes it less favorable to locally follow the Stranski-Krastanov growth mode [152]. The QDs density as a function of the Al percentage is shown in Figure 8-3-f, where we can see that the highest value was obtained for $In_{0.5}Al_{0.5}As$ QDs (2×10^{11} cm^{-2}) and is considerably higher than the typical value for $In_{0.5}Ga_{0.5}As$ QDs ($2\text{-}5\times10^{10}$ cm^{-2}) [190].

Since only one relaxed QD was detected in the AFM images of Figure 8-3 (wide white spot in Figure 8-3-b), we decided to vary the thickness of the best layers to see if it would be possible to further increase their QDs density. In Figure 8-3, all the layers had a thickness equivalent to 125% of the critical thickness of the respective alloy, and the highest QDs densities were obtained for $In_{0.7}Al_{0.3}As$ and $In_{0.5}Al_{0.5}As$. In the second set of samples that will be analyzed here, the total thickness of both types of $In_{1-x}Al_xAs$ ($x = 0.30$ or 0.50) layers was set to 105%, 125%, and 140% of their critical thickness to allow better analysis of the QDs density evolution.

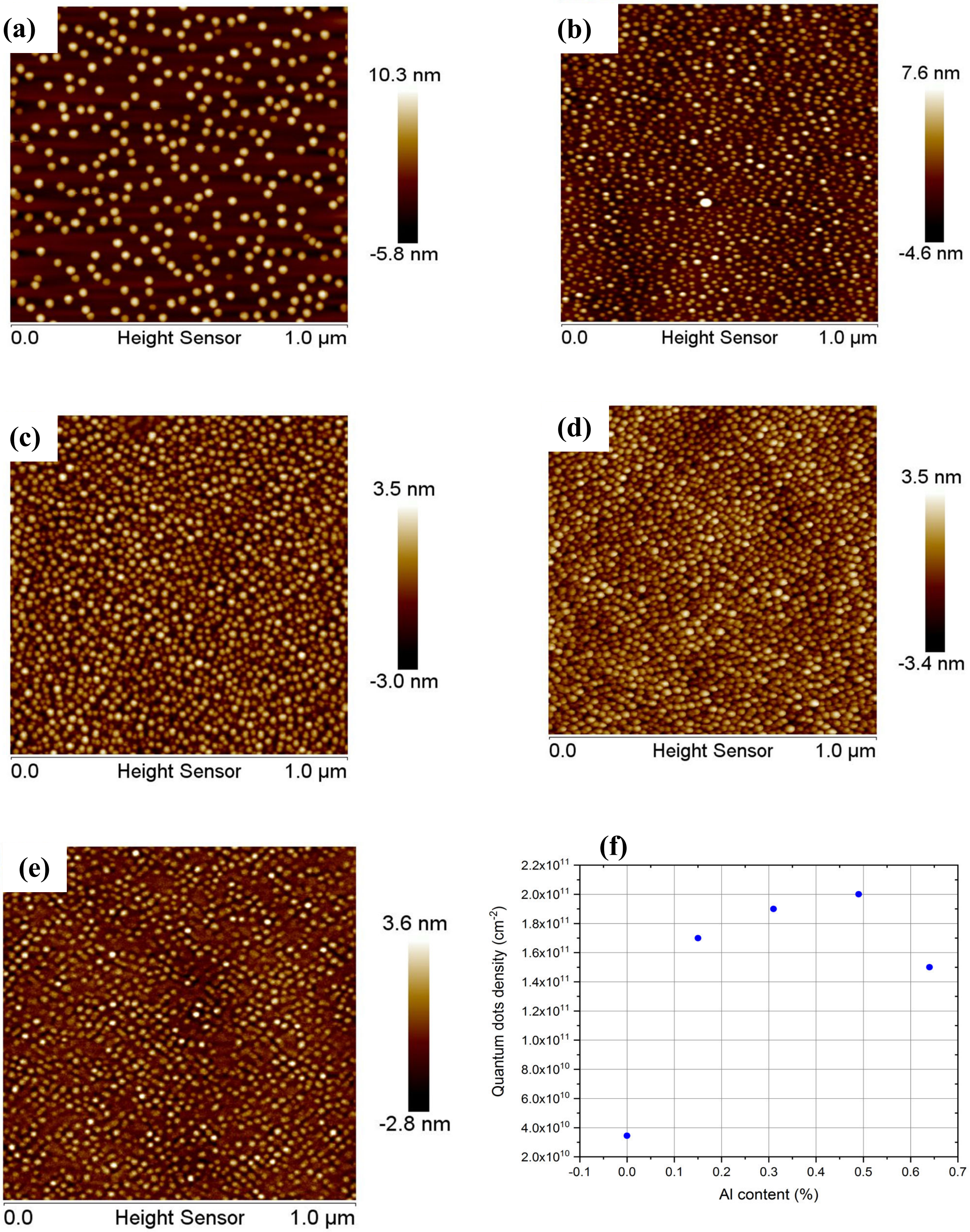

Figure 8-3: 1×1 µm^2 AFM images of the In$_{1-x}$Al$_x$As layers mentioned in Table 8-1 (first set of samples), showing the surface of a single layer of (a) InAs QDs; (b) In$_{0.85}$Al$_{0.15}$As QDs; (c) In$_{0.70}$Al$_{0.30}$As QDs; (d) In$_{0.50}$Al$_{0.50}$As QDs; (e) In$_{0.35}$Al$_{0.65}$As QDs. (f) QDs density (cm^{-2}) of the In$_{1-x}$Al$_x$As samples shown in Figures (a) to (e).

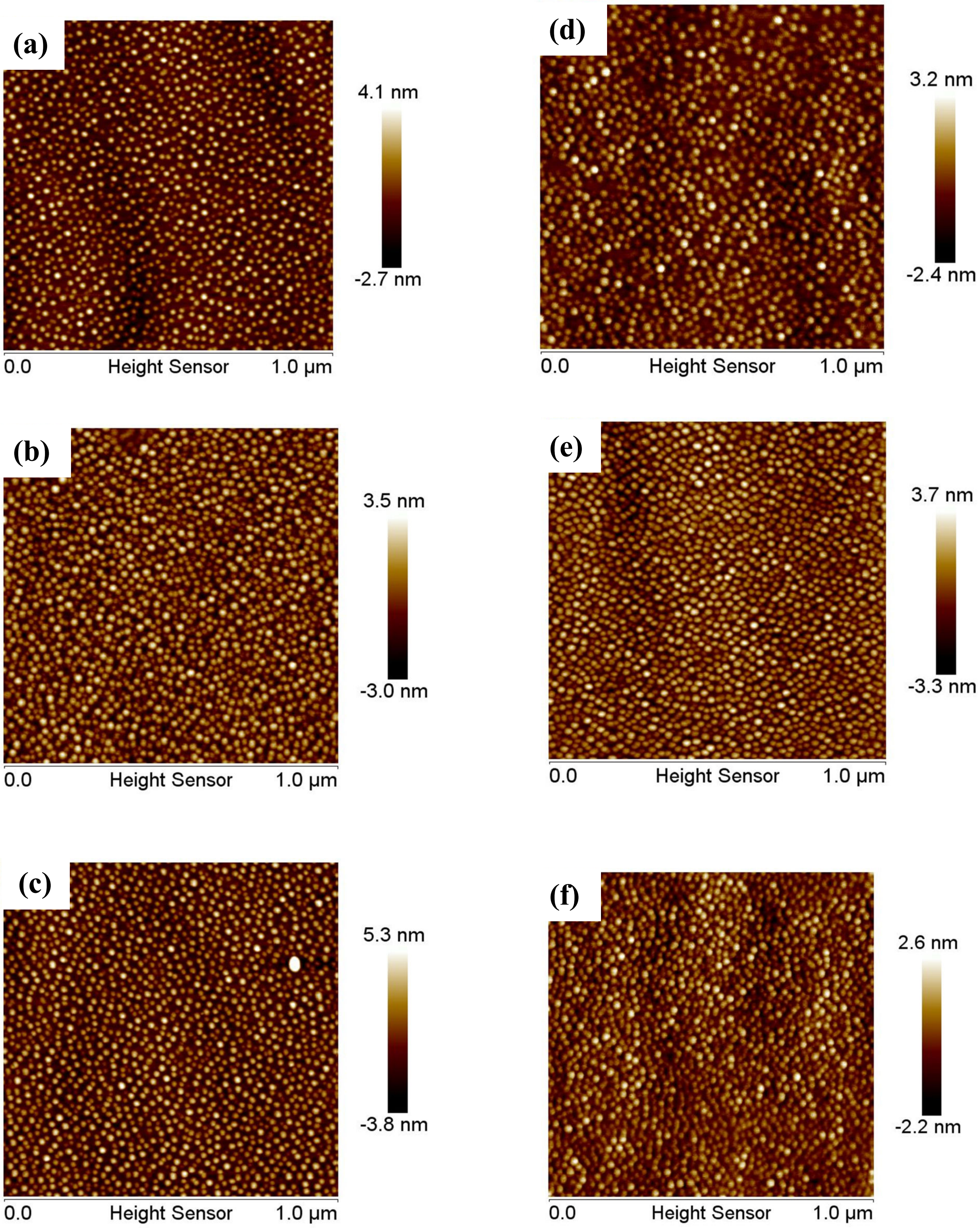

Figure 8-4: 1×1 µm^2 AFM images of the second set of samples showing the surface of a single layer of In$_{0.7}$Al$_{0.3}$As QDs (a), (b), (c), and of In$_{0.5}$Al$_{0.5}$As QDs (d), (e), (f) with a total thickness equivalent to 105%, 125% and 140% of their critical thickness, respectively (from top to bottom).

Figure 8-4 shows AFM images of the second set of samples. All images are very similar and the density of relaxed islands does not increase abruptly, even for the largest thickness (140%). Figure 8-5 shows the QDs density of all images and confirms that a total thickness of 125% of the critical thickness is the best choice. It also shows that, for this second set of samples, both layers have a very similar maximum density. Since the InAlAs QDs can be grown with such a high density, one could possibly think of using them directly (i.e., alone) in a device to improve its performance. However, since their size and composition are very different from those of usual InAs QDs, some of their properties are also very different, such as their operation wavelength in lasers and photodetectors. Therefore, another way to take advantage of their high density would be to use them as a seed and employ the strain field around them to induce a higher-than-usual density of InAs QDs.

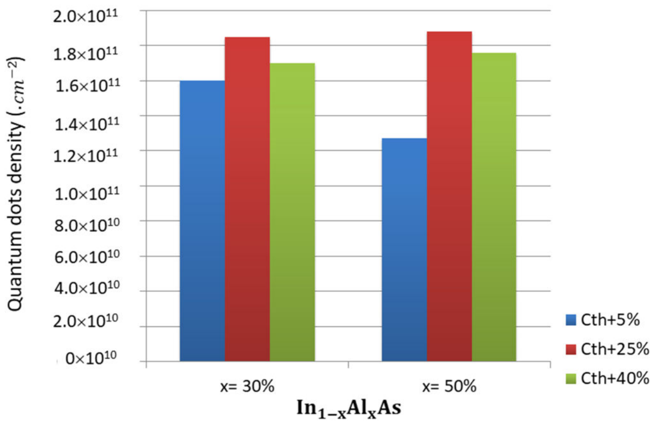

Figure 8-5: QDs density of $In_{1-x}Al_xAs$ layers (shown in Figure 8-4) with 30% and 50% of Al content for different total thicknesses (critical thickness +5%, +25%, and +40%).

8-3 Influence of the pre-deposited InAlAs layer on the InAs SK-QDs density

Depositing a thin layer of InAs material just a few nm above the layer of InAlAs QDs can result in a high density of InAs QDs, due to the strong coupling of the strain field between the two layers. Since Al adatoms have very low surface diffusion, they are expected to create more nucleation centers and lead to a very high density of small InAlAs SK-QDs [141]. As a result, the surface density of InAs QDs will increase as it will be affected by the underlying density of InAlAs

QDs that will act as nucleation centers. Based on the best results seen in the AFM images and data of Figures 8-3 to 8-5, we will now optimize the growth conditions of InAlAs/InAs QDs bilayers to check how far the density of the InAs QDs in the top InAs layer can be increased when InAlAs QDs are used as a seed.

Initially, two samples (third set of samples) were grown to investigate the effectiveness of the InAlAs seed layer (Figure 8-6) for both Al contents that previously provided the best results (30% and 50%): one sample contained $In_{0.7}Al_{0.3}As$ QDs and InAs QDs on top of them—both layers with a thickness equivalent to 125% of their respective critical thickness—separated by only 4 nm of GaAs. The second sample had exactly the same structure but had $In_{0.5}Al_{0.5}As$ QDs in the lowest layer. Figure 8-7 shows that the density of InAs QDs in the top layer was up to three times higher when we used a pre-deposition of InAlAs QDs, compared to a single layer of InAs QDs (reference sample). We can also see that the pre-deposition of InAlAs QDs with 30% of Al leads to a higher InAs QDs density than that with 50% of Al, although the $In_{0.5}Al_{0.5}As$ QD density was usually slightly higher than that of $In_{0.7}Al_{0.3}As$ QDs. This is probably because $In_{0.5}Al_{0.5}As$ QDs contain less In than $In_{0.7}Al_{0.3}As$ QDs and therefore generate a weaker local strain field that is not able to influence so effectively the nucleation of InAs QDs in the top layer.

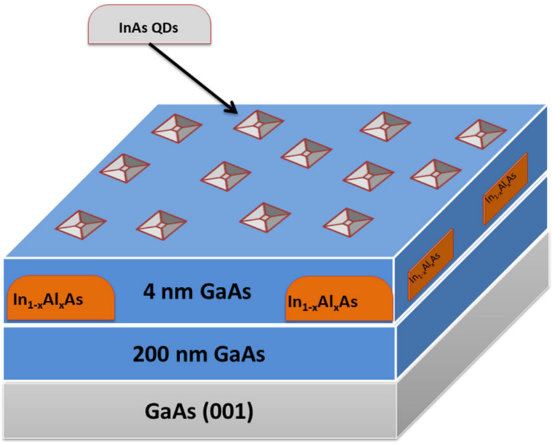

Figure 8-6: Structure of InAlAs/InAs QD bilayers, consisting of InAlAs QDs, serving as a seed, followed by InAs QDs. Both QD layers were separated by 4 nm of GaAs.

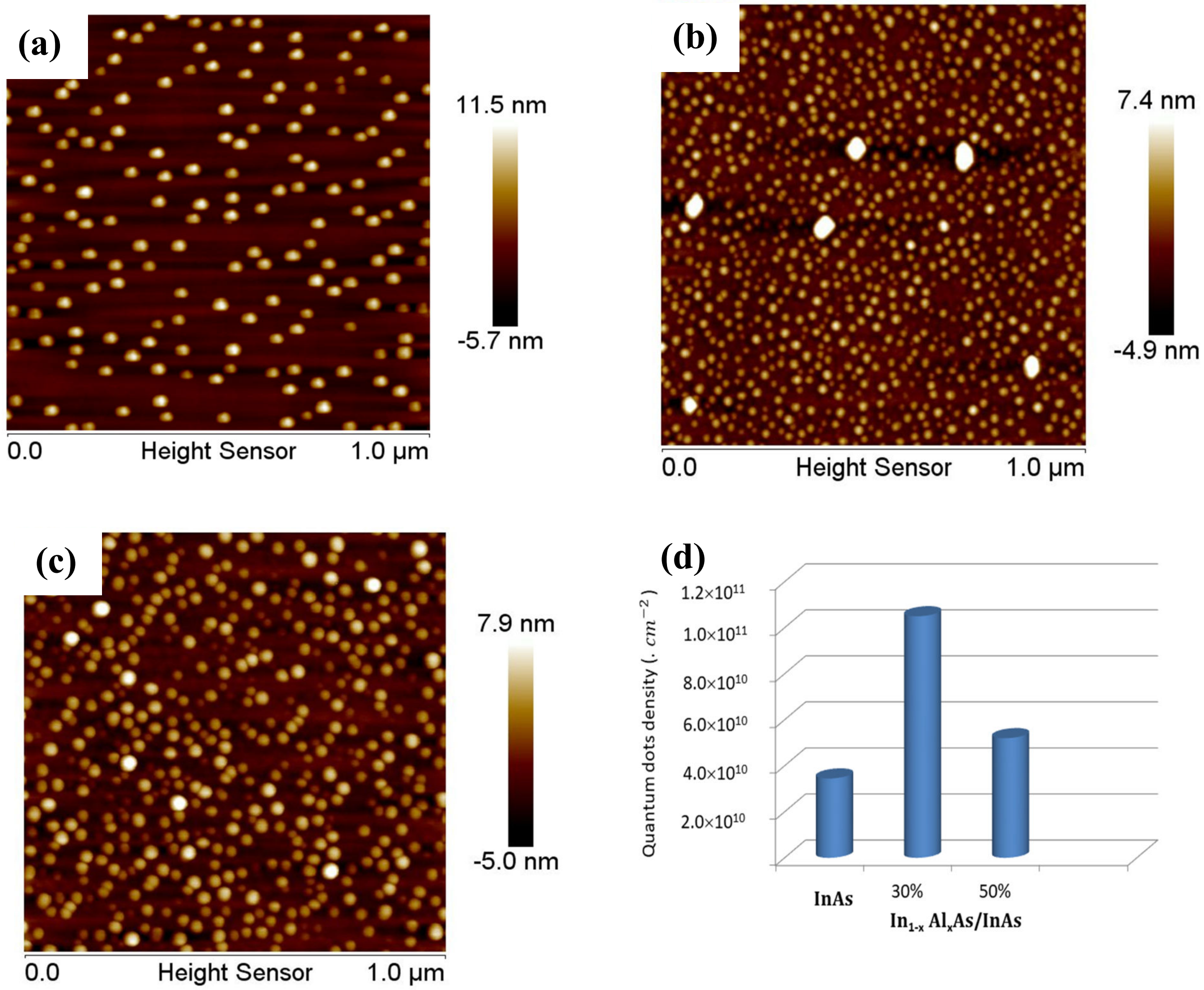

Figure 8-7: 1×1 μm^{2}AFM images of the third set of samples consisting of (a) 2.1 MLs of InAs only, to serve as a reference; (b) 2.1 MLs of InAs on top of In$_{0.7}$Al$_{0.3}$As QDs, separated by 4 nm of GaAs; (c) the same sample as in (b) but with In$_{0.5}$Al$_{0.5}$As QDs. The large white spots in Figures (b) and (c) indicate that some InAs QDs have relaxed. (d) InAs QDs density of AFM Figures (a) to (c) as a function of Al content. The first result represents the QDs density of a single 2.1 ML-thick InAs layer (reference sample).

8-4 Influence of the GaAs-separator thickness on the InAs SK-QDs density

Since the GaAs thickness between the InAlAs and InAs QDs is extremely important to determine the effectiveness of the strain field and, consequently, the final density of InAs QDs in the top layer, we also optimized its thickness to achieve the highest density. For this study, we grew a total of eight samples (Table 8-2). In three of them, we used pre-deposition of InAlAs QDs with 30% of Al, as they yielded a higher density of InAs QDs at the top than with 50% of Al (Figure 8-7-d). The three $In_{0.7}Al_{0.3}As$/InAs QDs bilayers were identical and differed only in the thickness of the GaAs spacer, which was 2, 4, and 8 nm (Figure 8-8). We also grew a sample with a single layer of InAs QDs and another with a single layer of $In_{0.7}Al_{0.3}As$ QDs to serve as a reference and to allow reliable comparison of the QDs density. To minimize the number of samples and to allow an optical and morphological investigation consistently, the same structure was repeated a second time on top of each sample and separated from the bottom structure by 100 nm of GaAs. As a consequence, AFM and PL measurements could be performed on the same samples; AFM on the top layer and PL on the buried layers at the bottom (Figure 8-8). Two other samples were grown to analyze the properties of the InAs and $In_{0.7}Al_{0.3}As$ wetting layers before they relaxed and formed QDs. Finally, samples #h was grown specifically grown for X-STM measurements and contained a layer or bilayer of the seven different types of the sample #a to #g described above to cross-sectionally observe their morphology and In content at the atomic scale and to obtain direct evidence of the vertical alignment of the QDs in the bilayers.

Sample number	GaAs thickness / description	QDs density (cm^{-2})
#a	2D InAs layer without QDs	-
#b	2D InAlAs layer without QDs	-
#c	InAs SK-QDs only	2.03×10^{10}
#d	InAlAs SK-QDs only	1.23×10^{11}
#e	2 nm	1.03×10^{11}
#f	4 nm	5.92×10^{10}
#g	8 nm	2.36×10^{10}
#h	Layers (a) to (g) in the same order for X-STM	-

Table 8-2: Description of the fourth set of samples. The QDs density (cm^{-2}) in the top layer and the value of the thin GaAs spacer in the InAlAs/InAs bilayers are also given where relevant.

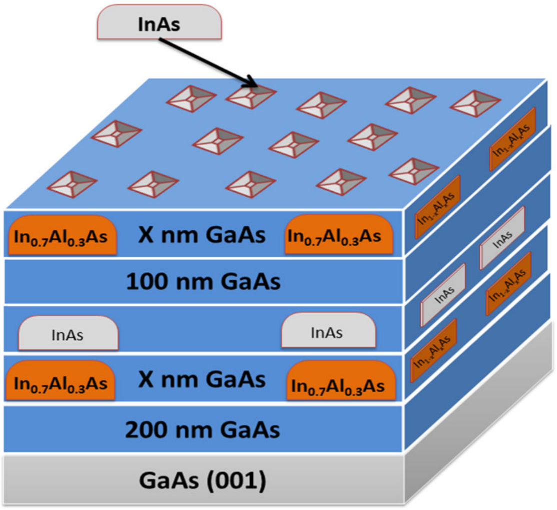

Figure 8-8: Structure of a sample of the fourth set consisting of bilayers of $In_{0.7}Al_{0.3}As$/InAs QDs. Both QDs layers were separated by X nm of GaAs, where X = 2, 4, or 8 nm. The structure of interest was duplicated and separated from the bottom one by 100 nm of GaAs to allow AFM measurements on the top and PL measurements on the bottom layers.

After removing the oxide and outgassing the sample at 615 °C for 5 min, a 200 nm-thick GaAs buffer was deposited at 570 °C. Then, the sample temperature was lowered to 515 °C to deposit the active region of each sample. The bilayers consisted of 3.50 MLs of $In_{0.7}Al_{0.3}As$ QDs, a GaAs spacer, and 2.1 MLs of InAs QDs followed by 15 nm of GaAs grown at the same temperature to prevent evaporation of the In atoms. The sample was then heated to 570 °C to deposit 85 nm of GaAs. Finally, the same bilayer was deposited without a cap layer to check the morphology of the InAs SK-QDs by AFM. The two samples containing only a single layer of QDs (InAs or $In_{0.7}Al_{0.3}As$) were grown under the same conditions described above to serve as a reference. The two additional samples containing only 2D layers of both materials without QDs were obtained by depositing 1.40 MLs of InAs and 2.30 MLs of $In_{0.7}Al_{0.3}As$.

8-4-1 AFM results

Figure 8-9 shows AFM images of the top layer of samples #a to #g listed in Table 8-2. No QDs were observed in samples #a and #b, because the deposition of the InAs and $In_{0.7}Al_{0.3}As$ layers, respectively, stopped before they could reach their critical thickness. Consequently, the surface only reflects the morphology of the 2D layer of each material. These two samples will be important in the discussion of the X-STM results in the next section. Samples #c and #d were used as a reference to know the usual QDs density of InAs and $In_{0.7}Al_{0.3}As$ when used individually. It can be seen that a single layer of $In_{0.7}Al_{0.3}As$ (Figure 8-9-d) naturally has a higher density (1.3×10^{11} cm^{-2}) of relatively smaller QDs (3 nm high and 10 nm wide) [141], while a single layer of standard InAs QDs (Figure 8-9-c) has a much lower density (2.0×10^{10} cm^{-2}) of comparatively larger QDs (7 nm high and 20 nm wide), as shown in Table 8-2. This increase in density by a factor of 6 for the InAlAs QDs is generally attributed to the lower surface mobility of the Al atoms [183]. Thus, it can be expected that, for thick GaAs spacers, the QDs of bilayers should be uncoupled and the density in the top InAs layer should be close to that of sample #c. On the other hand, for very thin values of the GaAs spacer, the InAlAs seed should be very effective and might increase the density to values close to that of sample #d.

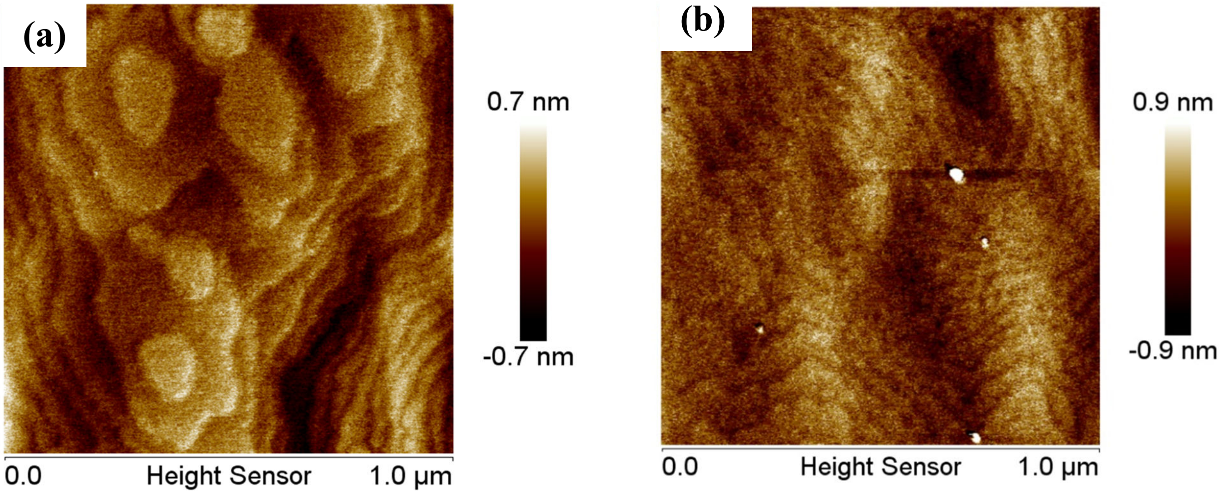

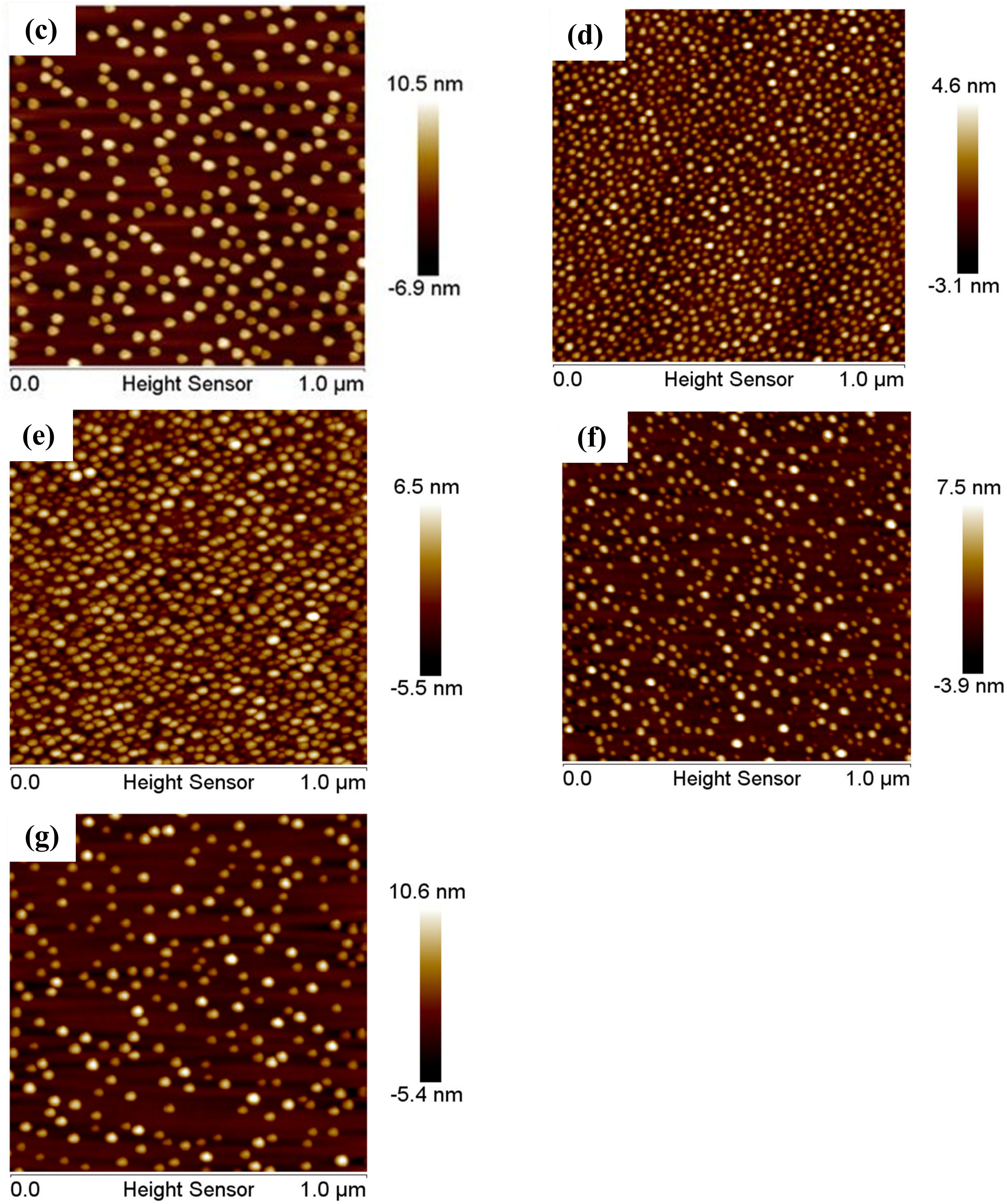

Figure 8-9: 1×1 µm^{2}AFM images of the top layer of samples #a to #g listed in Table 8-2. (a) 1.40 MLs of InAs and (b) 2.30 MLs of $In_{0.7}Al_{0.3}As$. For these 2 samples, deposition was stopped before the critical thickness was reached and therefore no QDs are observed (only the flat 2D layer). (c) 2.1 MLs of InAs QDs and (d) 3.50 MLs of $In_{0.7}Al_{0.3}As$ QDs. $In_{0.7}Al_{0.3}As$/InAs QDs bilayers with a GaAs spacer of (e) 2 nm, (f) 4 nm, and (g) 8 nm.

Figures 8-9- e to g show that, when these $In_{0.7}Al_{0.3}As$ QDs used as a seed layer in a bilayer structure, they can indeed increase the density of the InAs QDs in the top layer up to 1.0×10^{11} cm^{-2} when their separation is only 2 nm (Figure 8-9-e), and to 5.9×10^{10} cm^{-2} when the spacer is 4 nm thick (Figure 8-9-f). For an 8 nm thick spacer (Figure 8-9-g), it is reduced down to 2.36×10^{10} cm^{-2} which is close to the value of an individual layer of standard InAs SK-QDs (Figure 8-9-c). It means that the strain field within the thin GaAs spacer is hardly able to influence nucleation of InAs QDs in the top layer, and that the two QDs layers are almost decoupled as we will see below in the X-STM section.

8-4-2 X-STM results

To allow a detailed structural investigation at the atomic level of all layers involved in samples #a to #g, we grew a specific structure (sample #h) on a Si-doped GaAs(001) substrate ($n=1\times10^{18}$ cm^{-3}) containing the same layers (without duplication) deposited in the same conditions and in the same order as in samples #a to #g (Table 8-2), as shown in Figure 8-10. Each layer of interest was separated from the next one by 200 nm of GaAs, whose central region (120 nm) was Si-doped ($n=1\times10^{18}$ cm^{-3}). The high doping of these layers and substrate was necessary to provide a good conduction path for the tunneling current flowing between the sample and the STM tip.

The goal of this sample was to confirm by direct observation the vertical alignment of both types of QDs in the bilayers, and also to verify the incorporation sites of the Al atoms in the InAlAs wetting layer and QDs, since all the papers of the literature claim that these SK-QDs are made of InAlAs material (supposedly with the composition of the deposited nominal alloy, i.e., $In_{0.7}Al_{0.3}As$ in our case). However, in a recent paper of our group [187], we suggested that most of the Al atoms might remain in the WL and, consequently, the InAlAs QDs should consist of InGaAs material only (with possibly a few Al atoms from time to time).

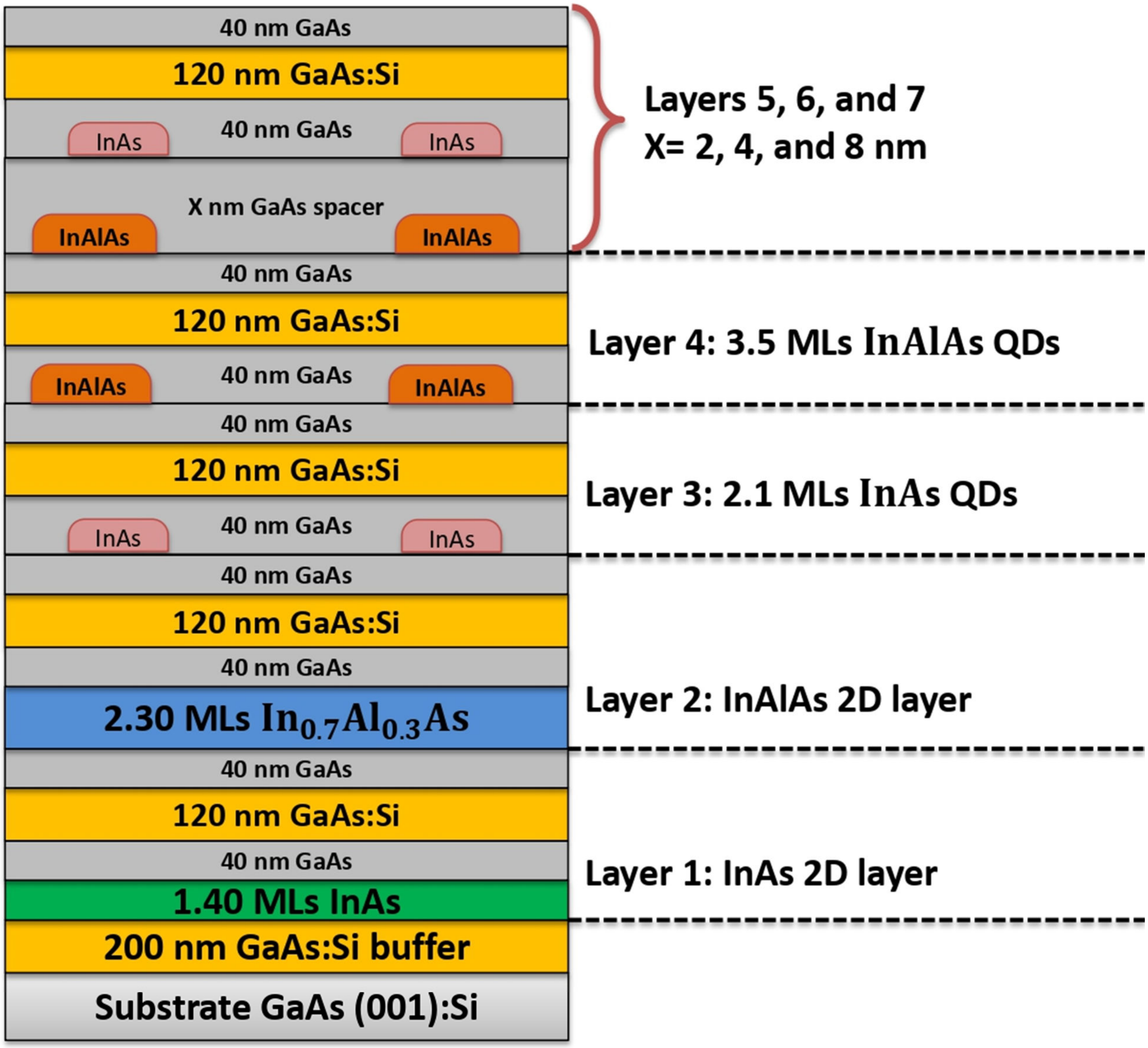

Figure 8-10: Structure of the X-STM sample #h grown on a Si-doped GaAs(001) substrate. Layers #1 to #7 are the same as in samples #a to #g, respectively, and were grown in the same conditions.

Due to the atomic arrangement of the {110} cleaved surface of GaAs(001)—which has a zincblende structure—used for the X-STM measurements, only every second monolayer along the [001] growth direction is visible in the images. Therefore, either the group-III or group-V atoms can be observed at a time, which means that an atomic row actually represents a bilayer of Ga and As atoms (not to be confused with the bilayers of InAs/InAlAs QDs).

In filled-state images obtained at high negative bias voltages, the group-V sublattice (As atoms) is imaged, while in empty-state images at high positive bias voltages, the group-III sublattice (Al, Ga, and In atoms) can be observed. The color contrast in the images represents the relative height of the STM tip from the cleaved surface. Due to strain, after cleaving the sample, the crystal structure relaxes locally out of the surface. As a consequence, the higher the In content of the layers, the higher the relaxation distance out of the plane.

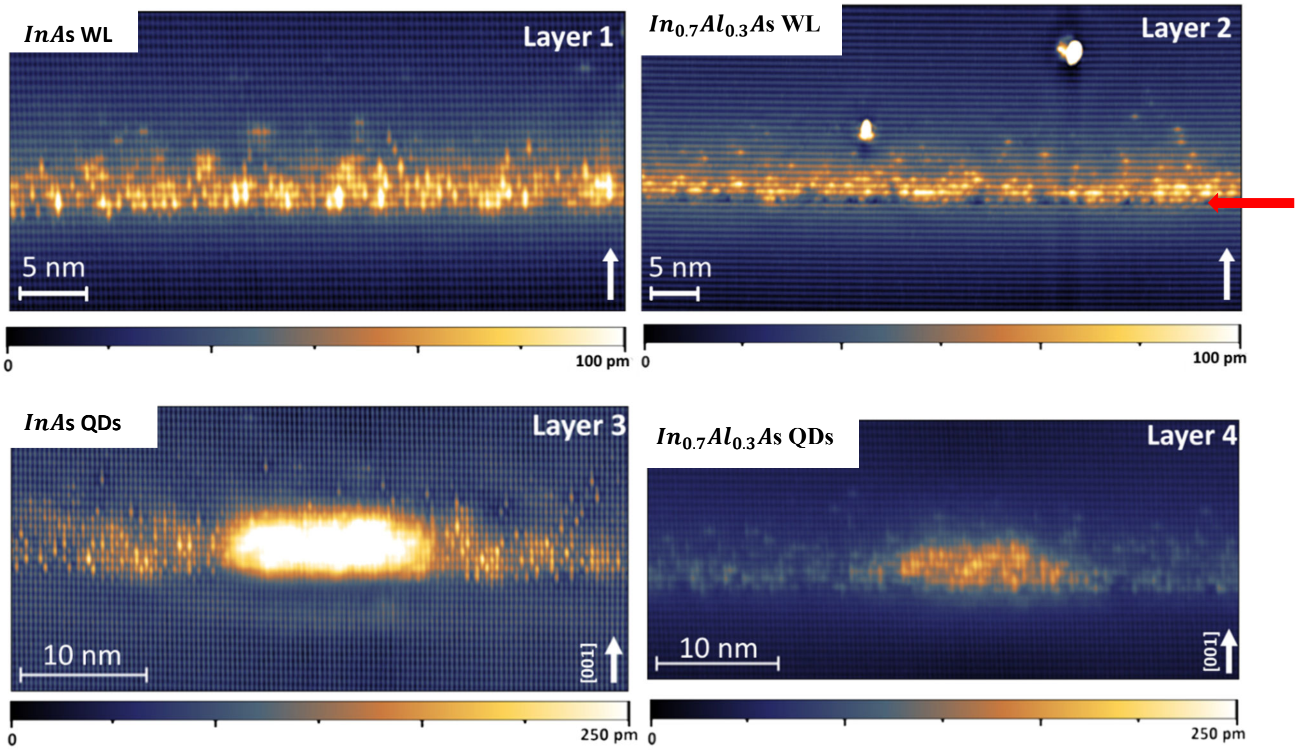

Figure 8-11: X-STM filled-state topographic images comparing the initial formation of the 2D InAs layer (layer #1) and $In_{0.7}Al_{0.3}As$ layer (layer #2), as well as their quantum dots (layers #3 and #4). The white arrow indicates the growth direction [001]. The two white spots in layer #2 indicate some contaminants or tip related artifacts. The red arrow shows the atomic plane where the Al atoms are located. The color scale represents the height of the relaxed surface outward of the cleaved plane [141].

Figure 8-11 shows that, in all layers, In atoms (related to the presence of bright spots) segregate strongly toward the surface when In(Ga)As layers are deposited on top of GaAs or covered by GaAs material, which is due to the strain present in the InAs/GaAs system. The In composition of the wetting layer and its (nominal) GaAs cap layer are well described by the phenomenological segregation model of Muraki *et al.* [144], where a segregation coefficient R around 0.85 is often observed in usual growth conditions—meaning that In atoms can be found up to 20 MLs away from the location they were initially deposited. On the other hand, Al atoms do not produce strain in the GaAs matrix (AlAs and GaAs have almost the same lattice parameter (Figure 8-2)) and have a very low surface diffusion coefficient [191]—resulting from the higher Al-As binding energy—which considerably limits Al segregation [192]. The bottom-most atomic layer in layer #2, marked with a red arrow, reveals many dark spots indicating the presence of Al atoms. This means that the Al atoms have settled down at the bottom of the WL and have not segregated. Layers #3 and #4 show individual InAs and $In_{0.7}Al_{0.3}As$ QDs, revealing that their size is similar, unlike those observed in the AFM images. In fact, a typical InAs QD of layer #3 has a base length of 18 ± 0.8 nm and a height of 4.0 ± 0.5 nm, while these values in layer #4 are 21.6 ± 0.8 nm and 4.2 ± 0.5 nm, respectively. Of course, this may be due to the fact that the X-STM images depend on the exact position of the cleavage plane within the volume of the nanostructure. However, it might also be related to the fact that the AFM tip has a certain volume (it is neither a point nor infinitely sharp) and can't detect the full height of the QDs when their density is very high. The lower brightness of the InAlAs QDs in layer #4 results from its lower indium concentration, which is due to the nominal alloy composition.

It is worth mentioning that no Al atoms can be observed inside the InAlAs QD of layer #4, unlike generally supposed in the literature, and they all remain in the bottom part of the WL. Therefore, unlike InAs QDs—where the WL is only found around the QDs—in the case of the InAlAs QDs the QDs really sit on top of it. This confirms that the high density of QDs achieved in the deposition of InAlAs is not due to the presence of Al atoms inside the QDs themselves, as is often claimed in the literature, but to the lower surface mobility of adatoms on the Al-rich wetting layer. In addition, if there are no Al atoms in the QDs, then such nanostructures consist only of InGaAs. A previous report from our group (Claro *et al.* [187]) suggests that their composition may be close to $In_{0.5}Ga_{0.5}As$, indicating that they may contain even less In than nominally. The present X-STM images of layer #4, combined with strain calculations to simulate the outward relaxation of the images, indicate that the In content of the QDs is actually even lower, reaching only 30% (instead of the nominal value of 70%). This implies that 70% of the alloy consists of Ga atoms originating from the GaAs substrate itself (underneath) and from the posterior GaAs cap layer to reduce the local elastic energy stored in the system. In addition, our X-STM data of layers #1 and #2 show that the presence of Al atoms at the bottom of the layer pins many In atoms to the sample surface, unlike what happens for the InAs WL, where the In atoms are free to segregate. However, the segregation coefficients calculated in both layers are similar [141].

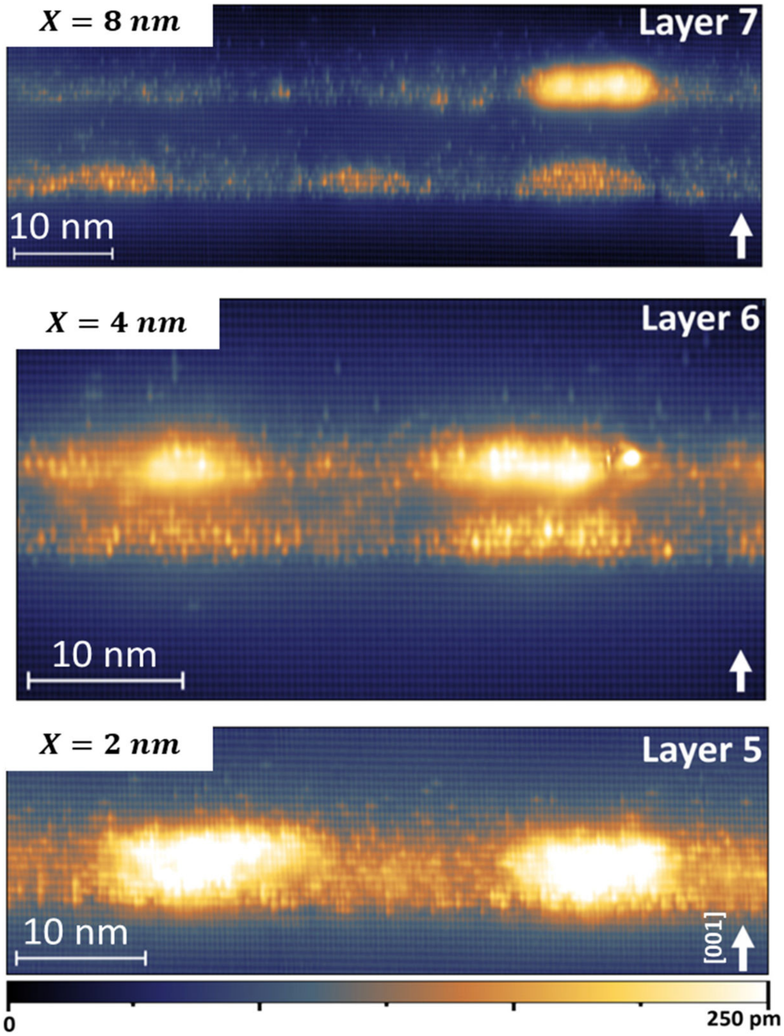

Figure 8-12: X-STM filled-state topographic images showing the effect of the GaAs spacer on the formation of InAs QDs in layers #5, #6, and #7. The InAs QDs are deposited on top of the InAlAs QDs seed layer. The intermixing and strain-induced stacking can be seen for X= 2 nm and X= 4 nm, respectively. The two QDs layers in layer #7 are already uncoupled for a GaAs spacer of 8 nm. The white arrow shows the growth direction [001].

Layers #5 to #7 contain bilayers of InAlAs/InAs QDs separated by thin GaAs layers having different thicknesses. In layer #5, the GaAs spacer is so thin (2 nm) that the InAs and the $In_{0.7}Al_{0.3}As$ intermixed completely (Figure 8-12) to form a single large QD, but it is the configuration that yields the highest InAs QDs density in the top layer, as previously confirmed in Table 8-2 and our AFM data. The very bright contrast in the QD region suggests a higher indium content compared to the other layers. It is difficult to determine the exact shape and size of these large QDs because both types of QDs merged and are indistinguishable. In the images of layers #6 and #7, both QDs layers can be gradually distinguished, as the GaAs spacer is thick enough to separate the seed layer from the top layer of InAs QDs. In layer #6, the strain-induced stacking of both types of QDs can be seen clearly. In layer #7, for a GaAs spacer of 8 nm, both InAlAs and InAs QDs appear to be completely uncoupled, with some occasional stacking from time to time. Consequently, when the two QD layers are separated by more than 8 nm, they can be treated as separate layers containing InAs and InAlAs QDs, as in layers #3 and #4, respectively. Once again, in all of these layers (#5 - #7), no Al can be detected in the QDs of the InAlAs layers [141], and nanostructures always lie on top of the Al-rich portion of the WL, as seen in layer #4.

Therefore, it seems that a very thin GaAs spacer (2 nm) is better if one wishes to have the highest possible density of InAs QDs in the top layer, and any thickness up to 8 nm will only take partly advantage of the seed. In the previous work of our group on InAlAs/InAs QDs bilayers applied to infrared photodetectors, a GaAs spacer of 4 nm was used [187]. Thus one could possibly expect better results by using a thinner GaAs spacer instead. However, a seed is only useful if its properties don't interfere with those of the top layer of interest (InAs QDs). It is therefore important to check that QD mixing with very thin GaAs spacers (2 nm)—as seen in Figure 8-12—doesn't change the optoelectronic properties of the system. We will investigate this in the next section.

8-4-3 PL experimental data

The optical properties of samples #a to #g were measured by PL at 77 K and their spectra are shown in Figure 8-13. Since the samples were small and contained duplicate copies of the layers of interest—one on the top for the AFM measurements and one covered with 100 nm of GaAs for the PL experiments—grown in the same conditions, we can expect both experimental techniques to allow a systematic investigation of the same system. Although capped and uncapped QDs may be different, the evolution of their optical and morphological properties will be correlated and may provide useful information.

Figure 8-13 shows the PL spectra of all samples analyzed by AFM in Figure 8-9. It can be seen that a single layer of conventional InAs QDs emits close to 980 nm, while the spectrum of a single layer of InAlAs QDs peaks at 880 nm due to their smaller size—although this might no longer be a valid argument, according to our X-STM data—and lower In content. The PL intensity of the single layer of InAlAs QDs is much lower than that of InAs QDs because their ground state (the only confined state of the system) is closer to the top of the GaAs barriers. As a result, the confined carriers can easily escape due to the temperature used for the PL measurements (77 K). The narrow peak around 860 nm is related to their WL. The signal coming from sample #a—which contains only a 2D InAs layer simulating the wetting layer around the InAs QDs—was easily measured and appears as a very narrow emission around 855 nm, just above the emission from the GaAs substrate that can be seen at 824 nm (gap of GaAs at 77 K). Sample #b—containing only the $In_{0.7}Al_{0.3}As$ WL—showed no signal at all when excited with a laser having a wavelength of 660 nm corresponding to an energy of 1.878 eV. This is probably due to the large band gap of the material forming the InAlAs WL, which results from the accumulation of all the Al atoms at the bottom. Its value must be much larger than that of the GaAs material at 77 K (1.503 eV) and suggests that the Al content of the WL is at least 30%, which is in good agreement with the X-STM data. Figure 8-13 also shows that the spectra of the $In_{0.7}Al_{0.3}As$/InAs QDs bilayers do not show any sign of the seed layer ($In_{0.7}Al_{0.3}As$ QDs) and appear to consist only of emission from the top InAs QDs, indicating that the InAlAs SK-QDs are not optically active—as expected from a good seed.

This is due to the deeper ground state of the top InAs QDs, where most carriers recombine, as already seen before [183, 187].

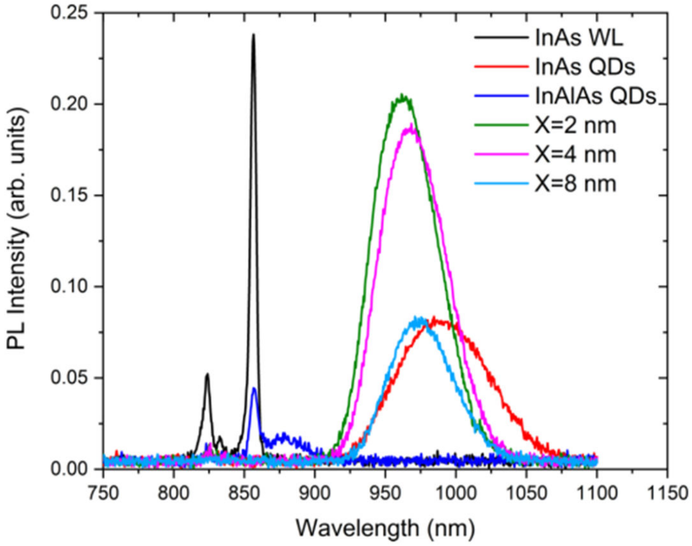

Figure 8-13: PL spectra at 77K of the samples from Figure 8-9 containing different combinations of InAs and $In_{0.7}Al_{0.3}As$ layers (Table 8-2). Sample #b, simulating the $In_{0.7}Al_{0.3}As$ WL, showed no signal at all.

The interpretation of the PL spectra of the samples containing bilayers is complex. They are all slightly different, because of the influence of the seed layer on the top InAs QDs, which should lead to an increase in their density and, consequently, to a reduction of their sizes with decreasing values of the spacer thickness. However, due to the strong In segregation, some of the In atoms from the seed layer are also transferred to the top InAs QDs, especially for thin GaAs spacers, as observed during growth on the RHEED screen—the critical thickness of the top InAs QDs was 1.7 MLs for the 8-nm-thick spacers, as usual for a single layer of InAs QDs, but was reduced to 0.7 ML for the thinnest GaAs spacer (2 nm). Thus, when the spacer is reduced, the strain field causes a blueshift in the emission, while at the same time, In segregation acts in the opposite direction, leading to a redshift. The spectra resulting from this complex competition depend on which of both effects prevails. The samples with the thinnest GaAs spacers (2 and 4 nm) have the highest PL intensity, probably due to their larger QDs density, while the sample with the thick spacer (8 nm) has an intensity similar to the single layer of InAs QDs, which is consistent with their similar QDs densities.

9- Conclusion

This thesis mainly consists of two parts. In the first one, we investigated the optical and structural characterization of InAs/GaAs SML-QDs and then optimized their growth conditions. In the second part, we studied the growth and electro-optical characterization of infrared photodetectors based on InAs/GaAs SML-QDs to determine how their performance improves under these optimized growth conditions.

Initially, several experimental techniques were tested to check which ones would be more adequate to investigate these nanostructures. PL spectra of InAs/GaAs SML-QDs sample showed a much narrower emission peaked at lower wavelengths when compared to SK-QDs. These features are mainly due to the smaller size and lower In content of SML-QDs. We also found that AFM was useless for analyzing their morphology because they are grown in a planar way and don't exhibit any surface profile. Therefore, the SML-QDs structure was analyzed using X-STM, which is more complex than AFM but can provide information about buried structures at the atomic scale.

Many InAs/GaAs SML-QDs samples were grown using MBE to optimize their growth conditions. PL was used as a guide to improve the optical properties of the nanostructures as much as possible. The experimental results showed that the best growth conditions and structure for InAs/GaAs SML-QDs consisted in a basic cycle of 0.5/2.5 MLs of InAs/GaAs repeated 6 times with a growth rate of 0.015 ML/s and 0.1 ML/s for the InAs submonolayer and thin GaAs interlayer, respectively, preferentially in the presence of a (2×4) surface reconstruction. X-STM was used to verify whether the 2D InAs islands—which are the building blocks of SML-QDs—were indeed formed on the GaAs(001) surface and could vertically align to provide the expected columnar structure. The data revealed that, actually, SML-QDs consist of In-rich InGaAs clusters embedded in a wider dilute InGaAs layer which behaves as a quantum well when surrounded by GaAs. These In-rich regions act as quantum dots—although their PL is similar to that of an InGaAs QW, but they do not develop the full height expected from SML-QDs nor consist of stacks of small 2D InAs islands (no periodicity is observed inside them). At high As flux, leading to a c(4×4) reconstruction of the GaAs(001) surface prior to InAs deposition, X-STM showed that they can reach an areal density in the mid-10^{11} cm^{-2} range. On the other hand, with a very low As flux necessary to get a (2×4) reconstruction of the GaAs(001) surface at low temperature, the density and size of these InGaAs nanostructures are considerably reduced, and lower incorporation and increased segregation of the In atoms are observed.

Several infrared photodetectors containing InAs/GaAs SML-QDs deposited in different conditions were grown by MBE, processed by photolithography in our clean room, and tested at 12 K. The electro-optical properties of such devices, where only the As flux was varied, revealed very similar figures of merit (D* around 10^{11} cm Hz$^{1/2}$ W^{-1}) which contrast with the X-STM results. We believe that the presence of strong In segregation (around 80% in this system) removes most In atoms from the original 2D InAs islands nucleated on the GaAs(001) surface (whenever they are formed), spreading them in the next layers, weakening the strain field around the original 2D islands, and allowing the random formation of In-rich agglomerates. Such clusters are smaller and contain less In than expected, leading to shallower energy levels and electronic wave functions that extend over the closest nanostructures, weakening thus their overall 3D confinement and decreasing the advantage of samples having a high density of nanostructures.

In an attempt to avoid the problems resulting from a very low As flux, we decided to grow the same device at a slightly higher temperature (525 °C), in order to keep the (2×4) reconstruction and avoid its transition to a c(4×4) reconstruction at a lower temperature (below 520 °C). This new device turned out to have a detectivity eight times higher than that of the previous ones, suggesting that this way to achieve the (2×4) reconstruction was much superior to the other one. Although the higher sample temperature may induce stronger In segregation and evaporation, these growth conditions—which are similar to those usually employed for SK-QDs—are also much easier to achieve.

To improve the quality of such SML-QDs, we reduced the GaAs interlayer to its minimum value—using a basic cycle consisting of 0.3 ML of InAs followed by 0.7 ML of GaAs—in an attempt to increase the average In composition and the strain field within the system to form better stacks of 2D islands. Although a device grown with such characteristics performed worse than the others, the study might still be inconclusive. Indeed, since the density of 2D InAs islands is expected to be higher for this lower InAs fraction, the doping of the samples—that was kept constant in all devices—might not be enough to fully populate the ground state of all In-rich clusters and provide the best performance of this device.

Finally, we used the seed concept in an attempt to increase further the density of InAs QDs which is generally close to 2×10^{10} cm^{-2} range. The seed was made of InAlAs, which is known to provide a higher density of QDs, and was separated from the top layer of InAs QDs by just a few nm of GaAs. Due to their close proximity, the seed is expected to generate a strain field around each InAlAs QD and serve as a template to influence the nucleation of InAs QDs just above. A systematic AFM study revealed that $In_{0.5}Al_{0.5}As$ was able to provide the highest density of QDs in an isolated layer (around 1.2×10^{11} cm^{-2}) but, when InAlAs/InAs QDs bilayers were concerned, the highest QDs density in the top InAs layer (around 1.0×10^{11} cm^{-2}) was actually achieved with $In_{0.7}Al_{0.3}As$ and separation of only 2 nm, due to the stronger strain field. X-STM measurements in the same type of samples showed strong vertical coupling between both types of QDs layers for GaAs spacers equal to or thinner than 4 nm. For that value, the nanostructures could be individually resolved while, for a separation of 2 nm, both types of QDs were completely intermixed and undistinguishable. The atomic resolution of the technique allowed us to point out for the first time that QDs formed from the $In_{0.7}Al_{0.3}As$ layer don't contain a single Al atom, as they are all confined in the bottom part of the wetting layer. As a consequence, the highest density of this type of QDs is not due to the presence of Al atoms inside the QDs themselves but, rather, to the fact that the adatoms have a lower diffusion coefficient on an Al-rich surface which results in a higher density of nucleation centers. PL measurements revealed that the InAlAs QDs are optically inactive when they are part of InAlAs/InAs QDs bilayers, which is the ideal situation for a seed.

10- Publications

10-1 Published papers:

[1]. **A. Alzeidan**, M. S. Claro, and A. A. Quivy, "High-detectivity infrared photodetector based on InAs submonolayer quantum dots grown on GaAs(001) with a 2 × 4 surface reconstruction", J. Appl. Phys. **126**, (2019), 224506; https://doi.org/10.1063/1.5125238

[2]. Tiago F. Cantalice, **Ahmad Alzeidan**, Sergio M. Urahata, and Alain A. Quivy, "In-situ measurement of indium segregation in InAs/GaAs submonolayer quantum dots", Mater. Res. Express **6,** (2019), 126205, https://doi.org/10.1088/2053-1591/ab55a8

[3]. **A. Alzeidan,** T. Cantalice, A. J. Garcia Jr, C. Deneke, and A. A. Quivy "Investigation of the quantum confinement anisotropy in submonolayer quantum dot infrared photodetectors", 34th symposium on microelectronics technology and devices (SBMicro), 2019 https://doi.org/10.1109/SBMicro.2019.8919349

[4]. R.S.R. Gajjela, A.L. Hendriks, **A. Alzeidan**, T.F. Cantalice, A.A. Quivy, and P.M. Koenraad "Cross-sectional scanning tunneling microscopy of InAs/GaAs(001) submonolayer quantum dots", Phys. Rev. Materials **4**, (2020), 114601. https://doi.org/10.1103/PhysRevMaterials.4.114601

[5]. **Ahmad Alzeidan**, Tiago F. de Cantalice, Kevin D. Vallejo, Paul J. Simmonds, and Alain A. Quivy, " Influence of the InAs coverage on the performance of submonolayer-quantum-dot infrared photodetectors grown with a (2×4) surface reconstruction", 35th Symposium on Microelectronics Technology and Devices (SBMicro), 2021. https://doi.org/10.1109/SBMicro50945.2021.9585765

[6]. T. Cantalice, **A. Alzeidan**, G. Jacobsen, J. F. M. Domenegueti, M. D. Teodoro, and A. A. Quivy, "Evidence of week strain field in InAs/GaAs submonolayer quantum dots", Micro and Nanostructures **172**, (2022), 207449,; https://doi.org/10.1016/j.micrna.2022.207449

[7]. **A. Alzeidan**, T.F. Cantalice, K.D. Vallejo, R.S.R. Gajjela, A.L. Hendriks, P.J. Simmonds, P.M. Koenraad, and A.A. Quivy, "Influence of the arsenic flux on the performance of infrared photodetectors based on InAs submonolayer quantum dots", Sensors and Actuators A: Physical, **334,** (2022), 113357,. https://doi.org/10.1016/j.sna.2021.113357

[8]. Victor M. O. Curbelo, **Ahmad Alzeidan**, and Alain A. Quivy, "Capping of InAs quantum dots by migration enhanced epitaxy", 36th Symposium on Microelectronics Technology and Devices (SBMicro) 2022, https://doi.org/10.1109/ SBMICRO55822.2022.9881016

[9]. Raja Sekhar Reddy Gajjela, **Ahmad Alzeidan**, Victor M. O. Curbelo, Alain A. Quivy, and Paul M. Koenraad "Atomic-scale characterization of InAlAs and InAs/InAlAs Bilayer Stranski-Krastanov Quantum Dots", Physical Review Materials **6**, 114604, (2022); https://doi.org/10.1103/PhysRevMaterials.6.114604

[10]. T. Borrely, **A. Alzeidan**, M.D. de Lima, G.M. Jacobsen, T.-Y. Huang, Y.-C. Yang, T.F. Cantalice, R.S. Goldman, MD. Teodoro, A.A. Quivy, "Viability of intermediate band solar cells based on InAs/GaAs submonolayer quantum dots and the role of surface reconstruction", Solar Energy Materials and Solar Cells, **254**, (2023), 112281, https://doi.org/10.1016/j.solmat.2023.112281

10-2 Papers to be submitted:

[11]. **A. Alzeidan**, T.F. Cantalice, K. Sautter, K.D. Vallejo, P.J. Simmonds, and A.A. Quivy, "Influence of the growth temperature on the performance of infrared photodetectors based on InAs submonolayer quantum dots", to be submitted to Sensors and Actuators A: Physical.

10-3 Participation in conferences:

1. **A. Alzeidan**, M.S. Claro, and A. A. Quivy, "Comparison between infrared photodetectors based on submonolayer quantum dots and on usual Stranski-Krastanov quantum dots ", poster presented at the "Workshop em Crescimento Epitaxial (WCE)," 27 – 28 June 2018, Campinas, Brazil.

2. T. Cantalice, **A. Alzeidan**, and A. Quivy "Estudo da Segregação de In em pontos quânticos de submonocamada", poster presented at the "Workshop em Crescimento Epitaxial (WCE)," 27 – 28 June 2018, Campinas, Brazil.

3. T. Cantalice, **A. Alzeidan**, A. J. Garcia Jr, C. Deneke, and A. A. Quivy "Growth of a submonolayer quantum dot infrared photodetector in the presence of a c(4×4) surface reconstruction", poster presented at the "Encontro de Outono da SBF 2019", 27–31 May 2019, Sergipe, Brazil.

4. **A. Alzeidan**, T. F. Cantalice, A. J. Garcia Jr, C. Deneke, and A. A. Quivy "Investigation of the quantum confinement anisotropy in submonolayer quantum dot infrared photodetectors", Poster presented at SBMicro 2019, 26 – 30 August, São Paulo, Brazil.

5. Kevin D. Vallejo, **Ahmad Al Zeidan**, Tiago F. Cantalice, Alain A. Quivy, and Paul J. Simmonds, "Influence of the growth conditions on the performance of InAs submonolayer quantum dot infrared photodetectors", Poster presented at the 35th North American Molecular Beam Epitaxy Conference (NAMBE 2019)" 22–25 September 2019, Ketchum, Idaho, USA.

6. **A. Alzeidan**, T. F. de Cantalice, K. D Vallejo, P. J. Simmonds, and A.A. Quivy "Influence of the In fraction on the performance of InAs/GaAs submonolayer quantum dot infrared photodetectors", Poster presented at the 19th Brazilian Workshop on Semiconductor Physics, 18–22 November 2019, Fortaleza – Ceará, Brazil.

7. T. F. Cantalice, **A. Alzeidan**, S. Urahata, A. A. Quivy, "In-situ measurement of indium segregation in InAs/GaAs submonolayer quantum dots", Poster presented at the 19th Brazilian Workshop on Semiconductor Physics, 18-22 November 2019, Fortaleza – Ceará, Brazil.

8. R. S. R. Gajjela, A. L. Hendriks, **A. Alzeidan,** T. F. Cantalice, A. A. Quivy, and P.M. Koenraad, "Cross-sectional scanning tunneling microscopy of InAs/GaAs submonolayer quantum dots", Poster presented at the 11th International Conference on Quantum Dots, 7 - 11 December 2020, Munich, Germany.

9. Tiago Cantalice, **Ahmad Alzeidan**, and Alain Quivy, "Influence of rapid thermal annealing on Stranski-Krastanov and submonolayer quantum dots ", poster presented at the "Encontro de Outono da SBF 2020", 23-26 November 2020, Online.

10. **A. Alzeidan** and A. A. Quivy, "Increasing the density of InAs quantum dots using InAlAs quantum dots as a seed ", poster presented at the "Encontro de Outono da SBF 2021", 21 – 25 June 2021, Online.

11. T. Cantalice, **A. Alzeidan**, G. Jacobsen, J. F. M. Domenegueti, M. D. Teodoro, and A. A. Quivy, "Unveiling the differences between submonolayer and Stranski-Krastanov quantum dots", poster presented at the "Encontro de Outono da SBF 2021", 21 – 25 June 2021, Online.

12. **Ahmad Alzeidan**, Tiago F. de Cantalice, Kevin D. Vallejo, Paul J. Simmonds, and Alain A. Quivy, " Influence of the InAs coverage on the performance of submonolayer-quantum-dot infrared photodetectors grown with a (2×4) surface reconstruction", poster presented at the 35th Symposium on Microelectronics Technology and Devices (SBMicro), 23 – 27 August 2021, Online.

13. **A. Alzeidan**, T. F. Cantalice, K. Sautter, K. D. Vallejo, P. J. Simmonds, A. A. Quivy, "Influence of the In content and surface reconstruction on the properties of SMLQDIPs", poster presented at the 21st International Conference on Molecular Beam Epitaxy, Virtual Conference, Mexico, 6 – 9 September 2021, Online.

14. **A. Alzeidan** T. F. Cantalice, and A. A. Quivy, "Influence of the Arsenic flux on the performance of infrared photodetectors based on InAs submonolayer quantum dots", poster presented at the "Encontro de Outono da SBF 2022", 10 – 14 Abril 2022, São Paulo, Brazil.

15. V. Curbelo, **A. Alzeidan**, and A. A. Quivy, "Improvement of InAs quantum dots using migration enhanced epitaxy", poster presented at the "Encontro de Outono da SBF 2022", São Paulo, 10 – 14 Abril 2022, São Paulo, Brazil.

16. T. Borrely, **A. Alzeidan**, G. Jacobsen, M. D. Teodoro, R. S. R. Gajjela, A. L. Hendriks, P. M. Koenraad, and A. A. Quivy "On the relation between growth, quantum dot morphology, optoelectronic properties, and performance in InAs/GaAs quantum dot intermediate band solar cell", poster presented at the "Encontro de Outono da SBF 2022", São Paulo, 10 – 14, Abril 2022, São Paulo, Brazil.

17. V. Curbelo, **A. Alzeidan**, and A. A. Quivy, "Capping of InAs quantum dots by migration enhanced epitaxy", poster presented at the 35th Symposium on Microelectronics Technology and Devices (SBMicro), 22 – 26 August 2022, Online.

18. V. Curbelo, **A. Alzeidan**, and A. A. Quivy, "Migration enhanced epitaxy applied to the growth of low-temperature InAs quantum dots" poster presented at the "Brazilian Workshop on Semiconductor Physics (BWSP)" 2022, 12 – 16 September 2022, São José dos Campos - São Paulo, Brazil.

Bibliography

[1]: Augusto Beléndez Vázquez; "Why celebrate an International Year of Light?" Física para todas, (2015). https://blogs.ua.es/fisicateleco/2015/05/celebrating-the-international-year-of-light/

[2]: W. Herschel; "Experiments on the refrangibility of the invisible rays of the Sun" Philosophical Transactions of the Royal Society of London **90**, (1800). https://doi.org/10.1098/rstl.1800.0015

[3]: A. Rogalski; "History of infrared detectors" Opto-Electronics Review, **20**, (2012), 279–308. https://doi.org/10.2478/s11772-012-0037-7

[4]: E. Scott Barr; "The Infrared Pioneers—II. Macedonio Melloni", Infrared Physics **2**, (1962), 67-74. https://doi.org/10.1016/0020-0891(62)90023-4

[5]: T.W. Case; "Notes on the change of resistance of certain substrates in light", Physics Reviews **9**, (1917), 305-310. https://doi.org/10.1103/PhysRev.9.305

[6]: T.W. Case; "Thalofide cell - a new photoelectric substance," Phys. Rev. **15**, (1920), 289. https://doi.org/10.1103/PhysRev.15.289

[7]: A. Rogalski, "Infrared detectors: Status and trends", Progress Quantum Electron **27**, (2003), 59–210. https://doi.org/10.1016/S0079-6727(02)00024-1

[8]: D. J. Lovell; "The Development of Lead Salt Detectors", American Journal of Physics, **37** (1969), 467–478. https://doi.org/10.1119/1.1975646

[9]: B.V. Rollin and E.L. Simmons; "Long wavelength infrared photoconductivity of silicon at low temperatures". Proc. Phys. Soc. **B 65**, (1952), 995. https://doi.org/10.1088/0370-1301/65/12/115

[10]: E. Burstein, J.J. Oberly, and J.W. Davisson; "Infrared photoconductivity due to neutral impurities in silicon". Phys Rev, **89**, (1953), 331. https://doi.org/10.1103/PhysRev.89.331

[11]: Tan, Chee Leong and Mohseni, Hooman; "Emerging technologies for high performance infrared detectors" Nanophotonics, **7**, (2018), 169–197. https://doi.org/10.1515/nanoph-2017-0061

[12]: G.A. Sarov; "Preparation of Quantum Structures: Quantum Well Infrared Detectors" In: Balkanski, M., Yanchev, I. (eds) Fabrication, Properties and Applications of Low-Dimensional Semiconductors. NATO ASI Series, **3**, (1995). Springer, Dordrecht. https://doi.org/10.1007/978-94-011-0089-2_2

[13]: P. W. Kruse, M. D. Blue, J. H. Garfunkel, and W. D. Saur; "Long wavelength photoeffects in mercury selenide, mercury telluride and mercury telluride-cadmium telluride", Infrared Phys. **2,** (1962), 53–60, https://doi.org/10.1016/0020-0891(62)90043-X

[14]: B.F. Levine, K.K.Choi, C.G. Bethea, J. Walker, and R. Malik; "New 10 um infrared detector using intersubband absorption in resonant tunneling GaAlAs superlattices". Appl. Phys. Lett. **50**, (1987),1092–1094. https://doi.org/10.1063/1.97928

[15]: S. D. Gunapala, S. V. Bandara, J. K. Liu, C. J. Hill, B. Rafol, J. M. Mumolo, J. Thang, M. Z. Tidrow, and P. D. LeVan; "MWIR and LWIR megapixel QWIP focal plane arrays" Proc. SPIE, **5563**, (2004), 141–148. https://doi.org/10.1117/12.560955

[16]: B.F. Levine; "Quantum−well infrared photodetectors" J. Appl. Phys. **74**, (1993), R1–R81. https://doi.org/10.1063/1.354252

[17]: A. Rogalski; "Quantum well photoconductors in infrared detectors technology" J. Appl. Phys. **93**, (2003), 4355–4391 https://doi.org/10.1063/1.1558224

[18]: Eric Costard, P. Bois, Alfredo De Rossi, A. Nedelcu, Olivier Cocle, François-Hugues Gauthier, and Francis Audier; "QWIP detectors and thermal imagers", Comptes Rendus Physique, **4**, (2003), 1089–1102. https://doi.org/10.1016/j.crhy.2003.10.024

[19]: Y. Arakawa, and H. Sakaki; "Multidimensional quantum well laser and temperature dependence of its threshold current", Appl. Phys. Lett. **40,** (1982), 939–941. https://doi.org/10.1063/1.92959

[20]: J. Phillips, K. Kamath, and Bhattacharya; "Far-infrared photoconductivity in self-organized InAs quantum dots", Appl. Phys. Lett. **72,** (1998), 2020–2022. https://doi.org/10.1063/1.121252

[21]: A. Weber, O. Gauthier-Lafaye, F. H. Julien, J. Brault, M. Gendry, Y. Désieres, and T. Benyattou; "Strong normal-incidence infrared absorption in self-organized InAs/InAlAs quantum dots grown on InP (001)" Appl. Phys. Lett. **74**, (1999) 413–415. https://doi.org/10.1063/1.123045

[22]: L. Chu, A. Zrenner, G. Böhm, and G. Abstreiter; "Normal-incident intersubband photocurrent spectroscopy on InAs/GaAs quantum dots" Appl. Phys. Lett., vol. **75**, (1999), 3599–3601. https://doi.org/10.1063/1.125400

[23]: S. Chakrabarti, A. D. Stiff-Roberts, P. Bhattacharya, S. Gunapala, S. Bandara, S. B. Rafol, and S. W. Kennerly; "High-temperature operation of InAs-GaAs quantum-dot infrared photodetectors with large responsivity and detectivity," in IEEE Photonics Technology Letters, **16**, (2004), 1361–1363. https://doi.org/10.1109/LPT.2004.825974

[24]: Jamie Phillips; "Evaluation of the fundamental properties of quantum dot infrared detectors" Journal of Applied Physics **91,** (2002), 4590–4594. https://doi.org/10.1063/1.1455130

[25]: Dong Pan, Elias Towe, and Steve Kennerly; "Normal-incidence intersubband (In, Ga)As/GaAs quantum dot infrared photodetectors" Appl. Phys. Lett. **73,** (1998) 1937–1939. https://doi.org/10.1063/1.122328

[26]: P. Martyniuk and A. Rogalski; "Quantum−dot infrared photodetectors: Status and outlook" Prog. Quantum Electron. **32**, (2008), 89–120 https://doi.org/10.1016/j.pquantelec.2008.07.001

[27] M.C. Löbl, S. Scholz, I. Söllner, et al. "Excitons in InGaAs quantum dots without electron wetting layer states". Commun Phys **2**, (2019), 93. https://doi.org/10.1038/s42005-019-0194-9

[28]: I.L. Krestnikov, N.N. Ledentsov, A. Hoffmann, and D. Bimberg; "Arrays of two-dimensional islands formed by submonolayer insertions: growth, properties, devices" Phys. Stat. Solidi (a) **183,** (2001), 207–233. https://doi.org/10.1002/1521-396X(200102)183:2<207::AID-PSSA207>3.0.CO;2-2

[29] hangcheng Xu, Dan Birkedal, Jørn M. Hvam, Zongyan Zhao, Yanmei Liu, Kuntang Yang, Aloke Kanjilal, Janusz Sadowski; "Structure and optical anisotropy of vertically correlated submonolayer InAs/GaAs quantum dots". Appl. Phys. Lett. **82,** (2003), 3859–3861. https://doi.org/10.1063/1.1581005

[30]: S. Sengupta, J. O. Kim, A. V. Barve, S. Adhikary, Y. D. Sharma, N. Gautam, S. J. Lee, S. K. Noh, S. Chakrabarti, and S. Krishna; "Submonolayer quantum dots in confinement enhanced dots-in-a-well heterostrucutures," Applied Physical Letters, **100**, (2012), 191111. https://doi.org/10.1063/1.4711214

[31]: Kim, Y., Kim, J., Lee, S. et al. "Submonolayer Quantum Dots for Optoelectronic Devices" J. Korean Phys. Soc. **73**, (2018), 833–840. https://doi.org/10.3938/jkps.73.833

[32]: L. Yu, D. Jung, S. Law, J. Shen, J. J. Cha, M. L. Lee, and D. Wasserman; "Controlling quantum dot energies using submonolayer bandstructure engineering". Appl. Phys. Lett. **105** (2014), 081103. https://doi.org/10.1063/1.4893983

[33]: Z. Xu, D. Birkedal, M. Juhl, and J. M. Hvam; "Submonolayer InGaAs/GaAs quantum-dot lasers with high modal gain and zerolinewidth enhancement factor" Applied Physics Letters, **85**, (2004), 3295–3261, https://doi.org/10.1063/1.1806564

[34]: F. Hopfer, A. Mutig, M. Kuntz, G. Fiol, D. Bimberg, N. N. Ledentsov, V. A. Shchukin, S. S. Mikhrin, D. L. Livshits, I. L. Krestnikov, A. R. Kovsh, N. D. Zakharov, and P. Werner; "Single-mode submonolayer quantum-dot vertical-cavity surface-emitting lasers with high modulation bandwidth" Appl. Phys. Lett. **89,** (2006), 141106. https://doi.org/10.1063/1.2358114

[35]: P. Lam, J. Wu, M. Tang, Q. Jiang, S. Hatch, R. Beanland, J. Wilson, R. Allison, and H. Liu; "Submonolayer InGaAs/GaAs quantum dot solar cells" Solar Energy Materials and Solar Cells, **126**, (2014), 83–87. https://doi.org/10.1016/j.solmat.2014.03.046

[36]: S. D. Gunapala *et al*., "640/spl times/486 long-wavelength two-color GaAs/AlGaAs quantum well infrared photodetector (QWIP) focal plane array camera". in IEEE Transactions on Electron Devices, **47**, (2000), 963–971. https://doi.org/10.1109/16.841227

[37]: H.S. Ling, S.Y. Wang, C.P. Lee, and M.C. Lo; "Confinement-enhanced dots-in-a-well QDIPs with operating temperature over 200K". Infrared Physics & Technology, **52,** (2009), 281–284, https://doi.org/10.1016/j.infrared.2009.05.026

[38]: https://ecohomeinsulation.com.au/thermal-imaging-for-insulation-inspections/

[39]: https://iactthermography.org/about/medical-infrared-imaging/

[40]: Saleh Taghvaeian, José L. Chávez, Jon Altenhofen, Tom Trout, and Kendall DeJonge, "Remote sensing for evaluating crop water stress at field scale using infrared thermography: potential and limitations", Hydrology Days, (2013), 74–83.

[41]: Infrared Detector Market by Fact. MR: https://www.factmr.com/report/infrared-detector-market.

[42] I. Lagraa, B. Soudini, H. Abid, S. Taleb, Study and optimization of structure InAs/InGaAs quantum dot in-a-well long-wave infrared photodetector, Optik, **251**, (2022), 168494. https://doi.org/10.1016/j.ijleo.2021.168494

[43]: David Z.-Y. Ting, Sumith V. Bandara, Sarath D. Gunapala, Jason M. Mumolo, Sam A. Keo, Cory J. Hill, John K. Liu, Edward R. Blazejewski, Sir B. Rafol, and YiaChung Chang; "Submonolayer quantum dot infrared photodetector", Appl. Phys. Lett. **94**, (2009), 111107. https://doi.org/10.1063/1.3095812

[44]: Andrea Lenz, Holger Eisele, Jonas Becker, Jan-Hindrik Schulze, Tim D. Germann, Franziska Luckert, Konstantin Pötschke, Ernst Lenz, Lena Ivanova, André Strittmatter, Dieter Bimberg, Udo W. Pohl, and Mario Dähne; "Atomic structure and optical properties of InAs submonolayer depositions in GaAs". Journal of Vacuum Science & Technology B **29,** (2011), 04D104. https://doi.org/10.1116/1.3602470

[45]: A. E. Zhukov, A. R. Kovsh, S. S. Mikhrin, N. A. Maleev, V. M. Ustinov, D. A. Livshits, and D. Bimberg; "3.9 W CW power from sub-monolayer quantum dot diode laser" Electronics Letters, **35**, (1999), 1845–1847. https://doi.org/10.1049/el:19991264

[46]: David Z.-Y. Ting, Yia-Chung Chang, Sir B. Rafol, John K. Liu, Cory J. Hill, Sam A. Keo, Jason Mumolo, Sarath D. Gunapala, and Sumith V. Bandara; "The sub-monolayer quantum dot infrared photodetector revisited" Infrared Phys. Technol. **70,** (2015), 20–24, https://doi.org/10.1016/j.infrared.2014.09.028

[47]: J. G. Belk, C. F. McConville, J. L. Sudijono, T. S. Jones, and B. A. Joyce; "Surface alloying at InAs-GaAs interfaces grown on (001) surfaces by molecular beam epitaxy" Surface Science **387**, (1997), 213–226. https://doi.org/10.1016/S0039-6028(97)00355-5

[48]: G. R. Bell, T. J. Krzyzewski, P. B. Joyce, and T. S. Jones; "Island size scaling for submonolayer growth of InAs on GaAs(001)-(2×4):Strain and surface reconstruction effects" Physical Review B, **61**, (2000), R10551–R10554. https://doi.org/10.1103/physrevb.61.r10551

[49]:https://www.britannica.com/science/light/The-electromagnetic-spectrum#/media/1/340440/ 736 77

[50] A. Sobrino, F. Del Frate, M. Drusch, J. C. Jiménez-Muñoz, P. Manunta and A. Regan, "Review of Thermal Infrared Applications and Requirements for Future High-Resolution Sensors," in IEEE Transactions on Geoscience and Remote Sensing, **54**,(2016), 2963-2972. https://doi.org/10.1109/TGRS.2015.2509179

[51]: Glenn J. Tattersall, "Infrared thermography: A non-invasive window into thermal physiology", Comparative Biochemistry and Physiology Part A: Molecular & Integrative Physiology, **202**, (2016), 78-98, https://doi.org/10.1016/j.cbpa.2016.02.022

[52]: C. Ibarra-Castanedo, S. Sfarra, M. Genest, and X. Maldague, Infrared Vision: Visual Inspection Beyond the Visible Spectrum. In: Liu, Z., Ukida, H., Ramuhalli, P., Niel, K. (eds) Integrated Imaging and Vision Techniques for Industrial Inspection. Advances in Computer Vision and Pattern Recognition. Springer, London. (2015), page 41. https://doi.org/10.1007/978-1-4471-6741-9_2

[53]: Thomas P. Sheahen, "Effect of atmospheric attenuation on temperature measurements made using IR scanning systems," Appl. Opt. **22**, (1983), 1070-1077. https://doi.org/10.1364/ AO.22.001070

[54]: https://upload.wikimedia.org/wikipedia/commons/6/64/Infrared_spectrum.gif

[55]: Shinpei Ogawa and Masafumi Kimata; "Wavelength- or Polarization-Selective Thermal Infrared Detectors for Multi-Color or Polarimetric Imaging Using Plasmonics and Metamaterials", Materials, **10**, (2017), 493. https://doi.org/10.3390/ma10050493

[56]: J. Piotrowski, W. Galus, M. Grudzien, Near room-temperature IR photo-detectors, Infrared Physics, **31**, (1991), 1-48. https://doi.org/10.1016/0020-0891(91)90037-G

[57]: E. Towe and D. Pan, "Semiconductor quantum-dot nanostructures: Their application in a new class of infrared photodetectors," in IEEE Journal of Selected Topics in Quantum Electronics, **6**, (2000), 408-421. https://doi.org/10.1109/2944.865096

[58]: Baker, I. II–VI Narrow-Bandgap Semiconductors for Optoelectronics. In: Kasap, S., Capper, P. (eds) Springer Handbook of Electronic and Photonic Materials. Springer Handbooks. Springer, Boston, MA. (2006), 855–885 https://doi.org/10.1007/978-0-387-29185-7_36

[59]: Paul Norton; "HgCdTe infrared detectors" Opto-Electronics Review **10**, (2002), 159–174 ISBN 1-56677-215-X

[60]: Antoni Rogalski; Infrared Detectors 2ndedition, CRC Press, Taylor & Francis Group, (2011), page 30. https://doi.org/10.1201/b10319

[61]: M.A .Kinch; "Fundamental Physics of Infrared Detector Materials," Journal of Electronic Materials **29**, (2000), 809–817. https://doi.org/10.1007/s11664-000-0229-7

[62]: R. A. Soref; "Extrinsic ir Photoconductivity of Si Doped with B, Al, Ga, P, As, or Sb" Journal of Applied Physics **38,** (1967), 5201–5209. https://doi.org/10.1063/1.1709302

[63]: A.Rogalski; "GaAs/AlGaAs QWIPs vs HgCdTe Photodiodes for LWIR Applications". In: Liu, H.C., Levine, B.F., Andersson, J.Y. (eds) Quantum Well Intersubband Transition Physics and Devices. NATO ASI Series, **270**. Springer, Dordrecht. (1994) https://doi.org/10.1007/978-94-011-1144-7_7

[64]: T. Edvinsson; "Opticalquantum confinement and photocatalyticproperties in two-, one- and zero-dimensional nanostructures".R. Soc. open sci. **5**, (2018), 180387. https://doi.org/10.1098/ rsos.180387

[65]: J. C. Campbell and A. Madhukar; "Quantum-Dot Infrared Photodetectors," Proceedings of the IEEE **95**, (2007), 1815–1827. https://doi.org/10.1109/JPROC.2007.900967

[66]: H. C. Liu, M. Gao, J. McCaffrey, Z. R. Wasilewski, and S. Fafard; "Quantum dot infrared photodetectors," Appl. Phys. Lett. **78**, (2001), 79–81. https://doi.org/10.1063/1.1337649

[67]: S. Fafard, R. Leon, D. Leonard, J. L. Merz, and P. M. Petroff; "Phonons and radiative recombination in self-assembled quantum dots," Phys. Rev. B **52**, (1995), 5752. https://doi.org/10.1103/PhysRevB.52.5752

[68]: M. Bayer, O. Stern, P. Hawrylak, et al. "Hidden symmetries in the energy levels of excitonic 'artificial atoms'". Nature, **405**, (2000), 923–926. https://doi.org/10.1038/35016020

[69]: P. Hawrylak, A. Wojs, D.J. Lockwood, P.D. Wang, C.M. Sotomayor Torres, A. Pinczuk, and B.S. Dennis; "Optical spectroscopies of electronic excitations in quantum dots," Surface Science, **361–362**, (1996), 774–777. https://doi.org/10.1016/0039-6028(96)00531-6

[70]: D. Leonard, M.Krishnamurthy, C. M. Reaves, S. P. Denbaars, and P. M. Petroff; "Direct formation of quantum-sized dots from uniform coherent islands of InGaAs on GaAs surfaces" Appl. Phys. Lett. **63**, (1993), 3203–3205. https://doi.org/10.1063/1.110199

[71]: J. Jiang, S. Tsao, T. O'Sullivan, W. Zhang, H. Lim, T. Sills, K. Mi, M. Razeghi, G. J. Brown, and M. Z. Tidrow; "High detectivity InGaAs/InGaP quantum-dot infrared photodetectors grown by low pressure metalorganic chemical vapor deposition". Appl. Phys. Lett. **84**, (2004), 2166–2168.

https://doi.org/10.1063/1.1688982

[72]: S. Sengupta and S. Chakrabarti; "Structural, Optical and Spectral Behaviour of InAs-based Quantum Dot Heterostructures" (2018). https://doi.org/10.1007/978-981-10-5702-1

[73]: J. Phillips, P. Bhattacharya, S. W. Kennerly, D. W. Beekman, and M. Dutta; "Self-assembled InAs-GaAs quantum-dot intersubband detectors," IEEE J. Quant. Electron. **35**, (1999), 936–943. https://doi.org/10.1109/3.766837

[74]: S. Y. Wang, S. D. Lin, H. W. Wu, and C. P. Lee; "Low dark current quantum-dot infrared photodetectors with an AlGaAs current blocking layer," Appl. Phys. Lett. **78**, (2001), 1023–1025. https://doi.org/10.1063/1.1347006

[75]: S.-F. Tang, S.-Y. Lin, and S.-C. Lee; "Near-room-temperature operation of an InAs/GaAs quantum-dot infrared photodetector," Appl. Phys. Lett. **78**, (2001), 2428–2430. https://doi.org/10.1063/1.1362201

[76]: Z. Chen, O. Baklenov, E. T. Kim, I. Mukhametzhanov, J. Tie, A. Madhukar, Z. Ye, and J. C. Campbell; "Normal incidence InAs/$Al_xGa_{1-x}As$ quantum dot infrared photodetectors with undoped active region," J. Appl. Phys. **89**, (2001), 4558–4563. https://doi.org/10.1063/1.1356430

[77]: S. Krishna, A.D. Stiff-Roberts, J.D. Phillips, P. Bhattacharya, and S.W. Kennerly; "Hot dot detectors" IEEE Circ. Dev. Mag. **18,** (2002), 14–24. https://doi.org/10.1109/MCD.2002.981296

[78]: Y. H. Kang, J. Park, U. H. Lee, and S. Hong; "Effect of the dot size distribution on quantum dot infrared photoresponse and temperature-dependent dark current," Appl. Phys. Lett. **82**, (2003), 1099–1101. https://doi.org/10.1063/1.1555711

[79]: S. Krishna, S. Raghavan, G. v. Winckel, P. Rotella, A. Stintz, C. P. Morath, D. Le, and S. W. Kennerly; "Two color InAs/InGaAs dots-in-a-well detector with background-limited performance at 91 K," Appl. Phys. Lett. **82**, (2003), 2574–2576. https://doi.org/10.1063/1.1567806

[80]: S. Chakrabarti, A. D. Stiff-Roberts, X. H. Su, P. Bhattacharya, G. Ariyawansa, and A. G. U. Perera; "High-performance mid-infrared quantum dot infrared photodetectors," J. Phys. D: Appl. Phys. **38**, (2005), 2135–2141. https://doi.org/10.1088/0022-3727/38/13/009

[81]: S. Chakrabarti, X. H. Su, P. Bhattacharya, G. Ariyawansa, and A. G. U. Perera; "Characteristics of a multi-color InGaAs/GaAs quantum dot infrared photodetector," IEEE Photon. Technol. Lett. **17**, (2005), 178–180. https://doi.org/10.1109/LPT.2004.838295

[82]: Eui-Tae Kim, Anupam Madhukar, Zhengmao Ye, and Joe C. Campbell; High detectivity InAs quantum dot infrared photodetectors. Appl. Phys. Lett. **84,** (2004), 3277–3279. https://doi.org/10.1063/1.1719259

[83]: J.-W. Kim, J.-E. Oh, S.-C. Hong, C.-H. Park, and T.-K. Yoo, "Room temperature far infrared (8-10 um) photodetectors using self-assembled InAs quantum dots with high detectivity," IEEE Electron Dev. Lett. **21**, (2000), 329–331. https://doi.org/10.1109/55.847370

[84]: S. D. Gunapala, S. V. Bandara, C. J. Hill, D. Z. Ting, J. K. Liu, S. B. Rafol, E. R. Blazejewski, J. M. Mumolo, S. A. Keo, S. Krishna, Y.-C. Chang, and C. A. Shott, "640×512 pixels long-wavelength infrared (LWIR) quantum-dot infrared photodetector (QDIP) imaging focal plane array,"

IEEE J. Quant. Electron. **43**, (2007), 230–237. https://doi.org/10.1109/JQE.2006.889645

[85]: N. Ledentsov, D. Bimberg, F. Hopfer, et al. "Submonolayer Quantum Dots for High Speed Surface Emitting Lasers," Nanoscale Res Lett **2**, (2007), 417. https://doi.org/10.1007/s11671-007-9078-0

[86]: F. Hopfer, A. Mutig, G. Fiol, M. Kuntz, V. A. Shchukin, V. A. Haisler, T. Warming, E. Stock, S. S. Mikhrin, I. L. Krestnikov, D. A. Livshits, A. R. Kovsh, C. Bornholdt, A. Lenz, H. Eisele, M. Dahne, N. N. Ledentsov, and D. Bimberg; "20 Gb/s 85 °C error-free operation of vcsels based on submonolayer deposition of quantum dots," in IEEE Journal of Selected Topics in Quantum Electronics, **13**, (2007), 1302–1308. https://doi.org/10.1109/JSTQE.2007.905133

[87]: A. Y. Cho and J. R. Arthur; "Molecular beam epitaxy," Prog. Solid State Chem. **10,** (1975), 157–192. https://doi.org/10.1016/0079-6786(75)90005-9

[88]: John Prineas; "The Art and Science of Molecular Beam Epitaxy and the Nobel Prize for Blue LEDs," Department of Physics and Astronomy, University of Iowa, (2014), page 44.

[89]: Lorenzo Morresi, Molecular Beam Epitaxy (MBE), Silicon Based Thin Film Solar Cells, 2013, page 84. e-ISBN: 978-1-60805-518-0

[90]: K. Ploog; "Microscopical Structuring of Solids by Molecular Beam Epitaxy—Spatially Resolved Materials Synthesis," Angewandte Chemie, **27**, (1988), 593–621. https://doi.org/10.1002/anie.198805933

[91]: https://www.sunnetsystems.com/thermal-sources

[92]: Jinkwan Kwoen and Yasuhiko Arakawa, "Classification of Reflection High-Energy Electron Diffraction Pattern Using Machine Learning," Crystal Growth & Design, **20**, (2020), 5289-5293. https://doi.org/10.1021/acs.cgd.0c00506

[93]: Marco Malinverni; Optimization of NH3 -MBE grown p-doped (Al)GaN layers and their implementation in long wavelength laser diodes and tunnel junctions, Ph.D. thesis, page 20, Ecole Polytechnique Fédérale de Lausanne -EPFL- (Switzerland), 2015

[94]: S. Munnix, R. K. Bauer, D. Bimberg, J. S. Harris, R. Köhrbrück, E. C. Larkins, Ch. Maierhofer, D. E. Mars, and J. N. Miller; "Growth kinetics, impurity incorporation, defect generation, and interface quality of molecular-beam epitaxy grown AlGaAs/GaAs quantum wells: Role of group III and group V fluxes," J. Vac. Sci. Technol B: Microelectronics Processing and Phenomena, **7,** (1989), 704–709. https://doi.org/10.1116/1.584629

[95]: B. F. Lewis, F. J. Grunthaner, A. Madhukar, T. C. Lee, and R. Fernandez; "Reflection high energy electron diffraction intensity behavior during homoepitaxial molecular beam epitaxy growth of GaAs and implications for growth kinetics and mechanisms," Journal of Vacuum Science & Technology B: Microelectronics Processing and Phenomena, **3**, (1985), 1317–1322. https://doi.org/10.1116/1.582986

[96]: Y. Wang, W. Chen, B. Wang, and Y. Zheng; "Ultrathin Ferroelectric Films: Growth, Characterization, Physics and Applications," Materials, **7**, (2014), 6377–6485. https://doi.org/10.3390/ma7096377

[97]: J. X. Chen, A. Markus, A. Fiore, U. Oesterle, R. P. Stanley, J. F. Carlin, R. Houdre, M. Ilegems, L. Lazzarini, L. Nasi M. T. Todaro, E. Piscopiello, , R. Cingolani, M. Catalano, J. Katcki, and J. Ratajczak; "Tuning InAs/GaAs quantum dot properties under Stranski-

Krastanov growth mode for 1.3 μm applications" J. Appl. Phys., **91**, (2002), 6710–6716. https://doi.org/10.1063/1.1476069

[98]: R. Cisneros Tamayo, I.J. Guerrero Moreno, G. Polupan, T.V. Torchynska, and J. Palacios Gomez; "Emission of InAs quantum dots embedded in InGaAs/InAlGaAs/GaAs quantum wells," Journal of Luminescence, **149**, (2014), 1-6. https://doi.org /10.1016/j.jlumin.2013.12.053

[99]: M. V. Maximov, Yu. M. Shernyakov, A. F. Tsatsul'nikov, A. V. Lunev, A. V. Sakharov, V. M. Ustinov, A. Yu. Egorov, A. E. Zhukov, A. R. Kovsh, P. S. Kop'ev, L. V. Asryan, Zh. I. Alferov, N. N. Ledentsov, D. Bimberg, A. O. Kosogov, and P. Werner; "High-power continuous-wave operation of a InGaAs/AlGaAs quantum dot laser". Journal of Applied Physics, **83** (1998), 5561–5563. https://doi.org/10.1063/1.367390

[100]: L. Chu, M. Arzberger, G. Böhm, and G. Abstreiter; "Influence of growth conditions on the photoluminescence of self-assembled InAs/GaAs quantum dots". Journal of Applied Physics **85**, (1999), 2355–2362. https://doi.org/10.1063/1.369549

[101]: L. Casas-Espinola, T.V. Torchynska, G.P. Polupan, and E. Velazquez-Lozada; "Multi excited state study in InAs DWELL structures", Materials Science and Engineering B **165**, (2009), 115–117. https://doi.org/10.1016/j.mseb.2009.01.006

[102]: Yagya D. Sharmaa, M. N. Kutty, R. V. Shenoi, Ajit V. Barve, S. Myers, J. Shao, E. Plis, S. Leeb), S. Nohb), and S. Krishna; "Investigation of multi stack InAs/InGaAs/GaAs self-assembled quantum dots-in-double-well structures for infrared detectors", Journal of Vacuum Science & Technology B **28**, (2010), C3G1–C3G7. https://doi.org/10.1116/1.3319324

[103]: Hong-Shi Ling, Shiang-Yu Wang, Wei-Cheng Hsu, and Chien-Ping Lee, "Voltage-tunable dual-band quantum dot infrared photodetectors for temperature sensing," Opt. Express **20**, (2012), 10484–10489. https://doi.org/10.1364/OE.20.010484

[104]: Benjamin Lingnau, Kathy Lüdge, Bastian Herzog, Mirco Kolarczik, Yücel Kaptan, Ulrike Woggon, and Nina Owschimikow; "Ultrafast gain recovery and large nonlinear optical response in submonolayer quantum dots," Phys. Rev. B **94**, (2016), 014305. https://doi.org/10.1103/PhysRevB.94.014305

[105]: J. O. Kim, S. Sengupta, A. V. Barve, Y. D. Sharma, S. Adhikary, S. J. Lee, S. K. Noh, M. S. Allen, J. W. Allen, S. Chakrabarti, and S. Krishna; "Multi-stack InAs/InGaAs sub-monolayer quantum dots infrared photodetectors" Appl. Phys. Lett **102**, (2013), 011131 https://doi.org/10.1063/1.4774383

[106]: S. Sengupta, A. Mandal, H. Ghadi, and S. Chakrabarti; "Comprehensive study on molecular beam epitaxy-grown InAs sub-monolayer quantum dots with different capping combinations", J. Vac. Sci. Technol B **31**, (2013), 03C136. https://doi.org/10.1116/1.4805018

[107]: J. O. Kim, Z. Ku, A. Kazemi, A. Urbas, S.-W. Kang, S. K. Noh, S. J. Lee, and S. Krishna; "Effect of barrier on the performance of sub-monolayer quantum dot infrared photodetectors," Opt. Mater. Express, **4**, (2014), 198–204. https://doi.org/10.1364/OME.4.000198

[108]: A.Y. Cho; "GaAs Epitaxy by a Molecular Beam Method: Observations of Surface Structure on the (001) Face", J. Appl. Phys. **42,** (1971), 2074–2081. https://doi.org/10.1063/1.1660490

[109]: Q.-K. Xue, T. Hashizume, and T. Sakurai; "Scanning tunneling microscopy of III-V compound semiconductor (001) surfaces," Prog. Surf. Sci., **56**, (1997), 1-131. https://doi.org/10.1016/S0079-6816(97)00033-6

[110]: V. P. LaBella, D. W. Bullock, C. Emery, Z. Ding, P. M. Thibado; Enabling electron diffraction as a tool for determining substrate temperature and surface morphology. Appl. Phys. Lett. **79**, (2001), 3065–3067. https://doi.org/10.1063/1.1416477

[111]: Akihiro Ohtake, "Surface reconstructions on GaAs(001)", Surface Science Reports **63,** (2008), 295–327. https://doi.org/10.1016/j.surfrep.2008.03.001

[112]: A. Y. Cho; "Bonding direction and surface-structure orientation on GaAs (001)". Journal of Applied Physics 1 July; **47**, (1976), 2841–2843. https://doi.org/10.1063/1.323081

[113]: A. Ohtake and N. Koguchi; "Two types of structures for the GaAs(001)-c(4×4) surface," Applied Physics Letters, **8,** (2003), 5193–5195. https://doi.org/10.1063/1.1635078

[114]: D. J. Chadi; "Atomic structure of GaAs(100)-(2×1) and (2×4) reconstructed surfaces" J. Vac. Sci. Technol A. **5**, (1987): 834–837. https://doi.org/10.1116/1.574366

[115] A. Alzeidan, M. S. Claro, and A.A. Quivy; "High-detectivity infrared photodetector based on InAs submonolayer quantum dots grown on GaAs(001) with a 2 × 4 surface reconstruction," Journal of Applied Physics, 126, (2019), 224506. https://doi.org/10.1063/1.5125238

[116]: Álvaro Diego B. Maia, Crescimento, fabricação e testedefotodetectores de radiaçãoinfravermelha baseados em pontosquânticos. Ph.D. Thesis, (2012), page 48, University of São Paulo.

[117]: M. M. Sobolev, I. V. Kochnev, V. M. Lantratov, N. A. Bert, N. A. Cherkashin, N. N. Ledentsov, and D. A. Bedarev; "Thermal annealing of defects in InGaAs/GaAs heterostructures with three-dimensional islands" Semiconductors **34**, (2000), 195–204. https://doi.org/10.1134/1.1187932

[118]: Sara Sabri, Abdelilah Faraji, Rachid Malek, Khalil Kassmi, "Photoluminescence (PL) characterization of InAs/GaAs quantum dots (QDs): A theoretical study", Materials Today: Proceedings, **45** , (2021), 7383-7387, https://doi.org/10.1016/j.matpr.2021.01.317

[119]: S. Harrison, M. P. Young, P. D. Hodgson, R. J. Young, M. Hayne, L. Danos, A. Schliwa, A. Strittmatter, A. Lenz, H. Eisele, U. W. Pohl, D. Bimberg; "Heterodimensional charge-carrier confinement in stacked submonolayer InAs in GaAs", Phys. Rev. B **93,** (2016), 085302-9. https://doi.org/10.1103/PhysRevB.93.085302

[120]: T.F. Cantalice, A. Alzeidan, G.M. Jacobsen, T. Borrely, M.D. Teodoro, A.A. Quivy, "Evidence of weak strain field in InAs/GaAs submonolayer quantum dots", Micro and Nanostructures, **172**, (2022), 207449. https://doi.org/10.1016/j.micrna.2022.207449

[121]: G. Binnig, C. F. Quate, and Ch Gerber. "Atomic force microscope" Physical Review Letters, **56**, (1986), 930–933. https://doi.org/10.1103/PhysRevLett.56.930

[122]: S. Morandat, S. Azouzi, E. Beauvais, A. Mastouri, and K. El Kirat. "Atomic force microscopy of model lipid membranes". Anal Bioanal Chem **405**, (2013), 1445–1461. https://doi.org/10.1007/s00216-012-6383-y

[123]: Typical atomic force microscope (AFM) setup: Opensource Handbook of Nanoscience and Nanotechnology, https://commons.wikimedia.org/wiki/Nanotechnology#/media/ File:AFMsetup.jpg

[124]: N. Jalili and K. Laxminarayana, "A review of atomic force microscopy imaging systems: application to molecular metrology and biological sciences", Mechatronics, **14**, (2004), 907–945, https://doi.org/10.1016/j.mechatronics.2004.04.005

[125]: A. Alessandrini, and P. Facci, "AFM: a versatile tool in biophysics". Measurement Science and Technology, **16**, (2005), R65–R92. https://doi.org/10.1088/0957-0233/16/6/R01

[126]: Bullen, R.A.W.a.H.A., Lecture notes: Introduction to Scanning Probe Microscopy. http://www.analyzetest.com/2021/03/16/623/

[127]: S. K. Arumugasamy, G. Chellasamy, S. Govindaraju, and K. Yun, "Chapter 30 - Recent developments in using atomic force microscopy in microbiology research: An update", Recent Developments in Applied Microbiology and Biochemistry, Academic Press, (2021), page 320. https://doi.org/10.1016/B978-0-12-821406-0.00030-8

[128]: C. Leung, A. Bestembayeva, R. Thorogate, J. Stinson, A. Pyne, C. Marcovich, J. Yang, U. Drechsler, M. Despont, T. Jankowski. "Atomic force microscopy with nanoscale cantilevers resolves different structural conformations of the DNA double helix". Nano Lett **12**, (2012), 3846–3850. https://doi.org/10.1021/nl301857p

[129]: Wenquan Ma, Richard Nötzel, Hans-Peter Schönherr, Klaus H. Ploog; "Shape transition of coherent three-dimensional (In,Ga)As islands on GaAs(100)". Appl. Phys. Lett. **79**, (2001), 4219–4221. https://doi.org/10.1063/1.1428107

[130]: Lihua Wang, Ze Zhang, and Xiaodong Han, "In situ experimental mechanics of nanomaterials at the atomic scale", NPG Asia Materials **5**, (2013), e40. https://doi.org/10.1038/am.2012.70

[131]: Zhong Lin Wang, Jean L. Lee, "Chapter 9 - Electron Microscopy Techniques for Imaging and Analysis of Nanoparticles", Editor(s): Rajiv Kohli, K.L. Mittal, Developments in Surface Contamination and Cleaning 2 Edition, (2008), 395–443. https://doi.org/10.1016/B978-0-323-29960-2.00009-5

[132]: N. Marturi. "Vision and visual servoing for nanomanipulation and nanocharacterization in scanning electron microscope". Micro and nanotechnologies/Microelectronics. Université de Franche Comté, (2013), page 13.

[133]: https://www.jeol.co.jp/en/products/detail/JEM-2100F.html

[134]: Tiago F Cantalice, Ahmad Alzeidan, Sergio M Urahata, and Alain A Quivy, "In-situ measurement of indium segregation in InAs/GaAs submonolayer quantum dots", Mater. Res. Express **6** (2019) 126205, https://doi.org/10.1088/2053-1591/ab55a8

[135]: T. Niermann, F. Kießling, M. Lehmann, J.-H. Schulze, T. D. Germann, K. Pötschke, A. Strittmatter, and U. W. Pohl, "Atomic structure of closely stacked InAs submonolayer depositions in GaAs", J. Appl. Phys **112**, (2012), 083505. http://dx.doi.org/10.1063/1.4758301

[136]: G. Binnig, H. Rohrer, Ch. Gerber, E. Weibel; "Tunneling through a controllable vacuum gap". Appl. Phys. Lett. **40**, (1982), 178–180. https://doi.org/10.1063/1.92999

[137]: https://commons.wikimedia.org/wiki/File:ScanningTunnelingMicroscope_schematic.png#/media/File:ScanningTunnelingMicroscope_schematic.png

[138]: D. A. Bonnell. "Scanning Tunneling Microscopy. In Encyclopedia of Materials: Science and Technology", Elsevier, (2001), 8269-8281. https://doi.org/10.1016/B0-08-043152-6/01480-7

[139]: Yu ET. "Cross-Sectional Scanning Tunneling Microscopy". Chem Rev. **97**, (1997), 1017-1044. https://doi.org/10.1021/cr960084n

[140]: A. Lenz, Atomic structure of capped In(Ga)As and GaAs quantum dots for optoelectronic devices, Ph.D. Thesis, page 3, TU Berlin, 2008.

[141]: Raja Sekhar Reddy Gajjela, Ahmad Alzeidan, Victor M. O. Curbelo, Alain A. Quivy, and Paul M. Koenraad, "Atomic-scale characterization of single and double layers of InAs and InAlAs Stranski-Krastanov quantum dots", Phys. Rev. Materials **6**, (2022), 114604. https://doi.org/10.1103/PhysRevMaterials.6.114604

[142]: R.S.R. Gajjela, A.L. Hendriks, A. Alzeidan, T.F. Cantalice, A.A. Quivy, and P.M. Koenraad "Cross-sectional scanning tunneling microscopy of InAs/GaAs(001) submonolayer quantum dots", Phys. Rev. Materials **4**, (2020), 114601. https://doi.org/10.1103/PhysRevMaterials.4.114601

[143]: Bert, N.A., Kolesnikova, A.L., Nevedomsky, V.N. et al. "Formation of dislocation defects in the process of burying of InAs quantum dots into GaAs" Semiconductors **43**, (2009), 1387–1393. https://doi.org/10.1134/S1063782609100236

[144]: K. Muraki, S. Fukatsu, Y. Shiraki, R. Ito; "Surface segregation of In atoms during molecular beam epitaxy and its influence on the energy levels in InGaAs/GaAs quantum wells". Appl. Phys. Lett. **61,** (1992), 557–559. https://doi.org/10.1063/1.107835

[145]: M.J. da Silva, S. Martini, T.E. Lamas, A.A. Quivy, E.C.F. da Silva, J.R. Leite, "Low growth rate InAs/GaAs quantum dots for room-temperature luminescence over 1.3 mm", Microelectronics Journal **34**, (2003), 631–633. https://doi.org/10.1016/S0026-2692(03)00066-1

[146]: P. B. Joyce, T. J. Krzyzewski, G. R. Bell, and T. S. Jones, Effect of growth rate on the size, composition, and optical properties of InAs/GaAs quantum dots grown by molecular-beam epitaxy, Phys. Rev. B **62**, (2000), 10891. https://doi.org/10.1103/PhysRevB.62.10891

[147]: P.M. Koenraad, D.M. Bruls, J.H. Davies, S.P.A. Gill, Fei Long, M. Hopkinson, M. Skolnick, J.H. Wolter, "Composition profiling at the atomic scale in III–V nanostructures by cross-sectional STM", Physica E: Low-dimensional Systems and Nanostructures, **17**, (2003), 526-532, https://doi.org/10.1016/S1386-9477(02)00860-3

[148]: Im Sik Han, Jong Su Kim, Jun Oh Kim, Sam Kyu Noh, Sang Jun Lee, "Fabrication and characterization of InAs/InGaAs sub-monolayer quantum dot solar cell with dot-in-a-well structure", Current Applied Physics, **16**, (2016), 587–592. https://doi.org/10.1016/j.cap.2016.02.009

[149]: S. Martini, A.A. Quivy, T.E. Lamas, M.J. da Silva, E.C.F. da Silva, and J.R. Leite; "Ex-situ investigation of indium segregation in InGaAs/GaAs quantum wells using high-resolution x-ray diffraction" J. Cryst. Growth **251**, (2003), 101 https://doi.org/10.1063/1.1621738

[150]: K. H. Schmidt, G. Medeiros-Ribeiro, J. Garcia, P. M. Petroff; "Size quantization effects in InAs

self-assembled quantum dots", Appl. Phys. Lett. **70**, (1997) 1727–1729. https://doi.org/10.1063/1.118682

[151]: J. G. Keizer, A. B. Henriques, A. D. B. Maia, A. A. Quivy, and P. M. Koenraad, Atomically resolved study of the morphology change of InAs/GaAs quantum dot layers induced by rapid thermal annealing, Appl. Phys. Lett. **101**, (2012), 243113. https://doi.org/10.1063/1.4770371

[152]: Qianghua Xie, Anupam Madhukar, Ping Chen, Nobuhiko P. Kobayashi, "Vertically self-organized InAs quantum box islands on GaAs(100)", Phys. Rev. Lett. **75**, (1995), 2542–2545, https://doi.org/10.1103/PhysRevLett.75.2542

[153]: A. Alzeidan, T. F. Cantalice, K. D. Vallejo, R. S. R Gajjela, A. L. Hendriks, P. J. Simmonds, P. M. Koenraad, A. A. Quivy, "Effect of As flux on InAs submonolayer quantum dot formation for infrared photodetectors", Sensors and Actuators: A. Physical. **334,** (2022), 113357:1-8. https://doi.org/10.1016/j.sna.2021.113357

[154]: Z. Ding, P. M. Thibado, C. Awo-Affouda, V. P. LaBella. "Electron-beam evaporated cobalt films on molecular beam epitaxy prepared GaAs(001)". Journal of Vacuum Science & Technology B: Microelectronics and Nanometer Structures. **22**, (2004), page 2069. https://doi.org/10.1116/1.1771674

[155]: Allwin21 Corp, modelo Accuthermo AW 610 RTP, https://allwin21.com/accuthermo-aw-610/

[156]: Tiago Fernandes de Cantalice: Fotodetectores de radiação infravermelha fabricados com pontos quânticos de InGaAs/GaAs", Ph.D. thesis, 2023, pages 28-35, University of São Paulo.

[157]: J. D. Vincent, Fundamentals of Infrared Detector Operation and Testing (Wiley, 1990). pp. 504. ISBN 0-471-50272-3.

[158]: Nasr A, El Mashade MB. "Theoretical comparison between quantum well and dot infrared photodetectors". IEE Proc—Optoelectron **153**, (2006), 183–90. https://doi.org/10.1049/ip-opt:20050029

[159]: A. D. Stiff-Roberts, X. H. Su, S. Chakrabarti and P. Bhattacharya, "Contribution of field-assisted tunneling emission to dark current in InAs-GaAs quantum dot infrared photodetectors," in IEEE Photonics Technology Letters, **16**, (2004), 867–869. https://doi.org/10.1109/LPT.2004.823690

[160]: L. Gendron, C. Koeniguer, V. Berger, and X. Marcadet. "High resistance narrow band quantum cascade photodetectors". Appl. Phys. Lett., **86**, (2005), 121116. https://doi.org/10.1063/1.1884257

[161]: F. Wang, T. Zhang, R. Xie, Z. Wang, And W. Hu. "How to characterize figures of merit of two-dimensional photodetectors". Nature Communications **14**, (2023), 2224. https://doi.org/10.1038/s41467-023-37635-1

[162]: R. C. Jones, "Phenomenological Description of the Response and Detecting Ability of Radiation Detectors," in Proceedings of the IRE, **47,** (1959), 1495–1502. https://doi.org/10.1109/JRPROC.1959.287047

[163]: Zhengmao Ye, Joe C. Campbell, Zhonghui Chen, Eui-Tae Kim, and Anupam Madhukar, "Noise and photoconductive gain in InAs quantum dot infrared photodetectors," Appl. Phys. Lett. **83**, (2003), 1234–1236. https://doi.org/10.1063/1.1597987

[164]: R. Clark Jones, "Proposal of the Detectivity D** for Detectors Limited by Radiation Noise" J. Opt. Soc. Am. **50**, (1960), 1058–1059. https://doi.org/10.1364/JOSA.50.001058

[165]: G. Jolley, L. Fu, H.H. Tan, and C. Jagadish, "Effects of annealing on the spectral response and dark current of quantum dot infrared photodetectors". Journal of Physics D: Applied Physics, **41**, (2008), 215101. https://doi.org/10.1088/0022-3727/41/21/215101

[166]: Yuwei Zhou, Zhifeng Li, Xiaohao Zhou, Jing Zhou, Yuanliao Zheng, Liang Li, Ning Li, Pingping Chen, Xiaoshuang Chen, Wei Lu; "Cut-off wavelength manipulation of pixel-level plasmonic microcavity for long wavelength infrared detection". Appl. Phys. Lett. **114** , (2019), 061104. https://doi.org/10.1063/1.5082830

[167]: S. Unsleber, M. Deppisch, C.M. Krammel, M. Vo, C.D. Yerino, P.J. Simmonds, M. Larry Lee, P. M. Koenraad, C. Schneider, S. Höfling, "Bulk AlInAs on InP(111) as a novel material system for pure single photon emission", Optics Express **24,** (2016), 23198-23206. https://doi.org/10.1364/OE.24.023198

[168]: S. Gallardo, Y. Kudriatsev, A. Villegas, G. Ramírez, R. Asomoza, E. Cruz-Hernández, J.S. Rojas-Ramirez, M. López-López, "SIMS characterization of segregation in InAs/GaAs heterostructures", Applied Surface Science, **255**, (2008), 1341–1344. https://doi.org/10.1016/j.apsusc.2008.05.174

[169]: T. V. Torchynska, A. Stintz; "Some aspects of emission variation in InAs quantum dots coupled with symmetric quantum wells". Journal of Applied Physics **108,** (2010), 024316. https://doi.org/10.1063/1.3455851

[170]: Koichi Yamaguchi, Kunihiko Y Ujobo and Toshiyuki K Aizu, ″Stranski-Krastanov Growth of InAs Quantum Dots with Narrow Size Distribution″ Jpn. J. Appl. Phys. **39,** (2000), L1245 https://doi.org/10.1143/JJAP.39.L1245

[171]: T. Kawai, H. Yonezu, Y. Ogasawara, D. Saito, and K. Pak; "Segregation and Interdiffusion of in Atoms in GaAs/InAs/GaAs Heterostructures". MRS Online Proceedings Library (OPL), **312**, (1993), 113-118. https://doi.org/10.1557/PROC-312-113

[172]: A.D.B. Maia, E.C.F. da Silva, A.A. Quivy, V. Bindilatti, V.M. de Aquino, and I.F.L. Dias "The influence of different indium-composition profiles on the electronic structure of lens-shaped InxGa1−xAs quantum dots". Journal of Physics D: Applied Physics, **45**, (2012), 225104. https://doi.org/10.1088/0022-3727/45/22/225104

[173]: Keun-Yong Ban, Woong-Ki Hong, Stephen P. Bremner, Som N. Dahal, Heather McFelea, Christiana B. Honsberg; "Controllability of the subband occupation of InAs quantum dots on a delta-doped GaAsSb barrier". Journal of Applied Physics, **109**, (2011), 014312. https://doi.org/10.1063/1.3527039

[174]: Tetsuya Asano, Anupam Madhukar, Krishnamurthy Mahalingam, Gail J. Brown; "Dark current and band profiles in low defect density thick multilayered GaAs/InAs self-assembled quantum dot structures for infrared detectors". Journal of Applied Physics, **104**, (2008), 113115. https://doi.org/10.1063/1.3039799

[175]: S. Martini, A.A. Quivy, E.C.F. da Silva, J.R. Leite, "Real-time determination of the segregation strength of indium atoms in InGaAs layers grown by molecular-beam epitaxy", Appl. Phys. Lett. **81,** (2002), 2863–2865. https://doi.org/10.1063/1.1513182

[176]: G. R. Bell, J. G. Belk, C. F. McConville, and T. S. Jones, "Species intermixing and phase transitions on the reconstructed (001) surfaces of GaAs and InAs" Phys. Rev. B **59**, (1999), 2947–2955. https://doi.org/10.1103/PhysRevB.59.2947

[177]: S. Martini, A. A. Quivy, T. E. Lamas, and E. C. F. da Silva, Real-time RHEED investigation of indium segregation in InGaAs layers grown on vicinal GaAs(001) substrates, Phys. Rev. B **72**, (2005), 153304. https://doi.org/10.1103/PhysRevB.72.153304

[178]: A. Alzeidan, T. F. de Cantalice, K. D. Vallejo, P. J. Simmonds and A. A. Quivy, "Influence of the InAs coverage on the performance of submonolayer-quantum-dot infrared photodetectors grown with a (2×4) surface reconstruction," 35th Symposium on Microelectronics Technology and Devices (SBMicro), (2021), 1-4. https://doi.org/10.1109/SBMicro50945.2021.9585765

[179]: R. Kaspi, K.R. Evans, "Improved compositional abruptness at the InGaAs on GaAs interface by presaturation with In during molecular-beam epitaxy", Appl. Phys. Lett. **67,** (1995), 819–821. https://doi.org/10.1063/1.115454

[180]: M. Kaminska, Z. Liliental-Weber, E. R. Weber, T. George, J. B. Kortright, F. W. Smith, B-Y. Tsaur, A. R. Calawa; Structural properties of As-rich GaAs grown by molecular beam epitaxy at low temperatures. Appl. Phys. Lett. **54,** (1989), 1881–1883. https://doi.org/10.1063/1.101229

[181]: Y. Horikoshi and M. Kawashima, "Growth mechanism of GaAs during Migration-enhanced epitaxy at low growth temperatures", Jpn. J. Appl. Phys., **28**, (1989), 200–209. https://doi.org/10.1143/JJAP.28.200

[182]: V. M. O. Curbelo, A. Alzeidan and A. A. Quivy, "Capping of InAs quantum dots by migration enhanced epitaxy," 36th Symposium on Microelectronics Technology (SBMICRO), 2022, 1-4. https://doi.org/10.1109/SBMICRO55822.2022.9881016

[183]: A.R Kovsh, A.E Zhukov, A.Yu Egorov, V.M Ustinov, Yu.M Shernyakov, M.V Maximov, V.V Volovik, A.F Tsatsul'nikov, Yu.V Musikhin, N.N Ledentsov, P.S Kop'ev, D Bimberg, Zh.I Alferov, "Molecular beam epitaxy (MBE) growth of composite (In,Al)As/(In,Ga)As vertically coupled quantum dots and their application in injection lasers", Journal of Crystal Growth, **201–202**, (1999), 1117-1120. https://doi.org/10.1016/S0022-0248(98)01538-3

[184]: P. B. Joyce, T. J. Krzyzewski, G. R. Bell, T. S. Jones, E. C. Le Ru, and R. Murray, "Optimizing the growth of 1.3 μm InAs/GaAs quantum dots", Phys. Rev. B **64**, (2001), 235317. https://doi.org/10.1103/PhysRevB.64.235317

[185]: O.G. Schmidt, N. Kirstaedter, N.N. Ledentsov, M.H. Mao, D. Bimberg, V.M. Ustinov, A.Y. Egorov, A.E. Zhukov, M.V. Maximov, P.S. Kop'ev, Zh.I. Alferov, "Prevention of gain saturation by multi-layer quantum dot lasers" Electron. Lett. **32**, (1996), 1302-1304. https://doi.org/10.1049/el:19960851

[186]: K. Akahane, N. Yamamoto, and T. Kawanishi, "Fabrication of ultra-high-density InAs quantum dots using the strain-compensation technique". Physica Status Solidi (a), **208**, (2010), 425–428. https://doi.org/10.1002/pssa.201000432

[187]: M.S. Claro, D.G. Stroppa, E.C.F. da Silva, A.A. Quivy, "Strong photovoltaic effect in high-density InAlAs and InAs/InAlAs quantum-dot infrared photodetectors", Sensors and Actuators A: Physical, **315**, (2020), 112262. https://doi.org/10.1016/j.sna.2020.112262

[188]: H. Cotal, C. Fetzer, J. Boisvert, G. Kinsey, R. King, P. Hebert, and N. Karam, "III–V multi junction solar cells for concentrating photovoltaics". Energy Environ. Sci. **2**, (2009), page 178. https://doi.org/10.1039/b809257e

[190]: S.S. Ruvimov, P. Werner, K. Scheerschmidt, U. Gosele, J. Heydenreich, U. Richter, N.N. Ledentsov, M. Grundmann,D. Bimberg, V.M. Ustinov, A.Yu. Egorov, P.S. Kop'ev, and Zh.I. Alferov, "Structural characterization of (In,Ga)As quantum dots in a GaAs matrix" Phys. Rev. B **51,** (1995), 14766(R). https://doi.org/10.1103/PhysRevB.51.14766

[191]: S. Koshiba, Y. Nakamura, M. Tsuchiya, H. Noge, H. Kano, Y. Nagamune, T. Noda, and H. Sakaki; "Surface diffusion processes in molecular beam epitaxial growth of GaAs and AlAs as studied on GaAs (001)-(111)B facet structures", J. Appl. Phys. 76, (1994), 4138–4144, http://dx.doi.org/10.1063/1.357364

[192]: J.M. Moison, F. Houzay, F. Barthe, J.M. Gérard, B. Jusserand, J. Massies, and F.S. Turco-Sandrorff, "Surface segregation in III-V alloys", J. Cryst. Growth **111**, (1991), 141-150. http://dx.doi.org/10.1016/0022-0248(91)90962-5